UNIVERSITEIT VAN PRETORIA
UNIVERSITY OF PRETORIA
YUNIBESITHI YA PRETORIA
Denkleiers • Leading Minds • Dikgopolo tša Dihlalefi

FLUID-STRUCTURE INTERACTION INVESTIGATION OF A MEDIUM-SIZED HELIOSTAT

By:
Joshua Raymond Wolmarans

Supervisor:
Prof KJ Craig

Submitted in partial fulfilment for the degree of
Master of Engineering (Mechanical)

Department of Mechanical and Aeronautical Engineering
2018

UNIVERSITY OF PRETORIA

ABSTRACT

Title: Fluid-structure interaction investigation of a medium-sized heliostat

Author: Joshua Raymond Wolmarans

Student number: 10030982

Study leader: Prof KJ Craig

Renewable energy, particularly solar energy is at the forefront of the fight against fossil fuels. Concentrated Solar Power plants utilizing heliostats, large reflecting mirrors, to concentrate the sun's solar energy onto a central tower are one are the main solar technologies in use today. These plants consist of hundreds to hundreds of thousands of heliostats. The heliostats in most cases make up the largest portion of initial capital expenditure of a solar plant. Consequently, the design of these heliostats is an important area of research to enable Concentrated Solar Power to be a viable competitor to not only fossil fuels but also photovoltaic solar technologies.

Vortex shedding and the resultant transient loadings on a medium sized heliostat are investigated in this paper. Reynolds-Averaged Navier-Stokes (RANS) Computational Fluid Dynamics (CFD) of an operational heliostat is used as a validation case. The Atmospheric Boundary Layer (ABL) is characterized and optimized. The ABL is implemented as the inlet flow boundary condition for both the RANS and Stress-Blended Eddy Simulation (SBES) simulations. The SBES Scale-Resolving Simulation (SRS) model was used which provided the transient peak wind loadings necessary to investigate the structural response of the heliostat. The synthetic turbulence technique used at the inlet of the SBES simulation was the Vortex Method. This method appears to produce unphysical pressure spikes in the flow but their effect appears to be negligible. The SBES results show a strong likeness to the experimental results of Peterka (1986) with a comparable mean and peak loading distribution. The SBES results couldn't be accurately compared to the experimental results of Huss et al (2011) due to the uncertainty of the turbulence intensity in the experimental values. The transient SBES CFD pressure was implemented in a one-way FSI simulation. These simulations shed light on the structural response of the heliostat to the transient wind loading. The results showed that the response of the heliostat conformed to and depended on the mode shapes and frequencies of the heliostat structure more so than the vortex shedding frequencies. The results from the transient structural analysis using the temporal SBES heliostat surface pressure fields as input indicate that the method holds promise in predicting the transient response of heliostats. Importantly it can be concluded that due to the difference in frequencies between the vortex shedding and modal frequencies, the structure is safe from self-excitation.

ACKNOWLEDGMENTS

I would like to my parents for their support and giving me the ability to complete this Master's degree. They have always encouraged me to do what I love and have been generous enough to allow me to pursue my dreams. Without them it would not be possible to be where I am today.

I would like to thank my girlfriend, Leandra Pienaar for her continuous support, constant encouragement and help. Without her this Master's would definitely have been delayed somewhat.

To my study leader, Prof Craig, I would like to thank you for guiding me through this very lengthy process. Thank you for steering me in the right direction and motivating me on a weekly basis, your guidance is much appreciated and will never be forgotten.

I would like to thank Dawie Marais for his help and guidance, having done a previous Master's thesis on heliostats his knowledge was invaluable. I would also like to thank Qfinsoft for their support with the ANSYS Fluent software. Finally, I would like to thank the CHPC and Dr. Charles Crosby for making the large amount of computing power at the CHPC available. Without this all the work in chapter 5 and 6 would not be possible.

TABLE OF CONTENTS

APPENDICES

LIST OF FIGURES

LIST OF TABLES

LIST OF SYMBOLS

Symbol	Explanation	Unit
a_i	Displacement components at a solid boundary	
A_{Ref}	Reference area	[m^2]
$C_{F_{x,y,z}}$	Force coefficients in the x,y,z direction	
$C_{MB_{x,y,z}}$	Base moment coefficient about x,y axis	
$C_{MH_{x,y,z}}$	Hinge moment coefficient about x,y axis	
C_d	Drag coefficient	
C_{CFD}	Loading coefficient from CFD	
C_{EXP}	Loading coefficient from experiment	
C_{ijkl}	Constitutive matrix	
C_s	Smagorinsky constant	
D_ω	Cross diffusion term of SST k- ω	
E	Empirical constant	
Er	Error	[%]
f	Frequency	[Hz]
f_{at}	Atmospheric attenuation factor	
f_i	Force in i,j,k direction	[N]
f_{int}	Intercept factor	
f_{sb}	Shadowing and blocking factor	
$f_{x,y,z}$	Force in x,y,z direction	[N]
$G_{k,\omega}$	Production of k or ω	
G	Filter function	
h	Reflector height	[m]
i, j, k	Cartesian coordinates	
$I_{u,v,w}$	Turbulence intensity in the x,y,z direction	[%]
k	Kinetic energy	[m^2/s^2]
k_p	Kinetic energy at wall adjacent cell centroid	[m^2/s^2]
K_s	Physical roughness height	[m]
L	Length	[m]
l_o	Integral length scale	[m]
L_s	Mixing length for sub grid scales	[m]

$M_{B_{x,y}}$	Base moment about x,y axis	[Nm]
$M_{H_{x,y}}$	Hinge moment about x,y axis	[Nm]
n	Local coordinate normal to the wall	
n_i	Unit normal	
P, p	Pressure	[Pa]
Q	Q criterion	[s^{-2}]
q_{Ref}	Reference dynamic pressure	[Pa]
Re	Reynolds number	
S	Modulus of the mean rate of strain tensor	[s^{-1}]
St	Strouhal number	
t	Time	[s]
t_i^f	Fluid traction vector	
t_i^s	Solid traction vector	
U	Velocity	[m/s]
$u_{i,j,k}$	Velocity in x,y,z coordinates	[m/s]
u_{Ref}	Reference velocity	[m/s]
u_p	Mean velocity at wall adjacent cell centroid	[m/s]
u^+	Dimensionless velocity	
u^*	Friction velocity	[m/s]
u', v', w'	Variances of velocity fluctuations	
V	Volume	[m^3]
x, y, z	Cartesian coordinate directions	
$Y_{k,\omega}$	Dissipation of k, ω	[m^2/s^3]
		[s^{-1}]
y_p	Distance to wall adjacent cell centroid	[m]
y^+	Dimensionless distance from the wall	
z_o	Aerodynamic roughness length	[m]
z_{Ref}	Reference height in z direction	[m]

Greek letters

α	Elevation angle	[^{o}]
β	Wind direction angle	[^{o}]
Γ	Circulation	

δ_{ij}	Kronecker delta	
Δ	Cell volume	[m^3]
ε	Dissipation rate	[m^2/s^3]
ϵ_{kl}	Strain	
η	Efficiency	[%]
κ	von Karman's constant	
μ	Dynamic viscosity	[kg/ms]
μ_t	Turbulent viscosity	[kg/ms]
ν	Kinematic viscosity	[m^2/s]
ξ	Total number of data points	
ρ	Density	[kg/m^3]
ρ_{mr}	Mirror reflectivity	
σ_{ij}	Stress	[Pa]
τ_{ij}	Shear stress/Reynolds stress	[Pa]
τ_w	Wall shear stress	[Pa]
φ	Data point	
ω	Specific dissipation	[s^{-1}]
ω_k	Angular velocity	[rad/s]
Ω	Vorticity	[rad/s]
Ω_{ij}	Rate of rotation tensor	

Abbreviations

ABL	Atmospheric Boundary Layer
BCD	Bounded Central Difference
CD	Central Difference
CFD	Computational Fluid Dynamics
CFL	Courant Friedrichs Lewy
CHPC	Centre for High Performance Computing
CSP	Concentrated Solar Power
DDES	Delayed Detached Eddy Simulation
DES	Detached Eddy Simulation
ELES	Embedded Large Eddy Simulation
FEM	Finite Element Method
FFT	Fast Fourier Transform
FSI	Fluid Structure Interaction

GGI	General Grid Interface
GIS	Grid Induced Separation
GUI	Graphical User Interface
HCL	Heliostat Centre Line
HFC	Heliostat Field Collector
IDDES	Improved Delayed Detached Eddy Simulation
LES	Large Eddy Simulation
NITA	Non Iterative Time Advancement
PSD	Power Spectral Density
PV	Photovoltaic
PVC	Polyvinyl Chloride
RANS	Reynolds Averaged Navier Stokes
RKE	Realizable k-ε model
RMS	Root Mean Square
SBES	Stress Blended Eddy Simulation
SD	Standard Deviation
SDES	Shielded Detached Eddy Simulation
SKE	Standard k-ε model
SRS	Scale Resolving Simulation
SST	Shear Stress Transport model
STERG	Solar Thermal Energy Research Group
TTH	Torque Tube Heliostat
UDF	User Defined Function
URANS	Unsteady Reynolds-Averaged Navier-Stokes
WALE	Wall Adapting Local Eddy viscosity model
WMLES	Wall Modelled Large Eddy Simulation

1 INTRODUCTION

1.1 BACKGROUND

It is globally accepted that there is a dire need for renewable energy due to the undeniable effects of global warming attributed to the release of greenhouse gases. Greenhouse gases are emitted mainly from the combustion and use of fossil fuels. Not only is the use of fossil fuels detrimental to the environment and sustainability of the planet but they are also limited, as all fossil fuels have a finite lifespan. Nuclear energy is a greener alternative compared to coal and oil but also has its drawbacks, such as nuclear waste and the high consumption of water which is slowly becoming a scarce resource. Many different types of renewable energy currently exist such as, wind, hydro, biomass, geothermal and the focus of this study, solar. In the solar energy field there exists a wide variety of different technologies, the two main branches of solar energy are photovoltaic (PV) and Concentrated Solar Thermal (CST). PV in recent years has seen a dramatic decrease in manufacturing costs and is thus currently the cheapest solar option. CST works by focusing the sun's energy on a receiver and transferring that energy to be used in a thermal cycle to generate electricity. There is currently a push to decrease the costs of CST plants around the world to make them a viable competitor to PV.

CST plants are fundamentally made up of the same three subsystems, namely the collector fields, solar receiver and the power generation systems. An advantage of CST is the option to have additional thermal storage facilities whereby the thermal energy can be reserved and utilised when there is limited solar radiation. CST plants are attractive in that they can easily be combined with a traditional fossil fuel power generation plant to increase the efficiency of the plant or have the fossil fuel plant provide power when there is limited solar radiation.

There are four main types of CST technologies in use today, these are the parabolic trough collector, the linear Fresnel reflector, the heliostat field collector and the parabolic dish reflector. The specific design of each of these technologies varies enormously and the efficiency and output of each is dependent on several variables. This particular project focuses on the heliostat field collector technology, specifically the aerodynamic and structural design of the individual heliostats that make up the collector field. A heliostat field collector plant typically consists of thousands of individual heliostats that can move independently of each other to reflect the sun's solar radiation onto a single central receiver tower. A working fluid is then heated by the sun's radiation and transported to a thermal cycle power plant to generate electricity.

Heliostat Field Collector (HFC) plants are the most recent of the CST technologies. The first HFC plant to be built and operated was the Solar One plant constructed in the Mojave Desert in California. This plant was built in 1981 and had a capacity of 10MW. It was followed in 1995 by Solar Two, both plants have since been decommissioned. HFC plants are usually quite large as they need to benefit from economy of scale in order to offset the extremely high costs associated with the technology.

It is estimated that roughly one third of the initial capital cost of an HFC plant comes from the heliostat field (Sun, et al., 2014). This clearly demonstrates the opportunity to drive down the costs of the heliostats which is the aim of this project. A pie chart breaking down the various costs of different CST technologies is seen in Figure 5. Focus in this thesis is given to the modelling of an LH-2 like heliostat with Computational Fluid Dynamics (CFD), Finite Element Method (FEM) and Fluid Structure Interaction (FSI) to attempt to understand the complex flow phenomena and use this information to drive a better, cheaper design. Whenever the term LH-2 is mentioned throughout this report it is inferred that the geometry of the heliostat is similar to that of the LH-2 heliostat. The results are therefore not directly applicable to the performance of the actual LH-2 heliostat in operation at Ivanpah.

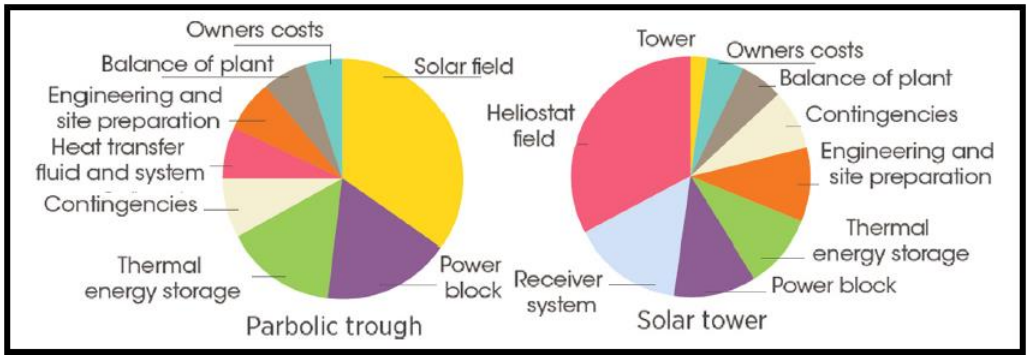

Figure 1: Breakdown of different CST costs (Sun, et al., 2014).

1.2 PROBLEM STATEMENT

Heliostats are active pieces of hardware, due to the fact that they are constantly moving, their function in reflecting the sun's solar radiation requires that they constantly track the sun's position with movement about at least two axes. The angle of the mirror constantly changes throughout the day, leading to varying wind loads on the heliostat, coupled with the individual heliostat placement in the field, creates fluctuating conditions that need to be designed for. Heliostats that are located on the outer edge of the heliostat field face greater wind loads than those that are sheltered near the centre. For optimal operation the heliostats are required to be as stiff as possible, both statically and dynamically.

The fact that the heliostats must face the natural elements, particularly wind, makes their design a highly complex task. Atmospheric Boundary Layer (ABL) modelling is needed to try and replicate the conditions experienced by the heliostats on the ground, ABL modelling is in itself a complicated area of science and numerous papers exist detailing the best approaches that should be used when modelling this in CFD. Many factors can influence the models such as boundary and inlet conditions. The nature of wind loading is in itself very unpredictable which makes modelling it tough. This leads to the problem of over and under-design of the heliostats. Over-design due to the poor prediction of the wind loads means that the heliostat structures are larger than they need to be and ultimately more expensive than they should be. This is the main issue that this project attempts to deal with, investigating methods to ultimately reduce cost. Under-design is just as much of an issue if not more of an issue as this would lead to the inevitable failure of the heliostat before its designed lifespan, causing excessive maintenance costs and possibly the closure of an operational plant.

The combination of CFD, FEA and FSI make the realisation of parametric design possible. There is no need to create a physical model that needs to be tested, altered and retested based on the results as this can now be done computationally with the final optimised model being built and validated. The problem with wind tunnel experiments is that it is equally as challenging to replicate the ABL conditions for the tunnel as it is in CFD with the added drawback of high operational costs.

There are currently a few studies that attempt to address these problems both numerically using CFD and FEA as well as experimentally in wind tunnels. No high fidelity FSI work on heliostats currently exists in the available open literature. Scale Resolving Simulation (SRS) CFD work on heliostats is currently very limited, with no FSI simulations either one-way or two-way having been conducted. There exists a gap where this project and work may benefit the future design of heliostats and eventually drive down their costs in order to become competitive with solar PV technology in the near future. This will be highly beneficial to the renewable energy market and the world in general.

1.3 OBJECTIVES

- Correct modelling of the ABL, using the experimental work of Peterka the ABL needs to be modelled as accurately as possible with the use of RANS methods. The ABL will be used throughout the thesis as the inlet flow condition.
- Validation of the CFD methods used, the RANS, URANS, and FSI methods need to be validated in order for these simulations to be implemented with any degree of trust.
- Modelling the vortex shedding phenomenon behind a medium sized heliostat as accurately and cheaply as possible using RANS CFD methods.
- Modelling vortex shedding as accurately as possible using SRS CFD methods in a manner that these can then be implemented and investigated via FSI
- Implementing the SRS high fidelity CFD results in an FSI environment to determine the effects of the vortex shedding on the heliostat structure and the response of the structure.

1.4 LAYOUT/SUMMARY

In this chapter a brief background is given into CST technology and specifically heliostats as this is the focus of this project. Through this introduction a basic understanding of the technology should be attained. A problem statement is given and demonstrates the need for such research in this field. Objectives of the study are listed.

In chapter 2 a literature study is performed to achieve a deeper understanding of CST, heliostats and the science behind the steps and procedures followed in this project. Further background will be given on CST and heliostats in general before focusing on the LH-2. Aerodynamic concepts relevant to heliostats including external flow around bluff bodies, vortex shedding and turbulence will be covered. A brief introduction into the CFD, FEM and FSI used later is also included in the literature study.

Chapter 3 consists of the setup and validation of the ABL using the work of Peterka (1986), the validation of the LH-2 heliostat and the FSI validation. Modal analysis, FSI and 2-dimensional CFD are investigated in

chapter 4. Chapter 5 includes the SRS simulations performed on the LH-2. The SRS CFD results are used in chapter 6 to perform 1-way FSI of the LH-2. The thesis is concluded in chapter 7.

2 LITERATURE REVIEW

2.1 INTRODUCTION

There is currently a vast amount of research and information relating to solar power and heliostats in general. Heliostat technology is regarded as the single biggest avenue for improvements in the reflector sector. New research is constantly being conducted and becoming available. The aim of this literature review is to briefly cover the more important aspects relating to the aerodynamics and design of a heliostat.

This literature review will look at the design of heliostat fields and how the layout affects the output and aerodynamics of the heliostats. Wind loading and bluff body aerodynamics pertaining to this study will be reviewed followed by computational fluid dynamics in the ABL and turbulent flows with a brief review of FSI. Finally, previous experimental and numerical studies will be reviewed and discussed.

Currently and for the foreseeable future, the largest HFC plant ever commissioned and under operation is the Ivanpah plant in California, the plant consists of three central towers each at a height of 140m. Each tower has the ability to produce 130MW of electricity using forced-recirculation drum-type boilers with a working fluid temperature of 560˚C. The most impressive aspect of this plant is the enormous number of individual heliostat mirrors. There are a total of 173 500 mirrors in the three fields and each mirror is roughly 15m^2, the mirrors used at Ivanpah are the LH-2. The plant as well as the mirror design can be seen in Figure 2 and Figure 3, respectively.

Figure 2: Ivanpah plant, California (Brightsource, 2014).

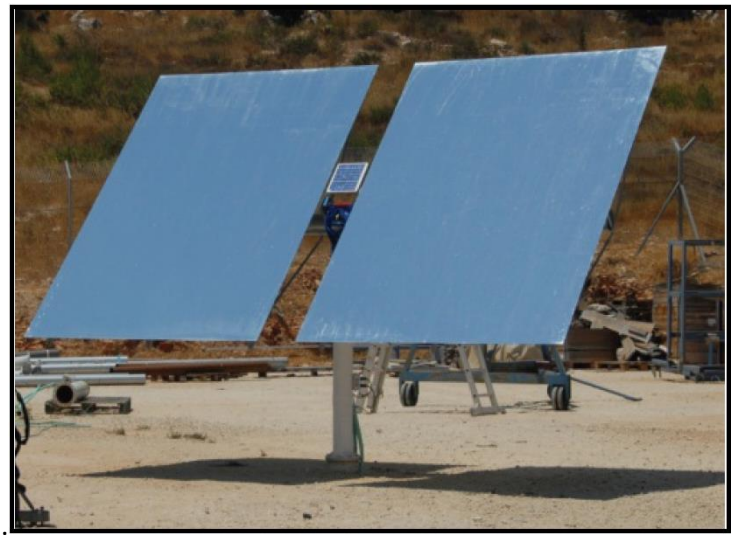

Figure 3: The LH-2 heliostat used in the Ivanpah plant (Huss, et al., 2011) .

2.2 HELIOSTAT FIELD DESIGN

The Heliostat field design is just as important if not more important than the individual heliostat design, the collector field's characteristics are based on studies that aim to minimize the cost and maximize the annual collected energy. These studies take into consideration the central receiver, receiver tower, plant and the overall heliostat collector field. Two main field designs have been developed, the first being a central tower, where the heliostats are placed all around the central tower. The tower may be offset from centre in order to maximize the irradiance depending on the location of the sun relevant to the plant and the plant relevant to the sun. The second field design is the north or south design, in a north configuration the tower is situated to the south of the collector field, this is done in the Northern hemisphere to maximize collection in accordance with the position of the sun. The configuration is the opposite for the Southern hemisphere (Mavis, 1989).

The performance of a heliostat field is defined by the optical efficiency. This is determined by the ratio of the net power obtained by the receiver with the product of the direct insolation times the total mirror area. The optical efficiency includes the cosine effect, blockage, shadowing, atmospheric transmission, mirror reflectivity and receiver spillage. The three main factors affecting the optical efficiency are the cosine effect, shadowing and blockage, these are illustrated in the Figure 4.

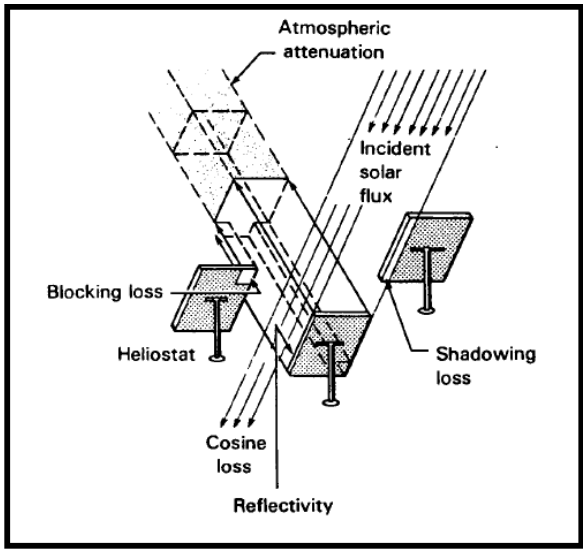

Figure 4: Collector field optical loss process (Mavis, 1989).

The amount of insolation reflected by the heliostat is directly proportional to the amount of sunlight received. The reflected power is proportional to the cosine of the angle (cosine effect) between the heliostat mirror normal and the incident sun rays; the ratio of the projected mirror area that is perpendicular to the sun's rays to the total area of the heliostat determines the magnitude of the cosine effect (Mavis, 1989). Some of the sunlight reflected by the heliostats does not reach the receiver due to scattering and absorption by the atmosphere, this type of loss is called attenuation loss. These losses increase when water vapour and aerosol content in the atmosphere are high. An equation given by (Collado & Guallar, 2013) to describe the optical efficiency is given below:

$$\eta(x,y,t) = \rho_{mr} \cos\omega(x,y,t) f_{at}(x,y) f_{int}(x,y,t) f_{sb}(x,y,t,neighbourheliostat) \quad (1)$$

where:

$\eta = efficiency$
$\rho_{mr} = mirror\ reflectivity$
$\cos\omega = cosine\ of\ incidence\ angle$
$f_{at} = Atmospheric\ attenuation\ factor$
$f_{int} = Intercept\ factor$
$f_{sb} = Shadowing\ and\ blocking\ factor$

The eventual layout of the heliostat field is thus of great significance to the success of an HFC plant. Clearly it would be ideal to place the heliostats as close as possible to the receiver and to each other to minimize costs. This is however, where the issues of shadowing and blocking come into effect, the closer the heliostats are to one another the greater these effects become. Blocking has a more pronounced effect on the eventual layout of the heliostat field than shadowing. Placing the heliostats farther radially means that the receiver becomes farther away thus the heliostats need to be placed farther apart with a radial separation in order to mitigate the loss to the receiver due to blockage. In the radial stagger arrangement developed by the University of Houston, the heliostats are laid out along radial spokes emanating from the central receiver. This ensures there is no heliostat directly in front of another causing blockage. This layout

can be seen in Figure 5. Heliostats close to the tower have field densities greater than 40% due to less significant shading effects and are typically spaced less than 20m apart for a typical heliostat mirror area of 120m^2. With increasing distance from the central tower, the field density decreases to less than 20% and spacing between heliostats of up to 45m at the outer boundary of the filed (Noone, et al., 2012).

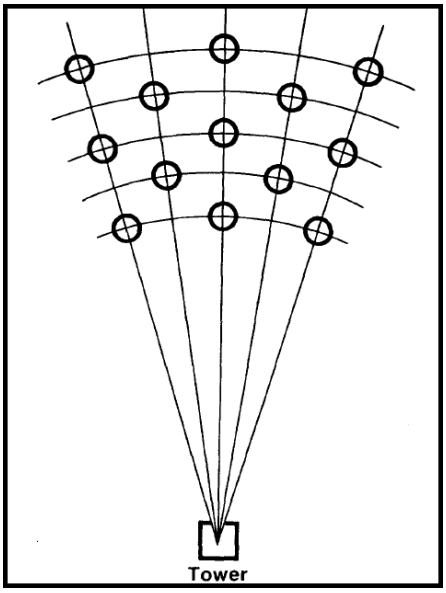

Figure 5: Radial stagger Heliostat layout (Mavis, 1989).

It stands to reason that the layout of a heliostat field is an avenue for its own research as many studies have been concluded on the design and optimization of the layout of the field. Research in this field is now aimed at computationally efficient models to optimize existing or new fields. Research done by (Noone, et al., 2012) introduces an efficient optimization model using a similar efficiency equation as given in Eq.1 with the same parameters and a staggered field layout previously discussed to try and optimize the annual insolation from the heliostat filed. In this study they were able to increase the optical efficiency by 0.36% and reduce the land area by 15.8%. The PS10 power tower plant in Andalusia, Spain was used as the test case, the original heliostat layout can be seen in Figure 6 together with the optimized layout.

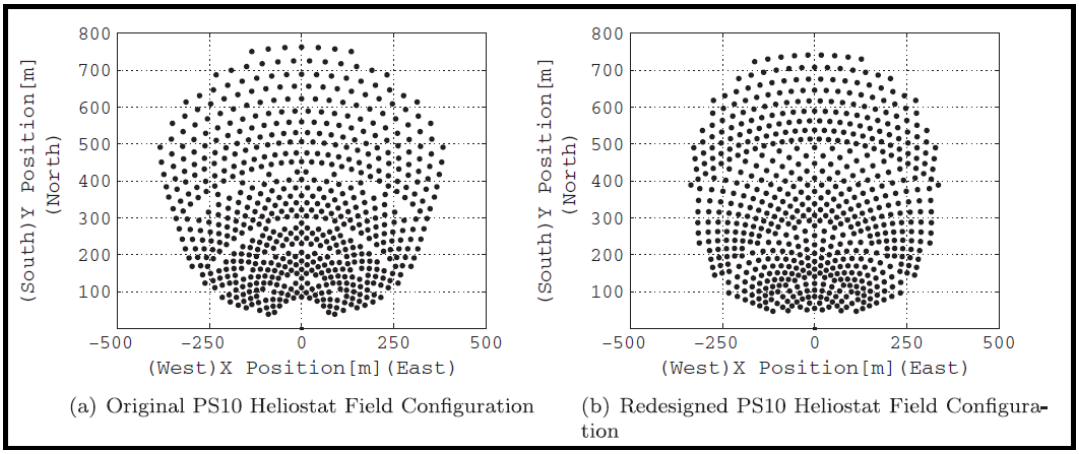

Figure 6: Original (a) and optimised (b) PS10 plant (Noone, et al., 2012).

(Lutchman, et al., 2014) showed that although optimizing an existing field layout is less computationally expensive than optimizing a field from scratch, it is not necessarily optimal. Allowing heliostat placement independent of a priori pattern may result in better performance. (Lutchman, et al., 2014) successfully developed an algorithm that is computationally cheap and was able to effectively redesign the same PS10 plant with an increase of 1.2% in annual intercepted energy. In Figure 7 the original PS10 plant can be seen compared to the optimized plant.

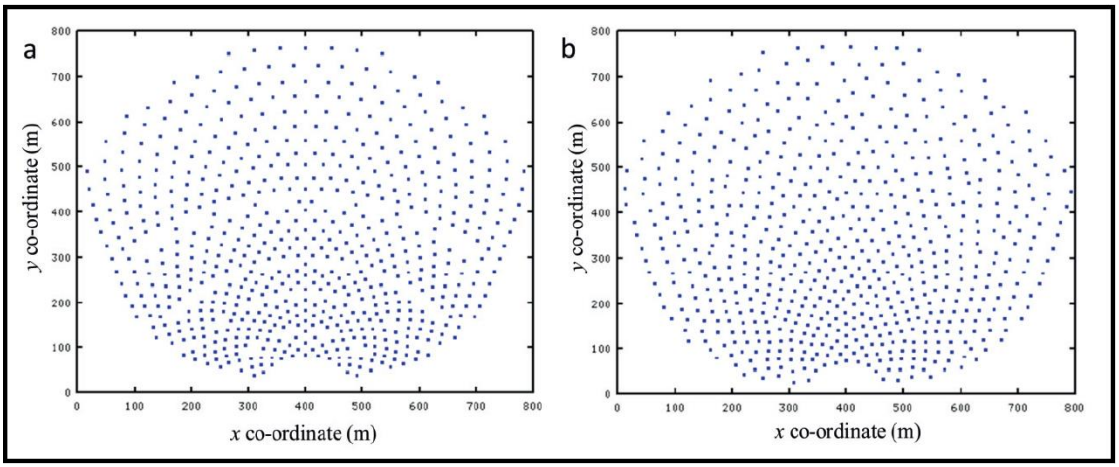

Figure 7: Original (a) and optimised (b) PS10 plant (Lutchman, et al., 2014).

The previous field layout studies mentioned above simply look at the optimal amount of solar radiation that can reach the receiver, due to the placement of the heliostats in the field without considering any aerodynamic or structural loads the heliostats may experience. Evidently ensuring the heliostats can withstand the numerous loads and last for their intended lifespan is a critical aspect of the initial design. Apart from changing and altering the individual heliostat, there are measures that can be put in place to reduce the aerodynamic loads on the field. (Peterka, et al., 1986) performed atmospheric boundary layer wind tunnel experiments and found that the mean wind loads on heliostats in operational positions within the field could be related to the area of upwind blockage of the heliostats. Wind load reductions of up to 70% could be achieved with the implementation of fences and barriers in the heliostat field (Peterka, et al., 1986). In Figure 8 a possible fence configuration can be seen.

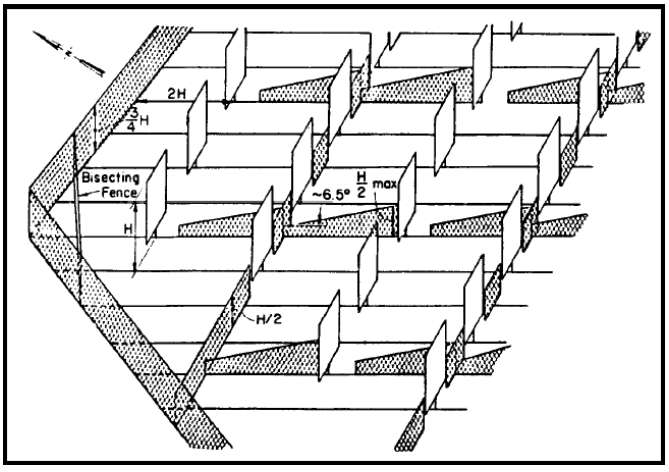

Figure 8: Potential fence design to reduce wind loads in a heliostat field (Peterka, et al., 1986).

2.3 HELIOSTAT AERODYNAMICS

The fact that heliostats operate while exposed to the elements, particularly the ABL, means they are subjected to both static forces, due to pressure differences and, dynamic forces, due to both the upstream buffeting flow and the downstream vortex shedding. The aim of this section is to attempt to shed some light on these phenomena.

Aerodynamic forces and moments are usually expressed in non-dimensional form using force and moment coefficients. This can often simplify problems and allow parameterization and scaling. In order to ensure that results are consistent, a coordinate system needs to be used to define the wind loading coefficients, characteristic lengths and orientation angles. The coordinate system adopted in this dissertation is that of (Peterka, et al., 1986) and it is used throughout, the coordinates along with the force and moment coefficients can be seen in Figure 9.

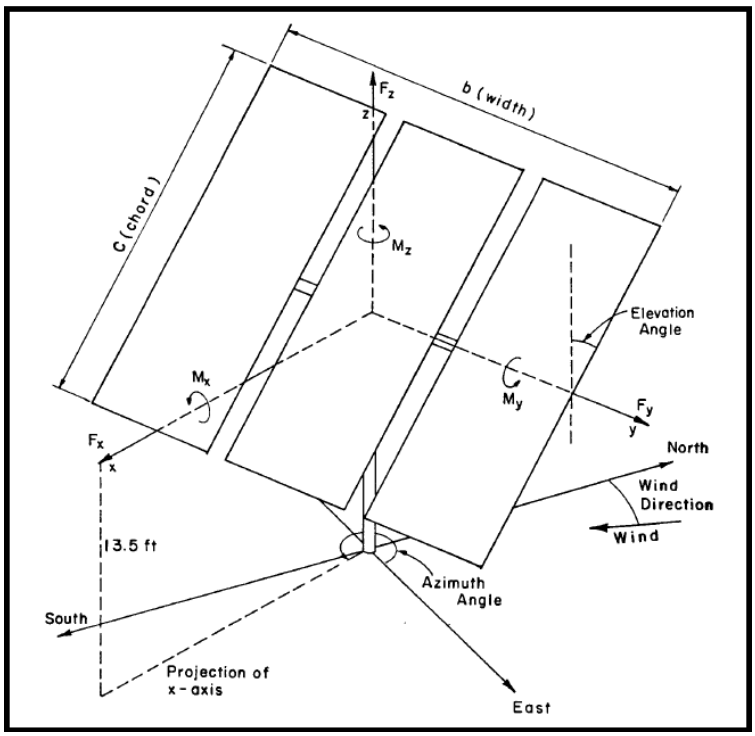

Figure 9: Force and Moment Coordinate system (Peterka, et al., 1986).

Using this coordinate system, the non-dimensional force and moment coefficients for the heliostat are given below:

- Force coefficients

$$C_{F_x} = \frac{F_x}{A_{Ref} q_{Ref}} \; ; \; C_{F_y} = \frac{F_y}{A_{Ref} q_{Ref}} \; ; \; C_{F_z} = \frac{F_z}{A_{Ref} q_{Ref}} \tag{2}$$

where:

$C_{F_{x,y,z}} = Force\ Coefficient\ in\ the\ x,y,z\ direction$
$F_{x,y,z} = Wind\ loading\ in\ x,y,z\ direction\ [N]$
$A_{Ref} = Mirror\ Area\ [m^2]$
$q_{Ref} = Reference\ dynamic\ pressure\ [Pa]$

- Hinge moment coefficients

$$C_{MH_x} = \frac{M_{H_x}}{A_{Ref} q_{Ref} h}\ ;\ C_{MH_y} = \frac{M_{H_y}}{A_{Ref} q_{Ref} h} \tag{3}$$

where:

$C_{MH_{x,y}} = Hinge\ moment\ Coefficient\ about\ the\ x,y\ axis$
$M_{H_{x,y}} = Hinge\ moment\ about\ the\ x,y\ axis\ [Nm]$
$h = Reflector\ height\ [m]$

The moments given in eq. 3 represent the moments about the torque tube and the pylon in the centre of the mirror, the moments about the base of the heliostat can also be calculated using equation 3 as seen in equation 4.

- Base moment coefficients

$$C_{MB_x} = \frac{M_{B_x}}{A_{Ref} q_{Ref} h}\ ;\ C_{MB_y} = \frac{M_{B_y}}{A_{Ref} q_{Ref} h} \tag{4}$$

where:

$C_{MB_{x,y}} = Base\ moment\ Coefficient\ about\ the\ x,y\ axis$
$M_{B_{x,y}} = Base\ moment\ about\ the\ x,y\ axis\ [Nm]$
$h = Reflector\ height\ [m]$

- Dynamic pressure

$$q_{Ref} = \frac{1}{2}\rho u_{Ref}^2 \tag{5}$$

where:

$\rho = Density\ of\ air\ \left[\frac{kg}{m^3}\right]$
$u_{Ref} = Reference\ velocity\ \left[\frac{m}{s}\right]$

Due to the large flat mirrors that are normally situated relatively perpendicular to the ground, heliostats can be considered to be bluff bodies; bluff bodies are characterised by pressure drag. This type of drag is caused by a high-pressure stagnation region on the front face of the heliostat with a low-pressure region in the separated wake on the rear of the heliostat. Pressure drag is different from friction drag caused by the

viscous effects of the fluid the body is immersed in (White, 2011). Objects such as spheres and flat plates will experience flow separation as the boundary layer transitions from laminar type behaviour to turbulent, for these objects the separation point can be calculated and is dependent on the Reynolds number. For bluff body objects however, flow separation occurs regardless of the boundary layer and is formed at the sharp edges of the body and is insensitive to the Reynolds number for sufficiently high Re. The Reynolds number is the ratio of the inertial forces to the viscous forces in a fluid. When the Reynolds number is low, the viscous effects of the fluid are able to suppress any random tendencies of the flow but as the Reynolds number increases beyond a certain critical point the inertial effects take over and the flow becomes turbulent. The equation for the Reynolds (Re) number is:

$$Re = \frac{\rho u_{Ref} L}{\mu} \tag{6}$$

where:

$\mu = Dynamic\ viscosity\ of\ air \left[\frac{kg}{ms}\right]$

Vortex shedding is an enormously important flow feature of bodies in a fluid as it introduces dynamic loading to the body or structure and if not correctly designed for, can lead to the failure of the given structure. The vortex shedding phenomenon is created when the shear layers, due to the flow separation, cause a vortex sheet to form from the difference in the velocities between the fast-outside flow and the relatively slow wake flow. In a viscous fluid the vorticity created at the boundary diffuses into the bulk of the fluid so that the thickness of the vortical region increases. In Figure 10, it can be seen that the vorticity gathers at down crossing points in the upper layer and up crossing points in the lower layer, this perturbation is amplified by the induced velocities due to the vortices. Eventually, these areas of re-circulating flow known as eddies, swell as the Reynolds number increases. Once the vortex grows large enough it is shed into the wake of the fluid, this process then repeats periodically and is known as the von Karman Vortex Street.

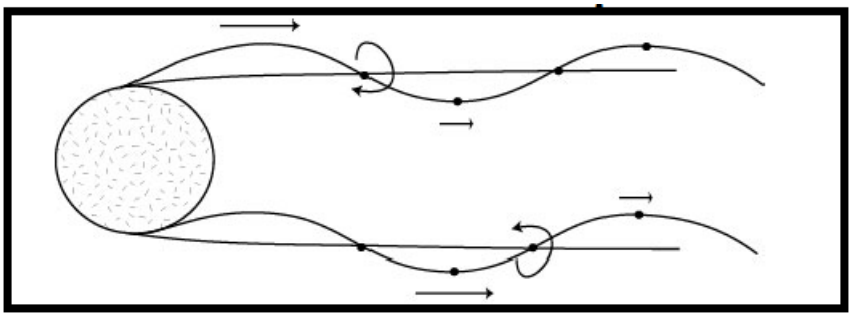

Figure 10: Vortex rollup instability (Techet, 2005).

The dynamic loading is introduced from the shed vortices, as the vortices alternate from each side of the bluff body this causes oscillations in the drag and lift forces on the body. For bluff bodies the frequency of the drag fluctuations is equal to the frequency of the lift fluctuations. For a cylinder in crossflow however the drag fluctuations occur at twice the vortex shedding frequency (Techet, 2005). The oscillations due to

the vortex shedding cause the structure to vibrate, if the vibration of the structure due to the shedding is close to one of the fundamental modes of the structure, resonant frequency may be achieved. Depending on the length of time this resonance is held, this can cause very severe structural damage to the heliostat. It is vitally important then to design the heliostat to ensure that resonance is not achieved for any sustained period. Changes in the design can include; stiffening the structure to alter the natural frequencies away from the vortex shedding frequencies and increasing or decreasing the size of the heliostat to alter the Strouhal number.

The Strouhal number is a dimensionless number that describes oscillating flow mechanisms, specifically vortex shedding. The equation for the Strouhal number is given by:

$$St = \frac{fL_{Ref}}{u_{Ref}} \tag{7}$$

where:

$St = Strouhal\ number$
$f = Shedding\ frequancy\ [Hz]$
$L_{Ref} = Reference\ length\ [m]$

The heliostat, essentially being a flat plate, is expected to produce vortex shedding, which in its operational state presents itself as a large bluff body. In Figure 11, vortex shedding behind a heliostat in an operational configuration is illustrated.

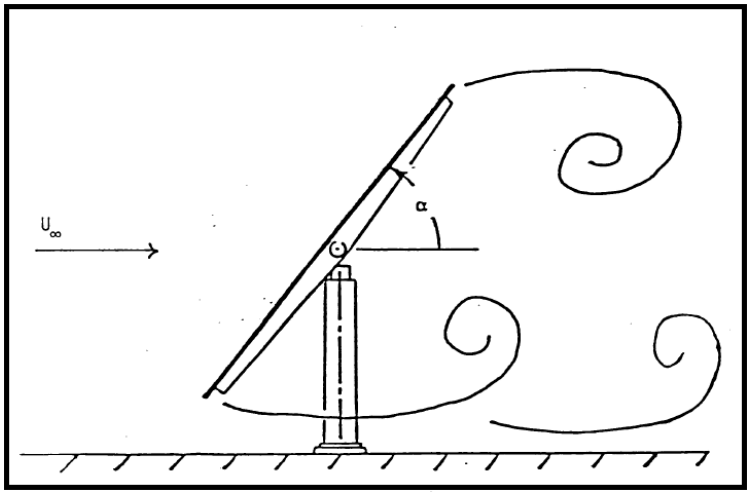

Figure 11: Illustration of vortex shedding behind a Heliostat (Matty, 1979).

An experimental study performed by (Matty, 1979) investigated the Strouhal number of heliostats due to vortex shedding. The study looked at various Reynolds numbers and heliostat height to ground clearance ratios. It was found that the Strouhal number was dependant on the Reynolds number to begin with, but appeared to approach a limit with the increase in Re. It was also found that it was dependent on the height to gap ratio for all Re studied. (Matty, 1979) also performed the experiment using slotted heliostats and it

was found that the difference between the slotted and un-slotted heliostats was negligible. The results of the wind tunnel experiments can be seen in Figure 12.

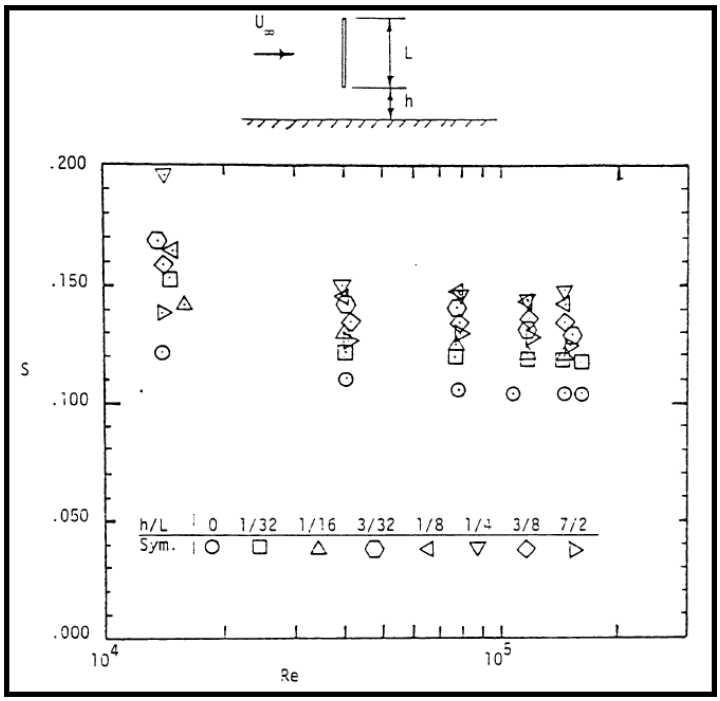

Figure 12: St vs. Re for flat plate (Matty, 1979).

2.4 COMPUTATIONAL FLUID MECHANICS

The heliostats and HFC plant are subject to the ABL which may well be expressed as being turbulent. Turbulence is arguably the most challenging area in fluid mechanics and the most limiting factor in accurate computer simulation of engineering flows. It constitutes a classical multi-scale problem, which is far beyond human intuitive understanding and beyond the resolution capabilities of even the most powerful modern parallel computers (Menter, 2011). Turbulent flows are characterised by their irregularity and randomness, a deterministic approach is nearly impossible and they are usually described statistically. Turbulent flows are diffusive in nature, the turbulence causes rapid mixing with increased rates of momentum, heat and mass transfer. Turbulence can also be described as a continuum phenomenon, where even the smallest eddies present in the flow are significantly larger than the molecular scales, thus turbulence is governed by the equations of fluid mechanics.

A brief description is given relating to turbulent eddies, length scales and energy transfer before moving on to the governing equations of fluid flow. In a fully turbulent flow, turbulence can be considered to consist of eddies of different sizes. An eddy can be seen as a turbulent motion localized over a region *l*, that is at least moderately coherent over this region. Eddies of size *l* have a characteristic velocity *u(l)* and timescale $\tau(l) \equiv l/u(l)$. Eddies in the largest range are characterized by a length scale l_o, which is comparable to the length scale of the flow *L*. We can derive an equation for the length scale of the larger eddies:

$$l_o \propto \frac{k^{\frac{3}{2}}}{\varepsilon} \tag{8}$$

$$k = \frac{1}{2}\left(\overline{u'^2} + \overline{v'^2} + \overline{w'^2}\right) \quad (9)$$

where:

$k = kinetic\ energy \left[\frac{m^2}{s^2}\right]$

$\varepsilon = dissipation\ rate \left[\frac{m^2}{s^3}\right]$

$\overline{u'^2} = variance\ of\ x - velocity\ fluctuation$ *likewise for y and z-direction*

The length scale described in Eq. 8 is usually referred to as the integral length scale. The eddies in the flow field undergo what is called an energy cascade, this is the process whereby energy is transferred from the large eddies to successively smaller eddies. This process continues until the Re of the flow is small enough that the molecular viscosity is effective in dissipating the kinetic energy of the flow. The rate of dissipation is determined by the first process in the sequence which is the transfer of energy from the largest eddies. Kolmogorov argued that the directional biases of the large eddies, those that are a feature of the flow, are lost in the chaotic scale reduction process as energy is transferred to smaller eddies. Hence Kolmogorov stated that "at sufficiently high Reynolds numbers the small-scale turbulent motions are statistically isotropic". This is a highly relevant remark, as this allows the large-scale eddies, which are anisotropic and have the greatest influence on the overall flow, to be resolved in Scale Resolving Simulation (SRS) CFD while the small isotropic eddies can be modelled with high accuracy using turbulence models (Pope, 2000).

The governing equations of fluid flow are the Navier-Stokes equations, these equations can be easily derived using the conservation laws of fluid motion. They are however almost impossible to solve analytically for complex geometries and turbulent flows, for simple flows using assumptions, an analytical expression for the solution can be derived. As the flow becomes progressively more complex, ever increasingly complex numerical methods are needed to find a solution. For turbulent flows such as the ones present in this research, the governing equations can be time-averaged to remove the small scales present in the flow, this results in modified governing equations that are less computationally expensive to solve. These new time-averaged equations are called the Reynolds-Averaged Navier-Stokes (RANS) equations.

In the RANS equations the effect of time averaging means that there are now extra terms in the flow equations due to the interactions between various turbulent fluctuations. Averaging the terms also results in the flow being averaged. This means flow and the turbulent effects on the mean flow are then modelled. These extra terms are calculated and solved using various turbulence models. The computational power used to solve these RANS equations and the various models is relatively cheap and as such RANS has become the preferred method for solving engineering flows.

With the heliostat functioning in the ABL, it is reasonable to assume that the flow is incompressible, and the air can thus be treated as an incompressible gas. The RANS equations for continuity and momentum can be written as:

$$\frac{\partial \rho}{\partial t} + \frac{\partial}{\partial x_i}(\rho u_i) = 0 \quad (10)$$

$$\frac{\partial}{\partial t}(\rho u_i) + \frac{\partial}{\partial x_j}(\rho u_i u_j) = -\frac{\partial p}{\partial x_i} + \frac{\partial}{\partial x_j}\left[\mu\left(\frac{\partial u_i}{\partial x_j} + \frac{\partial u_j}{\partial x_i} - \frac{2}{3}\delta_{ij}\frac{\partial u_l}{\partial x_l}\right)\right] + \frac{\partial}{\partial x_j}\left(-\rho\overline{u_i' u_j'}\right) \quad (11)$$

where:

$u_{i,j} = Mean\ velocity\ component\ in\ i,j\ direction\ \left[\frac{m}{s}\right]$

$t = Time[s]$

$p = Pressure\ [Pa]$

$x_{i,j} = Cartesian\ direction\ component$

$\delta_{ij} = Kronecker\ delta$

These RANS equations have the same general form as the instantaneous Navier-Stokes equations except the velocities and other solution variables are now time-averaged. The RANS equations now have additional terms present that represent the turbulence effects. These additional terms are called the Reynolds stresses, present in the last term of equation 11 and these need to be modelled in order to close equation 11 (ANSYS, 2016).The most common method for modelling the Reynolds stresses employs the Boussinesq hypothesis, which relates the Reynolds stresses to the mean velocity gradients as can be seen in equation 12.

$$\tau_{i,j} = -\rho\overline{u_i' u_j'} = \mu_t\left(\frac{\partial u_i}{\partial x_j} + \frac{\partial u_j}{\partial x_i}\right) - \frac{2}{3}\left(\rho k + \mu_t\frac{\partial u_k}{\partial x_k}\right)\delta_{ij} \quad (12)$$

where:

$\tau_{i,j} = Reynolds\ stress[Pa]$

$\mu_t = Turbulent\ viscosity\left[\frac{kg}{ms}\right]$

The Boussinesq hypothesis is used in the Spalart-Allmaras model, the k-ε models and the k-ω models with the advantage of this approach being the relatively low computational cost associated with the computation of the turbulent viscosity. In the case of the k-ε and k-ω models, two additional transport equations are solved, one for the turbulent kinetic energy, k, and one for the dissipation rate, ε, or the specific dissipation rate, ω. The turbulent viscosity, μ_t is computed as a function of k and ε or ω. The disadvantage of the Boussinesq hypothesis as presented is that it assumes the turbulent viscosity is an isotropic scalar quantity, which is not strictly true (ANSYS, 2016). In this research the k-ε, k-ω and realizable k-ε models are used extensively and are described briefly in the following sections. Later in the thesis a scale resolving model is used in order to resolve features of the fluid flow, the model used there is the Stress Blended Eddy Simulation (SBES) and will be discussed in the relative section.

The standard k-ε model and other two-equation models allow for the determination of both a turbulent length and time scale by solving the separate transport equations. The drawback of some of the k-ε models is their insensitivity to adverse pressure gradients and boundary layer separation, they tend to predict a delayed separation relative to experimental results and thus are not widely used in external aerodynamic applications. With the case of the heliostat however, the point of separation is predetermined by the edges of the reflector and is thus not particularly important. The models also suffer from the over-production of

turbulent kinetic energy in regions with large strain rates, such as near a stagnation point, resulting in inaccurate model predictions. The transport equations for k and ε are seen in Eqs. 13 and 16, respectively.

Transport equation for k:

$$\frac{\partial}{\partial t}(\rho k) + \frac{\partial}{\partial x_i}(\rho k u_i) = \frac{\partial}{\partial x_j}\left[(\mu + \frac{\mu_t}{\sigma_k})\frac{\partial k}{\partial x_j}\right] + G_k - \rho\varepsilon \tag{13}$$

with

$$G_k = -\rho\overline{u_i' u_j'}\frac{\partial u_j}{\partial x_i} = \mu_t S^2 \tag{14}$$

$$S = \sqrt{2S_{ij}S_{ij}} \tag{15}$$

where:

$G_k = Production\ of\ turbulent\ kinetic\ energy$
$S = Modulus\ of\ the\ mean\ rate\text{-}of\text{-}strain\ tensor$

Transport equation for ε:

$$\frac{\partial}{\partial t}(\rho\varepsilon) + \frac{\partial}{\partial x_i}(\rho\varepsilon u_i) = \frac{\partial}{\partial x_j}\left[(\mu + \frac{\mu_t}{\sigma_\varepsilon})\frac{\partial \varepsilon}{\partial x_j}\right] + G_k C_{1\varepsilon}\frac{\varepsilon}{k} - \rho C_{2\varepsilon}\frac{\varepsilon^2}{k} \tag{16}$$

with the turbulent viscosity calculated as follows:

$$\mu_t = \rho C_\mu \frac{k^2}{\varepsilon} \tag{17}$$

where:

$C_{1\varepsilon}, C_{2\varepsilon}, C_\mu, \sigma_k\ and\ \sigma_\varepsilon\ are\ model\ constants\ with\ the\ following\ values$:
$C_{1\varepsilon} = 1.44$
$C_{2\varepsilon} = 1.92$
$C_\mu = 0.09$
$\sigma_k = 1$
$\sigma_\varepsilon = 1.3$

These model constants were derived from experiments and are found to be reliable for a number of industrial flows (ANSYS, 2016).

The use of the Realizable k-ε (RKE) model is recommended relative to other k-ε models (ANSYS, 2016). Some of the benefits from the RKE model include, the accurate prediction of the spreading rate of both planar and round jets and the fact that the RKE is more likely to provide better performance compared to the Standard k-ε(SKE) model for flows involving strong adverse pressure gradients separation and recirculation (ANSYS, 2010). The RKE model attempts to address the deficiencies of the SKE model in two

important ways, firstly, the equation for the turbulent viscosity has been altered from the original constant to a variable form and secondly, it contains a modified transport equation for the dissipation rate. Mathematically the term "realizable" means that the model satisfies certain constraints on the Reynolds stresses that are consistent with the physics of the flow. Looking at the combination of the Boussinesq hypothesis and the eddy viscosity definition, one can obtain an expression for the Reynolds stress in an incompressible strained flow:

$$\overline{u^2} = \frac{2}{3}k - 2v_t\frac{\partial U}{\partial x} \tag{18}$$

with $v_t = \mu_t/\rho$ it is seen that when the strain becomes large enough the normal stress $\overline{u^2}$ which is by definition positive, becomes negative, or "non-realizable". It can also be shown that the Schwarz inequality for shear stress; $\overline{u_\alpha u_\beta}^2 \leq \overline{u_\alpha^2 u_\beta^2}$, can also be violated when the mean strain rate is large. The easiest way to ensure realizability is to make C_μ variable instead of a constant. The new transport equation for the dissipation rate for the RKE model is then:

$$\frac{\partial}{\partial t}(\rho\varepsilon) + \frac{\partial}{\partial x_i}(\rho\varepsilon u_i) = \frac{\partial}{\partial x_j}\left[(\mu + \frac{\mu_t}{\sigma_\varepsilon})\frac{\partial \varepsilon}{\partial x_j}\right] + \rho C_1 S\varepsilon - \rho C_2\frac{\varepsilon^2}{k+\sqrt{v\varepsilon}} \tag{19}$$

with

$$C_1 = max\left[0.43, \frac{\eta}{\eta+5}\right] and\ \eta = S\frac{k}{\varepsilon} \tag{20}$$

The eddy viscosity of equation 17 is computed the same in the RKE model as with the SKE model with the difference being that C_μ is not constant. The new C_μ value is calculated as:

$$C_\mu = \frac{1}{A_0 + A_s\frac{kU^*}{\varepsilon}} \tag{21}$$

with

$$U^* = \sqrt{S_{ij}S_{ij} + \widetilde{\Omega_{ij}}\widetilde{\Omega_{ij}}} \quad ; \quad \widetilde{\Omega_{ij}} = \Omega_{ij} - 2\varepsilon_{ijk}\omega_k \quad ; \quad \Omega_{ij} = \overline{\Omega_{ij}} - \varepsilon_{ijk}\omega_k \quad ; \quad A_s = \sqrt{6}\cos\phi\,,$$
$$\phi = \frac{1}{3}\cos^{-1}\left(\sqrt{6}W\right) \quad ; \quad W = \frac{S_{ij}S_{jk}S_{ki}}{\tilde{S}^3} \quad ; \quad \tilde{S} = \sqrt{S_{ij}S_{ij}} \quad ; \quad S_{ij} = \frac{1}{2}\left(\frac{\partial u_i}{\partial x_j} + \frac{\partial u_j}{\partial x_i}\right)$$

where:

$\overline{\Omega_{ij}} = The\ mean\ rate\ of\ rotation\ tensor$
$\omega_k = Angular\ velocity$
$A_0 = 4.04$
$C_2 = 1.9$
$\sigma_\varepsilon = 1.2$

The Shear Stress Transport k-ω (SST k-ω) equation is also used in this paper as its use was found to facilitate the oscillatory (vortex shedding) fluid flow behaviour of the wake behind the heliostat during RANS modelling. The ω equation offers many advantages over the ε equation, most of these benefits are to do with the boundary layer and wall treatment of the flow which is discussed in the next section. The downside of the standard k-ω model is its sensitivity of the solution to the freestream values of k and ω outside the shear layer. The SST k-ω equation has been designed to avoid freestream sensitivity by combining elements of the ω equation and the ε equation. The transport equations for k and ω are given below.

The transport equation for k:

$$\frac{\partial}{\partial t}(\rho k) + \frac{\partial}{\partial x_i}(\rho k u_i) = \frac{\partial}{\partial x_j}\left[\Gamma_k \frac{\partial k}{\partial x_j}\right] + G_k - Y_k \tag{22}$$

Transport equation for ω:

$$\frac{\partial}{\partial t}(\rho \omega) + \frac{\partial}{\partial x_j}\left(\rho \omega u_j\right) = \frac{\partial}{\partial x_j}\left[\Gamma_\omega \frac{\partial \omega}{\partial x_j}\right] + G_\omega - Y_\omega + D_\omega \tag{23}$$

The effective diffusivities for k and ω are given by:

$$\Gamma_k = \mu + \frac{\mu_t}{\sigma_k};\ \Gamma_\omega = \mu + \frac{\mu_t}{\sigma_\omega} \tag{24}$$

with

$$\mu_t = \frac{\rho k}{\omega}\frac{1}{max\left[\frac{1}{\alpha^*}, \frac{SF_2}{\alpha_1 \omega}\right]}\ ;\ F_2 = \tanh(\phi_2^2) \quad ; \quad \phi_2 = max\left[2\frac{\sqrt{k}}{0.09\omega y}, \frac{500\mu}{\rho y^2 \omega}\right]$$

$$\sigma_k = \frac{1}{\frac{F_1}{\sigma_{k,1}} + \frac{(1-F_1)}{\sigma_{k,2}}} \quad ; \quad \sigma_\omega = \frac{1}{\frac{F_1}{\sigma_{\omega,1}} + \frac{(1-F_1)}{\sigma_{\omega,2}}}$$

$$F_1 = \tanh(\phi_1^4) \quad ; \quad \phi_1 = min\left[max\left(\frac{\sqrt{k}}{0.09\omega y}, \frac{500\mu}{\rho y^2 \omega}\right) \ ; \ \frac{4\rho k}{\sigma_{\omega,2} D_\omega^+ y^2}\right] \ ; \ D_\omega^+ = max\left[2\rho \frac{1}{\sigma_{\omega,2}}\frac{1}{\omega}\frac{\partial k}{\partial x_j}\frac{\partial \omega}{\partial x_j}, 10^{-10}\right]$$

The production of k is represented by G_k in equation 14, the production of ω is represented by G_ω is:

$$G_\omega = \frac{\alpha \alpha^*}{\upsilon_t} G_k \tag{25}$$

The dissipation of k is given by:

$$Y_k = \rho \beta^* k \omega \tag{26}$$

The dissipation of ω is given by:

$$Y_\omega = \rho\beta\omega^2 \tag{27}$$

with

$$\beta_i = F_1\beta_{i,1} + (1 - F_1)\beta_{i,2} \tag{28}$$

The cross-diffusion term of the SST k-ω model which is used to blend together the two models is given by:

$$D_\omega = 2(1 - F_1)\rho\frac{1}{\omega\sigma_{\omega,2}}\frac{\partial k}{\partial x_j}\frac{\partial \omega}{\partial x_j} \tag{29}$$

with model constants:
$\sigma_{k,1} = 1.176$
$\sigma_{k,2} = 1$
$\sigma_{\omega,1} = 2$
$\sigma_{\omega,2} = 1.168$
$a_1 = 0.31$
$\beta_{i,1} = 0.075$
$\beta_{i,2} = 0.0828$

2.4.1 Wall bounded turbulent flows

When a turbulent flow interacts with a wall, non-trivial changes take place. Walls affect all flows in different manners but turbulent flows are significantly affected. On the wall surface, the no-slip condition ensures that all turbulence is non-existent but very close to the wall. The tangential fluctuations are damped out by the viscous effects of the fluid while the normal fluctuations are damped due to the kinematic blocking of the wall. Moving away from the wall, the turbulence increases drastically as it is augmented by the production of turbulence kinetic energy due to the large gradients in mean velocity. Since the near-wall region has solution variables with large gradients, the momentum and other scalar transports occur most vigorously, the accurate representation of the flow in this region is vitally important to successfully model the fluid (ANSYS, 2016).

It stands to reason that in the ABL the earth's surface can be seen as the wall boundary of the atmosphere and thus needs to be treated appropriately. It is widely accepted through experimental evidence that the near-wall region can be sub-divided into three main sections or layers as can be seen in Figure 13 below. With the wall taken as the vertical axis of the graph and the dimensionless distance on the horizontal axis, the innermost layer is called the viscous sub-layer where the flow is mostly laminar, and the viscosity plays a dominant role in momentum and heat transfer. Following the viscous sub-layer is the buffer layer or blending region where both viscous affects and turbulence are equally important. The turbulence region or log-law region is the last region of the inner layer where the turbulence plays a significant role.

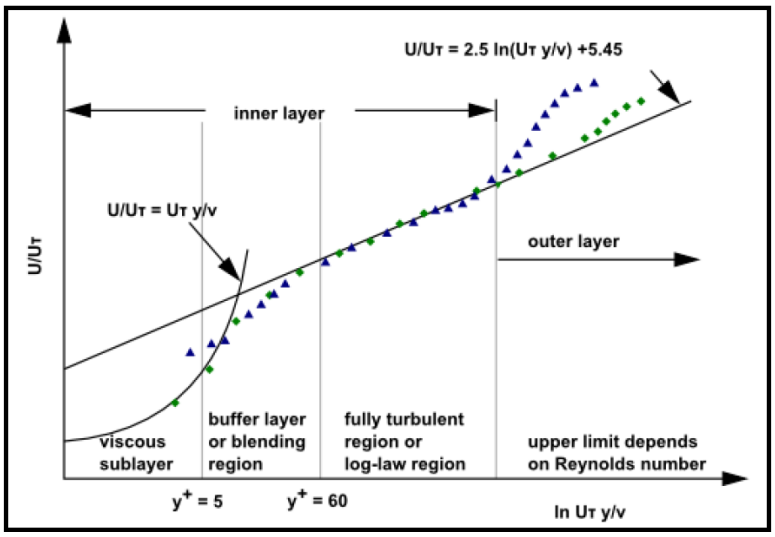

Figure 13: Subdivisions of the near wall region (ANSYS, 2016).

There are two main methods employed in dealing with the near-wall flows, namely, the wall function approach and the near-wall model approach. In the wall function approach the viscous sub-layer and the buffer region are modelled by semi empirical formulas rather than being resolved. This, in turn, means that the mesh resolution needed near the wall can be extremely coarse as only one cell is required in this region. In the near-wall model approach a sufficiently fine mesh is required as the turbulence models must be modified in order for them to resolve the flow to the wall. An illustration of the two methods can be seen in Figure 14.

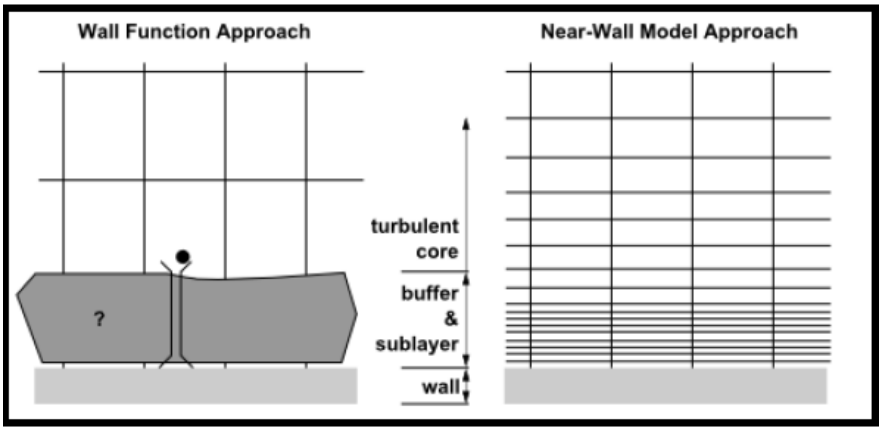

Figure 14: Near wall treatment for turbulent flows (ANSYS, 2016).

The law of the wall is given in ANSYS Fluent for mean velocity applied to a smooth wall as shown in equation 30:

$$\frac{u_p u^*}{u_\tau^2} = \frac{1}{\kappa} \ln\left(\frac{E u^* y_p}{\nu}\right) \tag{30}$$

where

$$u^* = C_\mu^{0.25} k_p^{0.5} \quad ; \quad u_\tau = \sqrt{\frac{\tau_\omega}{\rho}}$$

with

$u_p = Mean\ velocity\ at\ wall\ adjacent\ cell\ centroid\left[\frac{m}{s}\right]$
$k_p = Kinetic\ energy\ at\ the\ wall\ adjacent\ cell\ centroid\left[\frac{m^2}{s^2}\right]$
$\tau_\omega = Wall\ shear\ stress[Pa]$
$\kappa = von\ Karman's\ constant$
$E = Empirical\ constant$
$y_p = Distance\ to\ the\ wall\ adjacent\ cell\ centroid[m]$
$\nu = Kinematic\ viscosity\left[\frac{m^2}{s}\right]$

The law of the wall can be easily modified to account for wall roughness, the new modified equation is seen in equation 31.

$$\frac{u_p u^*}{u_\tau^2} = \frac{1}{\kappa}\ln\left(\frac{E u^* y_p}{\nu}\right) - \Delta B \tag{31}$$

The non-dimensional roughness height is given as:

$$K_s^+ = \frac{\rho K_s u^*}{\mu} \tag{32}$$

where:

$K_s = Physical\ roughness\ height$

There are three different regimes:

- Hydrodynamically smooth ($K_s^+ \leq 2.25$)

$$\Delta B = 0$$

- Transitional regime ($2.25 < K_s^+ \leq 90$)

$$\Delta B = \frac{1}{\kappa}\ln\left[\frac{K_s^+ - 2.25}{87.75} + C_s K_s^+\right] \times \sin\{0.4258(\ln K_s^+ - 0.811)\}$$

- Fully rough regime ($K_s^+ > 90$)

$$\Delta B = \frac{1}{\kappa}\ln(1 + C_s K_s^+)$$

where:

$C_s = Roughness\ constant$

The ABL is considered to be in the fully rough regime as the flow is primarily over rough terrain, the roughness elements are so large that the laminar sub-layer is eliminated and the flow is considered to be independent of the molecular viscosity (Blocken, et al., 2007).

Equation 31 can be simplified along with the ΔB value for the fully rough regime if we note that for an equilibrium boundary layer, $u^* = u_\tau$, $C_s K_s^+ \gg 1$, $u^+ = u/u^*$ and $y^+ = u^* y/\nu$, this can be seen in equation 33.

$$u^+ = \frac{1}{\kappa} \ln\left(\frac{y^+}{C_s K_s^+}\right) + 5.43 \tag{33}$$

where:

$u^+ = Dimensionless\ velocity$
$y^+ = Dimensionless\ distance\ from\ the\ wall$

The effect of adding roughness to the wall is to shift the intercept of the law of the wall, resulting in the viscous sub-layer being demolished, this can be seen in Figure 15.

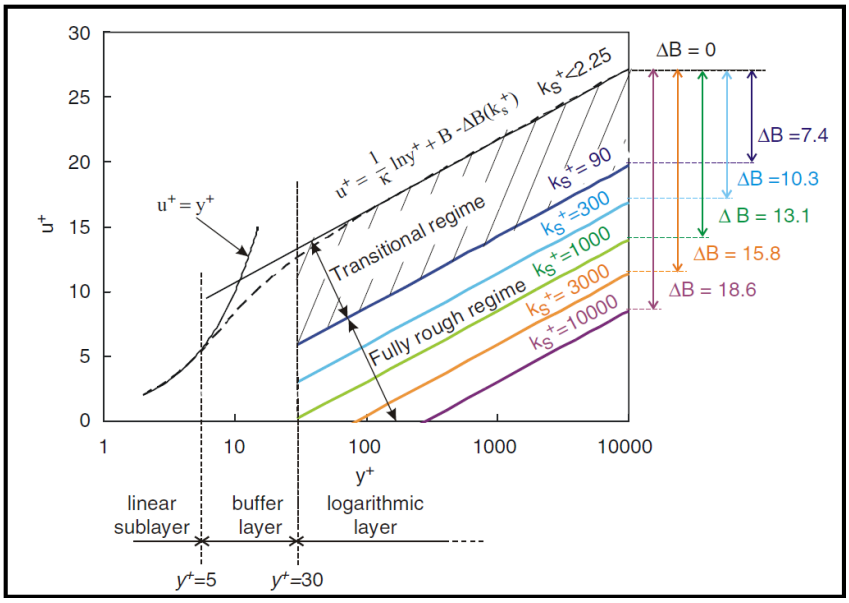

Figure 15: Law of the wall with varying sand grain roughness (Blocken, et al., 2007).

The addition of the roughness can be viewed as a layer of closely packed spheres forming a wall, this roughness subsequently introduces a blockage effect on the flow which is about 50% of its height. Therefore, the wall is virtually shifted 50% of the height of the roughness and the resulting $y^+ = y^+ + K_s^+/2$ (ANSYS, 2016). For the k -ε models the k -equation is solved over the entire domain including the wall-adjacent cells, the imposed boundary condition at the wall for k is seen in equation 34.

$$\frac{\partial k}{\partial n} = 0 \tag{34}$$

where:

$n = The\ local\ coordinate\ normal\ to\ the\ wall$

The production of kinetic energy, as well as the dissipation rate, are computed at the wall adjacent cells on the basis of the local equilibrium hypothesis. Under this assumption the production of k and the dissipation rate are said to be equal in the wall-adjacent control volume. The production of k and the dissipation are computed according to the equations below:

$$G_k = \tau_w \frac{\partial U}{\partial y} = \tau_w \frac{\tau_w}{\kappa \rho C_\mu^{1/4} k_p^{1/2} y_p} \tag{35}$$

$$\varepsilon = \frac{C_\mu^{3/4} k_p^{3/2}}{\kappa y_p} \tag{36}$$

2.4.2 Modelling the ABL with CFD

When accurately modelling the ABL with CFD it is not enough to simply prescribe a matching velocity and turbulence inlet profile for the domain. It is important to ensure that these profiles are highly accurate over the entire flow domain. Structures in the flow are extremely sensitive to the turbulent intensity of the flow. In an experiment performed by (Peterka & Derickson, 1992), it was shown that a difference in turbulence intensity of only 2% had a resulting effect of under-predicting the moment coefficient of a model heliostat by 12%. Good guidelines for the correct modelling of the ABL are given by both (Blocken, et al., 2007) and (Richards & Hoxey, 1993). (Blocken, et al., 2007) stresses the need for a horizontally homogeneous ABL in the upstream and downstream regions of the computational domain, this means that in the vertical profiles of the mean velocity and turbulence there is an absence of streamwise gradients, or in other words as the profiles flow through the domain, they maintain their original shape. This will occur when the mean velocity and turbulence profiles are in equilibrium with the roughness characteristics of the ground surface (Blocken, et al., 2007).

In addition to the horizontal homogeneity, (Blocken, et al., 2007) describes four requirements that need to be simultaneously satisfied if the wall roughness is expressed by an equivalent sand-grain roughness in the wall functions. The four requirements are listed below:

1. A sufficiently high mesh resolution in the vertical direction close to the bottom of the computational domain.
2. A horizontally homogeneous ABL flow in the upstream and downstream region of the domain.
3. A distance y_p from the centre point P of the wall adjacent cell to the wall that is larger than the physical roughness height K_s of the terrain.
4. Knowing the relationship between the equivalent sand grain roughness height and the corresponding aerodynamic roughness length z_0 (Blocken, et al., 2007).

It is important to note that point three describes the need for software purposes, that the roughness height is less than that of the distance from the wall to the first mesh cell centre. This obviously creates a modelling difficulty in the fact that one needs a certain roughness height to correctly model the terrain but also needs a fine mesh on the bottom wall as pointed out by point one. In earlier versions of ANSYS Fluent this was the requirement, thus it is given here by Blocken, however in later versions of this software this is no longer the case and the roughness height is independent of the mesh resolution near the wall.

(Richards & Norris, 2011) detail certain requirements for the ABL to achieve homogeneity, these are; boundary conditions, turbulence models and the associated constants must be consistent, this then implies the following:

1. The velocity profile that is used should not be power law but rather log law type
2. The inlet profiles for the velocity, kinetic energy and dissipation should have the form as shown in equation 37:

$$u(z) = \frac{u^*}{\kappa}\ln\left(\frac{z}{z_0}\right), k = \frac{{u^*}^2}{\sqrt{c_\mu}}, \varepsilon(z) = \frac{{u^*}^3}{\kappa z} \tag{37}$$

where:

$u(z) = Streamwise\ velocity\ component\ at\ height\ z\ \left[\frac{m}{s}\right]$

$z = Height\ above\ groundplane\ [m]$

3. The von Karman's constant which is a function of the particular model being used is given by equation 38 for the SKE:

$$\kappa_{SKE} = \sqrt{(C_{\varepsilon 2} - C_{\varepsilon 1})\sigma_{\varepsilon}\sqrt{c_{\mu}}} = 0.433 \tag{38}$$

The relationship between the sand-grain roughness and the aerodynamic roughness for the fully rough regime can be derived by first-order continuity fitting of the ABL log law and the wall-function log law including the appropriate roughness function at height $z = z_0$. Based on the data by (Cebeci & Bradshaw, 1977) this relationship is given as:

$$K_s = \frac{9.793 z_0}{C_s} \tag{39}$$

Equations 37 and 39 can be easily implemented into a User-Defined Function (UDF) in ANSYS Fluent. UDFs allow the equations to be parameterized thus allowing them to be used regardless of the particular geometry of the domain and can therefore be easily altered accordingly. It should be noted that at the Reynolds numbers of interest to this study, the shedding is much more dominant compared to the wall shear in terms of viscous drag components.

2.5 SCALE-RESOLVING COMPUTATIONAL FLUID MECHANICS

Whilst RANS modelling is the most widely used method in CFD today, as it is the most efficient way in solving many industrial flows, its accuracy is limited. RANS flows by definition are entirely averaged which makes them unsuitable in modelling applications where any sort of transient behaviour is expected or needed in order to further investigate a model or flow. The alternative to RANS modelling is known as SRS, where at least a portion of the turbulence over a portion of the domain is resolved. The most common type of SRS modelling is known as Large Eddy Simulation (LES), where the large turbulent structures of the flow are resolved up to the mesh grid limit everywhere in the flow. While LES is used extensively in the academic community, it is not widely used in industry due to the very high mesh resolution needed, especially for wall boundary layers.

To solve the issue of wall modelling and high mesh resolutions for LES, hybrid LES-RANS models have been developed in recent years. In these hybrid models, RANS is used to cover the attached wall boundary layers while the large detached regions are handled with LES, meaning a partial resolution of the turbulent spectrum in space and time (ANSYS, 2016). These hybrid models rely on strong flow instabilities in order to generate the turbulent structures in the separated regions, this is normally the case with bluff bodies and is the case when modelling heliostats. Using unsteady-RANS (URANS) one may be able to recover single mode periodic vortex shedding with a fine enough grid and the right RANS model, with a hybrid model these vortices can generate successively smaller eddies down to the available grid limit. The governing equations for LES are derived by filtering the time-dependent Navier-Stokes equations. The filtering process then effectively filters out the eddies whose scales are smaller than the grid spacing, or filter width used in the computations. A filtered variable denoted by an overbar is defined in equation 40:

$$\bar{\phi}(x) = \int_D \phi(x')G(x,x')dx' \tag{40}$$

where:

$D = fluid\ domain$
$G = filter\ function$

In ANSYS Fluent the finite volume discretisation itself implicitly provides the filtering operation:

$$\bar{\phi}(x) = \frac{1}{V}\int_V \phi(x')dx' \ , x'\epsilon v \tag{41}$$

where:

$V = Volume\ of\ a\ computational\ cell$

with

$$G(x,x') = \begin{cases} \frac{1}{V}, & x' \epsilon \nu \\ 0, & x' otherwise \end{cases}$$

The filtered continuity and momentum equations for incompressible flows then become:

$$\frac{\partial \rho}{\partial t} + \frac{\partial}{\partial x_i}(\rho \overline{u_\iota}) = 0 \tag{43}$$

$$\frac{\partial}{\partial t}(\rho \overline{u_\iota}) + \frac{\partial}{\partial x_j}(\rho \overline{u_\iota}\,\overline{u_j}) = -\frac{\partial \bar{p}}{\partial x_i} + \frac{\partial}{\partial x_j}\left[\mu\left(\frac{\partial \overline{u_\iota}}{\partial x_j} + \frac{\partial \overline{u_j}}{\partial x_i} - \frac{2}{3}\delta_{ij}\frac{\partial \overline{u_l}}{\partial x_l}\right)\right] - \frac{\partial \tau_{ij}}{\partial x_j} \tag{43}$$

where $\tau_{ij}$is the sub-grid scale stress defined by:

$$\tau_{ij} = \rho\overline{u_\iota u_j} - \rho\overline{u_\iota}\,\overline{u_j} \tag{44}$$

The important practical application of this modelling approach is that the modelled momentum equations for RANS and LES are identical if an eddy viscosity model is used in both cases. In other words, the modelled Navier-Stokes equations have no knowledge of their derivation (Menter, 2015). The difference lies exclusively in the size of the eddy viscosity provided by the underlying turbulence model. This has allowed turbulence models to be formulated that switch from RANS to LES by lowering the eddy viscosity in the LES zone appropriately, without any formal changes to the momentum equation.

In the LES formulation, the sub-grid scale stresses that result from the filtering of the governing equations need to be modelled similarly to the Reynolds stresses. In ANSYS Fluent the Boussinesq hypothesis is used in LES as in the RANS models, the sub-grid scale stresses are computed from:

$$\tau_{ij} - \frac{1}{3}\tau_{kk}\delta_{ij} = -2\mu_t\overline{S_{\iota j}} \tag{45}$$

where:

$\mu_t = Subgrid\ scale\ turbulent\ viscosity$
$\tau_{kk} = Isotropic\ component\ of\ subgrid\ scale\ stress\ (notmodelled)$
$\overline{S_{\iota j}} = Rate\ of\ strain\ tensor\ for\ resolved\ scale$

One of the simplest models for the sub-grid stresses in LES is the Smagorinsky-Lilly model, in this model the eddy viscosity is modelled by:

$$\mu_t = \rho L_s^2 |\bar{S}| \tag{46}$$

where:

$L_s = The\ mixing\ length\ for\ sub\ grid\ scales$

with

$$L_s = \min(\kappa d, C_s \Delta)$$

where

$d = Distance\ to\ closest\ wall$
$C_s = Smagorinsky\ constant = 0.1$
$\Delta = Equivalent\ cell\ size\ for\ isotropic\ meshes = V^{\frac{1}{3}}$

There are a few more complex models available for LES modelling which tend to focus more on the treatment of the walls and boundary layers, these are not of relevance here as the use of a hybrid model negates the need for wall treatment as this is dealt with by the RANS portion of the model.

2.5.1 DES and SBES

Following from LES, the simplest hybrid LES-RANS model is the Detached-Eddy Simulation (DES), this model uses the combination of LES and RANS modelling and conveniently switches between the two based on a comparison between the turbulent length scales and the grid spacing. LES mode will be activated once the model determines that the grid spacing, away from the wall bounded flow, is the minimum (ANSYS, 2016). This can be seen in equation 47 with the regular RANS dissipation and the DES dissipation:

$$\varepsilon = \frac{k^{\frac{3}{2}}}{L_t} \rightarrow \varepsilon = \frac{k^{\frac{3}{2}}}{\min(L_t, C_{DES}\Delta_{max})} \tag{47}$$

With this formulation the grid spacing is explicitly entered into the DES or hybrid model, this does however, have some drawbacks. In the computational domain where the grid is somewhere between RANS and LES resolution or where the flow is too weak to generate LES structures, the RANS solution can be compromised. One of the biggest issues facing the DES formulation is the problem of Grid Induced Separation (GIS). This occurs in an attached boundary layer if the grid has been refined to a point where the DES limiter becomes activated. This is an issue as the flow instability is not strong enough to balance the reduced RANS content by resolved turbulence (Menter, 2015). This will typically lead to an artificial flow separation at the location of this grid refinement and happens if the boundary layer thickness becomes greater than the cell volume. There have been numerous attempts to resolve the issue of GIS with blending functions, leading to the concept of Delayed DES or DDES. Further refinement was achieved with the introduction of Improved DDES or IDDES, where the LES region of the domain is taken to the outer part of the wall boundary layer and the boundary layer is modelled with Wall-Modelled LES (WMLES). The most recent powerful hybrid models are the Shielded Detached Eddy Simulation (SDES) and the SBES. In this thesis the SBES model is used as an SRS to accurately capture the transient flow over a heliostat. Both the SDES and SBES models provide an improved shielding function compared to IDDES with faster transition from RANS to LES in separating shear layers.

The shielding function of SDES takes its form from that of DES, with the ability to maintain RANS and shield the boundary layer under severe mesh refinement. Shielding the boundary layer simply means to preserve

RANS mode and delay the LES functionality. The dissipation then takes the form of equation 48 with the shielding function seen in equation 49:

$$\varepsilon_{SDES} = -\beta^* \rho \omega F_{SDES} \tag{48}$$

with

$$F_{SDES} = \left[\max\left(\frac{L_t}{C_{SDES}\Delta_{SDES}}(1 - f_{SDES}), 1\right) - 1\right] \tag{49}$$

When SDES switches to LES mode the eddy viscosity is lowered to that of a conventional LES model as seen in equation 50:

$$\nu_t = ((\frac{\beta}{\alpha})^{\frac{3}{4}} C_{LES}\Delta)^2 S \tag{50}$$

The only other change lies with the LES length scale, in the DES models the length scale is problematic due to overly high levels of eddy viscosity in separating shear layers due to high aspect ratio cells normally found there. To avoid the issue of a slow transition from RANS to LES the SDES model uses equation 51 for the LES length scale formulation, the first part of the equation is the normal cell volume and the second part ensures a limit for high aspect ratio cells:

$$\Delta_{SDES} = \max(\sqrt[3]{V}, 0.2\Delta_{max}) \tag{51}$$

The SBES model utilizes the same shielding function as the SDES model but adds the ability to switch from the underlying RANS model directly to the LES model. The stress blending between the RANS and LES formulations is seen in equation 52:

$$\tau_{ij}^{SBES} = f_{SDES}\tau_{ij}^{RANS} + (1 - f_{SDES})\tau_{ij}^{LES} \tag{52}$$

The advantages of the SBES model is that you can generically combine LES and RANS models, clearly distinguish between RANS and LES regions based on the shielding function and utilize rapid transition from RANS to LES in separated shear layers. SBES provides the quickest transition from RANS to LES structures as can be seen in Figure 16 for the flow from a nozzle.

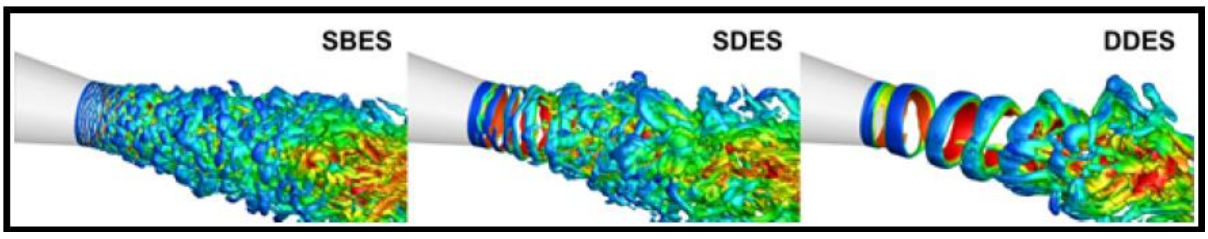

Figure 16: Comparison between SBES, SDES and DDES of the transition to LES (ANSYS, 2016).

2.5.2 Vortex Method at inlet

An additional requirement when modelling SRS flows using CFD is the need to have a method of generating fluctuating velocity components representing a turbulent flow field at the inlet. Since the velocity field generated is temporally and spatially correlated, it is a more realistic representation of turbulence than that obtained with a simple velocity distribution (Mathey, et al., 2006). To generate a time-dependent inlet condition a random 2D vortex method is considered, the velocity profile is perturbed with a vorticity field. The vortex method is based on the Lagrangian form of the 2D evolution equation of the vorticity and the Biot-Savart Law and is quite involved mathematically. The vortex points carry information about the vorticity field and are convected randomly, with N, the number of vortex points, A the area of the inlet, the circulation is given by Γ and is equated in equation 53 with η the spatial distribution:

$$\Gamma_i(x,y) = 4\sqrt{\frac{\pi A k(x,y)}{3N[2\ln(3)-3\ln(2)]}} \tag{53}$$

$$\eta(\vec{x}) = \frac{1}{2\pi\sigma^2}\left(2e^{-|\vec{x}|^2/2\sigma^2} - 1\right)2e^{-|\vec{x}|^2/2\sigma^2} \tag{54}$$

$\sigma$is a parameter that provides control over the size of the vortex particle, the resulting discretisation for the velocity field is given by:

$$\vec{u}(\vec{x}) = \frac{1}{2\pi}\sum_{i=1}^{N} \frac{(\vec{x_i}-\vec{x})\times\vec{z}\left(1-e^{\left|\vec{x}-\vec{x}'\right|^2/2\sigma^2}\right)}{\left|\vec{x}-\vec{x_i}'\right|^2} \tag{55}$$

The size of the vortex is specified through a mixing-length hypothesis where σ is calculated from a known profile of mean dissipation rate and turbulence kinetic energy at the inlet as given in equation 56. The minimum value of σ is bounded by the local grid size, for each characteristic time scale, the sign of the circulation of each vortex is randomly changed. This time scale is representative of the time necessary for a vortex to be convected by the bulk velocity in the normal direction n, multiplied by its characteristic length.

$$\sigma = \frac{ck^{3/2}}{2\varepsilon} \tag{56}$$

where:

$c = 0.16$

Setting up any type of computational fluid dynamics simulation is far from trivial, there are many complicated aspects of even the simplest RANS simulation that can affect the solution of the flow without the modeller realizing. The complications and difficulty increase tenfold when modelling an SRS flow. (Gerasimov, 2016) compiled a quick guide to setting up a SRS/LES simulation, which is used as a template in this thesis when modelling the flow over a single heliostat with SBES. A brief overview of the more important steps in the setup of the SBES simulation are listed below:

- All types of Scale-Resolving simulations should start from a precursor 2-equation eddy-viscosity RANS model such as the k-ε model.
- The use of the fully developed inlet boundary conditions is of great benefit to the SRS and should be used.
- Check the mesh resolution of the domain, from the precursor RANS, an approximation of the integral length scale can be calculated over the entire domain using equation 8, at least a couple of cells are needed in each direction to resolve an eddy with a length scale *l.* The ratio between the length scale and the size of the cells can be determined using a custom filed function, at least five cells across a single eddy should resolve 80% of the energy spectrum in the regions of interest.
- The wall modelling for SRS needs to be given careful consideration. For LES it is a very complicated area but for SBES the grid from the RANS simulation should be acceptable but still have at least 20 inflation layers and a $y^+ \sim 1$.
- The time step size needs to be evaluated, the temporal resolution should match or exceed the spatial resolution. The Courant number is used to ensure the correct time step size based on the RANS simulation, the Courant number is halved to account for differences between instantaneous and averaged velocities as well as errors introduced by RANS. The time step used is calculated as: $\Delta t \approx \Delta x/2U$, with Δx an estimate of the local grid size based on cell volume.
- Enable the generation of synthetic turbulence using the Vortex method, set the number of vortices to N/4, with N being the number of inlet cells.
- Finally, the numerical discretisation has to be considered. For the spatial discretisation, Central Difference (CD) or Bounded Central Difference (BCD) for the momentum equations must be used with the least-squares cell-based or Green-Gauss node-based gradient option. For the time discretisation the second-order scheme with Non-Iterative Time Advancement (NITA) should be used.
- The choice of the sub-grid model to be used in the LES potion of the flow. (Gerasimov, 2016). In this study, WALE is used.

2.6 FLUID STRUCTURE INTERACTION (FSI)

FSI is a classification of problems that deal with a strong dependency between solids and fluids, for these problems it is required that an interface surface exist between the solid and fluid domains. At the interface surface both the boundary conditions and governing equations of both the fluid and solid domain must be satisfied simultaneously. To close the system of equations at the FSI interface, kinematic and traction coupling boundary conditions are introduced, with the traction condition satisfying the stress balance and the kinematic condition defining the motion. In this thesis the single heliostat is modelled in the ABL and becomes a perfect candidate for modelling with FSI. The unsteady transient flow of the turbulent ABL imposes fluctuating forces onto the heliostat (seen as pressure and wall shear stress fields in the fluid domain). Once these forces have been successfully modelled in the fluid domain they need to be transferred to the structural domain. In this study, for one-way coupling, the subsequent pressure field is computed into the relevant stress of the structure in the structural solver, the displacement of the structure can then be computed and depending on the type of FSI be fed back to the fluid solver with the entire process being repeated. For two-way coupling, both pressure and shear stress are coupled. FSI will

enable the solution of not only the flow field around the heliostat but will enable the heliostat structure to be solved in terms of maximum stress, displacement and vibration, all of which play a critical role in the lifespan of the heliostat. In this study one-way FSI is used due to the CHPC not having system coupling available for ANSYS. Using system coupling would also dictate that no previous precursor RANS simulation can be performed and the SRS simulation would have to be implemented form the start.

FSI can be characterised by two distinct types of simulations, namely one-way or two-way FSI. In one-way FSI the fluid domain solution is provided to the structural analysis for computation, but the resulting structural solution is not used again by the fluid analysis. In contrast, for the two-way simulation, the fluid solution is provided to the structural component for solving and this new structural solution is given back to the fluid solver and the process repeats until a final solution is found for a specific time step. A simple FSI model example is seen in Figure 17:

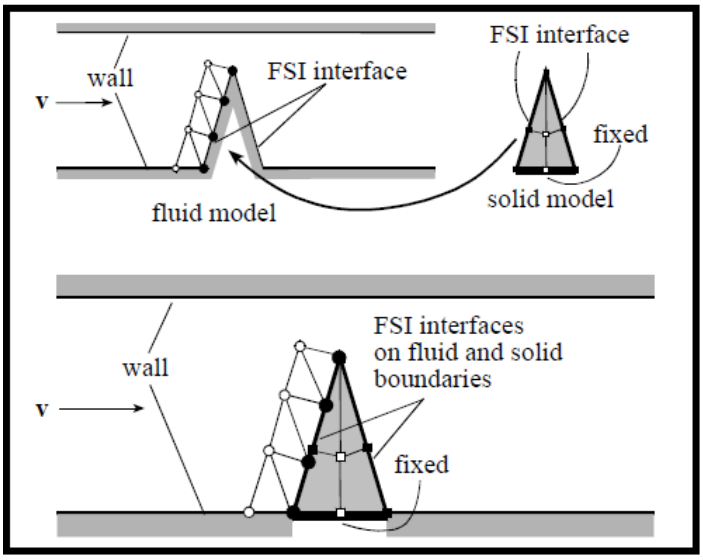

Figure 1: Simple FSI model (ADINA, 2012).

There are numerous modelling approaches available for FSI, the basics of which are listed briefly below:

- 2-way fully coupled, the fluid and solid equations are solved in a single monolithic matrix, similar to the coupled solver used in Fluent for the mass and momentum. The fields remain tightly coupled but it is very difficult to solve a monolithic fluid-structure matrix.
- 2-way iteratively implicit, the fluid and solid equations are solved separately, iterated within each time step to obtain an implicit solution. This is the method used in ANSYS between Mechanical and Fluent.
- 2-way explicit, this method is the same as the implicit solver except there are no iterations between the fluid and solid fields within a time step, this can be done in ANSYS but generally requires much smaller time steps. This should only be used when the coupling is weak.
- 1-way, the converged solution is obtained for one field then used as a boundary condition or external load for the second field. This is suitable for weak coupling such as determining the maximum structural stresses from a CFD simulation. (ANSYS, 2016)

A brief review of solid mechanics is given below as a prelude to the FSI coupling conditions. Analogous to the fluid mechanics systems, the solid mechanics physics is governed by the conservation of momentum, mass and energy. In order to solve these equations, constitutive models need to be developed, for instance the momentum equation uses a relation between stress and strain known as Hooke's law that can be seen in equation 57:

$$\sigma_{ij} = C_{ijkl}\epsilon_{kl} \tag{57}$$

where:

$\sigma_{ij} = Solid\ stress[Pa]$
$C_{ijkl} = Constitutive\ Matrix$
$\epsilon_{kl} = Strain$

The momentum equation for static equilibrium can be written as:

$$\frac{\partial \sigma_{ij}}{\partial x_j} = \rho f_i \tag{58}$$

Equation 58 after some manipulation can be developed and solved using the FEM. The most important region in an FSI simulation is the interface between the fluid and solid domain, at this surface data are transferred between the coupled systems. A set of coupling equations is needed at this interface in order to connect the governing equations. The boundary conditions at the interface are governed by kinematic and traction coupling conditions. As far as the kinematics are concerned, the fluid and solid structure are required to have the same motion at the interface wall. The traction condition ensures that the two systems are in local equilibrium. To satisfy the kinematic condition the relation seen is equation 59 can be applied, the fluid velocity at the wall is equal to the time derivative of the solid displacement at the fluid structure interface.

$$u_i = \frac{da_i}{dt} = \dot{a}_i \tag{59}$$

where:

$u_i = Fluid\ velocity\ [\frac{m}{s}]$
$a_i = Displacement\ components\ at\ solid\ boundary\ [m]$

The traction condition can be expressed by the force balance between the structure and the fluid, the traction vector represents the stresses as the force per unit area with a unit normal n_i. The traction vectors for both the structure and the fluid are seen in equations 60 to 62, respectively, with the boundary condition of equilibrium for the tractions, the sum of the vectors will be equal to zero.

$$t_i^S = \sigma_{ij} n_i^S \tag{60}$$

$$t_i^f = -pn_i^f + \tau_{ij} n_j^f \tag{61}$$

$$t_i^s + t_i^f = 0 \tag{62}$$

In ANSYS, the fluid and structural domains are meshed independently of one another and thus a non-conformal mesh is created at the interface, this means that the nodes of the one mesh do not match the nodes of the other mesh. Mapping methods are needed in order to transfer the relevant data between the fluid and structural domains. Depending on the type of data that is being transferred different algorithms are used in ANSYS system coupling. If a conservative quantity such as momentum or mass is transferred, a method called General Grid Interface (GGI) is applied, in this method weights are calculated to try and ensure the transferred quantities are conserved locally. The other method used in System Coupling is the Bucket Surface Mapping algorithm, this is used when the transferred quantity is not necessarily needed to be conserved globally such as deformation. When mapping deformations it is more important to preserve the shape of the surface (ANSYS, 2016).

In ANSYS there are numerous options for performing an FSI simulation, depending on whether the simulation is 1-way or 2-way and whether either or both the fluid and structural components are steady state or transient simulations. In the Workbench environment of ANSYS the structural and fluid components can be linked to a System Coupling component, this is the easiest way of performing 1-way and 2-way FSI of either steady or transient structures depending on which structural component is selected (Fluent can be steady or transient). The System Coupling component does not need to be used with static data transfers. Currently in ANSYS there are two distinct ways of performing transient 1-way FSI, firstly the System Coupling component can be used but this introduces complications when performing SRS CFD on a cluster as there may be no Graphical User Interface (GUI) from which Workbench can run. The second option is to incorporate the External Data component in Workbench and import the SRS CFD results and link this to the transient structural component where 1-way FSI can be performed. In Figure 18, the System Coupling component along with the Transient Structural and Fluent components with the links between them can be seen, this is the easiest method of performing FSI in ANSYS.

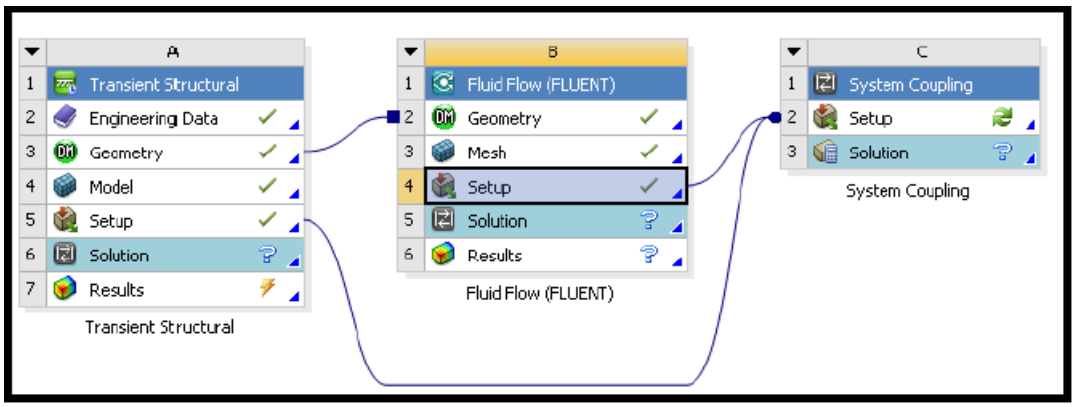

Figure 2: FSI simulation with System Coupling in ANSYS.

2.7 PREVIOUS STUDIES

As previously mentioned, there exists a vast amount of prior and ongoing research into the various aspects of heliostat design whether it be wind tunnel experiments, CFD simulations for wind or structural loading or just review papers. (Peterka, et al., 1986) conducted thorough research with wind tunnel experiments of heliostats and the reduction of wind loadings on them. These experiments used a wind tunnel specially designed to simulate the ABL and the corresponding wind profiles that matched full-scale site readings. The turbulent boundary layer is generated in the tunnel using vortex generators, spires at the entrance and a test section with roughness elements on the floor. The model used was a 1:60 scale heliostat mounted on a turntable. The model's angle of attack was able to be altered giving the ability to find the aerodynamic force and moment coefficients as a function of the wind angle and torque tube angle. The Reynolds number was approximately 30 000 to 70 000 providing independence of the Reynolds number and the aerodynamic coefficients.

(Peterka, et al., 1986) generated many data points in this study, over 2000 for a single heliostat. Using these wind tunnel generated data there are useful conclusions that can be made: for this isolated single heliostat it is the operational winds that control the desired design forces, while the moments used for design are controlled by the high velocity storage winds. Heliostats are stored with the mirror parallel to the ground in order to mitigate the effects of wind. A ratio between the stow position velocity and the operational position velocity where the forces would be equal is calculated in this study and is found that for the stow position, the velocity must be around 4 times greater than that in the operational position to generate the same force magnitude. This means that the design should be based on the operational wind speeds rather than storage wind speeds. With the abundant amount of data available from the (Peterka, et al., 1986) experiments for a single heliostat and the fact that the associated wind profiles for both the velocity and turbulence profiles are provided as seen below in Figure 19, this study is used in the proceeding chapter as the initial CFD validation case.

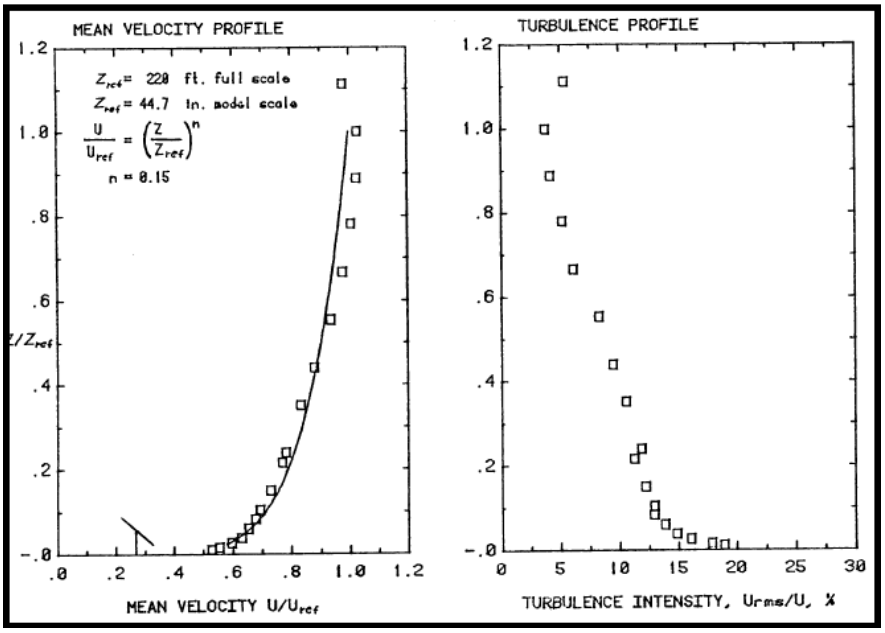

Figure 3: ABL wind profiles used in Peterka (Peterka, et al., 1986).

Another paper conducted wind tunnel and CFD simulations on the LH-2 heliostat used in the Brightsource Ivanpah plant in California (Huss, et al., 2011). The research made use of RANS CFD and an aeroelastic wind tunnel model with varying angles of attack and elevation angle. It was found that the heliostat vibrates at high winds near its natural frequencies due to turbulence containing frequency content close to the natural frequency of the heliostat and vortex shedding. The turbulent flow in the wind tunnel was achieved similarly to Peterka with the use of spires at the tunnel inlet, the longitudinal turbulence intensity was the primary objective used in the study and was I_u=20% with a vertical turbulence intensity of I_z=12.2%. No profile was provided for these quantities.

Two sets of experiments were conducted in the wind tunnel, the first was to establish whether flutter or galloping instabilities were of concern and the second was to check for vortex shedding. In this study by RWDI the maximum wind speed of 41.5m/s was used with the heliostat in the stow position, with this configuration it was found that no flutter or galloping was experienced. For the vortex shedding, the experiments used an unspecified range of wind speeds and configuration of the heliostat. It was concluded that the heliostat was stable against vortex shedding. This does however seem to be in contradiction to the previous statement about the heliostat vibrating at its natural frequencies solely due to turbulence and requires further investigation. The LH-2 is the focus of this research study along with the dynamic wind loading and subsequent structural response.

The turbulence in the ABL comprises of velocity fluctuations at different frequencies and amplitudes, this can be viewed as a superposition of eddies of different sizes and frequencies. The Power Spectral Density (PSD) gives the contribution of the different turbulence scales to the total variance of the velocity signals. The PSD of the velocity fluctuations is important in order to identify resonance effects with the structure that can arise from pressure fluctuations induced by the turbulence (Pfahl, et al., 2017). In order to achieve similarity between wind tunnel experiments and the real atmospheric boundary layer, the profiles of the turbulence intensity and the mean wind speed as well as the turbulent energy spectra need to be scaled, which is not achievable in practice. (Banks, 2011) noted that testing of heliostats in a conventional boundary layer wind tunnel does not yield the expected results due to their small dimensions, the heliostats need to be modelled at larger scales, 1:10-1:50, which are not in compliance with the typical wind tunnel flow scales of 1:100-1:300.

Due to the increase in turbulence intensity for lower heights, smaller heliostats are attacked by more turbulent flow and the peak load coefficients increase significantly. Due to the fact that in recent years there has been a trend for smaller heliostats, there is a need for the accurate estimation of the peak and mean wind loads. Hence for wind tunnel investigations of heliostats the turbulence intensity must correspond to both heliostat size and the surface roughness of the surrounding terrain (Pfahl, et al., 2017). In a work by (Peterka, et al., 1989), the potential impact of fatigue loads was investigated experimentally and it was noted that the fluctuating loads on the heliostats have very large amplitudes and can change sign. In (Peterka & Derickson, 1992) a reviewer commented with, "I must highly emphasize to designers of large pedestal supported arrays that resonant vibrations must be considered. In our earlier designs we experienced several drive failures in the field when only static wind loads were considered in the design. Naturally we were forced to consider dynamic effects to correct the problems". This statement gives validity to the research conducted in this dissertation and the need to not only use RANS CFD modelling

with FSI but also SRS modelling coupled with dynamic structural simulations in order to accurately design a heliostat.

(Ghanadi, et al., 2017) performed Embedded Large Eddy Simulation (ELES) with the ABL on the Peterka wind tunnel model and found that the mean and peak wind loading coefficients increased drastically with the increase of turbulence intensity. With a turbulence intensity of 2%, the mean drag coefficient is around 1.1 with very slight fluctuations. Increasing the intensity to 18%, the mean and peak drag coefficients rise sharply to 1.6 and 3.9, respectively. This simply reiterates the importance of correctly modelling the ABL to the accuracy of the simulation results. The two cases for the turbulence intensity can be seen in Figure 20 for the drag coefficient.

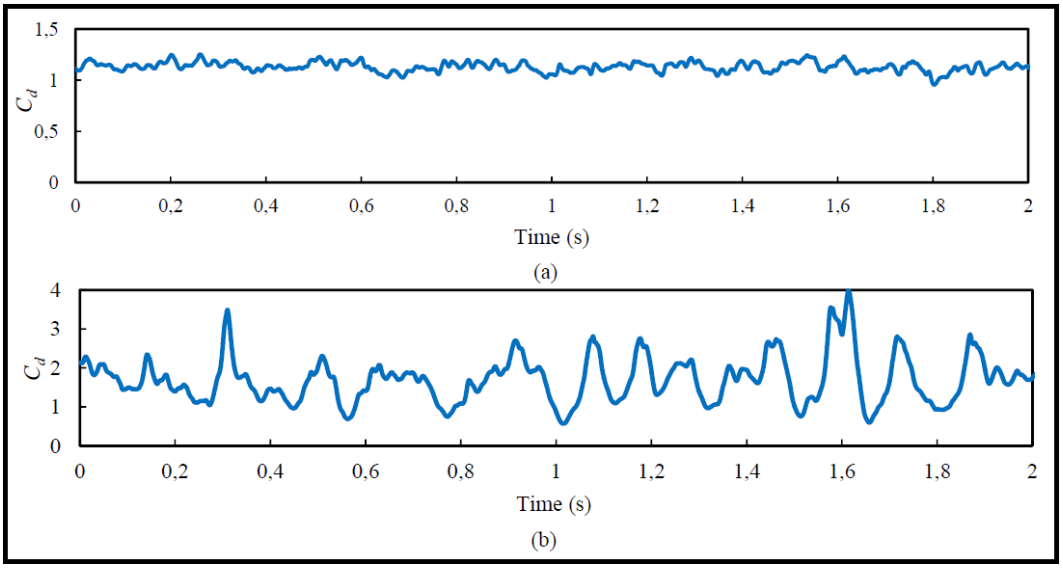

Figure 4: Drag coefficient for single heliostat in ABL at 15m/s with (a) Tu=2% (b) Tu=18% (Ghanadi, et al., 2017).

As stated previously, the use of RANS modelling in CFD has its limitations, particularly when trying to model transient behaviour even with URANS. There are many applications where URANS is able to model simple transient flow behaviour such as the 2D vortex shedding from a cylinder, but it is still not guaranteed that URANS can capture other types of flow phenomena, especially in 3D. By definition, the RANS equations are developed to average out all transient behaviour of the fluid flow. (Boddupalli, et al., 2017) conducted CFD experiments of a single heliostat using both RANS and LES modelling and found that RANS is only suitable for modelling the mean flow features of the fluid while LES provides a better estimation of the fluctuations. (Breuer, et al., 2003) conducted CFD simulations using RANS, DES and LES modelling on an inclined plate as shown in Figure 21. All the RANS simulations carried out in the study were performed with URANS but failed to show any unsteady shedding motion. Instead, the URANS simulations simply converge to a steady-state result, hence it is concluded that they are not capable of describing the unsteady nature of the flow field around an inclined plate. In contrast, the DES and LES simulations yield the main characteristics of the unsteady flow filed. This is an important finding as the setup can be viewed as being nearly identical to a heliostat in an operational configuration. If URANS is unable to model the unsteady vortex shedding, LES or some hybrid model is needed in order to achieve the unsteady results that can be used in a transient structural analysis.

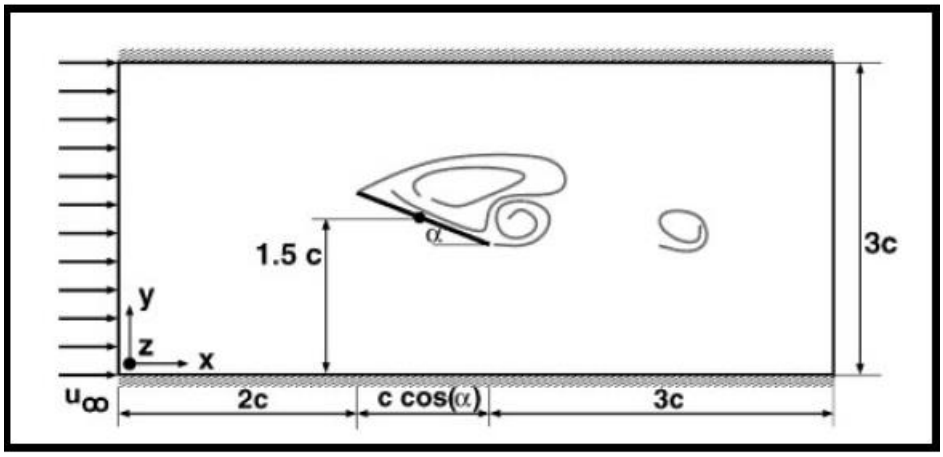

Figure 5: CFD flow configuration of inclined plate (Breuer, et al., 2003).

(Breuer, et al., 2010) conducted FSI of a flexible flap structure in both laminar and turbulent flow. The simulation consists of a 2D domain with a cylinder slightly offset from the centre, with a flexible flap attached to the back of the cylinder. The experimental setup can be seen in Figure 22 (Bungartz & Schafer, 2006). This paper details the setup and results of the laminar FSI and the LES FSI performed on the flap, this proves to be a very useful validation test case as the setup and run time is extremely short. The cylinder is positioned 0.2m downstream of the inflow section and 0.2m from the lower lateral wall. A constant parabolic inflow profile is used with a Reynolds number of Re = 400 for the laminar case and Re = 10000 for the turbulent case. The maximum amplitude, drag force, lift force and frequency of the flap are given.

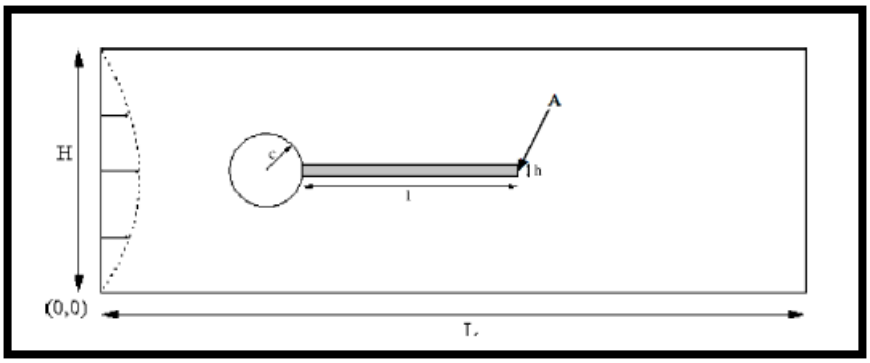

Figure 6: Configuration of the FSI simulation (Bungartz & Schafer, 2006).

2.8 CONCLUSION

This literature study covered some of the background information pertaining to heliostats and their design. Aerodynamic concepts relating to heliostats as well as the computational fluid dynamics used in the simulation of the fluid flow are covered. The literature highlighted the need to not only simulate the fluid flow for heliostats simply for mean loadings but for peak loadings too as these are critical to the design of these structures. Although studies have been conducted using SRS results, these have not gone further in applying the transient loadings to the heliostat structures, there therefore exists a gap in the research

where FSI is used with transient peak loadings. Past research pointed to the fact that the correct modelling of the ABL is anything but trivial and the importance of the turbulence intensity profile over and above the mean velocity wind profile.

3 VALIDATION OF MODELS

3.1 INTRODUCTION

Computational Fluid Dynamics provides engineers with the ability to rapidly test new designs and modifications without having to build prototypes and perform costly experiments. In order to ensure the CFD being used in either research or industrial applications is providing the correct results, it is imperative that the CFD models or methods used are validated. This means that the simulation results need to be compared to experimental data. In the event that the simulation is drastically different from any available experimental data, a comparable experiment needs to be used. The very same can be said for structural dynamics and FEM used in the FSI. This chapter contains the various validation cases used in this study.

3.2 CHARACTERISING THE ABL

As mentioned in the literature study, it is vitally important to model the ABL as accurately as possible to ensure realistic and useful results from the CFD. The ABL has many important characteristics associated with the flow. Possibly the most crucial is the horizontal homogeneity of the flow, ensuring that the inlet profiles of the mean velocity and turbulence remain unchanged through the domain apart from the interaction with the structure. It was also noted (Ghanadi, et al., 2017) the vital role the turbulence intensity has on the resultant drag of the structure. Using the guidelines set out in the literature study by (Blocken, et al., 2007) and (Richards & Norris, 2011), the ABL is investigated.

A simple 2D rectangular domain is used to characterise the ABL, the domain is empty and the ABL is able to flow through the domain unobstructed. (Blocken, et al., 2007), showed that even though turbulence is a 3-dimensional phenomenon, a 2-dimensional domain can still be used to illustrate the difficulties in achieving horizontal homogeneity with regards to boundary conditions and turbulence models used. Using a 2D domain allows one to easily model different boundary conditions and test them relatively cheaply.

To characterise the ABL, the (Peterka, et al., 1986) profiles for the mean velocity and turbulence intensity are used, these profiles are used as the proceeding CFD validation is done on the wind tunnel experiment of (Peterka, et al., 1986). The first step in modelling the ABL is to ensure the equations for the velocity profile are arranged in the correct manner. Looking at Equations 37, they can be rearranged to find the friction velocity u* for a given reference velocity, u_{Ref}, at a certain reference height, z_{Ref}, as seen in equation 63.

$$u^* = \frac{u_{Ref}\kappa}{\ln\left(\frac{z_{Ref}}{z_o}\right)} \tag{63}$$

The normalized velocity profile may be attained by substituting Equation 63 into the velocity profile of Equation 37 and rearranging:

$$\frac{u(z)}{u_{Ref}} = \frac{\ln\left(\frac{z}{Z_o}\right)}{\ln\left(\frac{Z_{Ref}}{Z_o}\right)} \tag{64}$$

Applying the boundary conditions of (Richards & Hoxey, 1993), the only value that can be altered to match a given velocity profile is that of the aerodynamic roughness z_o. Using equation 64, a fitted curve is obtained to match the mean velocity profile of (Peterka, et al., 1986). A least-squares minimization problem is solved using equation 65 in MATLAB to find the aerodynamic roughness that gives the best fit for the mean velocity profile.

$$Er(z_o) = \sum_{\varphi=1}^{\xi} \left[U_\eta - U_{Ref} \frac{\ln\left(\frac{z}{Z_o}\right)}{\ln\left(\frac{Z_{Ref}}{Z_o}\right)} \right]^2 \tag{65}$$

where:

$Er(z_o) = Sum\ of\ the\ squared\ error$
$\varphi = Experimental\ data\ point$
$\xi = Total\ number\ of\ experimental\ data\ points$

The result of equation 65 provides an aerodynamic roughness constant that will optimally match the velocity profile of (Peterka, et al., 1986) to that of the simulation. Unfortunately, in ANSYS Fluent it is not possible to specify a turbulence intensity profile, rather *k* and ε have to be specified at the inlet. From the definition of *k* and the assumption of isotropic turbulence we can relate the turbulence intensity I_u to *k* as seen in equation 66:

$$I_u(z) = \frac{\sqrt{\overline{u'^2}}}{u(z)} = \frac{\sqrt{\frac{2}{3}k}}{u(z)} \tag{66}$$

Since *k* is defined in Equation 37, subsequently looking at Equation 66 there is no way to control the turbulence intensity profile after the velocity profile has been determined. It can be concluded that the turbulence intensity profile is a direct consequence of the velocity profile. After some substitution and manipulation of Equations 37, 63 and 66, a form for the optimisation via least squares is obtained to find the aerodynamic roughness constant that will provide the best profile fit to the (Peterka, et al., 1986) turbulence intensity profile. Applying an aerodynamic roughness constant that best fits the turbulence intensity means the mean velocity profile is no longer an optimum fit to (Peterka, et al., 1986). Luckily, using Equation 64 to model the mean velocity profile allows for the reference height to be changed along with the reference velocity at that specific height. This means that the velocity profile can still match the (Peterka, et al., 1986) profile at the areas of interest while having a more accurate accompanying turbulence intensity profile. As stated in the literature study, this is a better means of modelling the ABL flow as the drag coefficient and subsequent fluctuations are highly sensitive to the turbulence. The least-squares minimization problem solved in MATLAB to find the aerodynamic roughness that gives the best fit for the turbulence intensity profile is seen in equation 67.

$$Er(z_o) = \sum_{\eta=1}^{\xi} \left[I_{u\eta} - \frac{\sqrt{\left(\frac{2}{3}\right)\left(\frac{u_{Ref}\kappa}{\ln\left(\frac{z_{Ref}+z_o}{z_o}\right)}\right)^2}}{U_{Ref}\frac{\ln\left(\frac{z}{z_o}\right)}{\ln\left(\frac{z_{Ref}}{z_o}\right)}} \right]^2 \quad (67)$$

The results of the (Peterka, et al., 1986) MATLAB profile optimisation can be seen in Figures 23 and 24 for the mean velocity and turbulence intensity profiles, respectively. In Figure 23 the profiles are given for an aerodynamic roughness z_o that optimises the velocity profile. In Figure 24 the profiles are given for an aerodynamic roughness z_o that optimises the turbulence intensity profile.

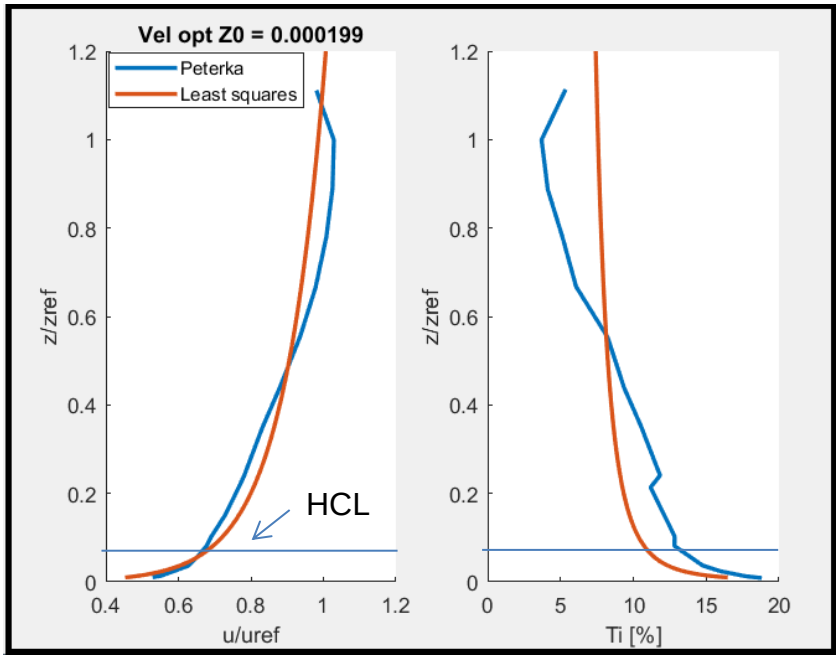

Figure 7: MATLAB optimised profiles (velocity) compared with Peterka (1986).

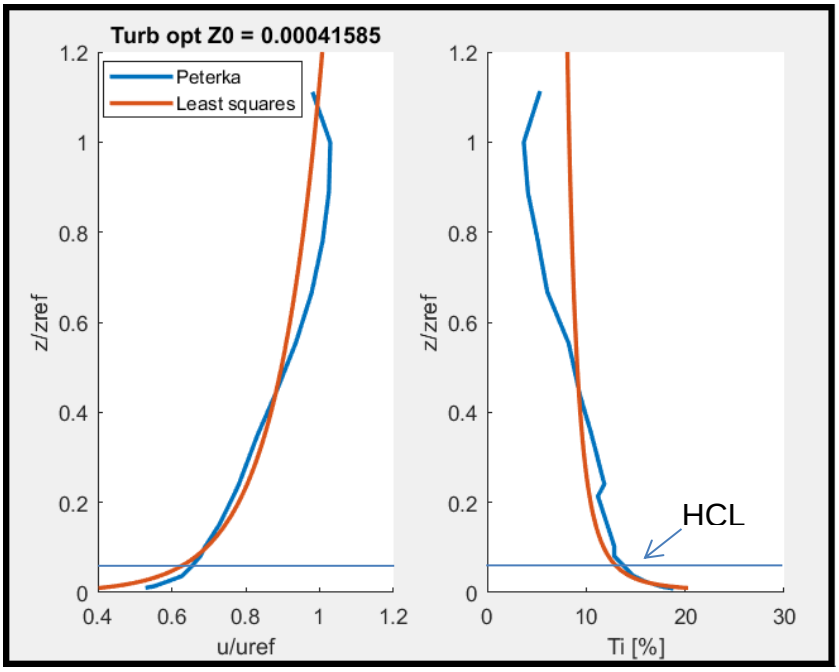

Figure 8: MATLAB optimised profiles (turbulence intensity) compared with Peterka (1986).

Looking at Figure 23, it can be seen that the velocity profile matches the experimental data closely, while there is a substantial difference in the turbulence intensity profile, it is rather under predicted near the wall. This is concerning as this is the area that the heliostat is modelled in and as noted in the literature study, the turbulence intensity has a considerable effect on the accuracy of the results. When the roughness constant is optimised to the turbulence intensity experimental results, it can be seen from Figure 34 that the profiles for the turbulence intensity and the mean velocity are closely matched and there is no longer an under-prediction near the ground plane at the heliostat height (indicated on the figures). This suggests that using a roughness constant that better approximates the turbulence intensity would result in a more accurate simulation of the force components on the heliostat. Both aerodynamic roughness constants are used in the following section on the validation of the (Peterka, et al., 1986) heliostat experiments.

The 2D domain used in the characterisation of the ABL can be seen in Figure 25. The mesh contains 16 900 mapped quadrilateral elements that are stretched in the direction away from the wall to ensure the gradient is accurately captured.

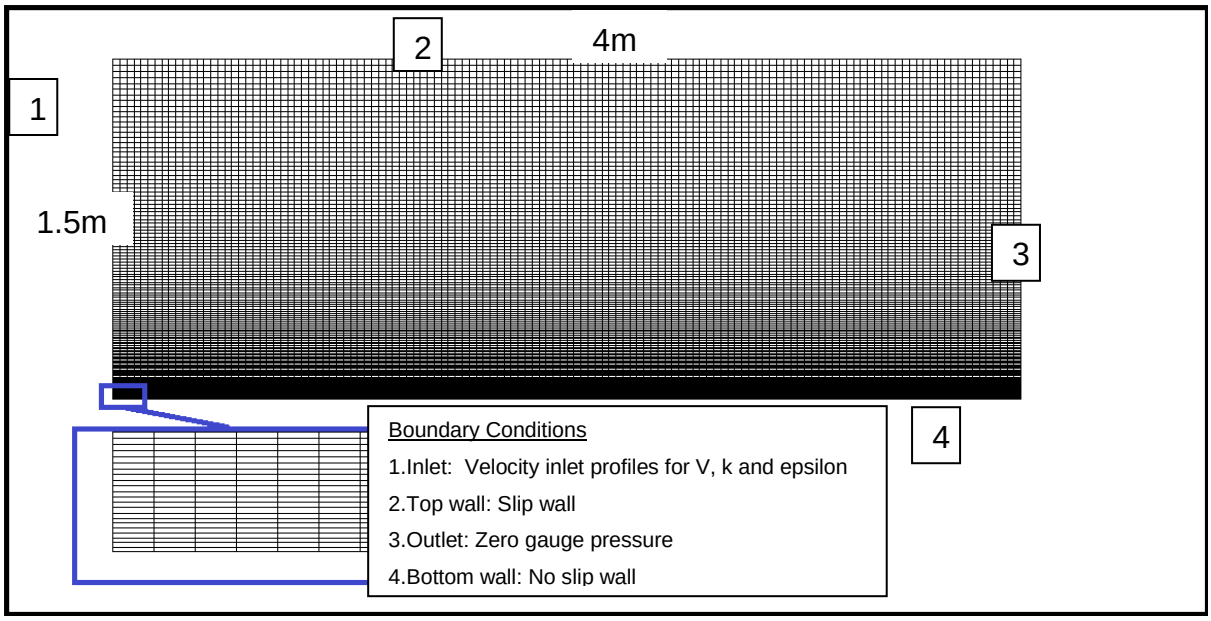

Figure 9: Two-dimensional domain used in the ABL characterisation.

The boundary conditions used at the inlet are those of Equation 37, these equations along with the corresponding aerodynamic roughness constant are coded into a UDF that is read into Fluent. As it is not currently possible in Fluent to prescribe an aerodynamic roughness constant as a boundary condition, Equation 39 is also coded into a UDF (Appendix A). This allows a sand-grain roughness to be specified as a boundary condition on the bottom wall where a no-slip boundary condition exists. The domain is 4m long and 1.5m high. The velocity and turbulence intensity profiles are shown in Figures 26 and 27 at the inlet, mid-plane and outlet. It can be seen that the horizontal homogeneity of these two flow properties remains fairly constant as the fluid flows through the domain with the rough bottom wall.

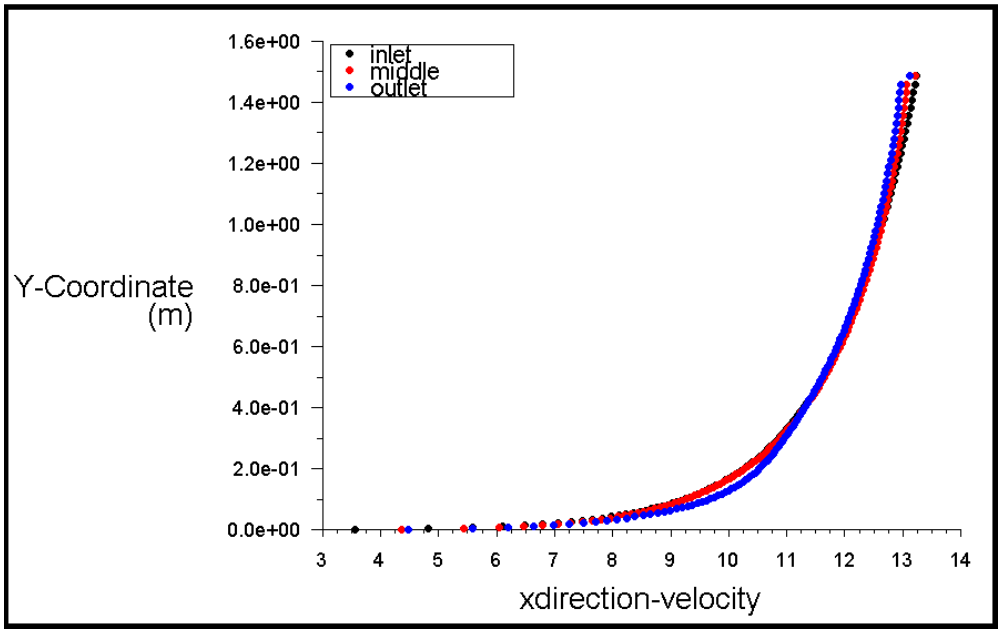

Figure 10: Mean velocity profile plotted at inlet, mid-plane and outlet for roughened wall, z_o = 0.00041585.

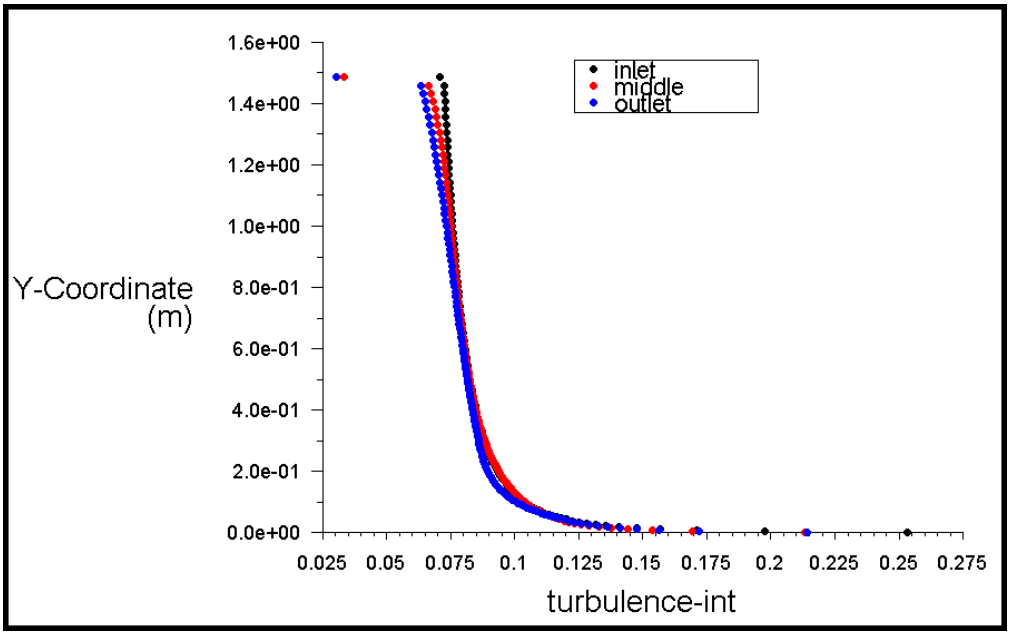

Figure 11: Turbulence intensity profile plotted at inlet, mid-plane and outlet for roughened wall, z_o = 0.00041585.

Noting that the Heliostat Centre Line (HCL) in the (Peterka, et al., 1986) wind tunnel experiment and in the validation case to follow is only at 0.069m, the consistency of the profiles is promising. In order to verify the improvement made to the horizontal homogeneity of the ABL by the roughening of the bottom wall, the same profiles are given in Figure 27 and Figure 28 except the bottom wall of the domain is now smooth.

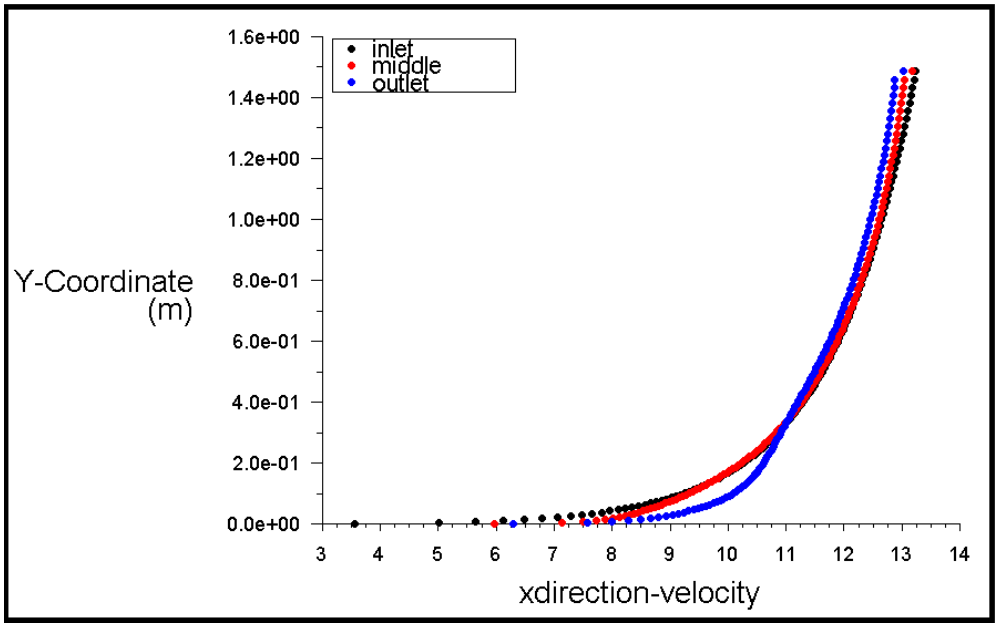

Figure 12: Mean velocity profile plotted at inlet, mid-plane and outlet for smooth wall.

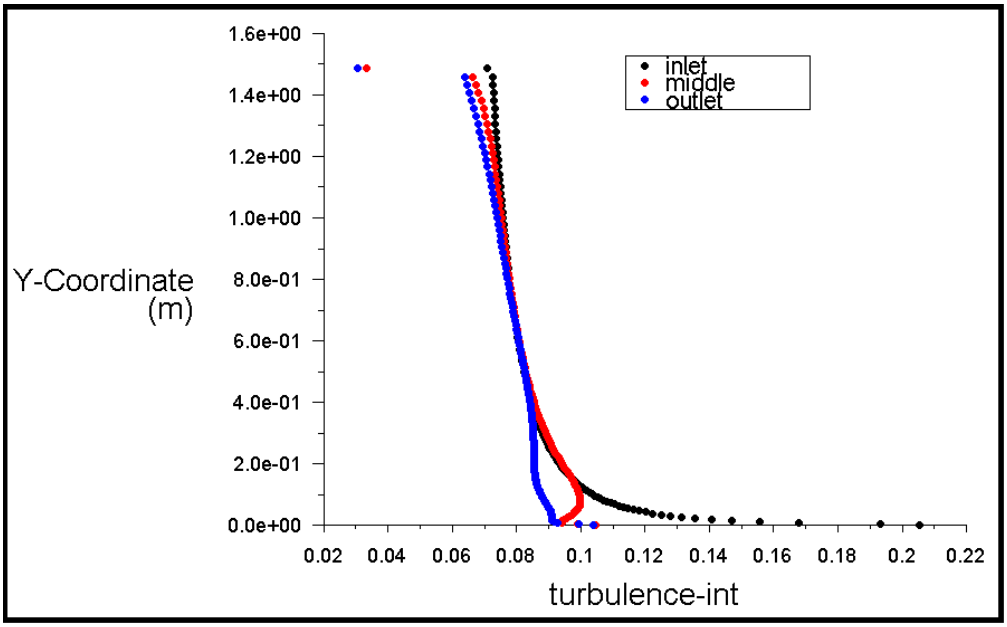

Figure 13: Turbulence intensity profile plotted at inlet, mid-plane and outlet for smooth wall.

The improvements in the homogeneity of the profiles are evident when looking at the corresponding graphs. There is a substantial discrepancy between the turbulence intensity profiles of Figure 29, in the absence of a rough bottom wall, the intensity in the area of interest tends to fade from the desired value. The difference in the velocity profiles is less obvious (compared to Figure 26) although still visibly present. Comparing the inlet profiles with the mid-plane profiles for the roughened wall almost no difference is visible. This is promising as the heliostat is placed well before the mid-plane in the computational domain.

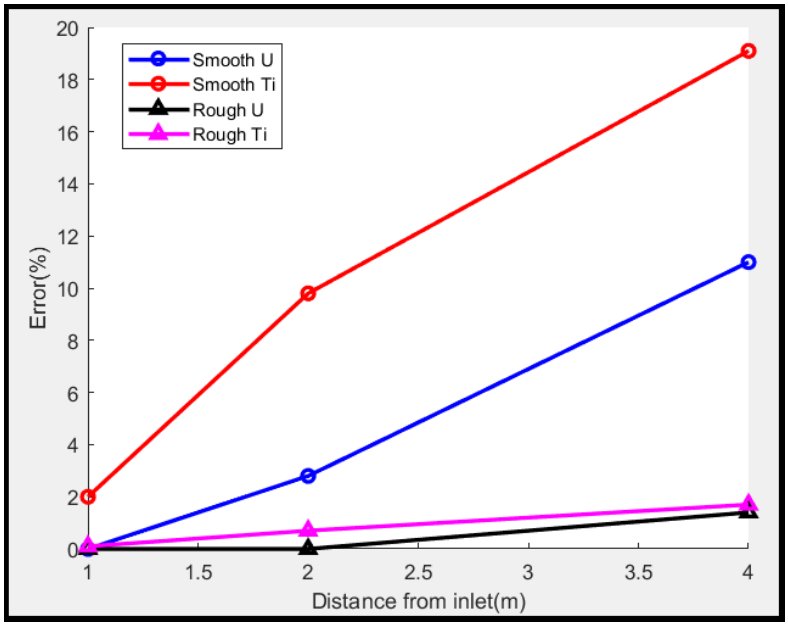

Figure 14: Profile errors at HCL for rough and smooth wall at different locations downstream of the inlet.

Figure 30 shows the error in the profiles for the velocity and turbulence intensity for both the smooth and rough walls. The error is normalised with the inlet value and gives the relative error to the profiles specified at the inlet at the HCL value of 0.069m. The graph shows that the error increases for both rough and smooth bottom walls as the downstream distance increases, but this error is significantly larger when the wall is smooth, in fact there is an order of magnitude difference between the turbulence intensities for the rough and smooth walls. It can be concluded that to reduce the effects of horizontal inhomogeniety the bottom wall should be rough and the distance downstream from the inlet to the heliostat should be kept to a minimum.

3.3 PETERKA VALIDATION CASE

The first heliostat validation case performed in this study is the wind tunnel experiment of Peterka (1986). This experiment is simulated with the use of CFD as accurately as possible in order to ensure that CFD can precisely replicate the results obtained by (Peterka, et al., 1986). This research is chosen first as the ABL characterisation from the previous section is used and there is an extensive amount of data available from (Peterka, et al., 1986) that can be used to compare to the CFD simulation. Along with the inlet profiles available, peak, RMS and mean wind load data are available for numerous heliostat orientations.

There is some ambiguity with regards to the exact velocities used in the (Peterka, et al., 1986) experiment and at which reference heights the velocities refer to. For this validation study run #99 from (Peterka, et al., 1986) is chosen and replicated. For this case the wind direction is approaching the heliostat directly head on and the heliostat is configured upright at 90^{o}, the experimental velocity is 40ft/s which equates to 12.192m/s at a reference height of 0.167m. Using the (Peterka, et al., 1986) inlet profiles the reference velocity can be found at the HCL of 0.0686m to be 10.542m/s. This equates to a Reynolds number of approximately 60 000.

The heliostat model is replicated to match the (Peterka, et al., 1986) wind tunnel model shown and dimensioned in the report. The model from (Peterka, et al., 1986) can be seen in Figure 31. The computational model of the heliostat can be seen in Figure 32.

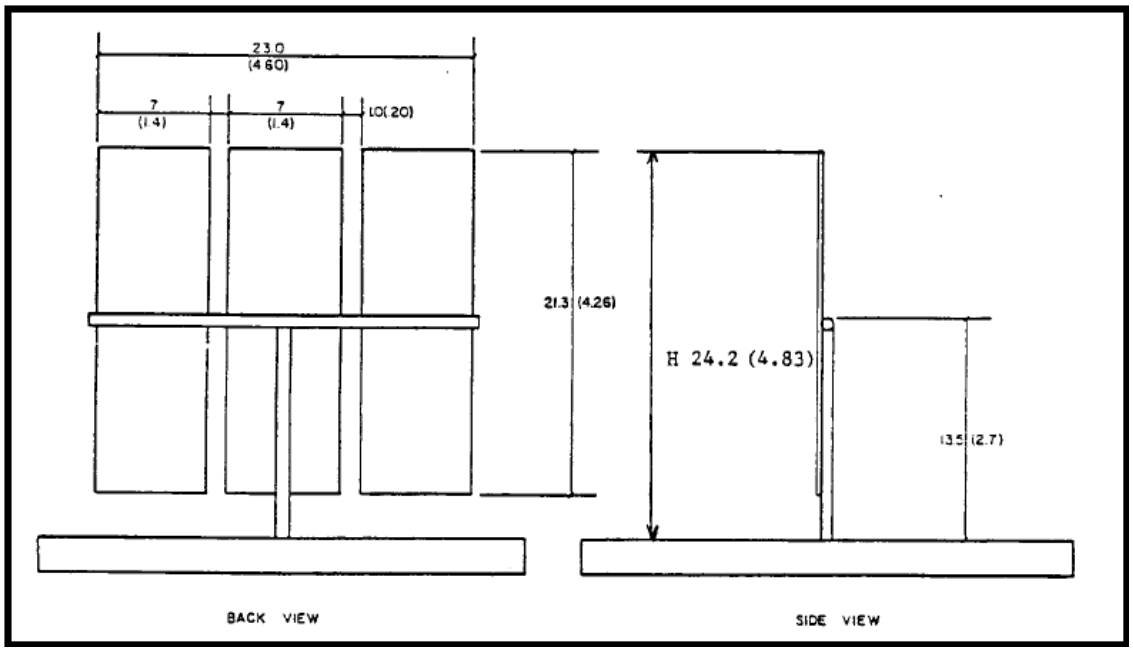

Figure 15: Heliostat model used in wind tunnel experiments (dimensions in brackets in inches) (Peterka, et al., 1986).

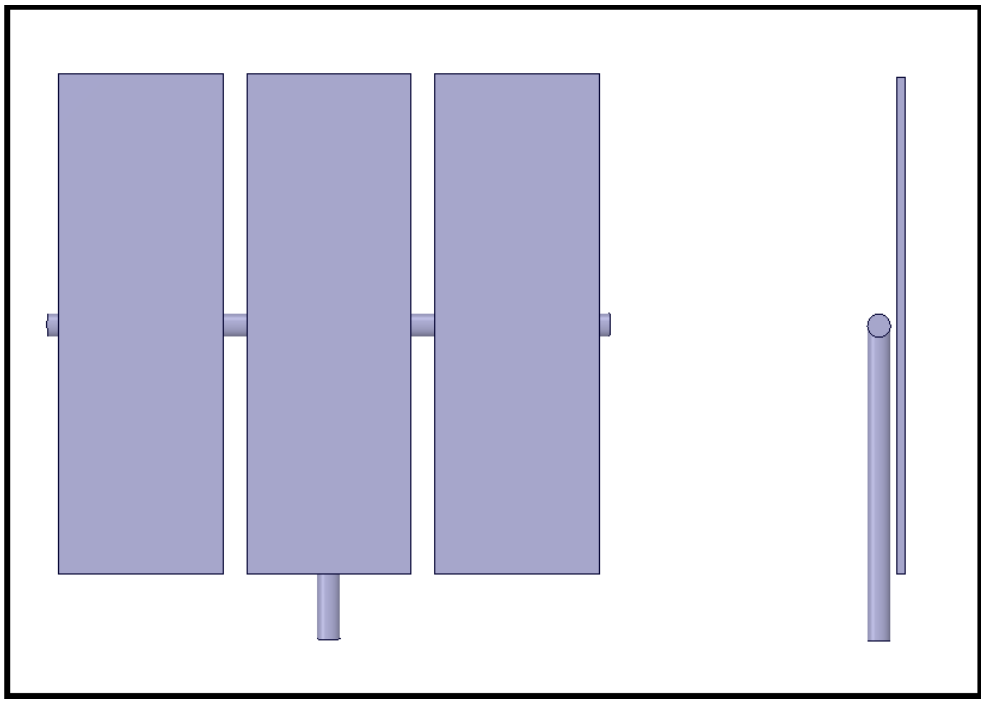

Figure 16: Computational heliostat model of (Peterka, et al., 1986) used in the CFD simulation.

The boundary conditions used for this simulation are similar to those of the ABL characterisation, the same inlet profiles are used for the velocity, turbulent kinetic energy and the dissipation. The top and side walls are slip walls while the outlet is a zero-gauge pressure boundary. The bottom wall has a prescribed sand-grain roughness. The boundary conditions used can be seen in Figure 33.

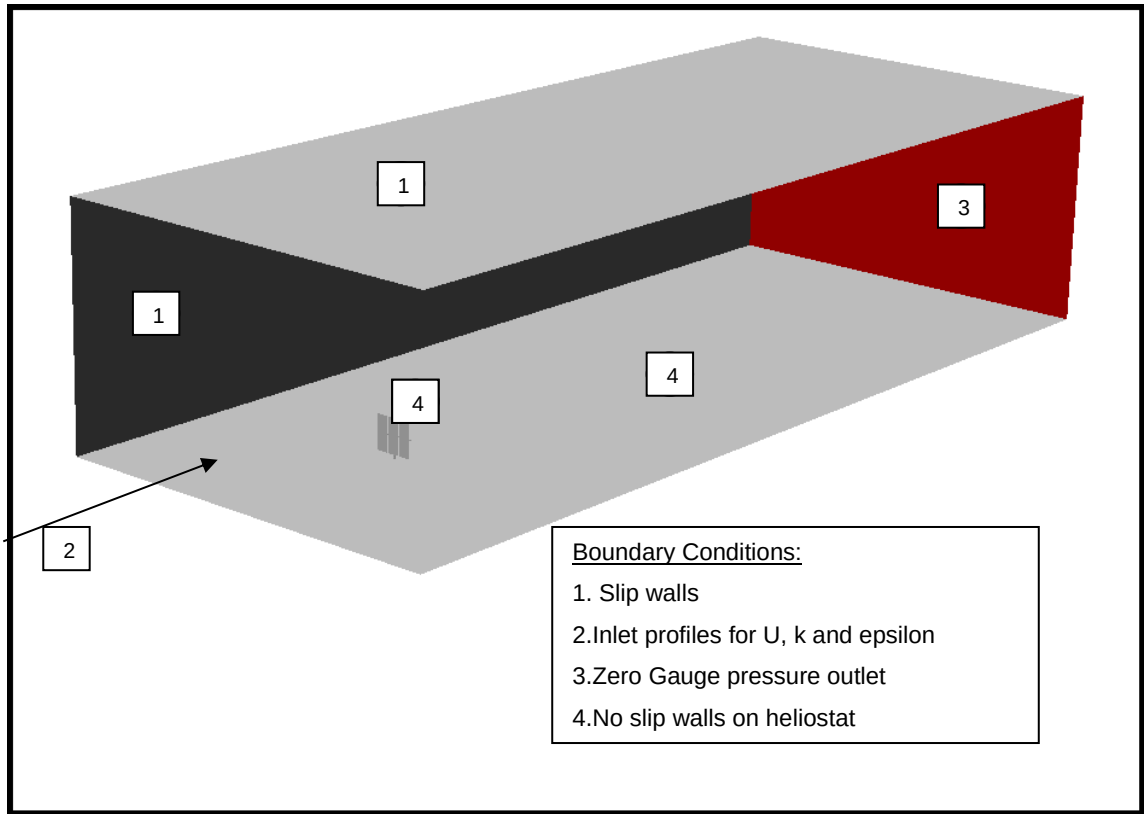

Figure 17: Computational domain of Peterka (1986) showing the boundary conditions.

The mesh used in this simulation is a hybrid tetrahedral-hexahedral mesh. In the immediate vicinity of the heliostat an unstructured tetrahedral mesh is used in order to mesh the geometry of the heliostat easily. The rest of the domain consists of a block-structured hexahedral mesh. This is used in order to control the element size in the specific blocks, allowing a finer mesh in the areas of high gradients and interest. The mesh and domain extent can be seen in Figure 35 and Figure 36. The mesh consists of approximately 4.6 million cells, with a maximum cell size of 1mm on the heliostat.

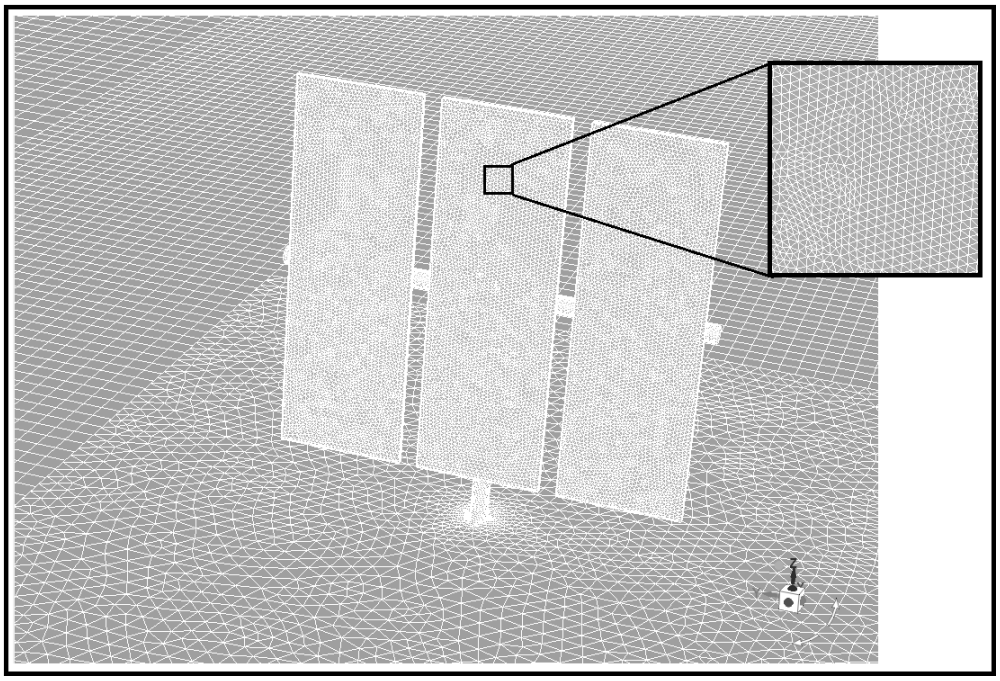

Figure 18: Heliostat geometry mesh with close-up of the tetrahedral mesh.

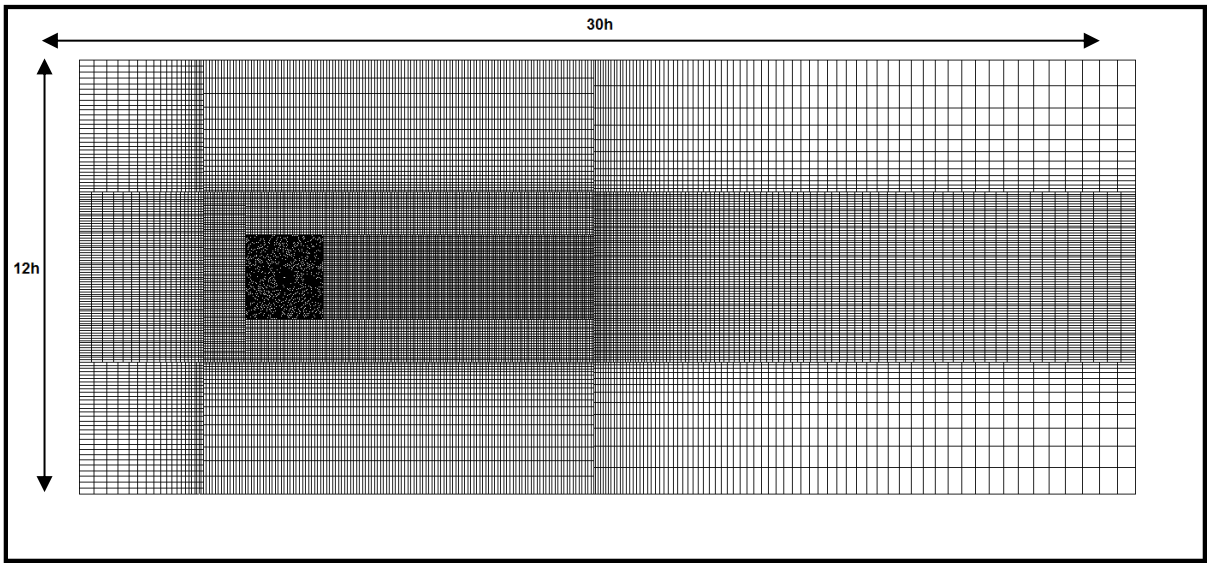

Figure 19: Bottom view of the computational domain showing the unstructured mesh around the heliostat.

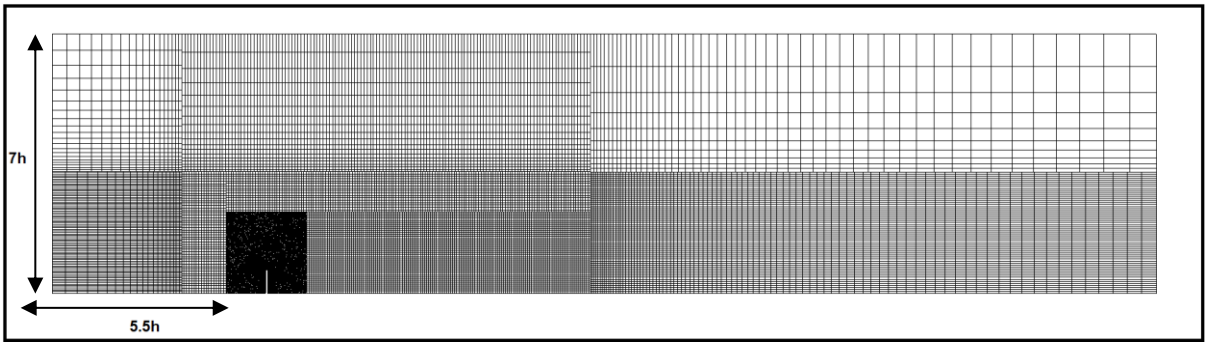

Figure 20: Side view of the computational domain (h is heliostat height).

In ANSYS Fluent, the force and moment coefficients are calculated from the shear and pressure forces on selected surfaces. In this simulation, the mirrors, torque tube and pylon are selected as the surfaces where force coefficients need to be determined. These forces are then summed and exported to ANSYS workbench as coefficient parameters. The moments for this particular simulation are taken about the torque tube axis. As this is the first of two RANS validation cases presented, only the x-direction drag coefficient and the torque tube moment are calculated and compared to that of (Peterka, et al., 1986).

The RKE RANS equations are used with standard wall functions. The double precision, SIMPLE solver is used with second-order spatial discretisation schemes. The reference values used in Fluent as well as the material properties for air that are implemented in the solver can be seen in Table 1. The steady-state flow field is assumed to be converged when the scaled residuals reach a value of $1x10^{-4}$ or the wind loading coefficients reach a steady-state value. The turbulence intensity at the HCL is 13.5%.

A_{REF}	0.01168 m^2
L_{REF}	0.0686 m
u_{REF}	12.192 m/s
ρ	1.225 kg/m^3
μ	$1.7894x10^{-5}$ kg/ms

Table 1: Reference values and material properties used in Fluent (Peterka validation).

Two simulation runs were completed on the (Peterka, et al., 1986) heliostat setup, the first run used the aerodynamic roughness length optimised in MATLAB that gave the best fit for the mean velocity inlet profile, z_o=0.000199, this was coded into the UDF and set as the inlet boundary condition. The second simulation used the roughness length optimised in MATLAB that gives the best fit for the turbulence intensity, z_o=0.00041585. The results can be seen in Table 2:

	Peterka	VelOpt Run	Error (%)	TurbOpt Run	Error (%)
C_D	1.26	1.1571	8.2	1.1913	5.5
C_{My}	0.07	0.0498	29	0.051173	27

Table 2: Results of the (Peterka, et al., 1986) validation.

The error percentages in Table 2 are calculated according to equation 68:

$$Error(\%) = \frac{C_{EXP} - C_{CFD}}{C_{EXP}} \times 100 \tag{68}$$

where:

$C_{CFD} = Wind\ loading\ coefficient\ obtained\ in\ CFD$
$C_{EXP} = Wind\ loading\ coefficient\ from\ experiment$

As can be seen from table 2, the results of the CFD simulations show that the RKE CFD model can predict the loading on the heliostat structure with reasonable accuracy. There is still however, an under-prediction of the force and moment coefficients which may be due to the under-prediction of the turbulence intensity

as well as other factors such as the mesh. The simulation using the higher z_o that was optimised for the turbulence intensity inlet profile resulted in higher turbulence intensity at the HCL, this then resulted in lower errors for both the drag and moment coefficients. This corroborates the importance of the turbulence intensity for finding loading data for bluff bodies in the ABL in CFD. The z_o optimised for turbulence intensity will thus be used in future simulations ahead of the z_o optimised for velocity.

General flow field results are shown below for the (Peterka, et al., 1986) validation simulation using the RKE model and the aerodynamic roughness length optimised for turbulence intensity. The heliostat is orientated upright with the flow attacking it directly head on. Figure 37 shows the velocity contour plot of the side of the heliostat with flow moving from left to right. It can easily be seen that at the top and bottom edges of the mirror separation occurs, this is expected where there is a high velocity flow past a bluff body. There is a large recirculation region behind the heliostat with secondary smaller recirculation regions on the back face of the heliostat. The low-pressure turbulent wake can be seen to continue downwind for a considerable distance from the heliostat resulting in the massive pressure drag seen by bluff bodies. Figure 38 shows a velocity vector plot where the recirculation zones are clearly visible. It can be seen from Figure 37 that there is a low velocity bubble of the windward side of the mirror above the torque tube, this results in a high-pressure stagnation point which is the reason for the torque tube moment that is experienced. This high-pressure zone can be seen in Figure 39.

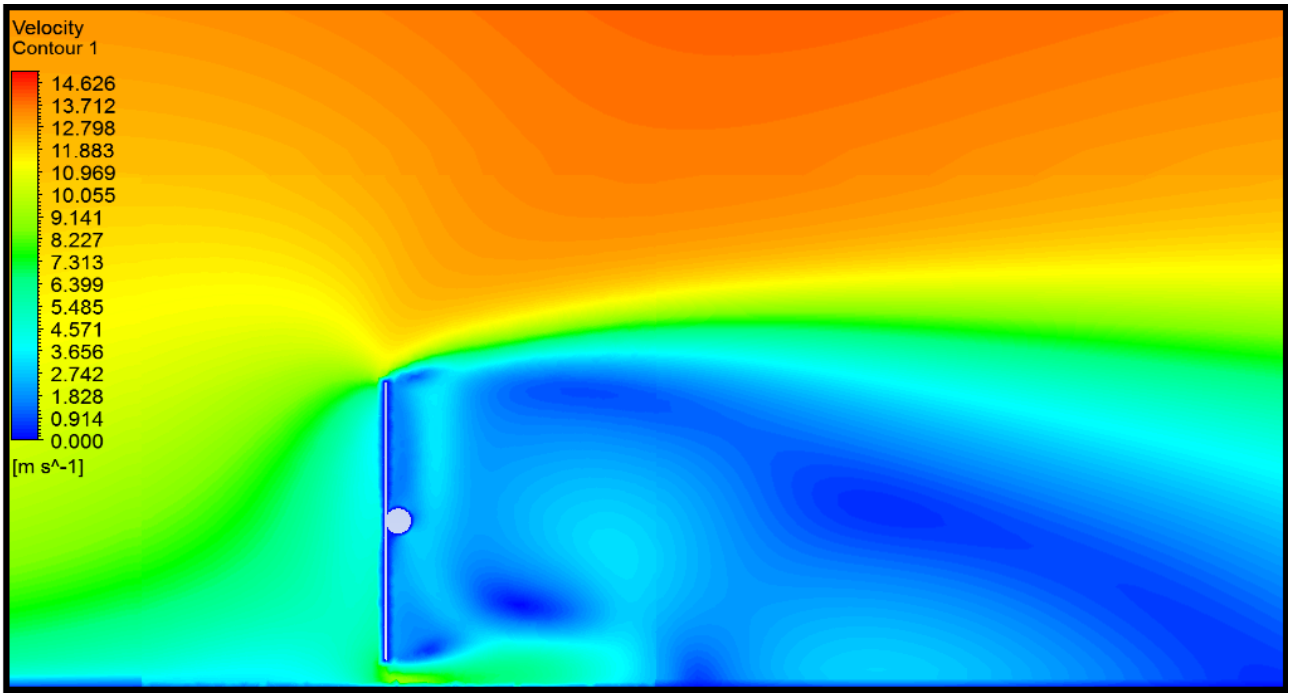

Figure 21: Velocity contour plot of Peterka (1986) heliostat (m/s).

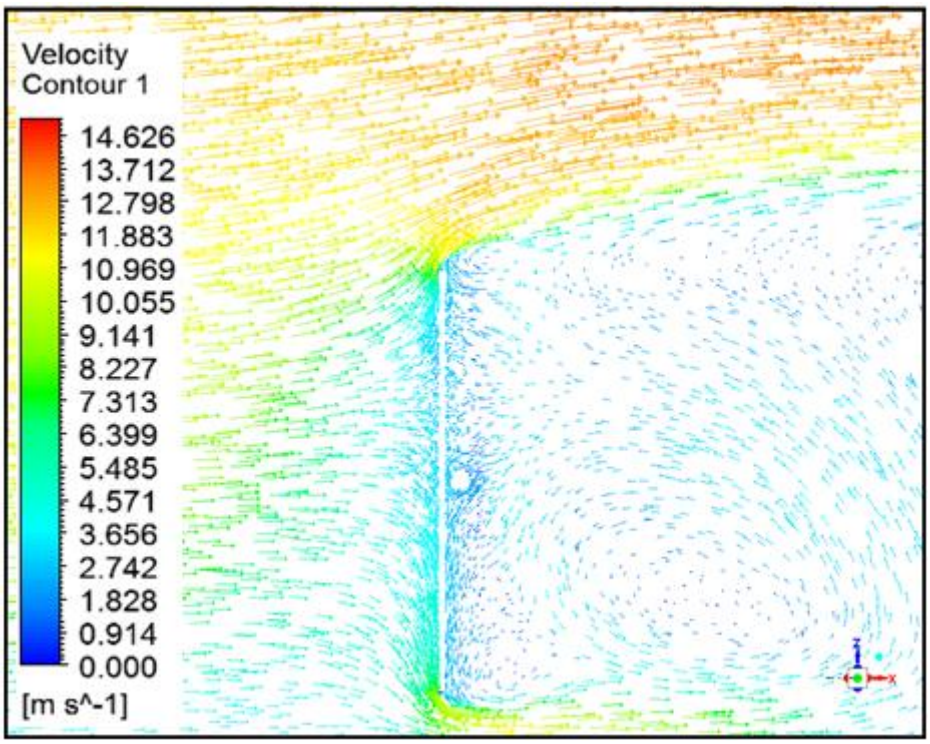

Figure 22: Velocity vector plot (m/s).

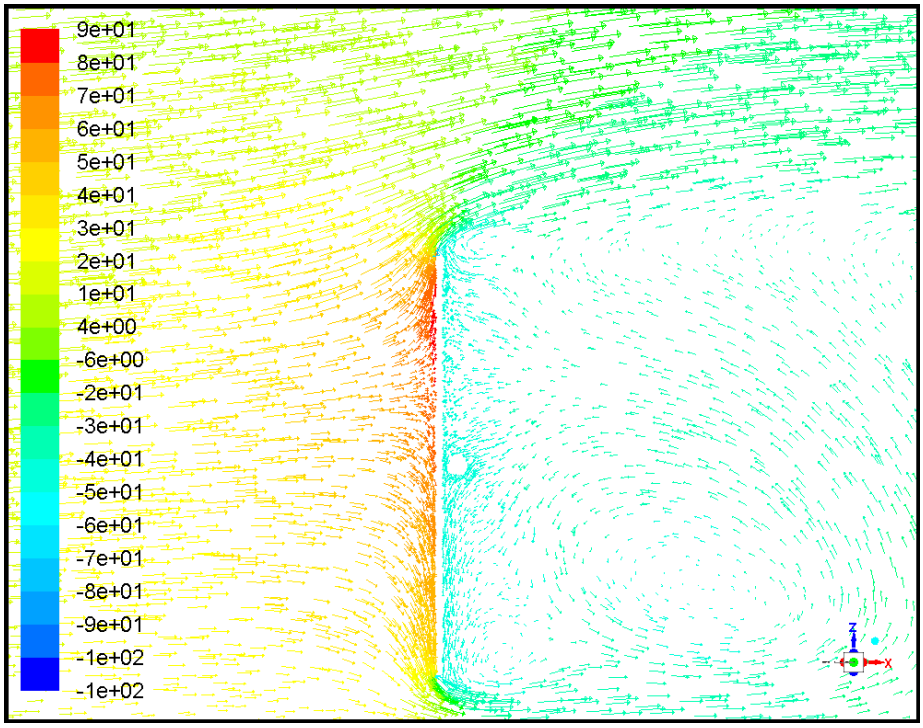

Figure 23: Velocity vector plot coloured by static pressure (Pa).

Figure 40 provides the velocity magnitude contour plot from a bird's eye view, from this figure the jet like flow through the gaps between the mirrors are visible. As the flow reaches the leeward side of the

heliostat, two distinct recirculation zones are created behind the outer mirrors, this can be confirmed by looking at Figure 40 of the velocity vector plot of the same view.

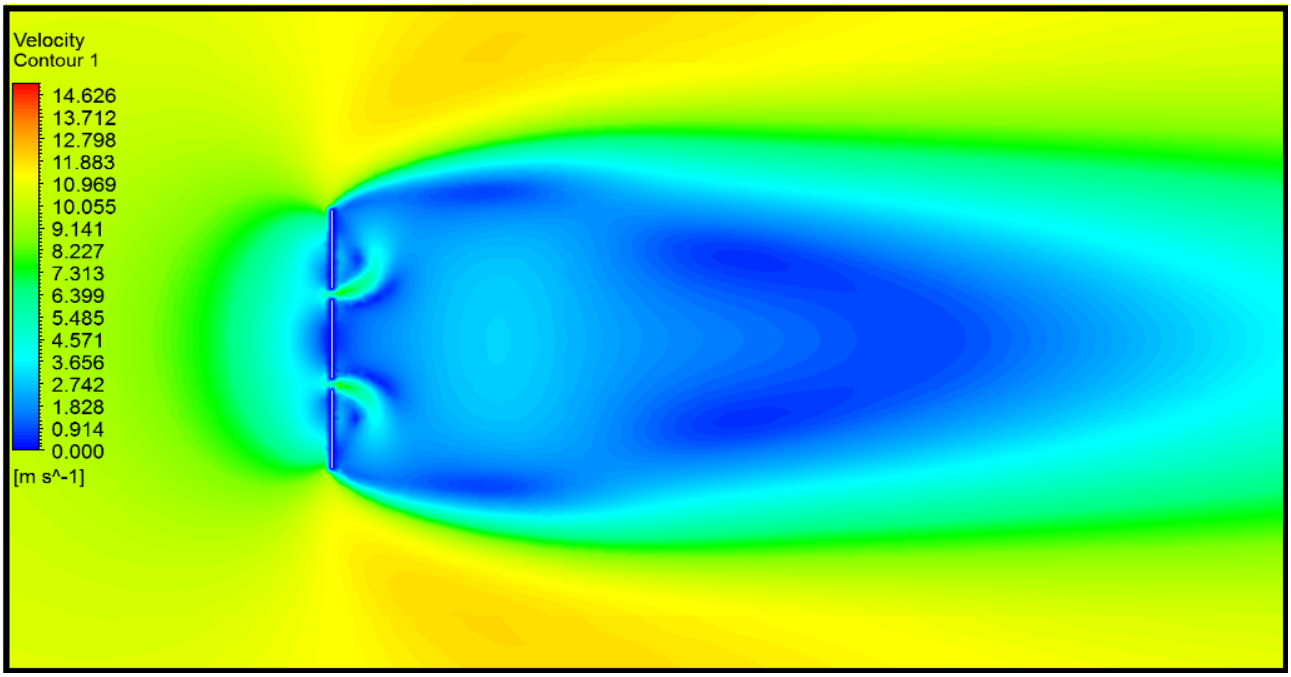

Figure 24: Velocity contour plot, bird's eye view (m/s).

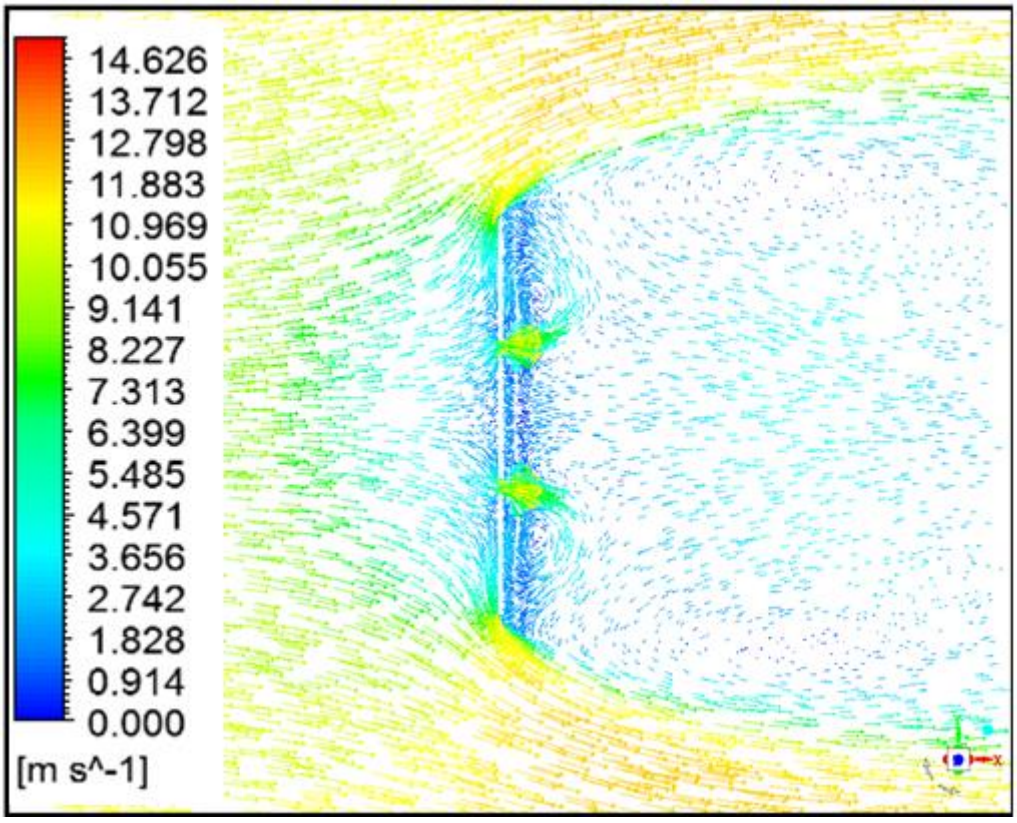

Figure 25: Velocity vector plot, bird's eye view (m/s).

In conclusion to the validation case of (Peterka, et al., 1986), it can be said that using RANS modelling to find the mean loading coefficients for a heliostat in the ABL leads to fairly accurate results. The biggest hurdle in the modelling of the heliostat lies in the matching of the velocity and turbulence profiles. One important outcome of these RANS simulations is the fact that there is no transient behaviour of the flow which is expected from a bluff body and is known to exist (Matty, 1979). The shortcoming of RANS is that it cannot be used to find any peak loadings or transient behaviour which is expected as the flow behind the heliostat is a highly complex 3-dimensional field. Flow from around the sides interacts with flow separating from the top and bottom edges as well as the gap through-flow creating intricate flow behaviour. RANS at the end of the day is designed to average out any flow anomalies.

3.4 RWDI LH-2 VALIDATION CASE

The second heliostat validation case performed in this study is the (Huss, et al., 2011) experiment of the LH-2 heliostat. The LH-2 heliostat is currently in operation at the Ivanpah CSP plant in California, over 173 000 heliostats are operational at this plant. The research done by (Huss, et al., 2011) includes wind tunnel experiments of an aeroelastic scale model of the LH-2 as well as RANS CFD modelling of the LH-2. The CFD code used by RWDI is COSMOSFloWorks. The dimensions of the LH-2 are given in Figure 42.

Double Mirror Heliostat	
	
Mirror Size	**Two mirrors, 3210 x 2250 x 4mm each, with 352mm gap between mirrors**
Height between horizontal axis to the ground	**1900 mm**

Figure 26: LH-2 heliostat dimensions (Huss, et al., 2011).

The wind tunnel model used in the experiments is a 1:7 scale model of the LH-2. No inlet flow profiles are provided but the turbulent intensity is specified at a height of 1.9m for the longitudinal intensity of I=20% while the intensity in the vertical direction is I=12%. As no inlet profiles are specified, the ABL inlet profiles from (Peterka, et al., 1986), used in the previous validation case, are specified as inlet boundary conditions for this case, the difference being the specified turbulence intensity used. The turbulence intensity is altered by changing the aerodynamic roughness length, z_o, to match the 20% at the reference height of 1.9m. The optimised z_o that resulted in Iu=20% at 1.9m was found to be z_o= 0.0107615. The velocity used is 10.5m/s which results in a Reynolds number of approximately Re=500 000, which should ensure Reynolds

number independence of the flow. Using a scale of 1:7, the resulting reference area is 0.3028m^2 with the HCL height being 0.2714m. The computational model of the LH-2 can be seen below in Figure 43.

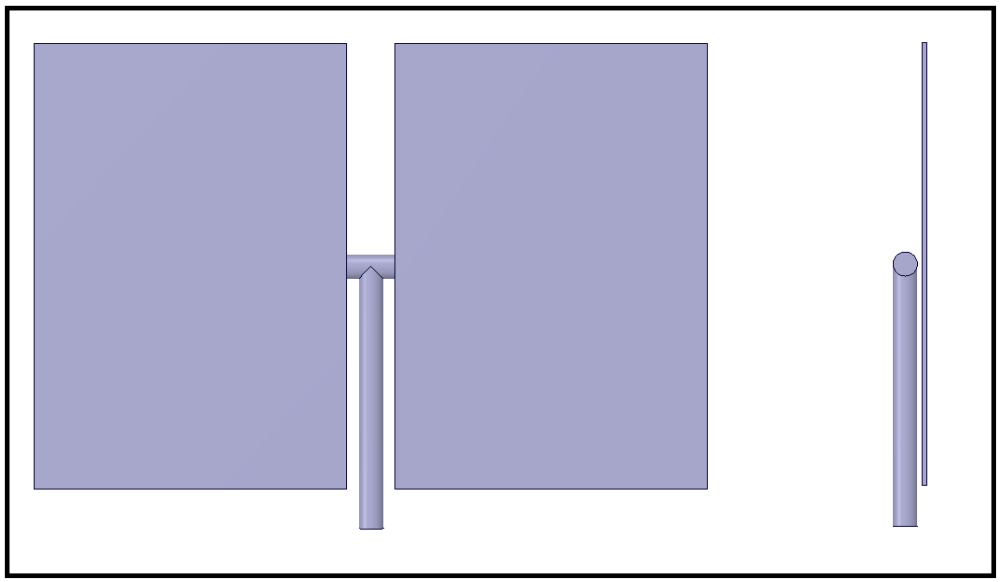

Figure 27: Computational model of the LH-2 used in the validation case.

The boundary conditions used for the validation of the RWDI case are the same as those used for the (Peterka, et al., 1986) case, the only difference being the change to the aerodynamic roughness length in the UDF. The change in the roughness results in slightly different values from the same profiles. The top and side walls are slip walls while the outlet is a zero-gauge pressure boundary. The bottom wall has a prescribed sand-grain roughness. The boundary conditions can be seen in Figure 44.

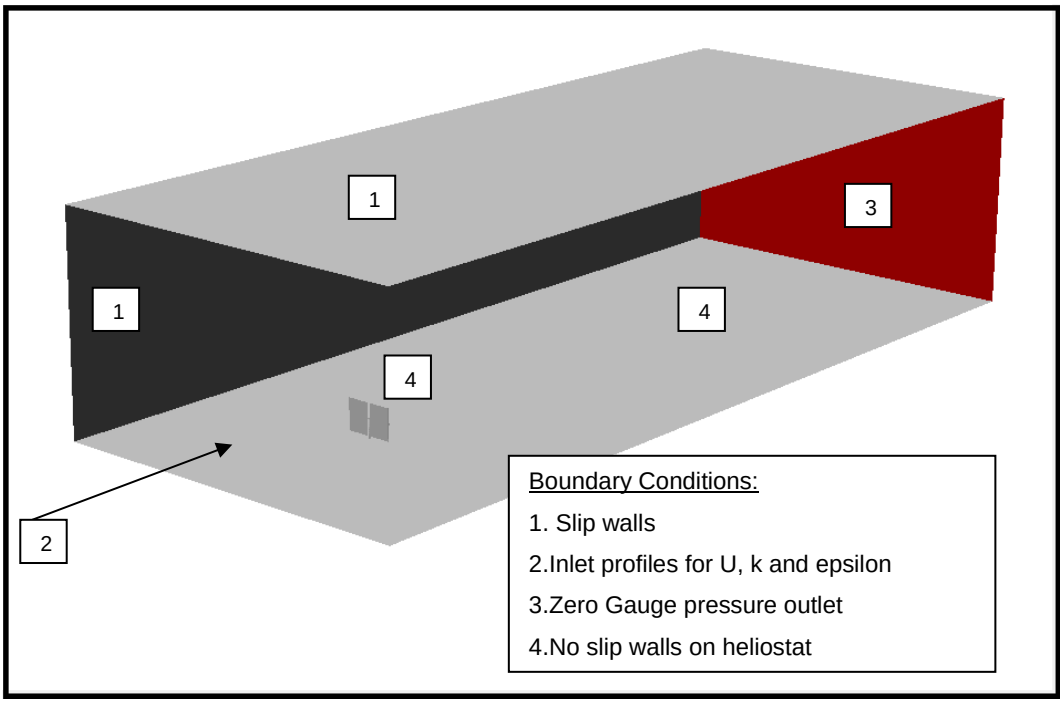

Figure 28: Computational domain of (Huss, et al., 2011) case showing boundary conditions.

The mesh used for the (Huss, et al., 2011) validation case is almost identical to the mesh used for the (Peterka, et al., 1986) case. The only distinctions being the size of the domain, due to the heliostat model difference, and the number of computational cells. A hybrid tetrahedral-hexahedral mesh is used as before. The mesh contains roughly 5 million cells with the cell size on the heliostat surface specified at a maximum of 3mm. A close-up of the heliostat mesh can be seen in Figure 45. The domain extent can be seen in Figure 46 and Figure 47.

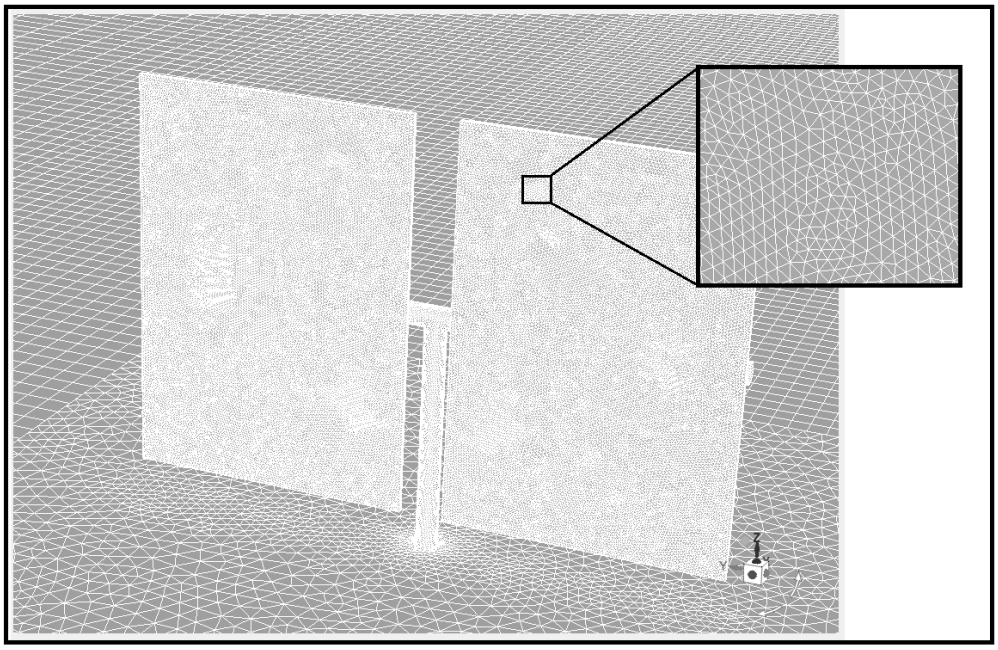

Figure 29: LH-2 heliostat mesh with close up of the tetrahedral mesh.

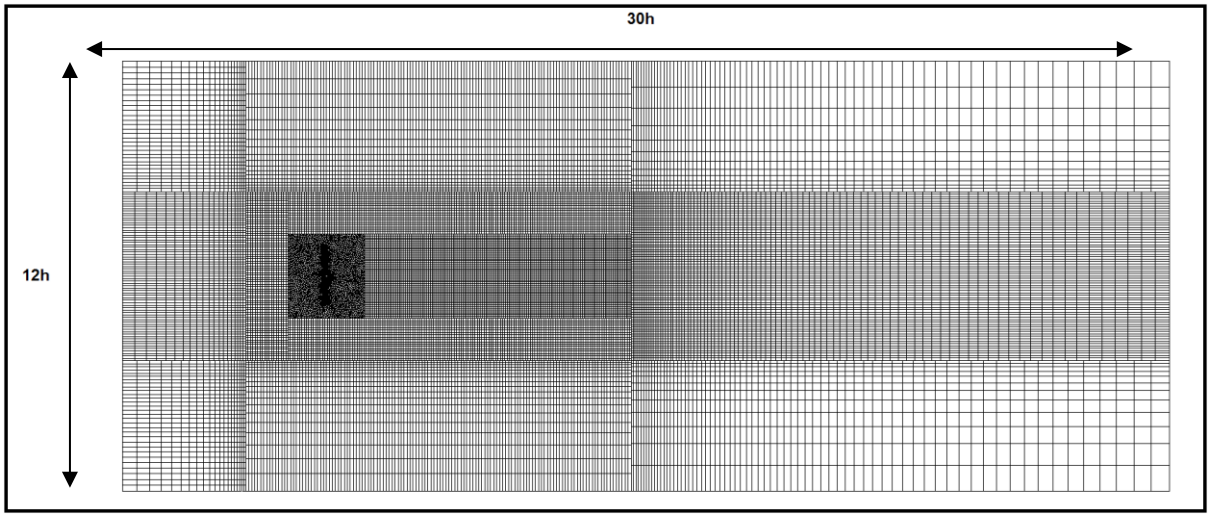

Figure 30: Bottom view of the LH-2 computational domain.

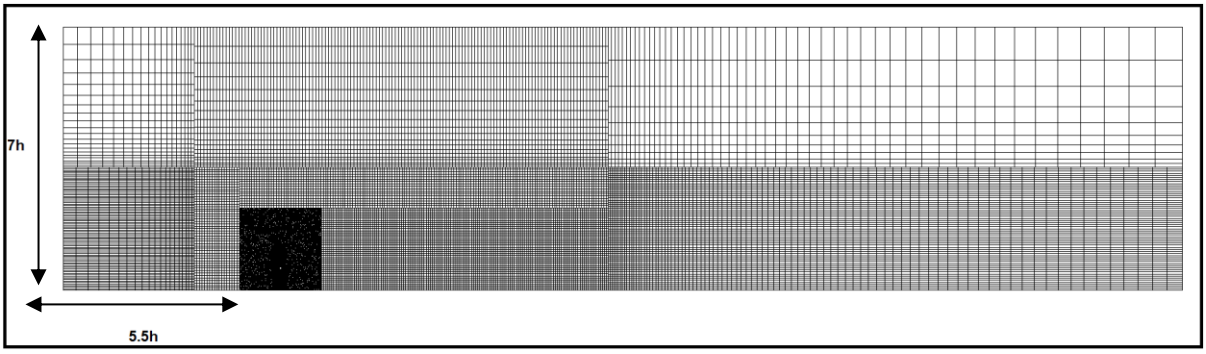

Figure 31: Side view of the LH-2 computational domain.

The RKE RANS equation is used for this simulation with standard wall functions. The double precision, SIMPLE solver is used with second-order spatial discretisation schemes. The reference values used in Fluent are listed in Table 3. The steady-state flow field is assumed to be converged when the drag coefficient residual monitor reaches a value of $1x10^{-4}$ or the residuals reach a value of $1x10^{-4}$.

A_{REF}	$0.3028m^2$
L_{REF}	0.2714m
u_{REF}	10.5 m/s
ρ	1.225 kg/m^3
μ	$1.7894x10^{-5}$ kg/ms

Table 3: Reference values and material properties used in Fluent (LH-2 case).

For this validation, the heliostat is positioned with the flow approaching normal to the mirror faces. The angle of the mirrors around the torque tube is parameterized and a parametric study is performed in ANSYS Workbench. Seven simulations are performed with the mirror being rotated around the torque-tube (elevation angle) starting at 0° (upright) and increasing in increments of 15°up to the final position of 90° (the stow position).

For all seven simulations, the drag, lift, pylon moment and torque tube moment coefficients are solved for. These coefficients are compared to the (Huss, et al., 2011) wind tunnel results as well as the (Huss, et al., 2011) CFD results. The pylon moment is the moment of the entire heliostat about the ground plane through the pylon. The torque tube moment is the moment created by the mirrors about the torque tube. The resultant coefficients can be seen in the Figures 48 to 51.

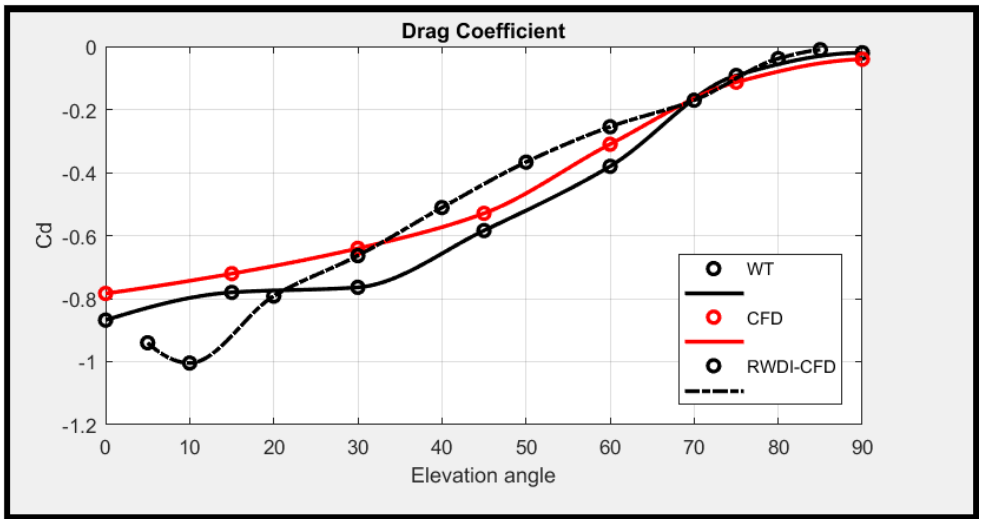

Figure 32: Drag coefficient versus elevation angle (°) results compared to (Huss, et al., 2011).

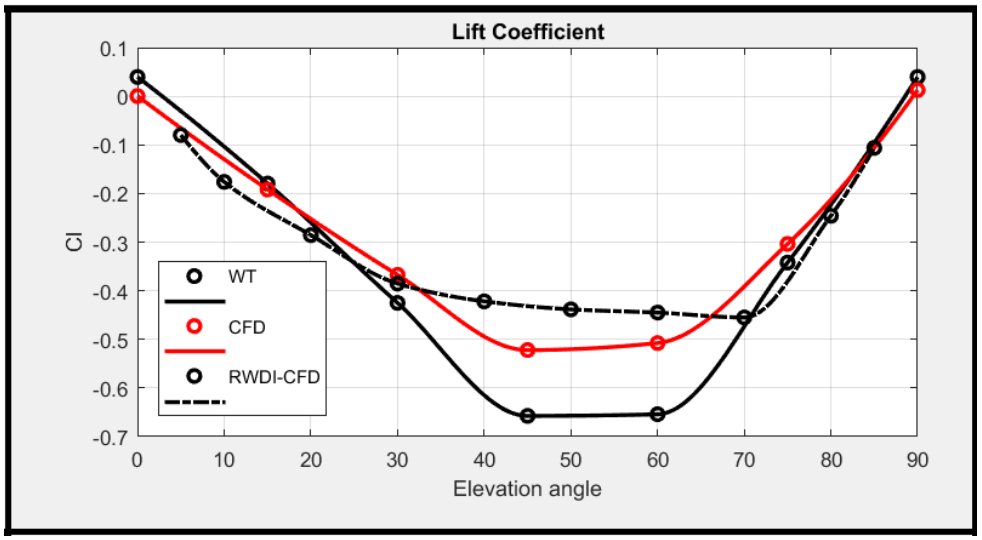

Figure 33: Lift coefficient versus elevation angle (°) results compared to (Huss, et al., 2011).

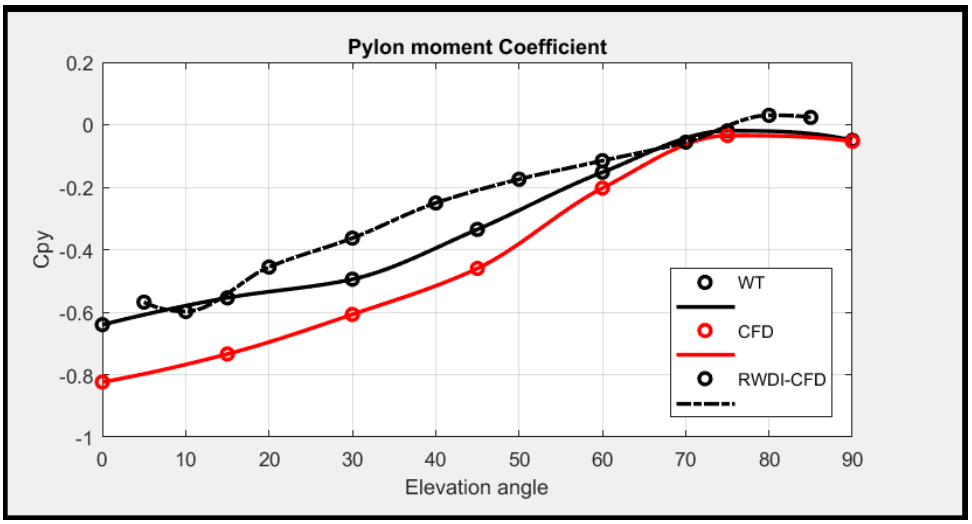

Figure 34: Pylon moment coefficient versus elevation angle (°) results compared to (Huss, et al., 2011).

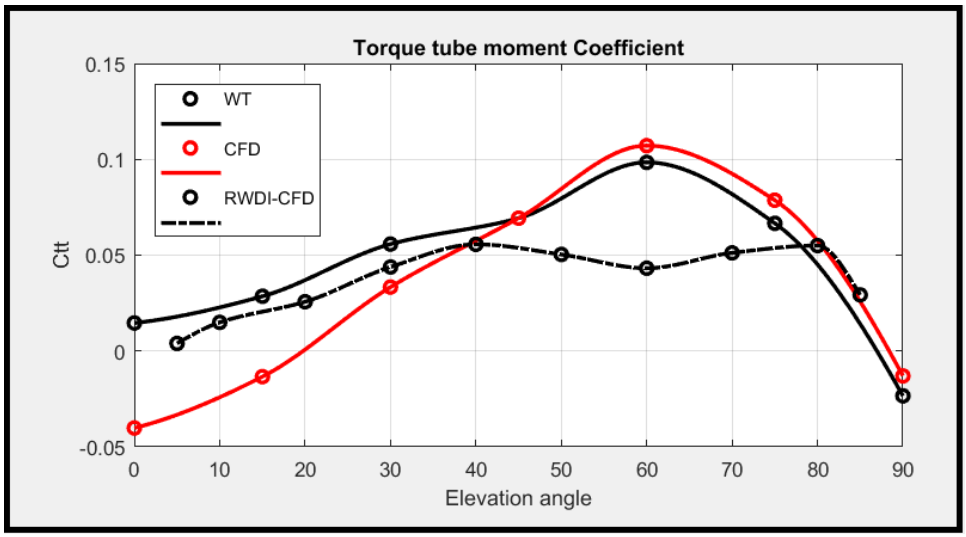

Figure 35: Torque tube moment coefficient versus elevation angle (°) results compared to (Huss, et al., 2011).

As can be seen from the force and moment coefficient plots above, the CFD results obtained for this study and the (Huss, et al., 2011) wind tunnel results show a strong similarity. Looking at Figure 48 for the drag coefficient, it can be seen that the CFD predicts the drag accurately over the various elevation angle orientations. The two angles of particular interest for the drag are the upright (0°) and operational (60°) angles where the error in the drag is 9.7% and 18% respectively. These errors are quite acceptable when modelling CFD. The maximum drag coefficient is correctly predicted to be at the upright angle where the mirrors present the largest obstruction to the flow.

The lift coefficient, seen in Figure 49, also shows a strong similarity between the CFD and the wind tunnel results, this is particularly true for the upright and stowage configurations. At both 40° and 60° there is a noticeable distinction between the CFD and wind tunnel results. This may be due to the fact that at these heliostat mirror configurations the lift force is significantly higher and may lead to a higher degree of inaccuracy in the lift prediction. Again, it can be said that the CFD predicts the lift of the heliostat with a fair degree of precision. No lift is present when the mirrors are in the upright position. The lift gradually increases to a maximum at 45° as expected along the negative y-axis and decreases as the mirrors approach the stowage or horizontal position.

The pylon moment coefficient displays the expected behaviour as this particular moment is directly influenced by the drag force of the heliostat. As such, the trend of the pylon moment correlates strongly with the trend of the drag coefficient curve as seen from the Figures above. The torque tube moment coefficient results also behave as expected and display an improved trend compared to the (Huss, et al., 2011) CFD results, except for the 0° configuration. This may be the result of the stagnation point being higher than the HCL on the windward mirror surface, this offset of the pressure then creates a torque about the torque tube. As can be seen from Figure 51, the highest torque tube moment is achieved at 60° along with the highest lift force coefficient. The operational configuration of the heliostat is in the proximity of this angle thus it is of particular interest, along with the upright configuration. The cause of the high torque tube moment will be investigated below with a look at the contour and vector plots of the heliostat.

The general flow field results are now presented for the worst-case orientation of 60° using the RKE model. In Figure 52, the streamlines, coloured by the velocity magnitude, are shown as they interact with the heliostat structure. As expected, the separation can be seen on both the bottom and top mirror edges with the large separation bubble forming on the leeward side of the leading mirror edge.

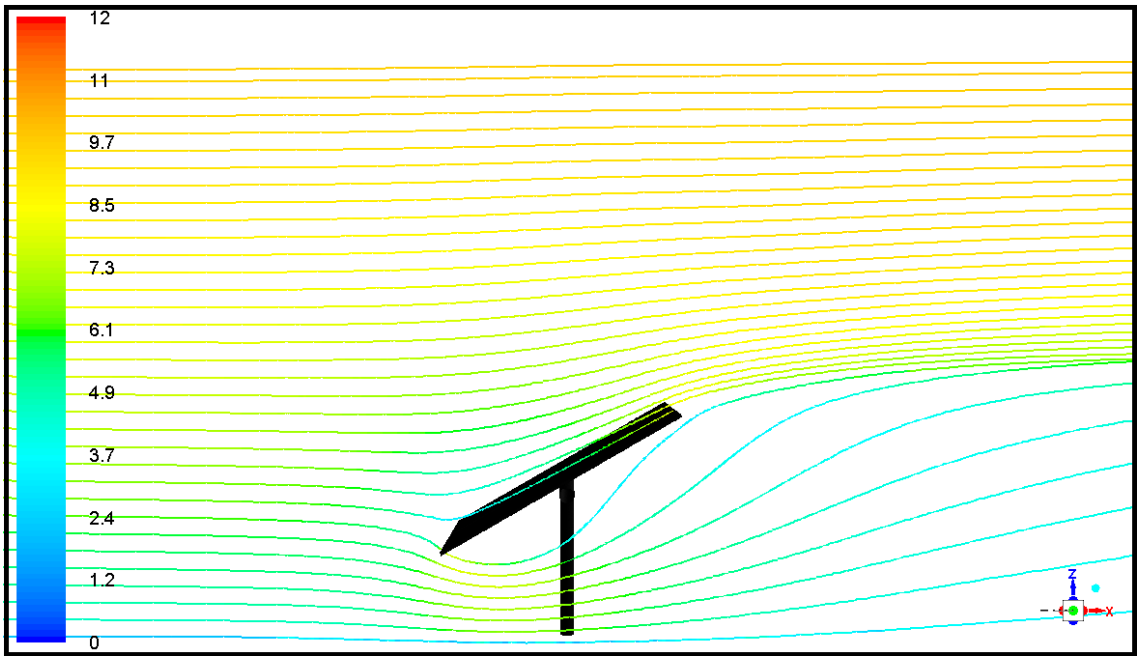

Figure 36: Streamlines coloured by velocity magnitude for 60 degrees (m/s).

In Figure 53 and Figure 54, the velocity contour plot and the velocity vector plot are displayed respectively. The flow separation from both the leading and trailing edge of the mirror face is clearly visible in the contour plot along with the velocity stagnation point at the leading edge. The separation region behind the heliostat can be seen. Looking at the velocity vector plot the recirculation zone in the separation region on the leeward side of the leading edge is evident.

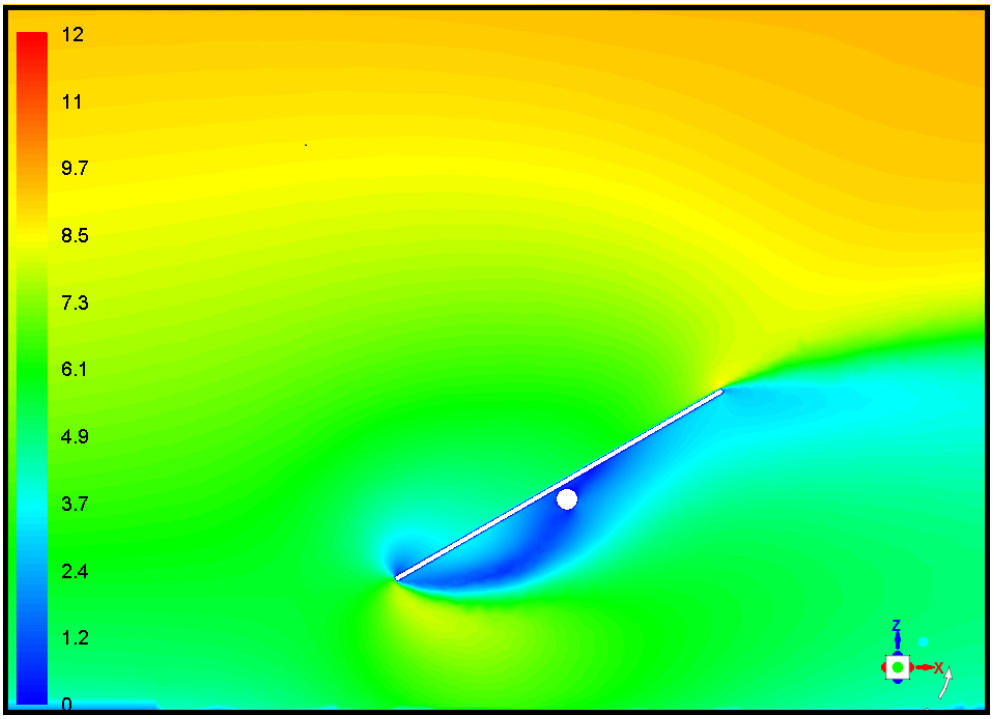

Figure 37: Velocity magnitude contour plot at 60 degrees (m/s).

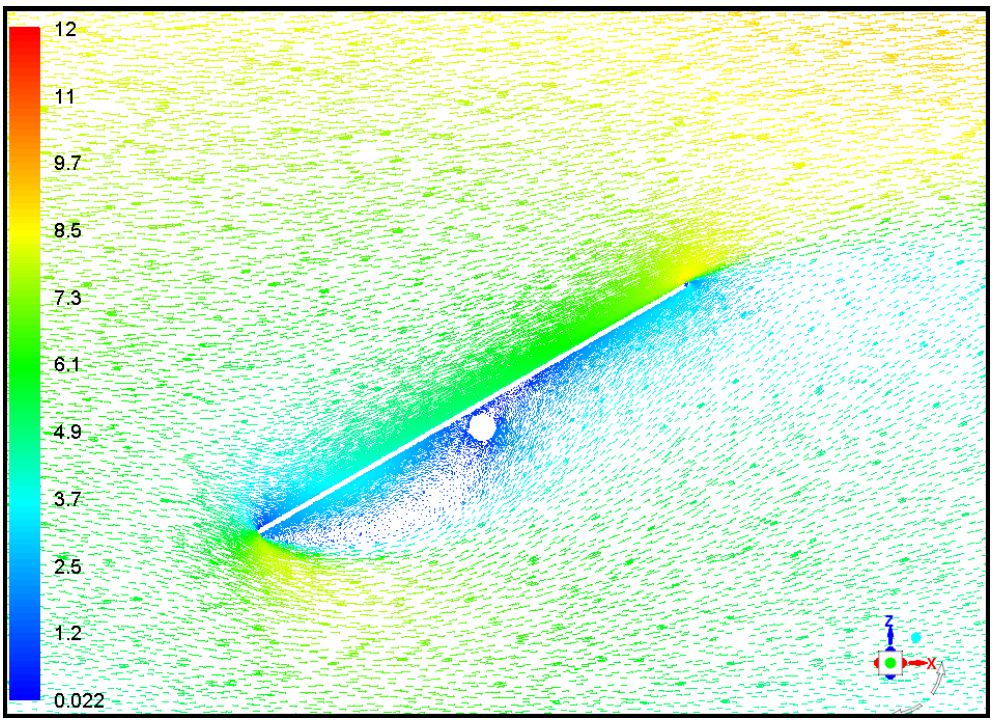

Figure 38: Velocity magnitude vector plot at 60 degrees (m/s).

The following three figures; Figure 55, Figure 56 and Figure 57, show the static pressure experienced by the heliostat in the flow field. Figure 55 shows the static pressure contour plot while Figures 56 and 57 show the pressure field directly on the heliostat surface. Looking at the contour plot of the static pressure it is clearly visible that there is a high pressure on the windward face of the heliostat with a stagnation zone on

the leading edge. The low-pressure zone on the leeward side of the heliostat is also evident, together these two opposing pressures create the downward lift force on the heliostat structure. The large torque tube moment experienced at this orientation is due to the highly uneven pressure distribution on both the windward and leeward sides of the mirrors. As can be seen (Figure 55) the low-pressure zone is concentrated just behind the leading edge with an almost unaffected pressure behind the trailing edge, these unequal pressures create a force imbalance and subsequent moment about the torque tube.

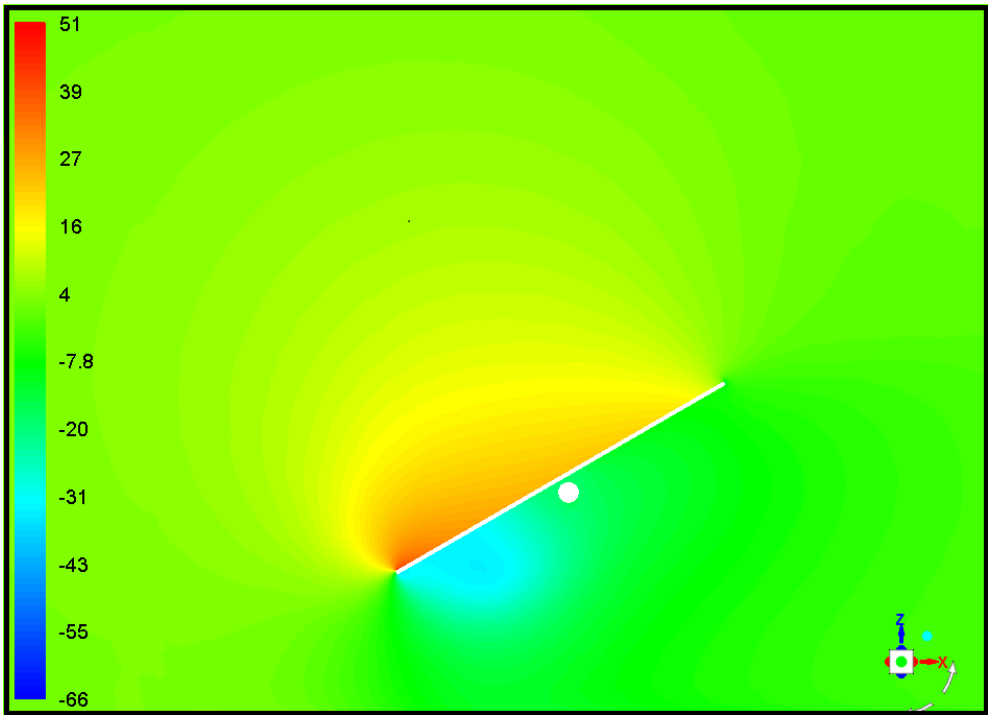

Figure 39: Static pressure contour plot at 60 degrees (Pa).

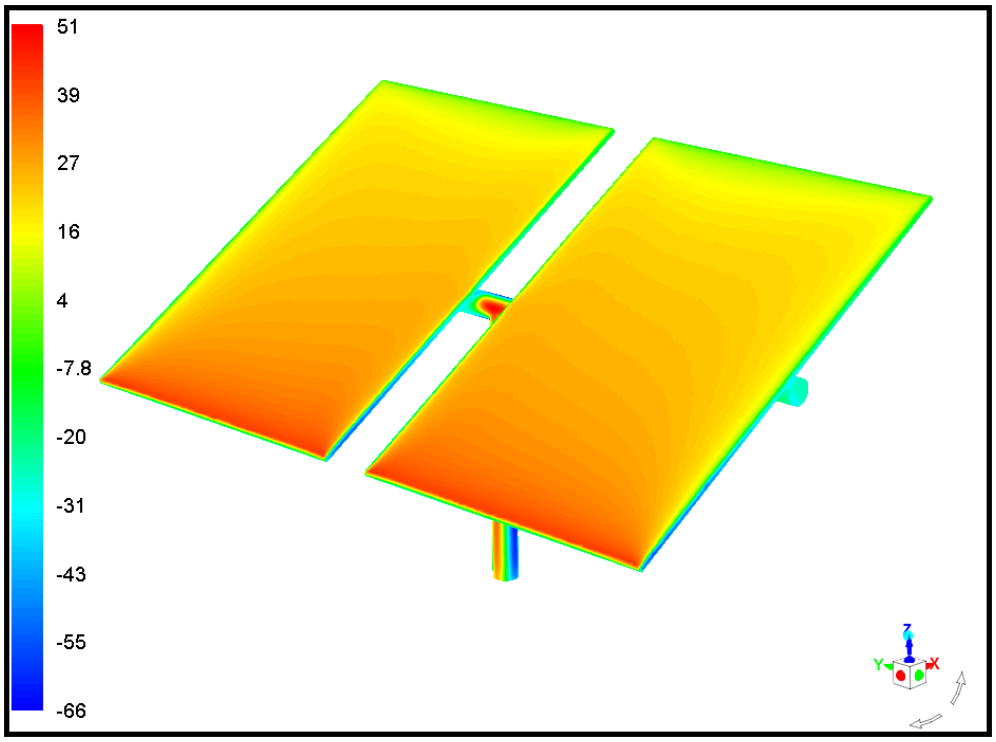

Figure 40: Static pressure contours on the windward heliostat surface at 60 degrees (Pa).

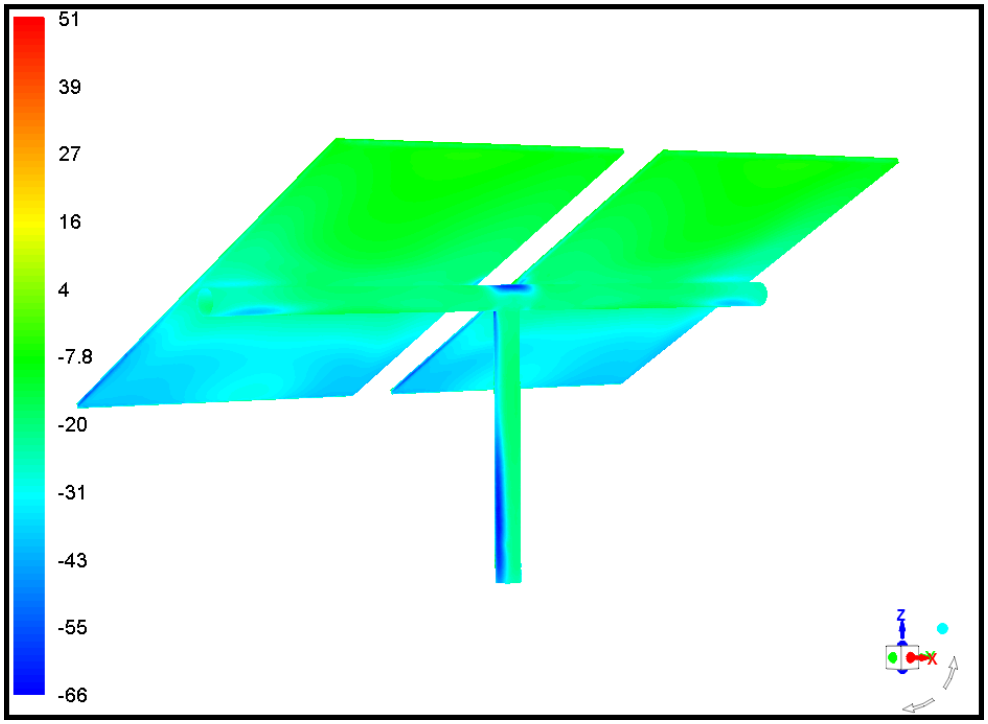

Figure 41: Static pressure contours on the leeward heliostat at 60 degrees (Pa).

In conclusion to the (Huss, et al., 2011) validation case, it can be said that with the use of RANS modelling the force and moment coefficients over various orientations can be accurately predicted. There are some discrepancies in the results which may be due to the difficulties in modelling the ABL and for this particular

case, the lack of knowledge of the experimental inlet boundary conditions. The results instil confidence in the use of RANS CFD modelling to model mean loading on heliostats.

3.5 FSI VALIDATION CASE

In this section, a Fluid Structure Interaction validation is performed in order to determine the validity of not only the CFD but also the Transient Structural simulation and the Coupling of the relevant codes. The validation performed replicates the work done by (Breuer, et al., 2010), where both a laminar and turbulent FSI case are solved. The simulation considers a thin elastic bar immersed in an incompressible fluid. The bar develops self-induced time-periodic oscillations of different amplitudes depending on the material properties used (Bungartz & Schafer, 2006). The configuration can be seen in Figure 58.

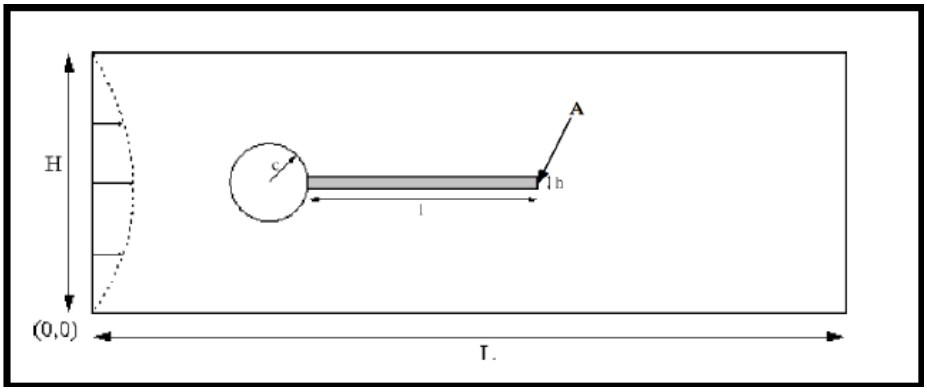

Figure 42: Configuration setup of the FSI validation case (Bungartz & Schafer, 2006).

The computational domain has a length L = 2.5m, height H = 0.41m and the origin at the bottom left corner at (0,0)m. The circle centre is positioned at C = (0.2,0.2)m with a radius of r = 0.05m. The elastic bar has a length of l = 0.35m and height h = 0.02m, with the left side of the bar clamped to the circle. There is a control point at A, the top right point of the bar A(0) = (0.6,0.2)m. The computational model can be seen in Figure 59.

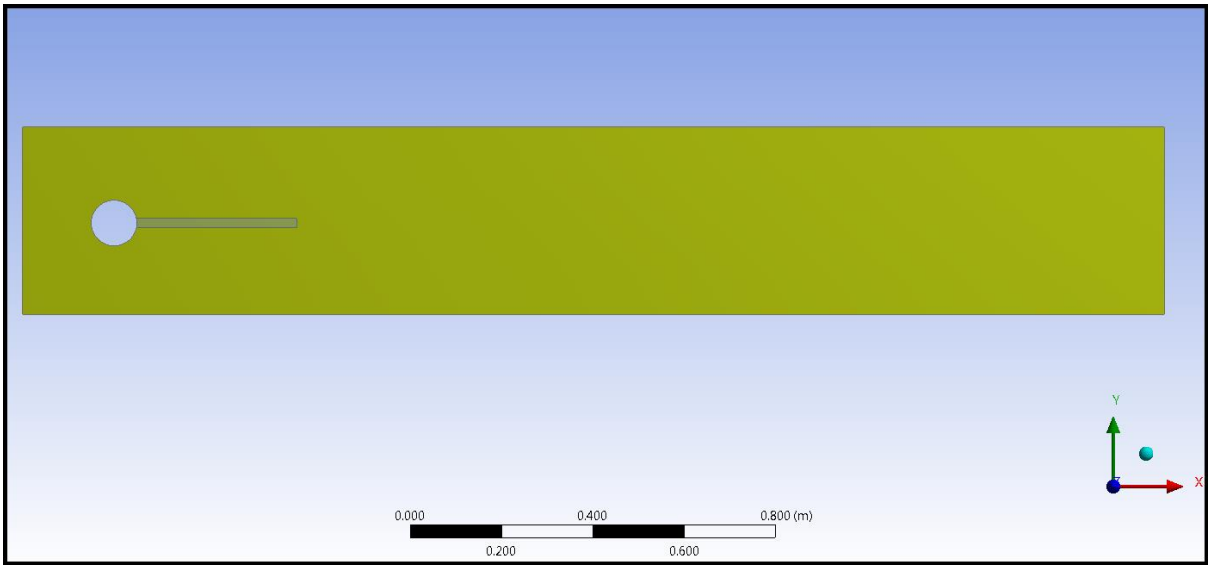

Figure 43: Computational model used in FSI validation.

No slip boundary conditions are prescribed for the top and bottom walls as well as the cylinder and flap surfaces. The outlet is a zero-gauge pressure outlet. At the inlet (on the left) a constant parabolic inflow profile is used with the shape of Equation 69.

$$v(0,y) = 1.5U\frac{4y(H-y)}{H^2} \qquad (69)$$

Velocities of U = 2m/s for the laminar case and U = 20m/s for the turbulent case are prescribed producing a Reynolds number of Re = 200 and Re = 2000 respectively. The fluid is considered to be an incompressible Newtonian fluid with the flap being a compressible St. Venant-Kirchoff type. The material properties used for the fluid and structure are listed in Table 4.

Fluid Properties	Value
Density ρ	1.225 kg/m^3
Kinematic Viscosity ν	1x10^{-3}m^2/s
Structural Properties	
Poisson's Ratio ν	0.4
Density ρ	1000 kg/m^3
Young's Modulus E	5.6x10^6 Pa

Table 4: Material properties used in the FSI validation cases.

The simulation is 2D but in order to perform FSI in ANSYS, the fluid and structural domains are required to have a thickness. To satisfy this condition a one-cell thick domain is used for both the fluid and transient structural domains. The mesh used by (Bungartz & Schafer, 2006), is a regionally refined hexahedral mesh with a maximum of 2784 cells. In ANSYS Fluent, in order to use remeshing due to the structural displacement, in this case the flap, the cells need to be tetrahedral. The mesh used for the fluid domain can

be seen in Figure 60 and consists of approximately 37 000 cells. The laminar flow model is used for the laminar case.

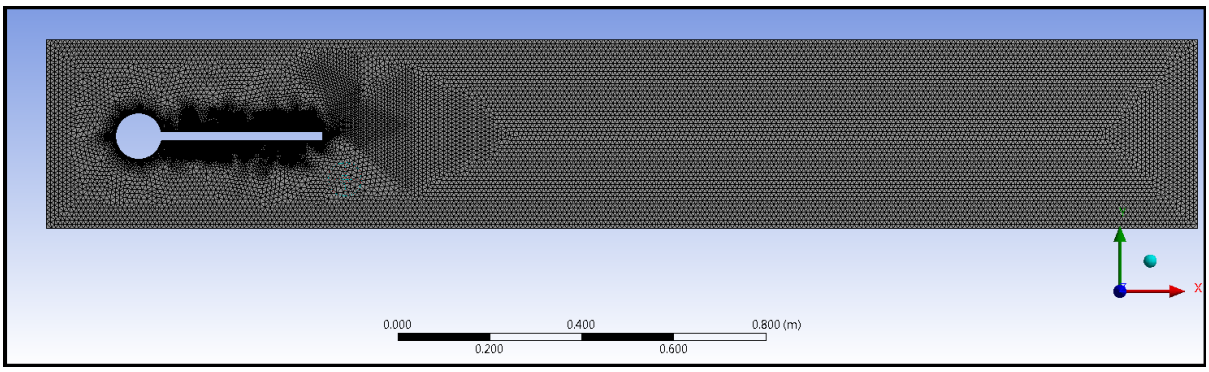

Figure 44: Computation mesh used for FSI fluid flow.

The flap is meshed in ANSYS mechanical using a sweep method and a maximum face size of 1mm with a 1 cell thickness of 5mm. The flap has a fixed support on the left side to the cylinder with a zero-initial displacement. The mesh consists of approximately 7 400 elements. The flap mesh can be seen in Figure 61.

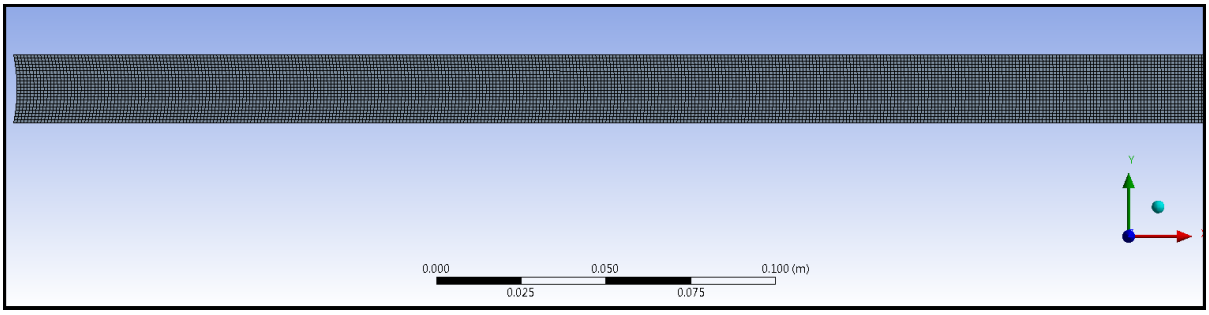

Figure 45: Flap mesh used in Mechanical component of FSI validation.

The transient analysis is set up in the System Coupling component of ANSYS Workbench. The FSI interface is prescribed as the edge of the flap in both Fluent and Mechanical. The simulation is run for a total of 6 seconds with a step size of 0.002 seconds and a maximum of 5 iterations per time step. The Workbench FSI layout can be seen in Figure 62, showcasing separate fluid flow and transient structural components along with the linking of the setup cells to the System Coupling component. The timestep is chosen in order to have the correct Courant number of the flow with the iterations chosen due to the convergence of the flow in the system coupling iteration.

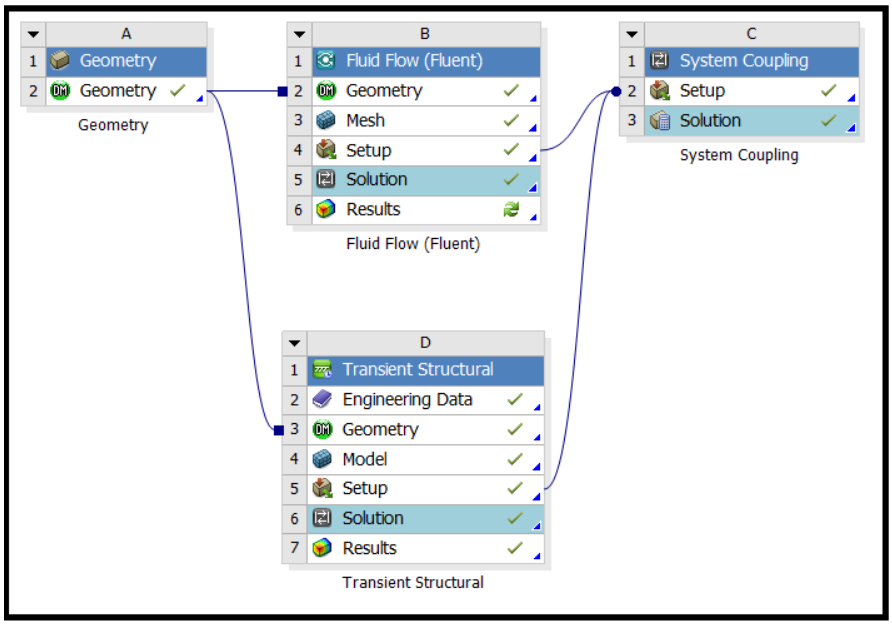

Figure 46: ANSYS Workbench FSI workflow layout for FSI validation case.

The fluid flow results are shown below for the laminar regime, with the velocity magnitude contour plot shown in Figure 63. Due to the laminar nature of the flow, the transient behaviour of the flow in the wake region is difficult to visualize but can be seen in the contour plot in the wake region. Plots of the x and y component velocities across the domain at distances of 2m and 2.4m are given in order to better demonstrate the transient characteristics of the flow. The plots are given in Figures 64 and 65.

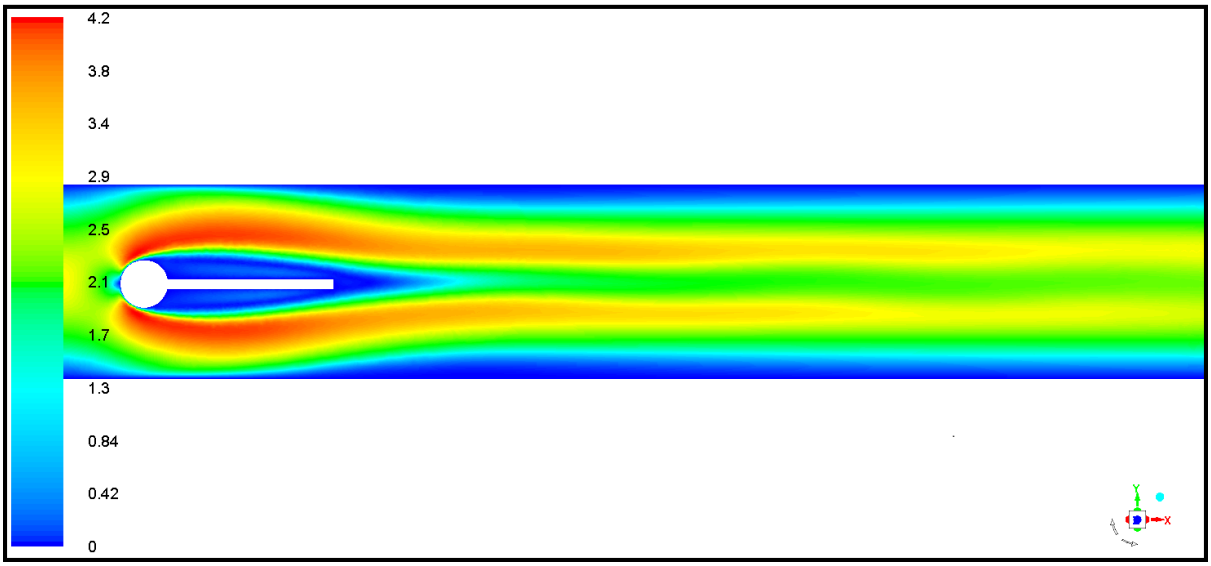

Figure 47: Velocity contour plot of the FSI validation case (m/s) at time = 6s.

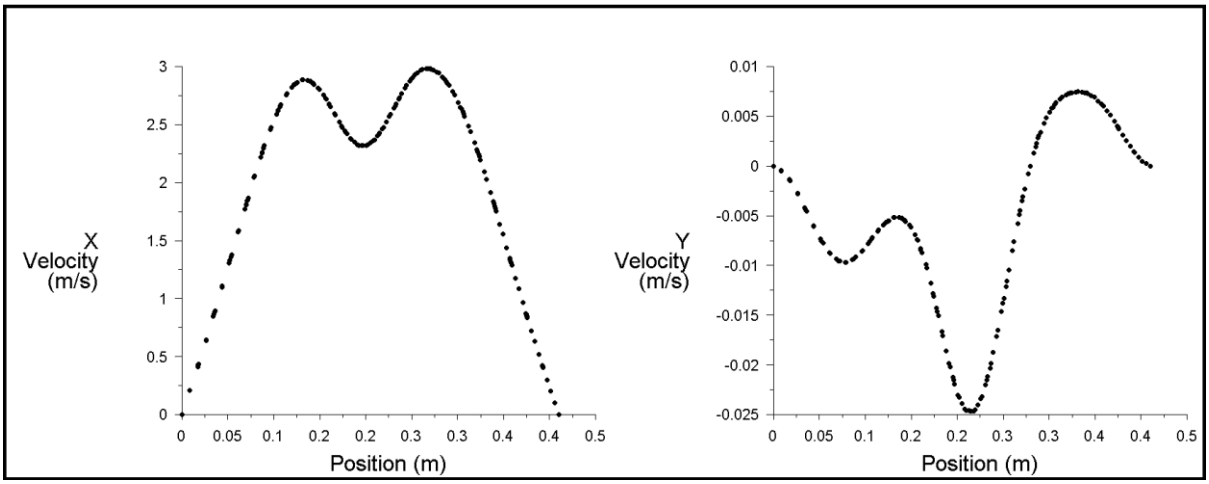

Figure 48: X and Y velocity components across the domain at 2m downstream from the inlet.

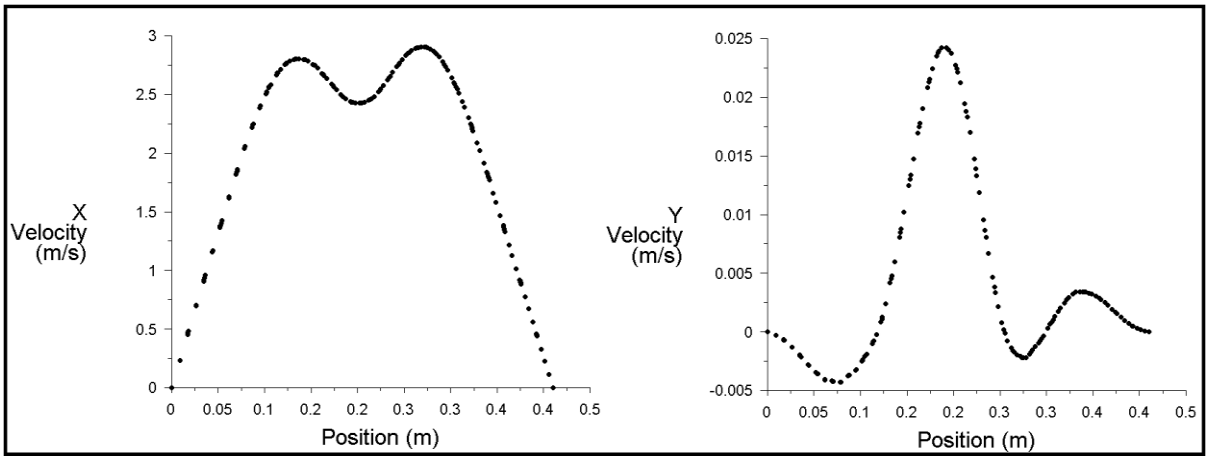

Figure 49: X and Y velocity components across the domain at 2.4m downstream from the inlet.

The Mechanical displacement results are given in Figure 66. The figure shows the displacement of point A, at the top right corner of the flap as described earlier (see Figure 58), for the 6 seconds of simulation time. The maximum displacement experienced by the flap in laminar flow is about 8.8×10^{-5}m.

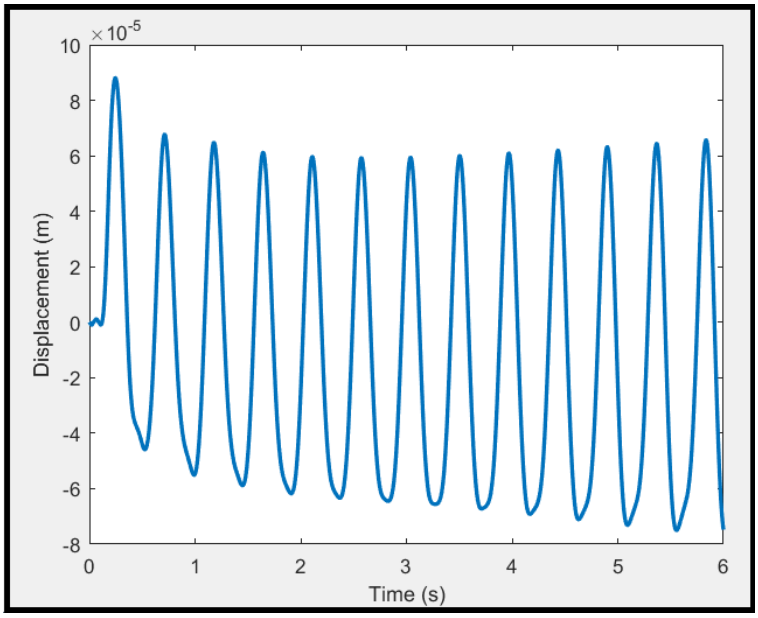

Figure 50: Time displacement results of the flap for point A.

In order to compare the results with those of (Bungartz & Schafer, 2006), a Fast Fourier Transform (FFT) of the displacement signal is calculated in MATLAB. The FFT converts the signal from the original time domain to the frequency domain where the major frequencies present in the signal can be visualised

The FFT of the resultant displacement signal for the flap in the laminar FSI test case is shown in Figure 67.

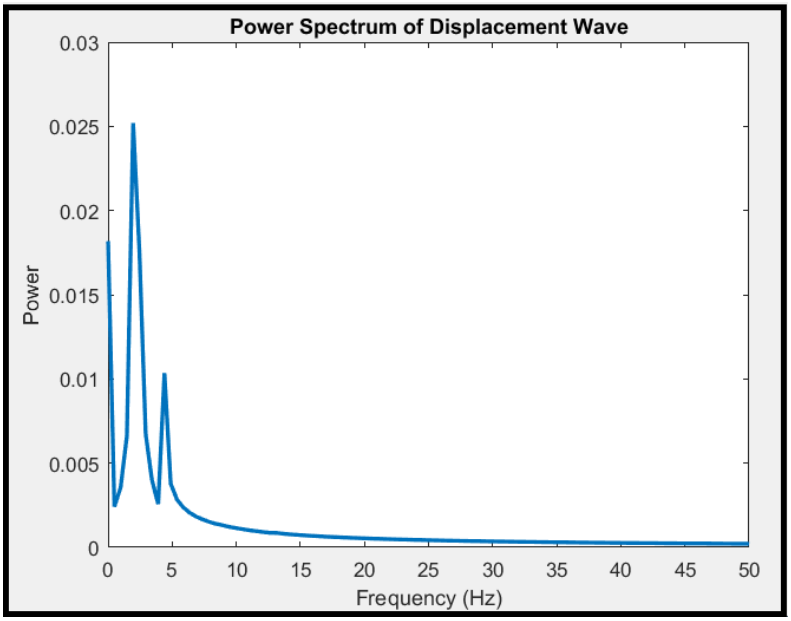

Figure 51: FFT of the displacement signal of the flap in laminar flow.

Two dominating spikes in the FFT can be seen, the first spike at a frequency of 1.95Hz corresponds to the frequency of the displacement of the control point A on the flap. (Bungartz & Schafer, 2006) gives the flap displacement frequency as 1.953Hz, this is almost an exact match to the simulation carried out in the current work. The second smaller spike on the right of the main peak has a frequency of 4.4Hz, this corresponds to the underlying lift force frequency, which is the driving force for the flap displacement. The lift force is solved in Fluent and transferred to Mechanical via the System coupling component. The lift force frequency given by (Bungartz & Schafer, 2006) is 4.99Hz which represents an 11% error. The results of the laminar FSI test case demonstrate the ability of ANSYS Workbench to successfully and accurately solve an FSI simulation.

(Breuer, et al., 2010) completed turbulent LES FSI simulations using this particular setup. The turbulent simulations are repeated in this work. The fluid domain mesh used is identical to the laminar mesh used. The structural mesh, boundary conditions and solver setup are also identical to the laminar case. The Fluent fluid flow model is changed to LES with Wall-Adapting Local Eddy-viscosity (WALE) used as the sub-grid scale model. The SIMPLE solver is used with BCD employed for the momentum discretisation. The second-order Implicit transient formulation is implemented. The only other variation in the setup between the laminar and turbulent cases lies with the System Coupling setup. The simulation is run for a total of 1.2 seconds with a time-step size of 0.0002 seconds with the maximum number of iterations set at 5.

The velocity magnitude contour plot is shown in Figure 68 at time = 1.2s. The displacement of the flap is clearly visible as well as the transient nature of the flow in the wake behind the cylinder and flap. Looking at the cylinder, the vortex shedding phenomenon can be observed by the higher velocity fluid zone experienced on the bottom surface of the cylinder compared to the top surface. Evidently, the influence of the vortex shedding on the motion of the flap is unmissable by looking at Figure 68.

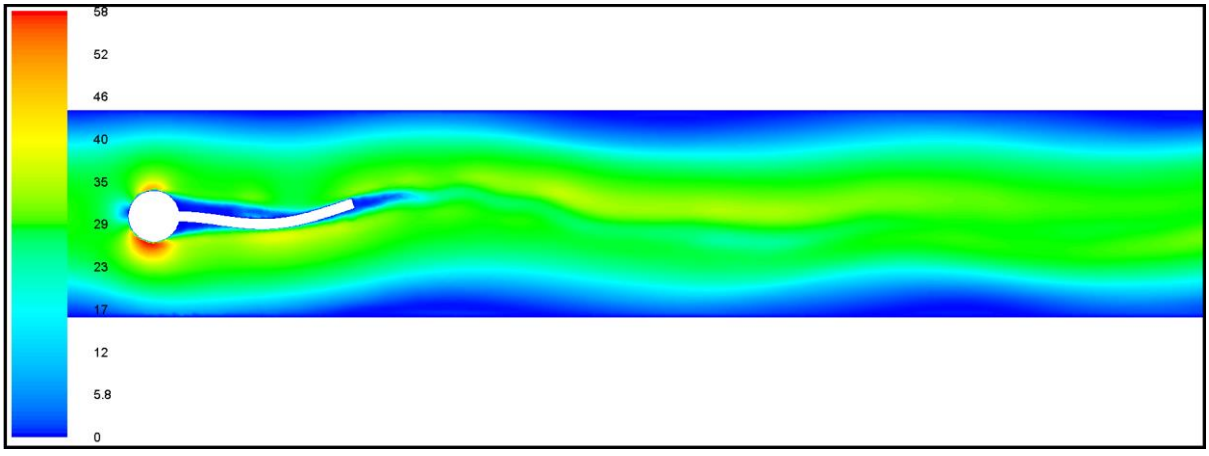

Figure 52: Velocity magnitude contour plot of the turbulent LES FSI validation (m/s) (time = 6s).

The static pressure contour plot corresponding to the velocity magnitude plot above is shown below in Figure 69. Once again the transient behaviour of the wake due to vortex shedding on the cylinder and subsequent influence of the flow on the flap are clearly visible.

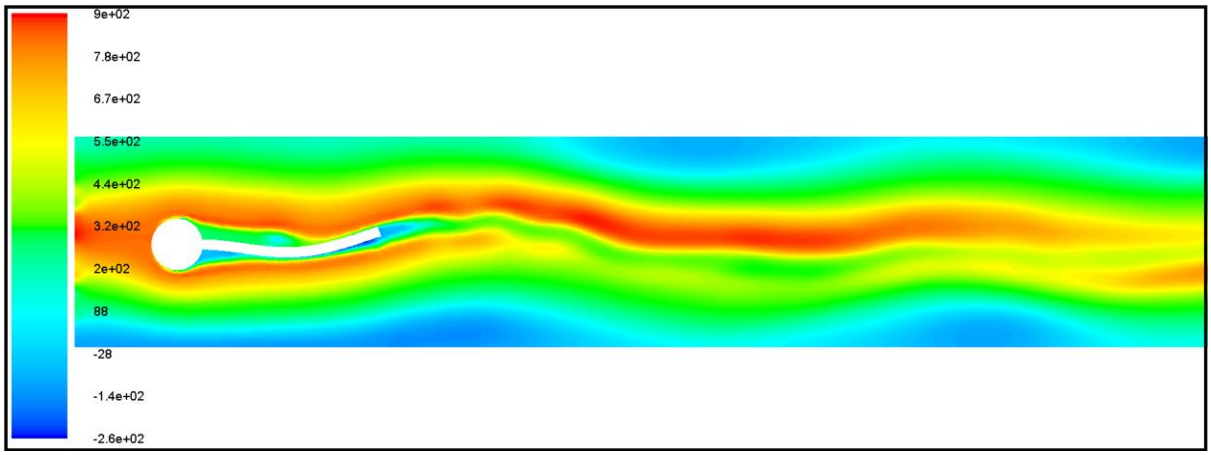

Figure 53: Static pressure contour plot of the turbulent LES FSI validation (Pa).

The displacement of the flap is shown in Figure 70 with a displacement contour mapping; the flap is at the maximum displacement position for this particular time where the tip experiences a displacement of 2.68cm. The maximum displacement experienced by the tip for the simulation period was 3cm.

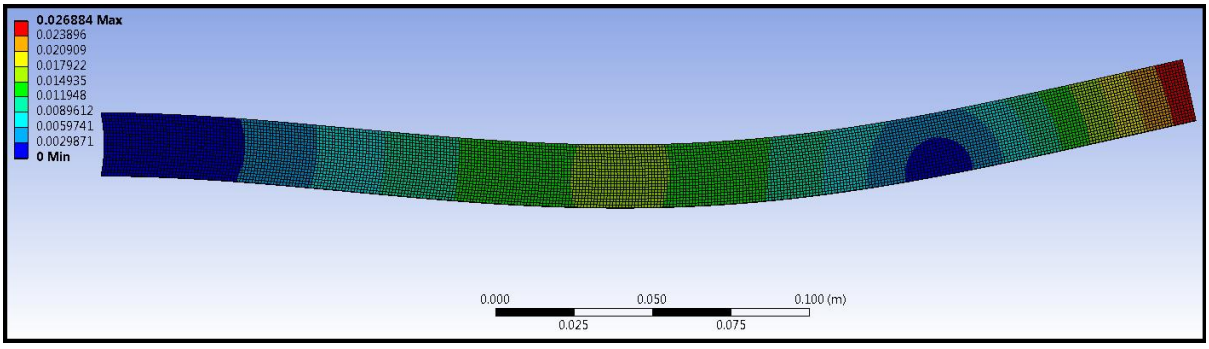

Figure 54: Displacement contour map of the flap for the LES FSI validation (m).

The time dependent displacement signal of point A on the flap is shown in Figure 71. The signal can be seen developing a greater amplitude, but the wavelength and frequency appear to be fairly well developed with no need to run the simulation any longer.

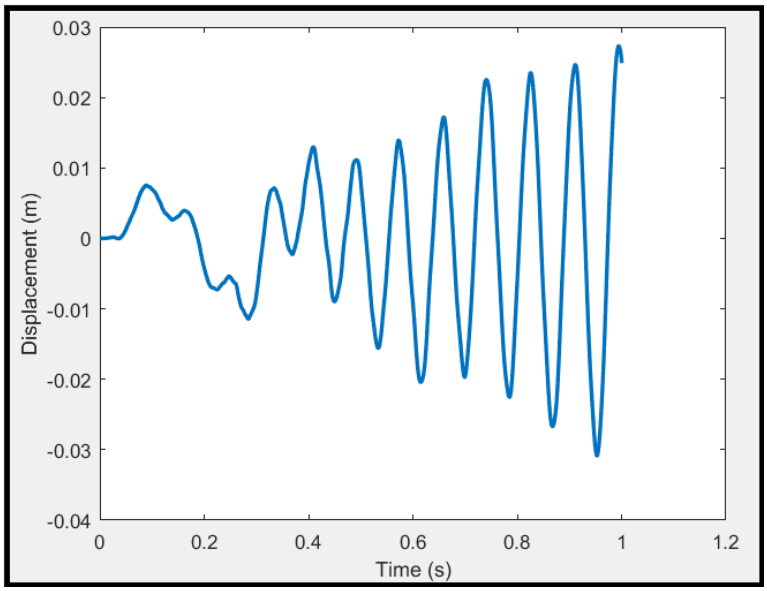

Figure 55: Time dependent displacement signal of the flap.

The FFT of the displacement signal can be seen below in Figure 71 with the spike representing the dominant frequency of 12.2Hz. The dominating frequency is attributed to the oscillation of the flap, similarly to the laminar case. The small peak on the right which represents the underlying lift frequency has a value of 35.4Hz.

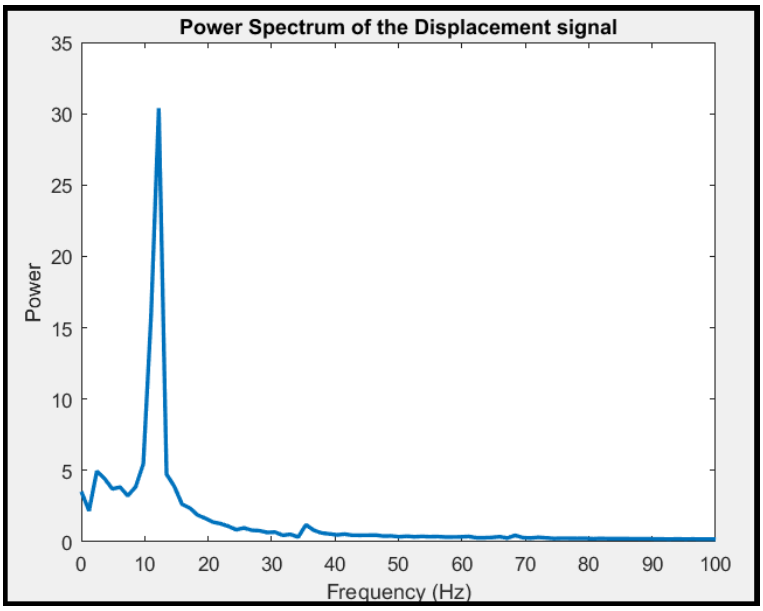

Figure 56: FFT of the flap displacement signal.

(Breuer, et al., 2010) does not give the results of the turbulent LES FSI case in his paper but instead gives the value of the Strouhal number for the case when the flap was prescribed to be a rigid structure. (Breuer, et al., 2010) then describes how the rigid flap acts like a splitter plate, attenuating the generation of vortex shedding behind the cylinder. (Breuer, et al., 2010) found the rigid flap turbulent Strouhal number to be St=0.172. Using Equation 7 for the Strouhal number, the Strouhal number for the underlying lift force is

found to be St=0.177 in the current study. This result gives validity to the FSI validation as it shows the ability of ANSYS to perform FSI where the lift force from the fluid can be retrieved from the structural response.

Together, the laminar and turbulent FSI validation cases demonstrate the ability of the ANSYS software to accurately solve FSI problems. There exist some discrepancies between the results of (Breuer, et al., 2010) and the results given in this research which can be attributed to the difference in computational meshes and the difference in fluid densities used in the simulations. Overall this means that future FSI simulations carried out can be treated with a high level of confidence depending on the accuracy of the setup of such simulations.

3.6 CONCLUSION

In order for any numerical method or model to be used with a level of confidence it needs to be validated against experimental results or existing trusted numerical simulations. In this validation chapter, the ABL is shown to be accurately modelled by RANS equations with the ABL used to model the flow over the Peterka (1986) heliostat yielding valuable results. The ABL is modelled again over the LH-2 heliostat used in the Ivanpah plant. Once again the results show that the use of RANS provides very accurate results for the loading coefficients over various orientations of the heliostat. Finally, the FSI capabilities of ANSYS are validated using the work of (Breuer, et al., 2010) and (Bungartz & Schafer, 2006), where both laminar and turbulent flow cases are used. This validation case gives validity not only to Fluent but also to Mechanical and the System Coupling of ANSYS.

The work in this chapter provides credibility to the use of the numerical simulations that are carried out and performed in the following chapters.

4 FLUID-STRUCTURE INTERACTION MODEL DEVELOPMENT

4.1 INTRODUCTION

In this chapter computational models are developed and investigated in order to better understand the need and fit of FSI in the modelling of heliostats. The first section of this chapter introduces the modal analysis of the heliostat structure in order to appreciate the fundamental frequencies at which the flow should not excite the structure. A one-way FSI of the LH-2 heliostat using RANS modelling is concluded. This provides an indication of the mean forces due to the fluid on the heliostat along with the corresponding mean stress experienced by the structure. A 2D URANS validation of the vortex shedding of the (Matty, 1979) heliostat is performed in order to assess whether URANS can be used successfully in determining vortex shedding. Finally, a two-way 2D FSI of the LH-2 is conducted, this is used again in order to better evaluate the vortex shedding of the heliostat and to provide a rough estimate of the Strouhal number of the shedding.

4.2 MODAL ANALYSIS

A modal analysis of the LH-2 heliostat is conducted in this section. A modal analysis uses the mass and stiffness matrices of the structure to find the natural modes and frequencies at which the structure will resonate. This provides the designer of the heliostat with vital information, if the structure is excited for a prolonged time at one of the modal frequencies, structural damage and failure will ensue. It is important then that the vortex shedding from the heliostat does not excite one of the modes. It is consequently a complex issue as the interaction of the fluid and the structure needs to be carefully investigated. The vortex shedding from the heliostat is bound to change when the structure is no longer stiff (standard CFD simulation vs. two-way FSI) and can interact with the flow as is the case in a two-way FSI.

The heliostat used in the modal analysis is the full-scale LH-2 as this is the heliostat model used in the following sections. The full-scale computational model of the LH-2 is seen in Figures 73, 74 and 75 with all the relevant dimensions. The key differences between the 1:7 scale model used in the RANS validation and the full-scale model are the addition of the backing truss support structures. The model is still a simplification of the actual heliostat in that the material is specified to be structural steel with the material properties seen in Table 5. No connections are used and the entire structure is designed to be one part, it is assumed that the effect of the connections to the response of the entire structure is negligible.

Young's Modulus	$2x10^{11}$ Pa
Poisson's Ratio	0.3
Density	7 850 kg/m^3

Table 5: Structural steel material properties of LH-2 heliostat.

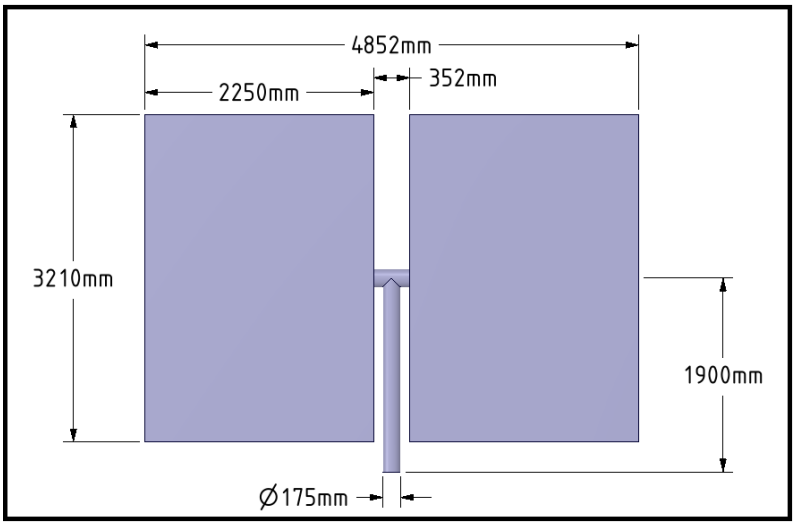

Figure 57: Front view of the full-scale LH-2.

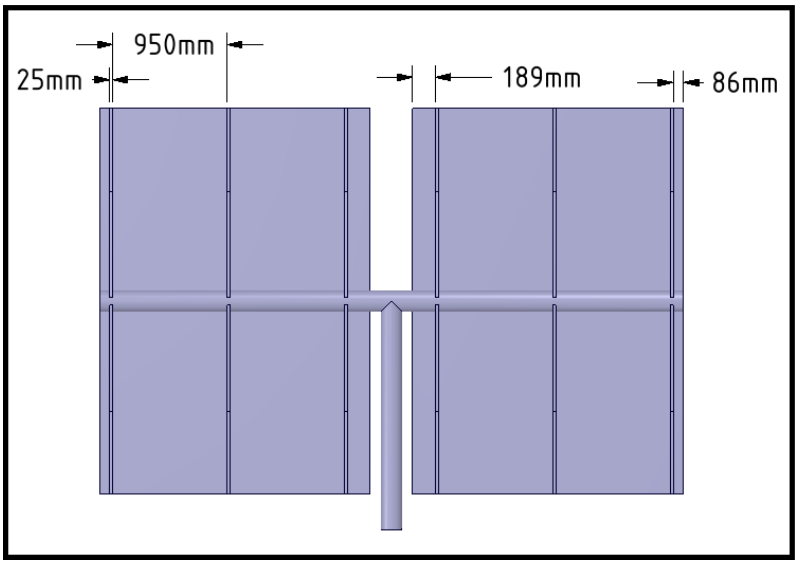

Figure 58: Rear view of the LH-2.

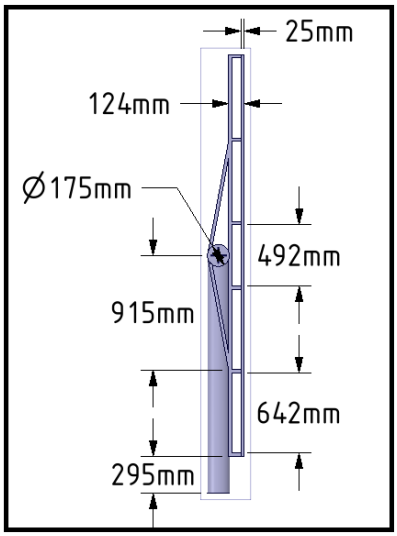

Figure 59: Side view of the LH-2.

The geometry is meshed using 3D tetrahedral elements and can be seen below in Figure 76. The structural mesh contains approximately 50 000 elements.

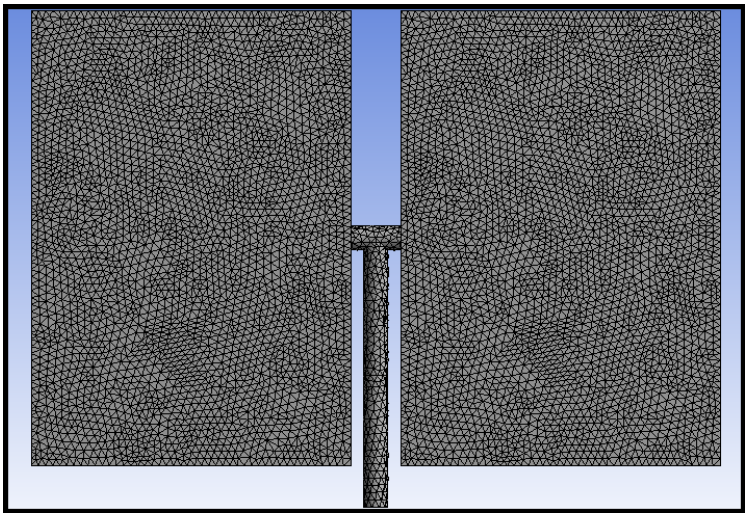

Figure 60: Structural mesh used in Modal analysis of LH-2.

The only boundary condition prescribed for the analysis is a fixed support at the bottom of the pylon. The first 10 modes of the structure are solved for and the results of the modal analysis can be seen in Table 6.

Mode	Frequency (Hz)
1	1.7807
2	2.1378
3	2.6334
4	5.4719
5	5.9819
6	6.2626
7	7.4145
8	12.591
9	17.141
10	17.743

Table 6: First ten modal frequencies of the LH-2.

The results shown in table 6 for the first ten natural frequencies of the LH-2 heliostat reveal that the structure's modes occur at relatively low frequencies. This is in agreement with the results of (Griffith, et al., 2015) for a similar sized heliostat. This is concerning when designing a heliostat as the vortex shedding frequency from the LH-2, according to the Strouhal number results of (Matty, 1979), should be in a similar range as the natural frequencies of the LH-2. As expressed earlier, excitation of the LH-2 structure at a natural frequency will lead to resonance and possible failure of the heliostat. The first six mode shapes are shown in Figure 77. (Griffith, et al., 2015) performed experimental and computational modal analyses on a large heliostat operating at a Sandia National Laboratory test site. The results of these experiments provided modal frequencies of a very similar range to those found above for the LH-2. Their first modal frequency was 1.63Hz.

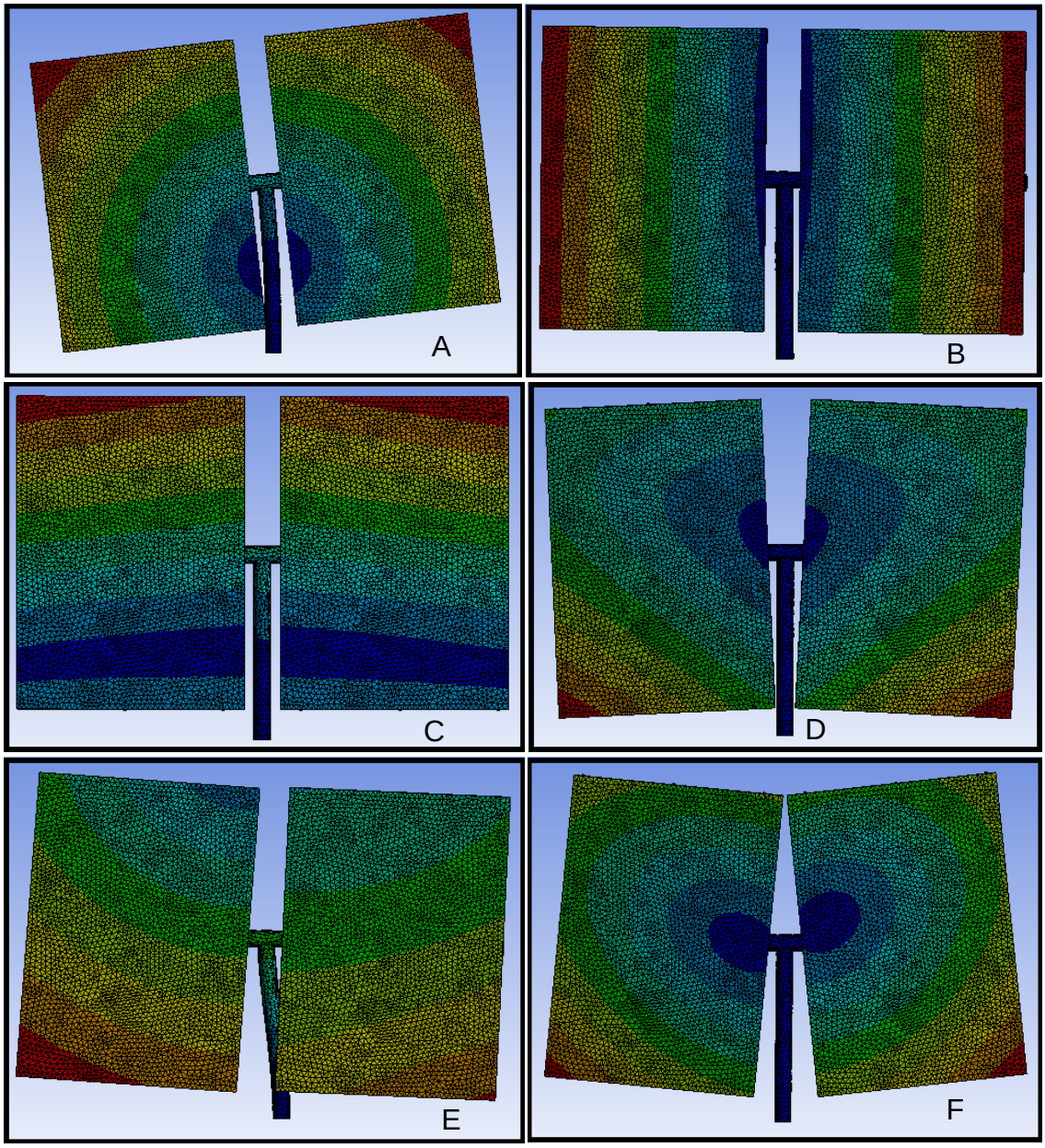

Figure 61: The first six mode shapes of the LH-2 heliostat, A=1st, B=2nd, C=3rd, D=4th, E=5th, F=6th.

The results of the modal analysis give a good initial indication that further investigation needs to be conducted into the possible vortex-induced vibration of the heliostat. This is not a trivial endeavour by any means. The introduction of the structural model into a two-way FSI environment means there is additional damping introduced by the fluid on the structure, altering the response of the heliostat. Movement of the heliostat in the fluid will most likely change the dynamics of the vortex shedding compared to having a rigid structure. SRS simulations need to be concluded in order to comprehend the peak loadings and transient behaviour of the flow. The completion of a full two-way FSI simulation is expensive and additional cheaper simulations can be completed in order to provide a better understanding of the nature of the heliostat behaviour.

4.3 1-WAY FLUID-STRUCTURE INTERACTION

In this section the development of a 1-way FSI simulation is presented. In a 1-way FSI the fluid flow is solved independently of the structural response of the system. The resolved pressure field of the fluid is then read into the Mechanical solver and the structural response is solved for. The response of the structure has no influence on the fluid simulation whatsoever. This type of simulation is useful for finding the loadings, deformation and stress on the heliostat due to the mean flow features. The designer should be able to ascertain the mean stress on the heliostat and design a safety factor around this.

There are currently two ways of implementing a 1-way FSI simulation in the Workbench environment. The first method, a static data transfer, requires the fluid field to be solved. This solved fluid provides the pressure field which is read into a static Structural solver whereby the structure is solved using this single averaged pressure field. This method as implemented neglects the effect of viscous shear stresses, although these could be implemented. For a bluff body like the heliostat, they are assumed to be negligible in comparison to the pressure or normal stresses. The second method of performing a 1-way FSI in Workbench is to implement System Coupling. Here both the fluid system and the structural system are linked to the Coupling and the 1-way FSI is implemented through the choice of one coupling iteration between the two systems. In this section a transient 1-way FSI is performed using URANS and Transient Structural. The time-dependent flow is solved using a specified time-step and the ANSYS Fluent results are translated to ANSYS Mechanical where the structural solution is solved for every time step. This results in a transient structural response to the transient fluid system.

Both a medium velocity ABL flow of 10.5m/s and a high velocity ABL flow of 45m/s are used to perform the FSI in this section. The medium velocity represents the day-to-day operating conditions experienced by the heliostat while the high velocity represents the worst-case scenario loading that could possibly be seen during the heliostat's lifetime.

The heliostat is in the upright configuration of 0^{o} as seen in the Modal analysis section. As stated earlier this is the worst-case configuration for drag and subsequent stress. The same computational LH-2 model is used as seen above in the Modal section. The Fluent setup is identical to the setup of the scaled LH-2 presented in the validation section apart from the domain and heliostat being seven times larger. An isometric view of the domain can be seen in Figure 78 showing the block structuring which allows for mesh sizing and refinement in areas of particular interest. The mesh used in Fluent is the same hybrid tetrahedral-hexahedral used in the validation case. The mesh and domain extent can be seen in Figures 78, 79 and 80 respectively. The final fluid mesh consists of approximately 3.5 million cells.

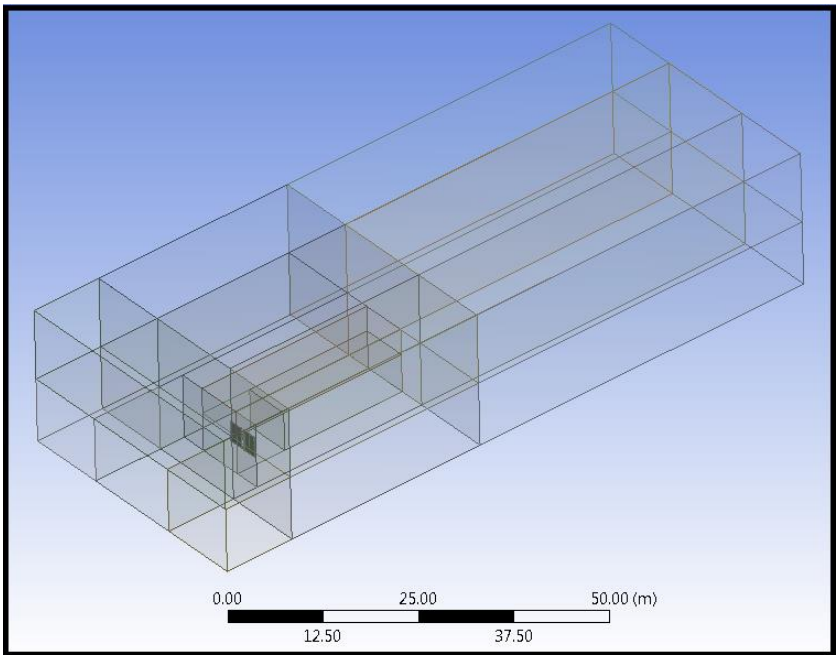

Figure 62: Computational fluid domain of LH-2.

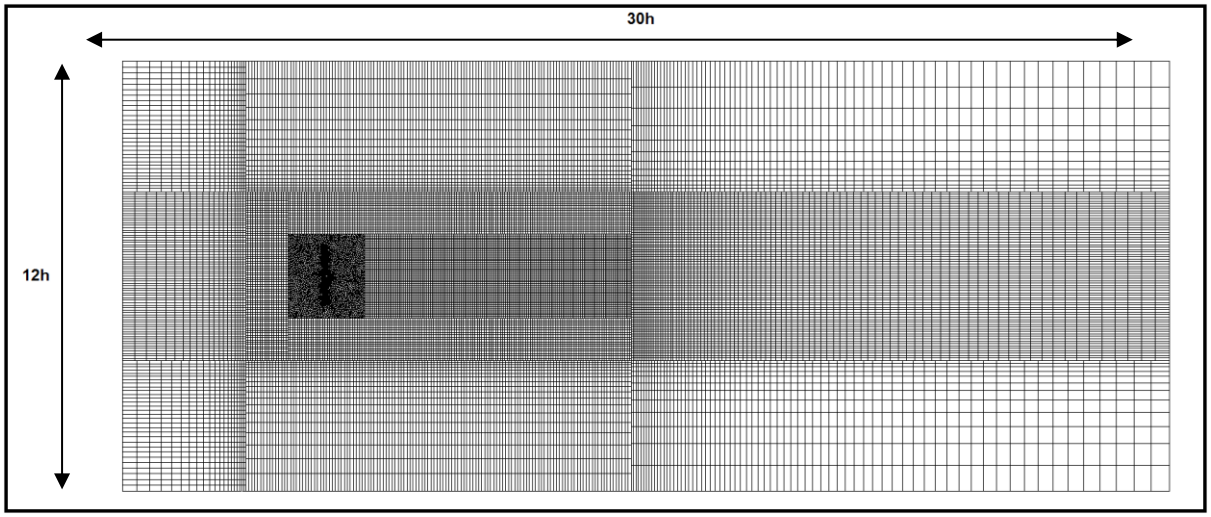

Figure 63: Bottom view of the full-scale LH-2 computational domain.

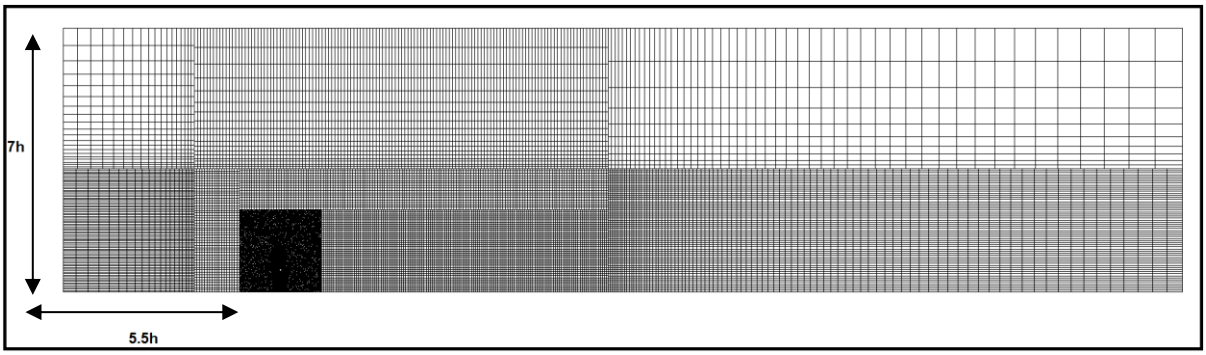

Figure 64: Side view of the full-scale L-2 domain.

The transient RKE RANS equation is used for the FSI simulation with standard wall functions. The double-precision SIMPLE solver is used with second-order spatial discretisation schemes. The inlet profiles used are the same as those used for the LH-2 validation scheme with the exception of scaling and velocity. These profiles are coded and used via a UDF in Fluent. The turbulence intensity was found via altering the aerodynamic roughness length using the same MATLAB optimisation as before. The aerodynamic roughness length was found to be $z_o = 0.25$. The reference values used in Fluent can be seen in Table 7:

A_{REF}	14.448 m^2
L_{REF}	1.9 m
u_{REF}(slow)	10.5 m/s
u_{REF}(fast)	45 m/s
ρ	1.225 kg/m^3
μ	1.7894x10^{-5} kg/ms

Table 7: Reference values and material properties used in Fluent.

The structural mesh used is identical to the Modal analysis mesh except that fewer elements were used in an attempt to speed up the simulation time. The final structural mesh contains approximately 31 000 elements and can be seen in Figure 81.

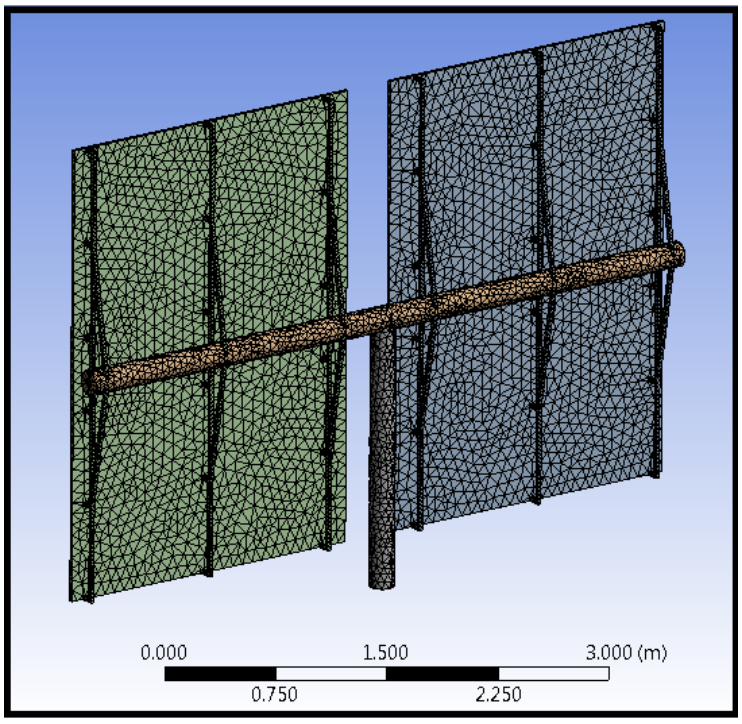

Figure 65: Structural mesh of LH-2 used in ANSYS Mechanical solver.

Structural steel is specified as the material used for the entire heliostat with the material properties seen in Table 5. The system coupling boundary condition is prescribed in both Fluent and Mechanical on the rear and front mirror faces as well as the torque tube and pylon. These faces are the FSI interface where the

pressure data will be exchanged during the simulation. The System Coupling analysis settings used are as follows. A time step of 0.001s (in order to ensure the correct Courant number of <1) with a maximum number of iterations set to one, this ensures only one-way FSI coupling with the fluid data sent to Mechanical while no data are transferred back to Fluent. The Workbench setup of the system is identical to the two-way FSI validation setup in chapter 3 as seen in Figure 82. The simulation was run for 1 second or 1000 time steps.

The velocity magnitude contour plots of both the 10.5m/s and 45m/s cases can be seen in Figure 82 and 83.

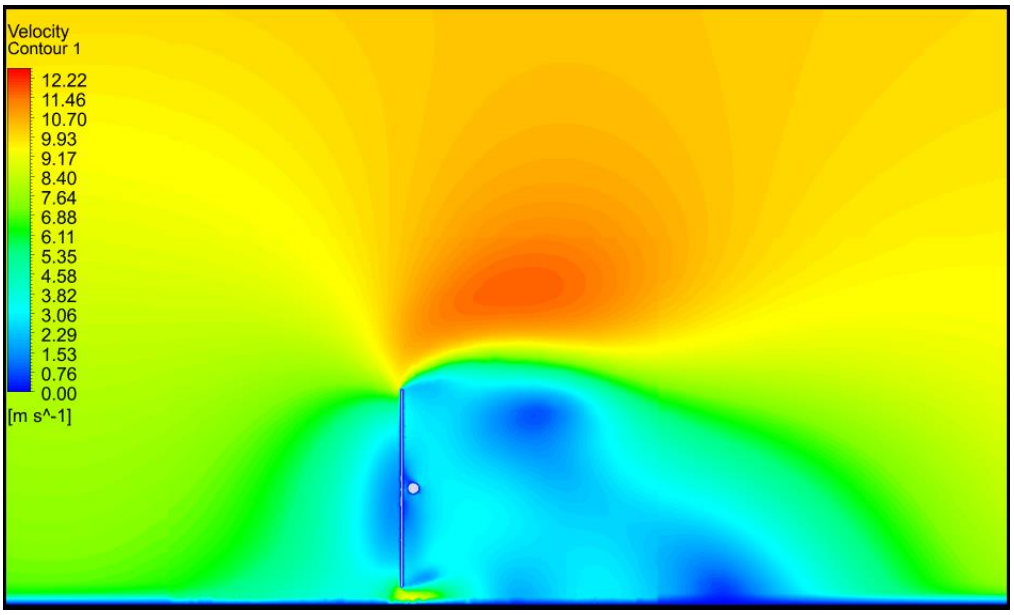

Figure 66: Velocity magnitude contour plot (U=10.5m/s).

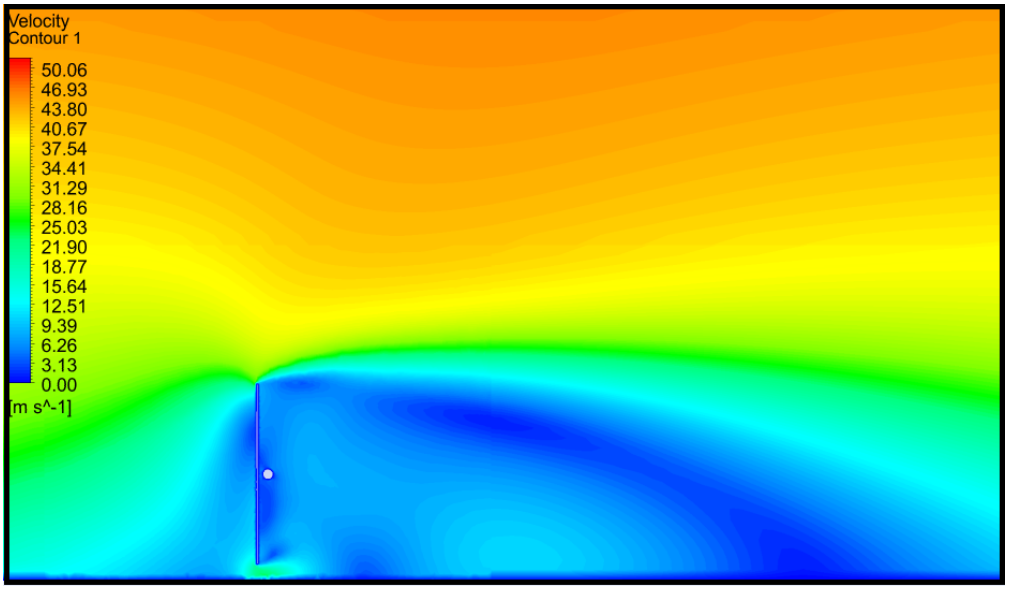

Figure 67: Velocity magnitude contour plot (U=45m/s)

Looking at the contour plots above, it can be seen that the wake and recirculation zone behind the heliostat grows considerably as the velocity increases. The stagnation area on the front face of the heliostat for the 10.5m/s case can be seen to be relatively symmetrical with regard to the torque tube. Looking at the 45m/s case, the stagnation zone is no longer symmetrical with a low-pressure concentration on the upper half of the mirror face. This asymmetry will cause a considerable moment to be experienced by the torque tube.

In Figures 84 and 85, the static pressure contour plots can be seen for both the 10.5m/s and 45m/s cases, respectively. The symmetry of the stagnation zone for the 10.5m/s case is confirmed by the pressure contours with the asymmetry in the 45m/s case also confirmed. This may be due to the much larger stagnation region on the windward face of the heliostat in the 45m/s case, effectively creating a cushioning bubble that limits the overall flow from interacting with the bottom half of the mirror surface. It is interesting to note that the pressure experienced in the stagnation zone for the 45m/s case is 11.76 times greater than that in the 10.5m/s case and not about 18 times as expected using the velocity squared relationship of pressure to velocity.

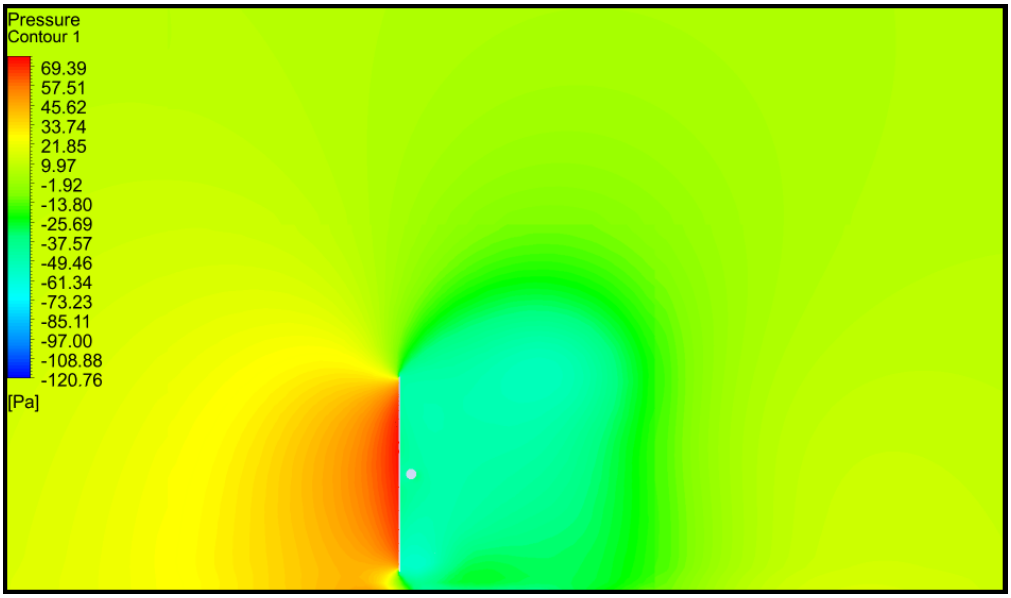

Figure 68: Pressure contour plot (U = 10.5m/s).

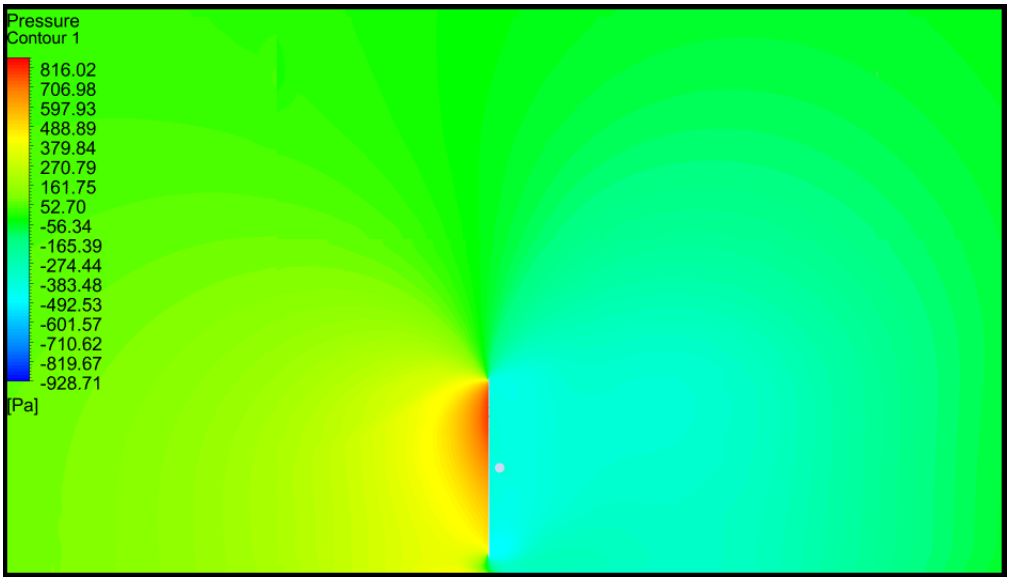

Figure 69: Pressure contour plot (U = 45m/s).

This higher stagnation zone in the 45m/s case will create a greater bending moment about the pylon and ground when compared to the symmetric zone seen in the 10.5m/s case.

The Mechanical results of the FSI simulation can be seen below. In Figure 86, the graphs of the total deformation of the heliostat can be seen for both cases. The graphs have the exact same shape due to the deflection from the fluid flow. As can be seen from the graphs, the maximum deformation due to the 10.5m/s case is 1.4325×10^{-2} m while the maximum deformation due to the 45m/s case is 0.168 m. This is an increase of 11.72 times, which corresponds to the 11.76 times greater pressure difference between the two cases. This is a considerable increase in loading as the velocity difference is only 4.3 times; this relationship is defined in the Bernoulli equation.

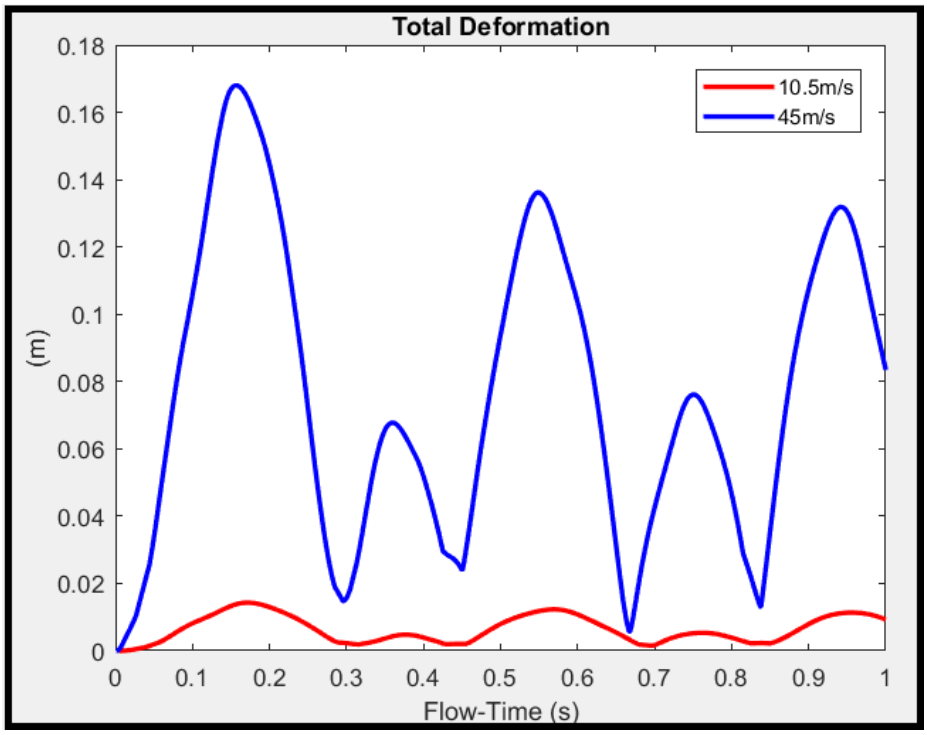

Figure 70: Graphs of the total deformation of the heliostat.

The deformation of the heliostat for both cases can be below in Figures 87, 88 and 89, using a deformation contour at the maximum deformation time of 0.16s.

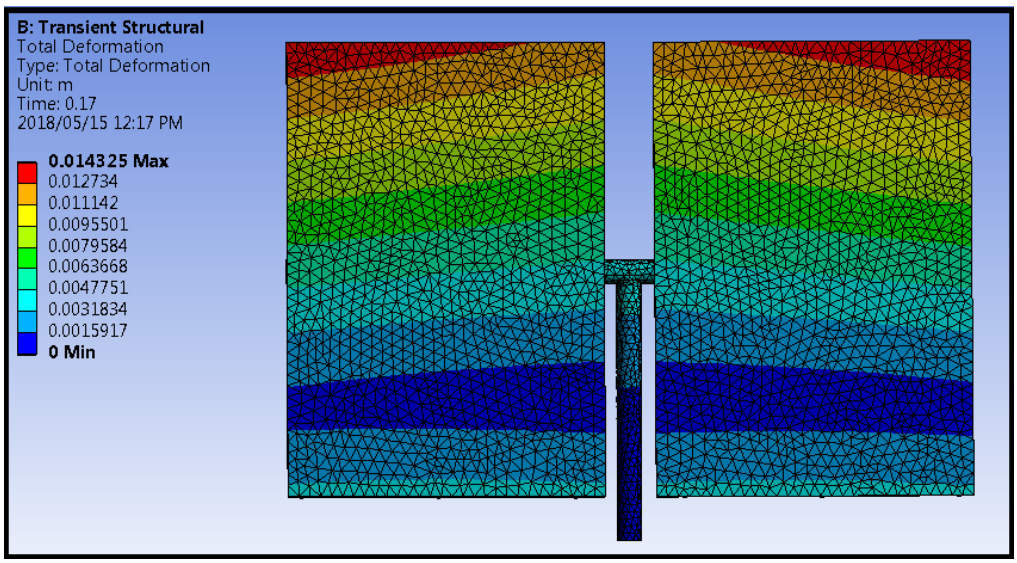

Figure 71: Deformation of the LH-2 heliostat (U=10.5m/s).

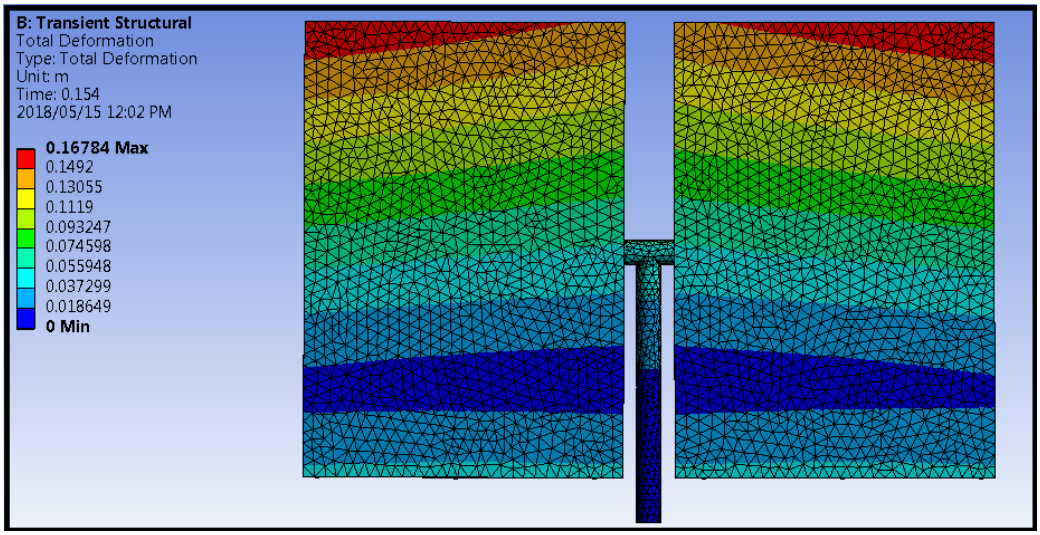

Figure 72: Deformation of the LH-2 heliostat (U=45m/s).

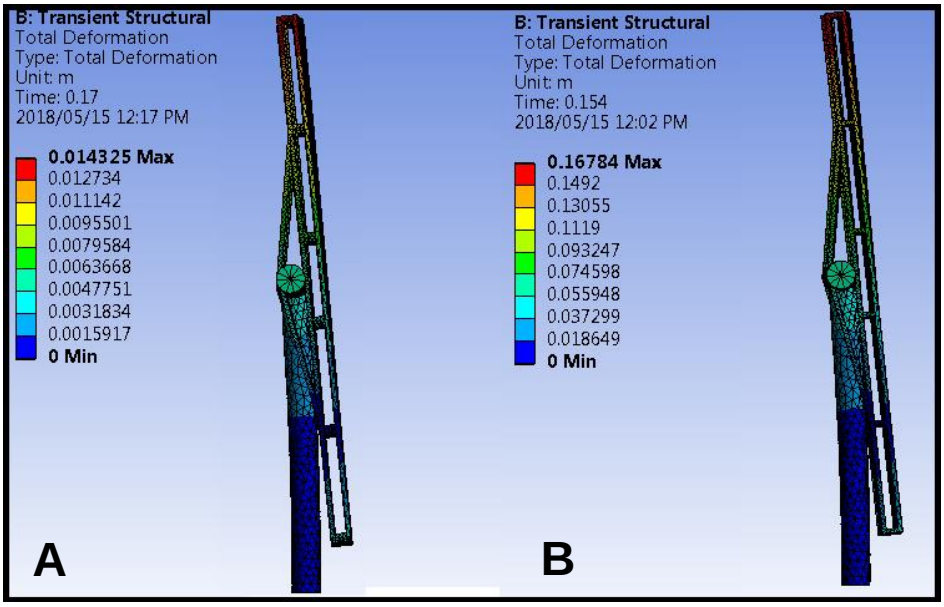

Figure 73: Side view of the deformation of the LH-2. A) U=10.5m/s B) U=45m/s.

From the above Figures for the deformation it is interesting to note that the shape of the deformation for both cases is almost identical regardless of the difference in pressure distribution of the mirror faces. The top edge of the mirrors experiences the greatest deflection with an area on the bottom half of the mirrors experiencing zero deflection.

The equivalent von-Mises stress experienced by the heliostat for both cases is seen in Figure 90. The maximum stress present in the LH-2 structure for the duration of the 1 second simulation for the 10.5m/s case is 74.5 MPa while the maximum stress for the 45m/s case is 939 MPa.

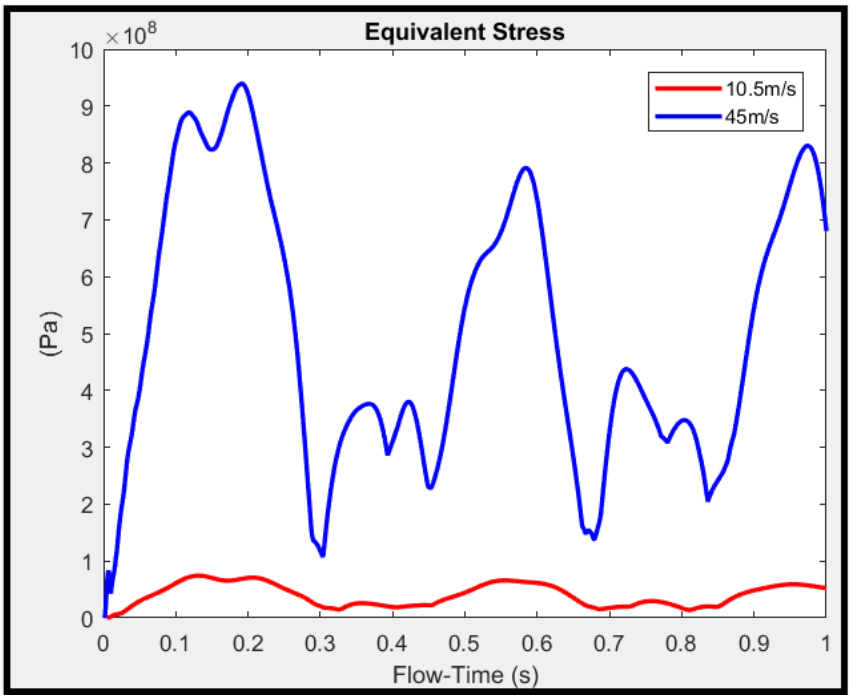

Figure 74: Graphs of the equivalent von-Mises stress.

The maximum stress occurs at a time of 0.198s. The equivalent stress results from the one-way transient FSI for the 45m/s case demonstrate the need for computer aided analysis. The maximum stress of 939 MPa is approximately 3 times greater than the yield strength of a low-grade structural steel. Clearly the heliostat structure would either fail if exposed to the simulated wind conditions or the structure would need to be manufactured from high strength steel. Below, the stress contour plots for the front and back of the LH-2 heliostat are presented for the 45m/s case in Figures 91 and 92. It can be clearly seen that the pylon is the most heavily loaded member in the mirror support structure. The highest stress is localised at the base of the pylon where the heliostat will be attached to a fixed support. The point where the stress is a maximum is the front portion of the pylon base. This is due to the high drag force experienced by the heliostat that is supported by a single pylon. The stress can be seen to dissipate further up the pylon moving into the torque tube where it averages out to a minimum value. A consequence of this localised stress would be to consider modifying the pylon to a material that can withstand the high stress experienced.

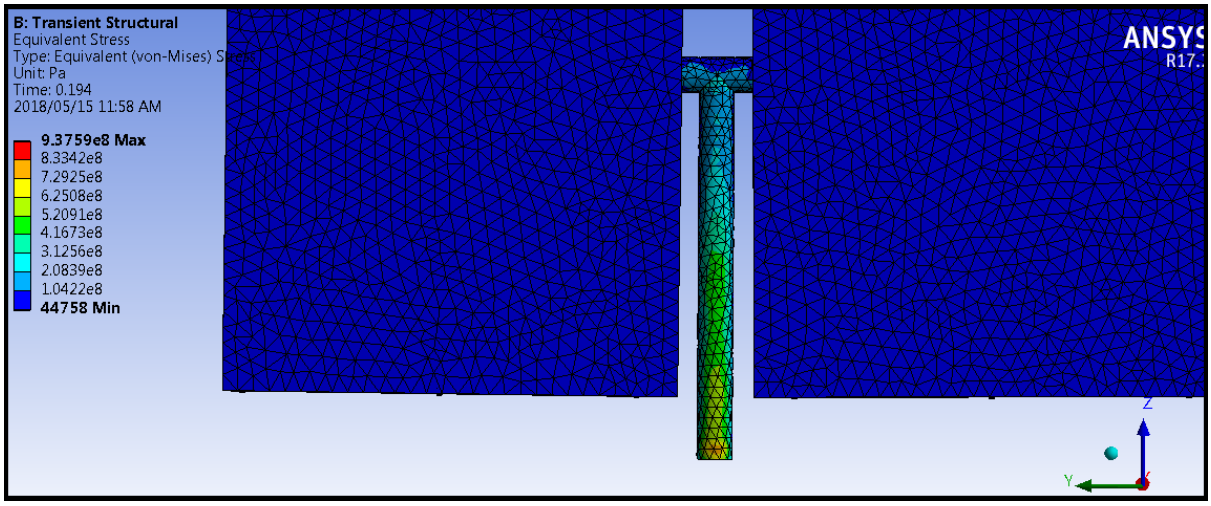

Figure 75: Equivalent von-Mises stress on the front face of the LH-2 (U = 45m/s).

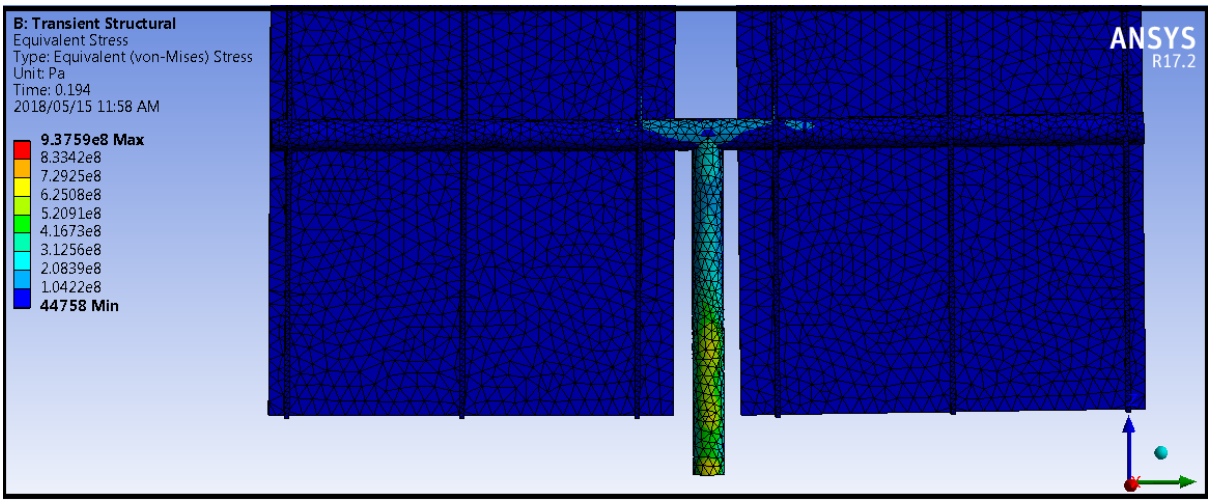

Figure 76: Equivalent von-Mises stress on the rear face of the LH-2 (U=45m/s).

One downside of the System Coupling Workbench setup for FSI simulations is the inability to perform the FSI from a pre-cursor RANS simulation. This consequence of this can be seen looking at the results graphs in Figure 86 of the deformation. The heliostat is initially at rest in effectively an empty domain when the full force of the fluid attacks it. The transient motion is therefore due to the oscillation of the heliostat owing to the initial force of the fluid. This motion can be seen to damp slightly and will come to rest at a constant deflection when modelled with RANS. The results of the FSI show that there is considerable deflection of the heliostat for both cases. This suggests that two-way FSI could yield interesting results for not only the flow but for the structure as well. An attempt to recover transient flow phenomena behind the heliostat with URANS is concluded in the next section but it is evident that RKE URANS is unable to generate the vortex shedding that should be present with this geometry. Even if URANS could generate vortex shedding, only the large transient flow features would be modelled and the smaller peak loadings would be neglected. This means that any stress, peak loading, resonance and fatigue information is incomplete when modelling the FSI with RKE URANS. The information in this section is advantageous to designers looking for the mean loading on the heliostat and is definitely a go-to simulation route in the overall process.

4.4 URANS MODELLING

As seen in the previous section, URANS is unable to model the transient behaviour of the flow around a heliostat. The geometry of the heliostat in three dimensions means the interaction of the shed vortices from all four edges results in highly complex turbulent fluid flow. The addition of a gap between the mirrors complicates this even further as this adds a jet-like flow into the middle of the wake. This is confirmed according to (Breuer, et al., 2003) and (Boddupalli, et al., 2017) as seen in section 2.8 of the literature study.

In order to assess the results of the URANS modelling the experiment of (Matty, 1979) is replicated in this section in 2 dimensions. (Matty, 1979) conducted wind tunnel experiments investigating the vortex shedding frequencies from a square plate model. The plate has dimensions of 10.16 cm x 10.16 cm with a plate thickness of 0.3175 cm. The ratios between the heights of the centre line of the plates above the ground plane to the heights of the plates were investigated for different Reynolds numbers. The Matty wind tunnel model can be seen in Figure 93.

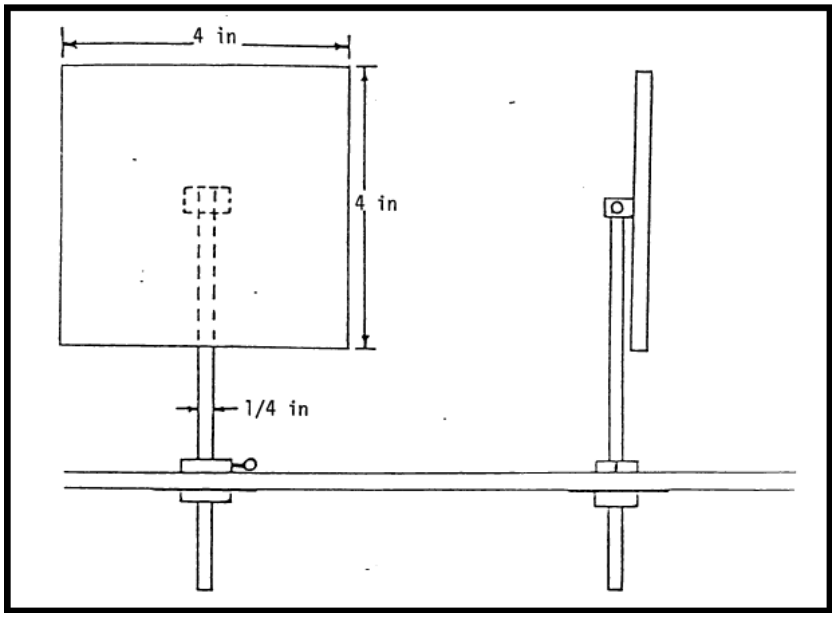

Figure 77: Wind tunnel model used in Matty experiments (Matty, 1979).

The (Matty, 1979) experiments were conducted over a Reynolds number range of 10 000 to 200 000 with a ratio range from 1/32 to 7/2 for h/L as defined in Figure 21. For this simulation, the ratio of 1/4 is chosen with a Reynolds number of around Re = 70 000 based on the heliostat width. The velocity inlet profile used in the Matty's experiment has a negligible boundary layer, therefore a uniform inlet velocity profile of U = 10m/s is used. There is no mention of the turbulence intensity used in the experimental setup. The turbulence intensity used in the simulations were therefore taken at a low value of 0.1%, also with a uniform profile. The SIMPLE solver is used with second-order spatial discretisation schemes with the use of the second-order implicit transient formulation. The RANS turbulence model used is SST k-ω. The fluid domain can be seen in Figure 94.

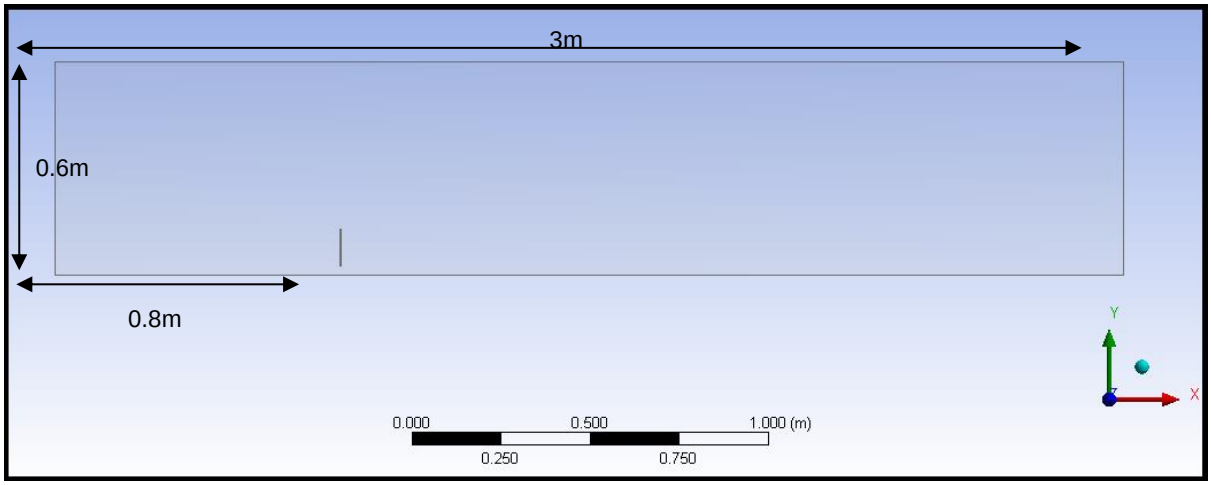

Figure 78: 2-dimensional fluid domain for simulation of the Matty experiment.

The mesh used in this simulation is a mapped face quadrilateral mesh containing approximately 68 000 elements. The mesh is regionally adapted in Fluent twice using a rectangular box around the heliostat, each box being gradually smaller. The final Fluent mesh has a cell count of 378 000 and can be seen in Figures 95 and 96.

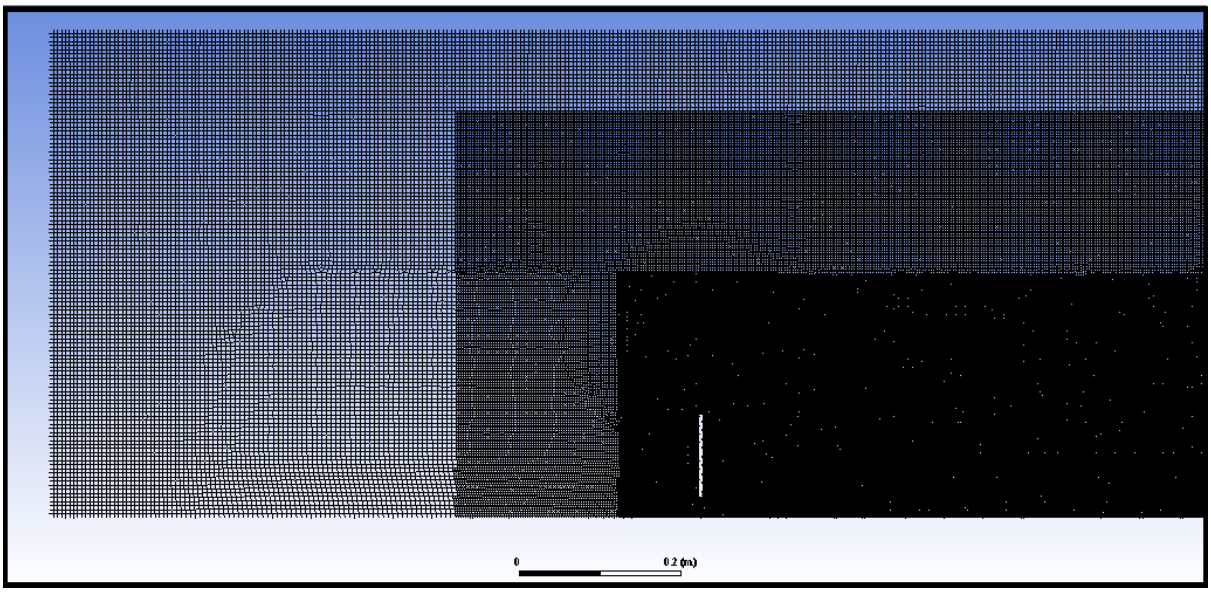

Figure 79: Adapted refined mesh of 2D domain around the heliostat in Fluent.

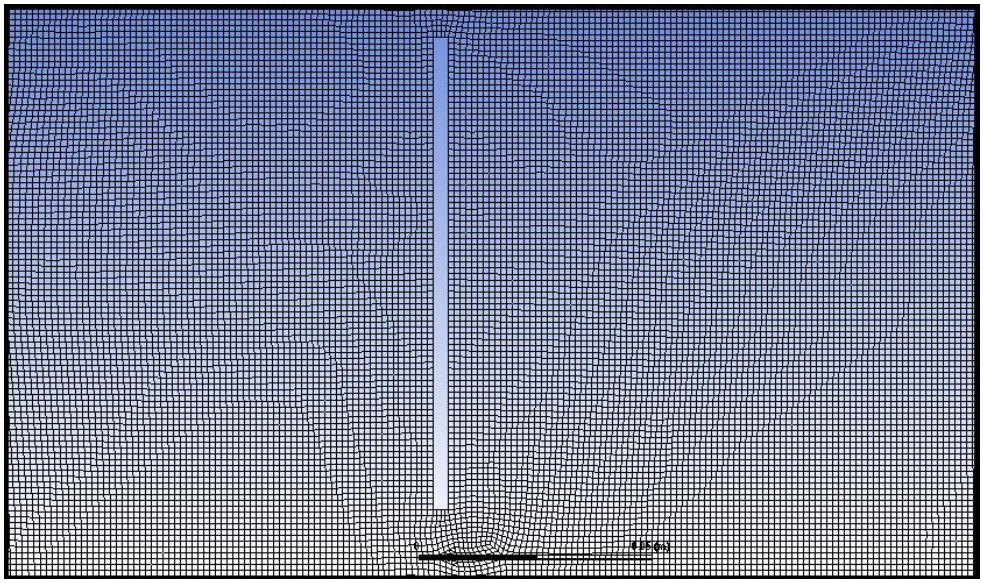

Figure 80: Close up of the refined mesh around the heliostat.

The simulation is run with a time-step size of 0.0005 seconds over 4 000 time-steps with 40 sub-iterations per time step.

The results of the 2-dimesional URANS simulation are extremely promising with regards to the major flow instabilities such as the vortex shedding. The Strouhal number attained by Matty for the 1/4 ratio heliostat configuration for the Reynolds number used was St=0.15. Using the equation for Strouhal number (7) the frequency of the vortex shedding in the wind tunnel experiment is found to be 14.763Hz. An FFT of the URANS simulation is performed on the velocity monitor signal at the HCL, 0.4572m downstream of the heliostat in Fluent and a frequency of 14.53Hz is achieved, this is a 1.5% error. The velocity monitor signal and FFT can be seen in Figure 97 and Figure 98, respectively. The resulting Strouhal number is St=0.147.

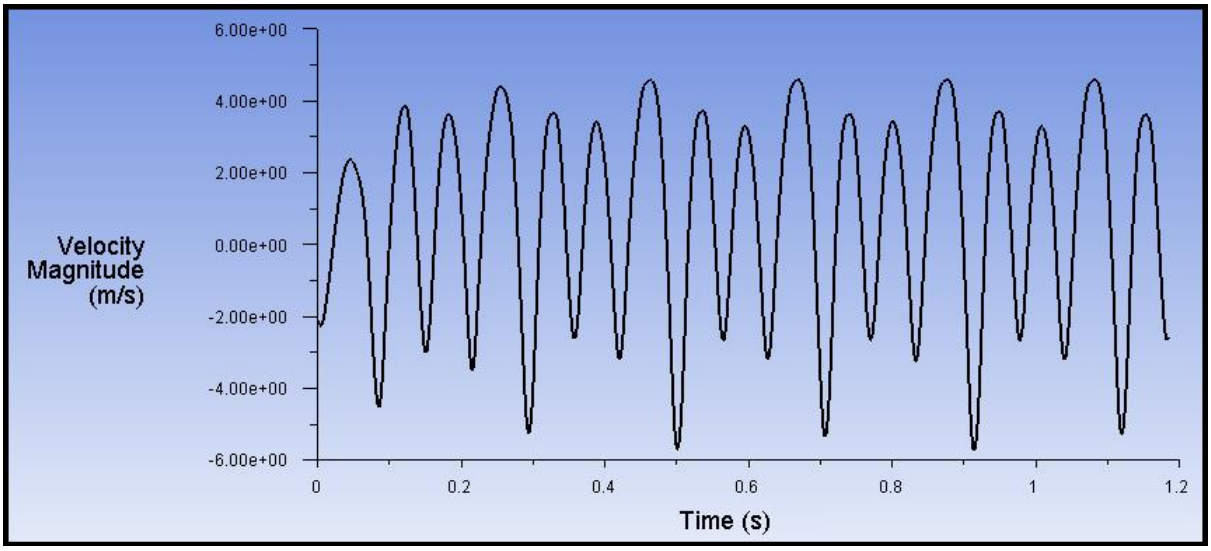

Figure 81: Velocity point monitor signal used in FFT (x,y) = (0.4572,0.127).

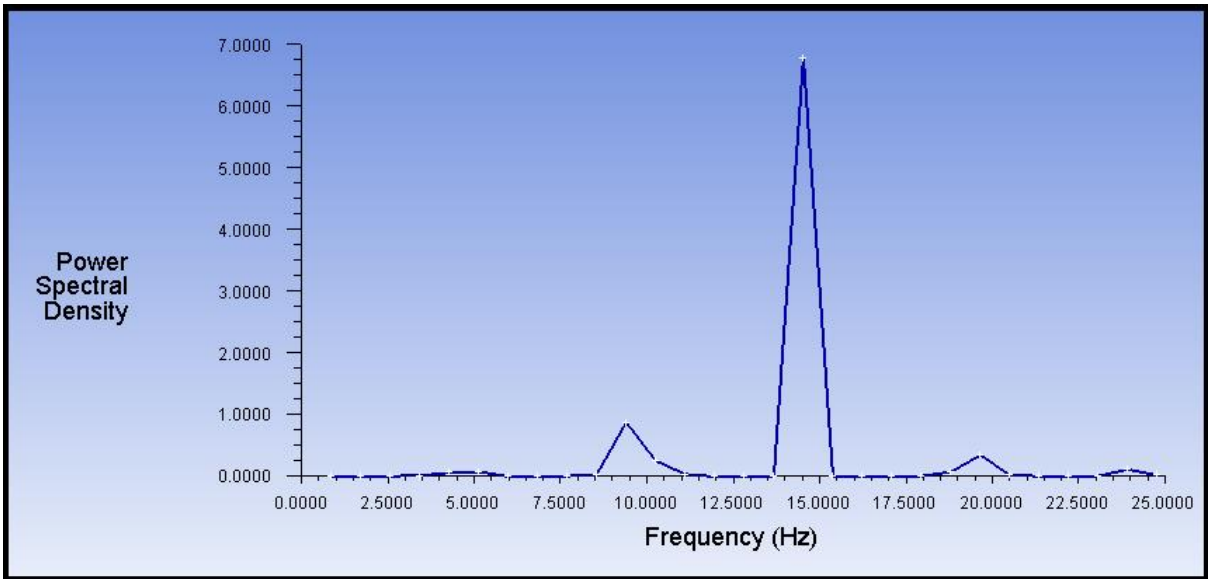

Figure 82: FFT of the velocity monitor signal for the 2D URANS case.

The FFT results show that for the reduced dimension domain and simulation that the vortex shedding that is expected from the heliostat is attainable with 2D URANS. The CFD results are shown below starting with the velocity magnitude contour plot in Figure 99 and the velocity vector plot coloured by velocity in Figure 100.

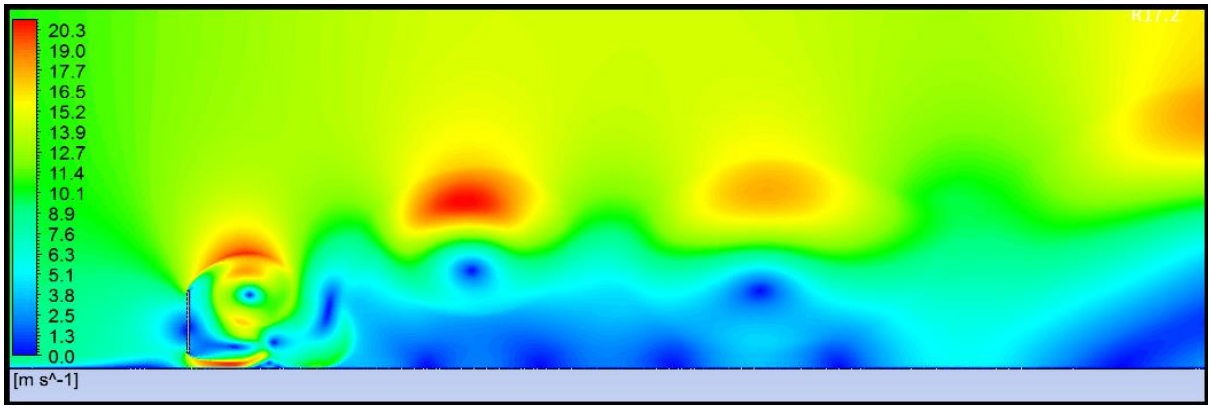

Figure 83: Velocity magnitude contour plot of 2D Matty 1/4 ratio case (m/s).

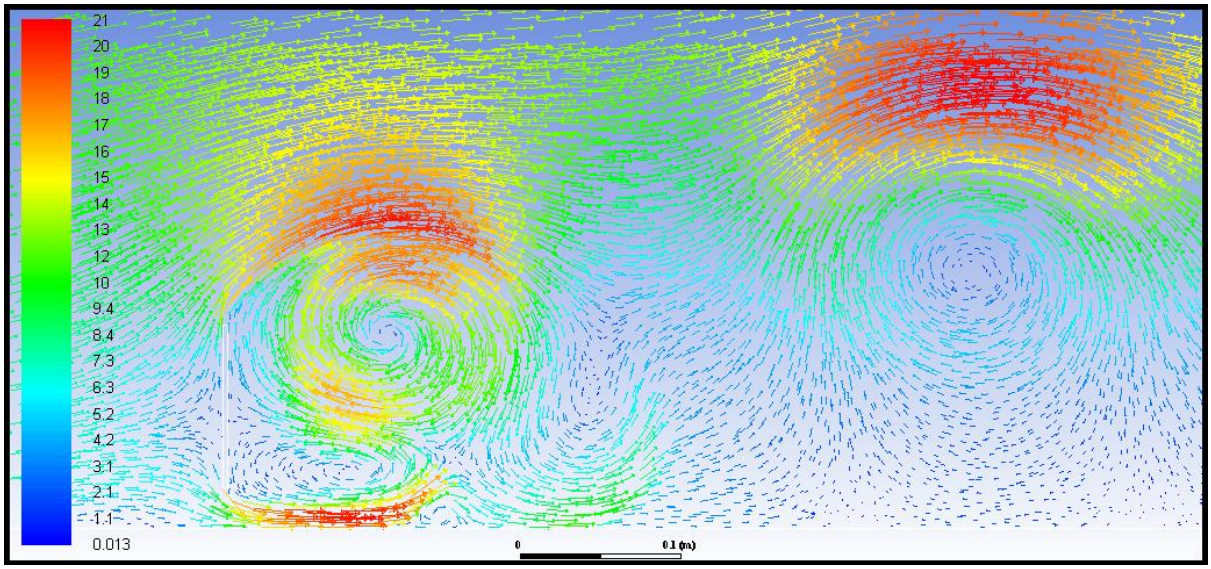

Figure 84: Velocity vectors of 2D Matty 1/4 ratio case coloured by velocity magnitude (m/s).

It can clearly be seen from the two Figures above that there is substantial vortex shedding taking place in the flow. Looking at Figure 100, the velocity vector plot, on the right-hand side there is clear evidence of a large vortex. The interaction of the shear layers and subsequent vortex development from the heliostat edges can be seen.

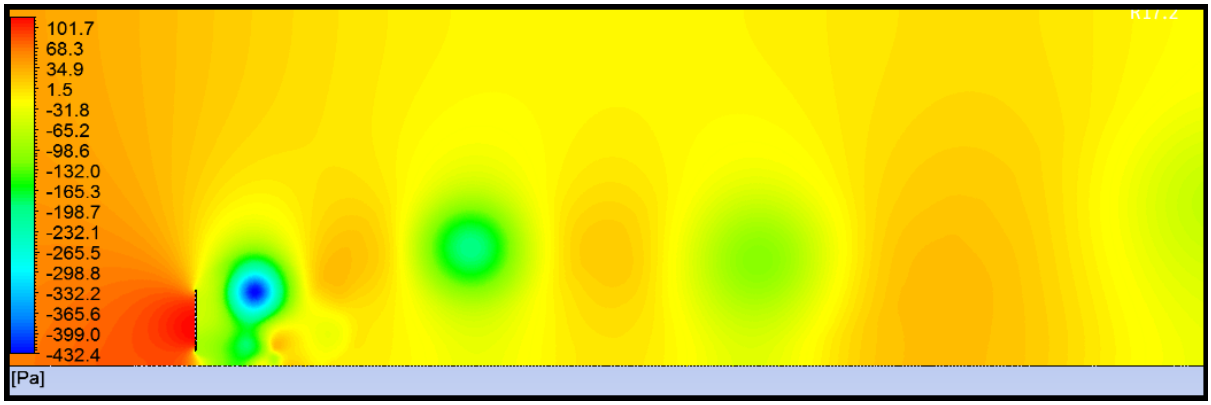

Figure 85: Pressure contour plot (Pa).

The pressure contour plot in Figure 101 shows the shed vortices travelling downstream from the heliostat. The low-pressure regions, seen as blue and green circles represent the vortices' centres. The strength of the vortices can be seen to disperse downstream as their energy is dissipated into the flow and some numerical dissipation takes place. A contour plot of the turbulent kinetic energy of the flow provides a striking visual representation of the vortex shedding taking place from the heliostat. The plot can be seen in Figure 102.

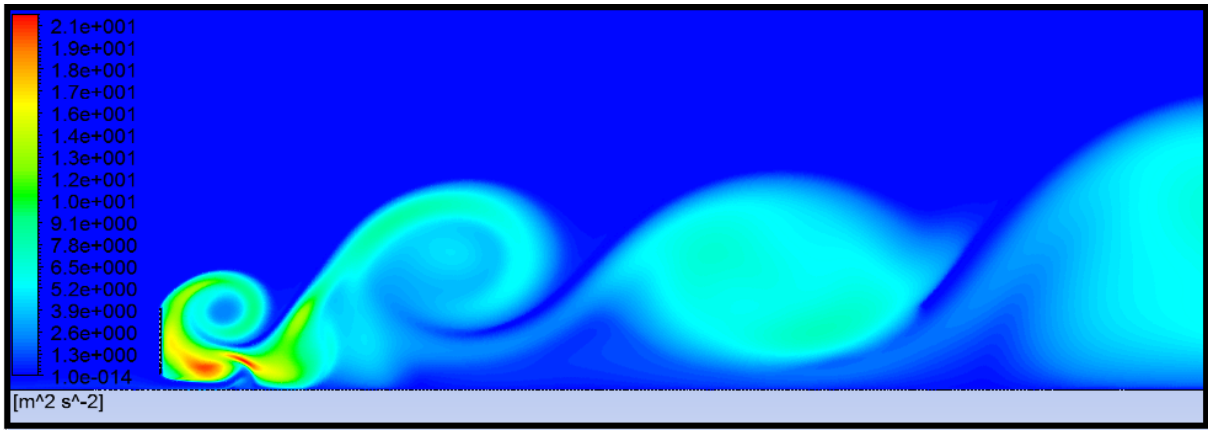

Figure 86: Contour plot of the turbulent kinetic energy in the 2D domain.

The results of 2D URANS (Matty, 1979) simulation demonstrate the ability of URANS to model vortex shedding from a 2D heliostat. This may be possible due to the simplified flow field behind the heliostat, when the vortex shedding from the side edges is eliminated, as is the case for 2D. The dominating shedding from the top and bottom edges can develop. Without the interaction from the side flow and jet-like flow through the middle between the mirrors the vortices are able to form and be modelled with URANS equations.

In order to ensure that the result obtained for this particular 2-dimensional case, where the Reynolds number is Re = 70 000, is attainable for higher Reynolds number flows, the computational domain is scaled in Fluent. Five subsequent simulations are performed whereby the Reynolds number is doubled from case to case by way of scaling the domain dimensions. The final case has a Reynolds number of Re = 2.24×10^6. This is approximately the same Reynolds number that the full-scale LH-2 heliostat is simulated in. If the result obtained from the final Reynolds number simulation is reasonable this will mean that a 2D simulation of the LH-2 heliostat can be performed. The graph of the results of the six simulations can be seen in Figure 103. The graph shows the Strouhal number versus the Reynolds number.

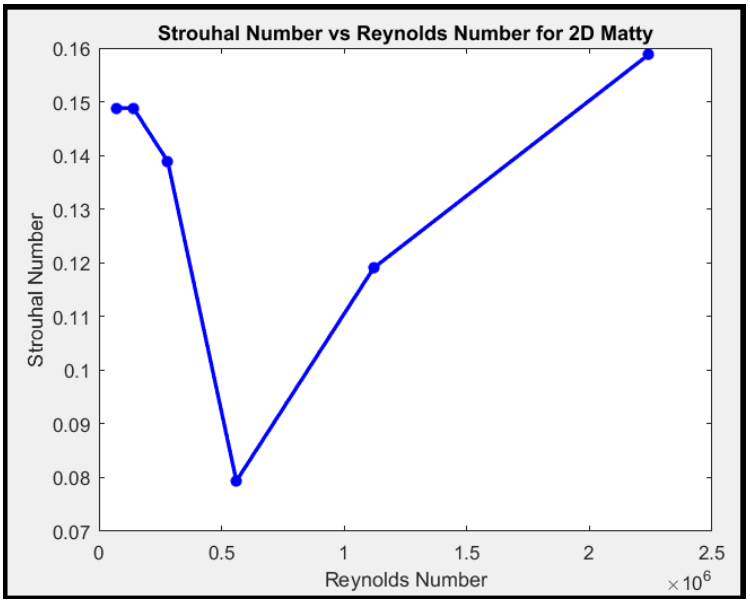

Figure 87: Strouhal number obtained for varying Reynolds numbers.

The graph shows that for a Reynolds number of around Re=560 000 there is a decrease in the Strouhal number. This may be due to the fact that the flow before this point had an almost laminar vortex street phenomenon present, as the Reynolds number increased to around Re=500 000 the flow became increasingly turbulent and the vortex street and subsequent shedding broke down. Increasing the turbulence once again with the increase of the Reynolds number the more turbulent vortex shedding presents itself. The Strouhal number increases again as the Reynolds number increases with the Strouhal number for the Re=2.24x10^6 case being very similar to that of the Re=70 000 case. The important result here is that vortex shedding is present and attainable over the range of Reynolds numbers of importance. This means that a 2D simulation of the LH-2 heliostat should provide reasonably accurate results for the vortex shedding frequency that is otherwise not possible to simulate without SRS modelling.

Having vortex shedding being attainable with URANS for a 2D configuration has both advantages and disadvantages. The advantages of this result means that the shedding frequency can be found with reasonable accuracy for new heliostat dimensions. This is an important result as the shedding frequency and Strouhal number plays an important role in the resonant frequency of the heliostat structure and subsequent design. If this can be found using cheap 2D simulations instead of expensive 3D simulations with SRS modelling, this is an enormous saving in both cost and time. This result is not ideal and the disadvantages mean that this flow and vortex shedding cannot be replicated in 3D using URANS modelling. Obviously, the 3D structure can be excited by a force with the pre-determined 2D frequency but the flow will not be able to be altered with the change in displacement of the heliostat as in 2-way FSI.

4.5 2D TWO-WAY FSI OF LH-2

In this section the LH-2 heliostat is investigated further. Following from the previous section it will be entirely modelled in two-dimensions. Firstly, a 2D URANS CFD simulation is performed to determine the flow features of the LH-2 such as the drag coefficient and velocity point monitors. A 2D modal analysis is also performed on the structure. This is compared to the 3D modal analyses conducted in section 4.2. Lastly a full two-way 2D FSI is performed with the results compared to the CFD and modal analysis.

In the previous section on the 2D URANS modelling of the (Matty, 1979) wind tunnel experiment, it was concluded that the 2D approach for modelling the vortex shedding is reasonably accurate for this particular setup. It makes sense then that this approach is extended to the full-scale LH-2 heliostat as the only other way vortex shedding can be resolved is highly expensive SRS modelling.

The computational domain used has the same dimensions as the one-way FSI model used in section 4.3 above. The only difference is the top wall height has been reduced to 26m. In order to perform an FSI analysis in ANSYS workbench the domain has to have a finite thickness. For this reason the domain in this case is given a thickness of 0.005m in the third dimension. The CFD domain is meshed with a face swept tetrahedral mesh containing roughly 67 000 cells with a refinement on the heliostat edges with a maximum element size of 1cm. The same mesh is used for the CFD simulation in this section and the FSI simulation in order for an accurate comparison of the results of each. The use of a relatively coarse mesh for these

simulations is due to the need of accelerating the coupling process. The mesh can be seen in Figure 104 with a close up of the heliostat in Figure 105.

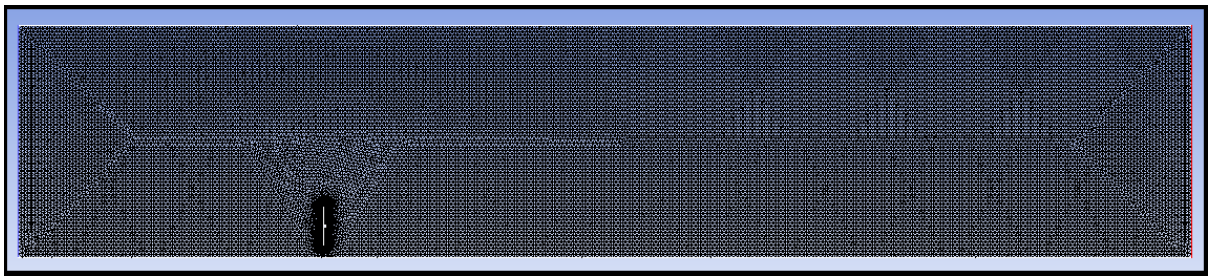

Figure 88: CFD mesh of the 2-dimensional domain containing the LH-2.

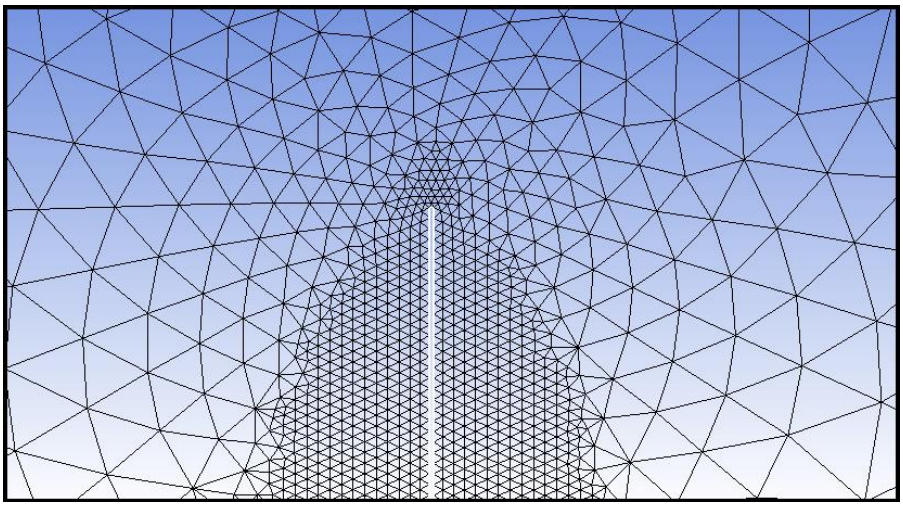

Figure 89: Close up of the mesh around the top vertex of the LH-2.

The mesh has the requirement of containing unstructured tetrahedral elements as this is a requisite of the dynamic remeshing. The boundary conditions for this simulation consist of a uniform inlet velocity profile of 10m/s with a turbulence intensity of 20%. This equates to a Reynolds number of approximately $Re = 2.2x10^6$. A no-slip wall is prescribed on the bottom wall with a slip wall on the top wall. The side walls of the domain are prescribed with symmetry and a zero-gauge pressure outlet is used. The material properties are identical to those used in section 4.3, with the reference area changed to the cross-sectional height of the heliostat of 3.21m. The SIMPLE solver is used with second-order spatial discretisation schemes with the use of the second-order implicit transient formulation. The turbulence model used is SST k-ω. The simulation is run with a time step size of 0.001 seconds with a total of 15 000 time steps. This provides a total of 15 seconds of run time.

The CFD results are shown below. The velocity magnitude contour plot can be seen in Figure 106. Looking at the velocity contours, the vortex shedding is clearly evident in the zigzag of high and low velocity regions in the wake. This is confirmation that the vortex shedding can be resolved and captured for the LH-2 dimensions and Reynolds number using 2D URANS methods. Two velocity point monitors were placed in the wake of the LH-2, point A = (4,3)m and point B = (5,4)m, visible in Figure 106.

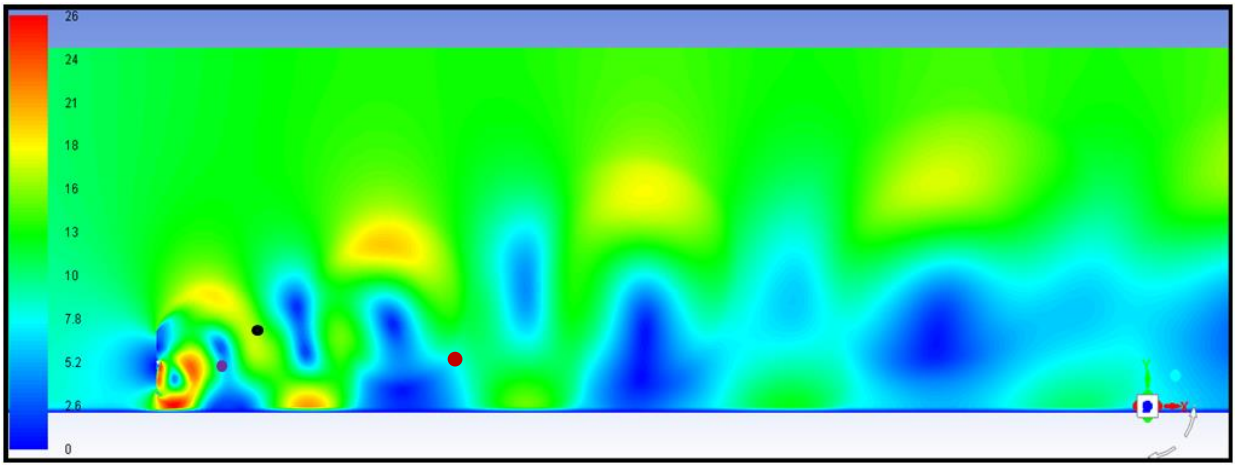

Figure 90: Velocity magnitude contour plot of 2D LH-2 (m/s) with point A (purple), B (black).

The pressure contour plot can be seen in Figure 107. An interesting phenomenon visualised here is the almost partial shedding of the top edge vortex followed by the shedding of the bottom edge vortex. This vortex pair then appears to travel downstream in the wake as a unit.

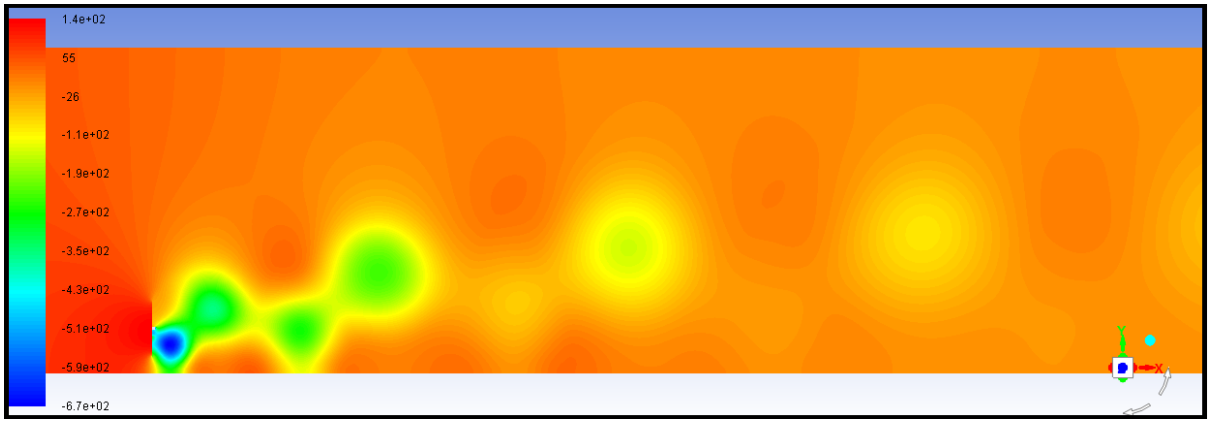

Figure 91: Pressure contour plot of 2D LH-2 (Pa).

This can be confirmed by looking at the contour plot of the turbulent kinetic energy in Figure 108.

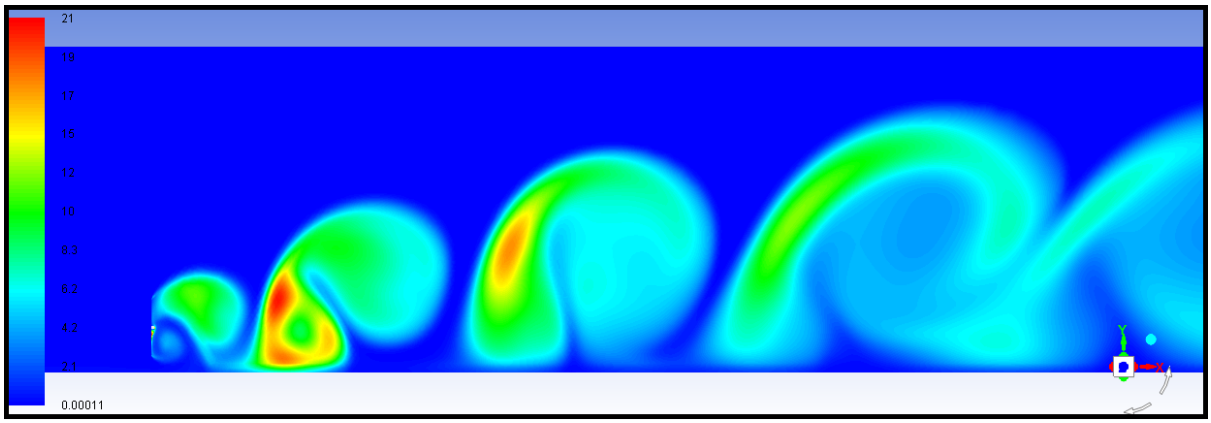

Figure 92: Turbulent kinetic energy contour plot of the 2D LH-2.

The signal and FFT of point A can be seen in Figures 109 and 110 respectively.

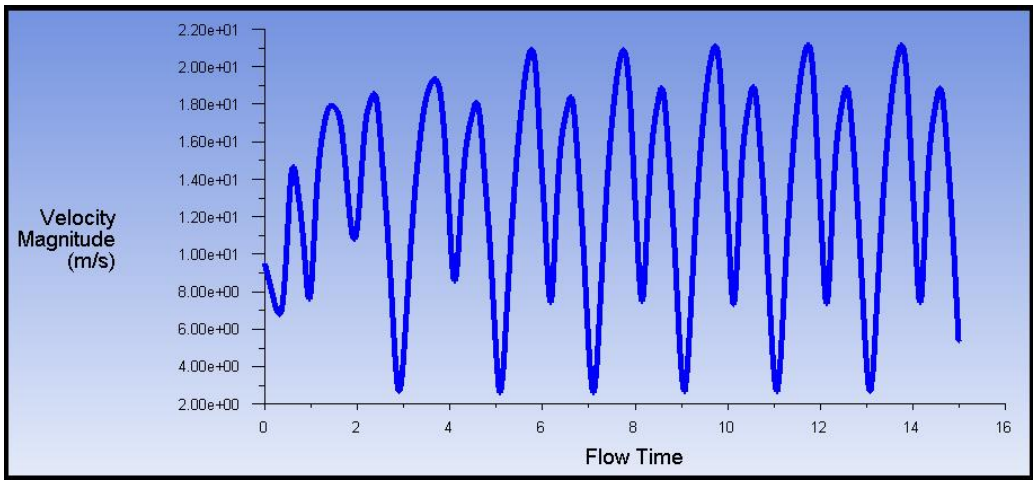

Figure 93: Velocity monitor of point A (4,3)m.

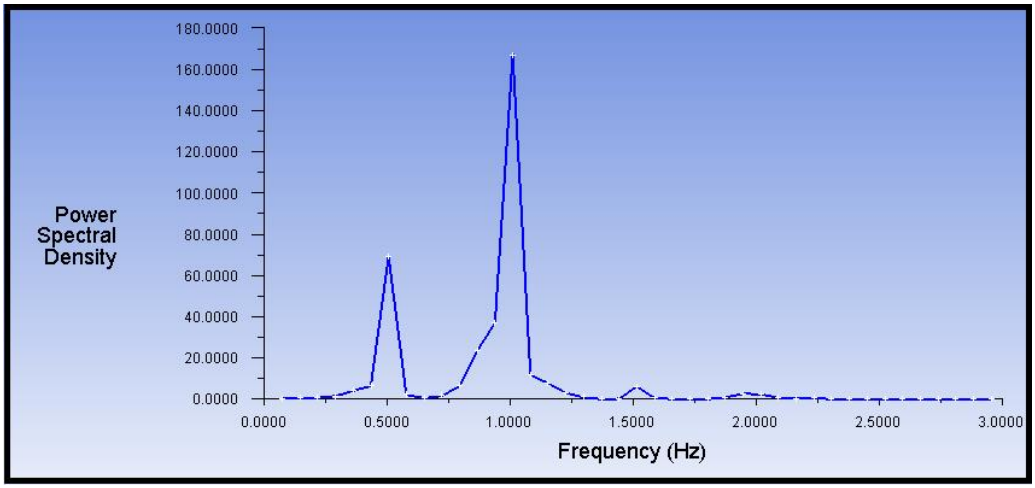

Figure 94: FFT of velocity monitor point A (4,3)m.

The signal and FFT of point B can be seen in Figures 111 and 112 respectively.

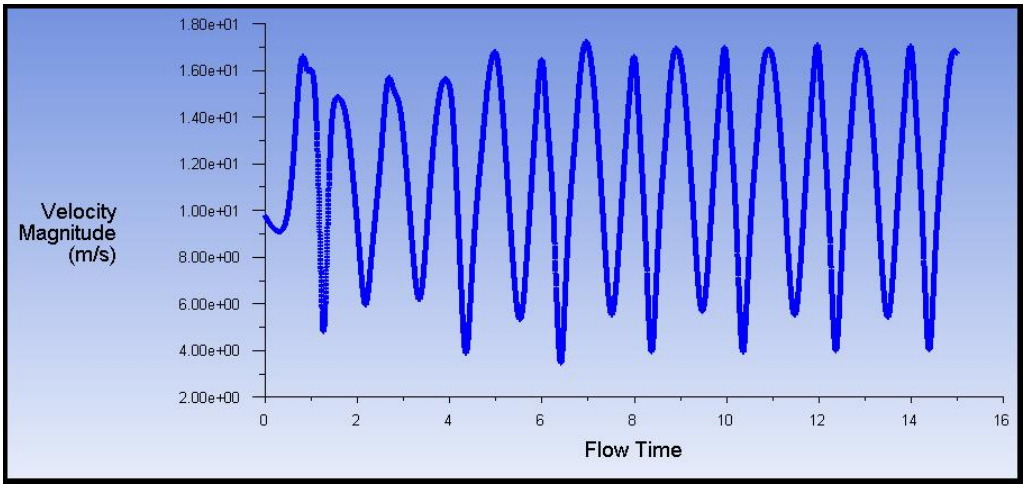

Figure 95: Velocity monitor of point B (5,4)m (Seconds).

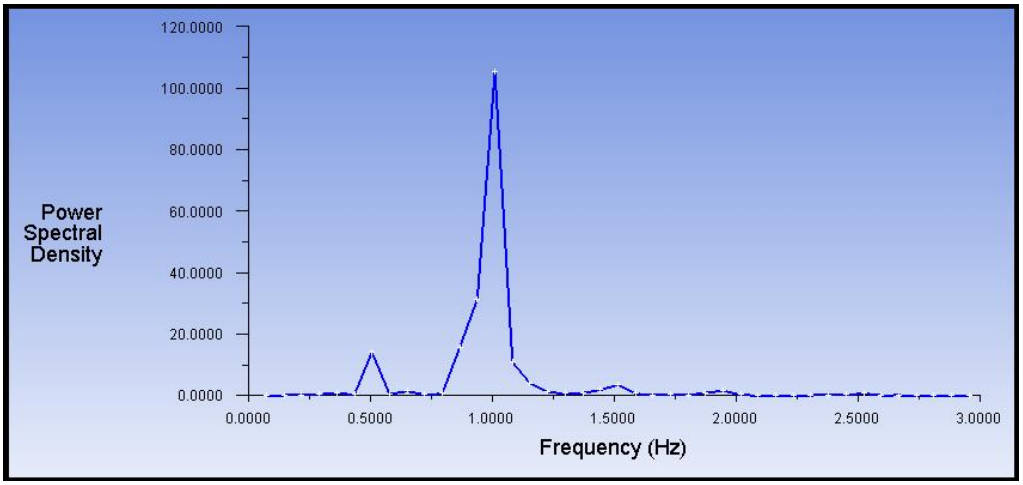

Figure 96: FFT of velocity monitor point B (5,4)m.

Looking at the FFT of point A, there are two very prominent frequencies present in the velocity signal. The first is a frequency of 0.505Hz and the second is a frequency of 1.01Hz. The expected vortex shedding frequency of the LH-2 using Figure 21 and a velocity of 10m/s with a Strouhal number of St=0.15, is determined to be approximately 0.467Hz. Looking at Figure 110 for the FFT of point B it is apparent that the signal with a frequency of 0.505Hz has diminished somewhat. This is due to the fact that this monitor point is at a higher position in the wake and the effects of the secondary vortex shed from the bottom edge of the heliostat is not influencing this point as much as it did for point A. Ultimately this means that vortices are being shed from the LH-2 at a frequency of 0.505Hz with the vortices from the bottom edge or top edge (the top edge vortices being the dominant signal due to the position of the monitor point) shedding at 1.01Hz. This again confirms what can be seen in the contour plots of a delayed total shed of the vortex as it peels off the top then the bottom edge separately to form one elongated double vortex. Looking at the drag coefficient FFT plot in Figure 113, the vortex shedding frequency of 0.5Hz is confirmed. Another

powerful conclusion that can be drawn from the CFD result is that the shedding frequency from the 2D URANS has only a 7% difference from the experimental results of (Matty, 1979), giving validation to the use of 2D methods and the potential use of 2D FSI.

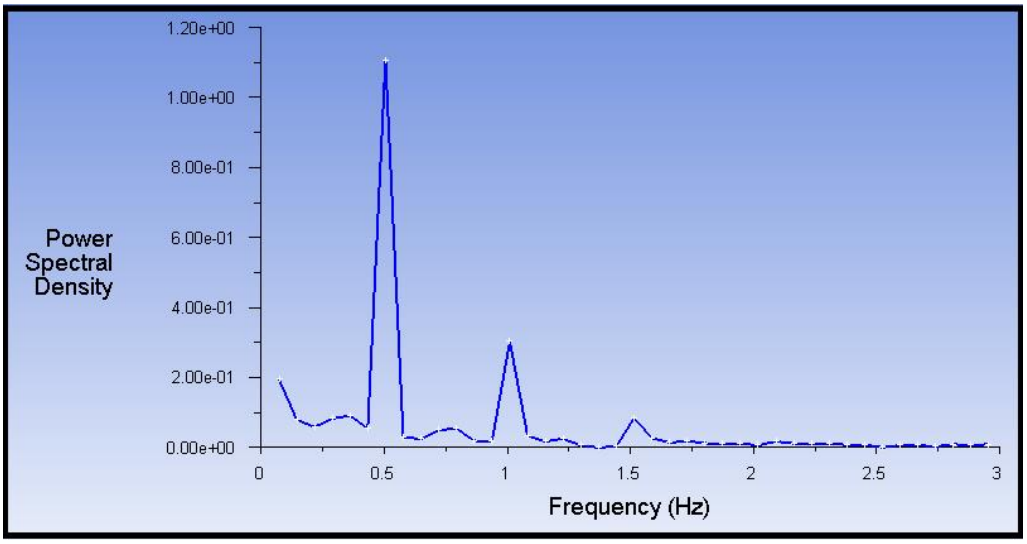

Figure 97: FFT of the drag coefficient signal.

The 2D URANS simulation is repeated for the 60 degree case as these two cases will be simulated using SRS CFD in chapter 5. Using simple trigonometry, the 2D frontal area for the 60 degree case is found to be 1.605m compared to the 3.21m for the 0 degree case. The expected vortex shedding frequency calculated from the Strouhal number approximated from (Matty, 1979), for the 60 degree case is 0.93Hz. The velocity magnitude contour plot and the turbulent kinetic energy contour plot are shown below.

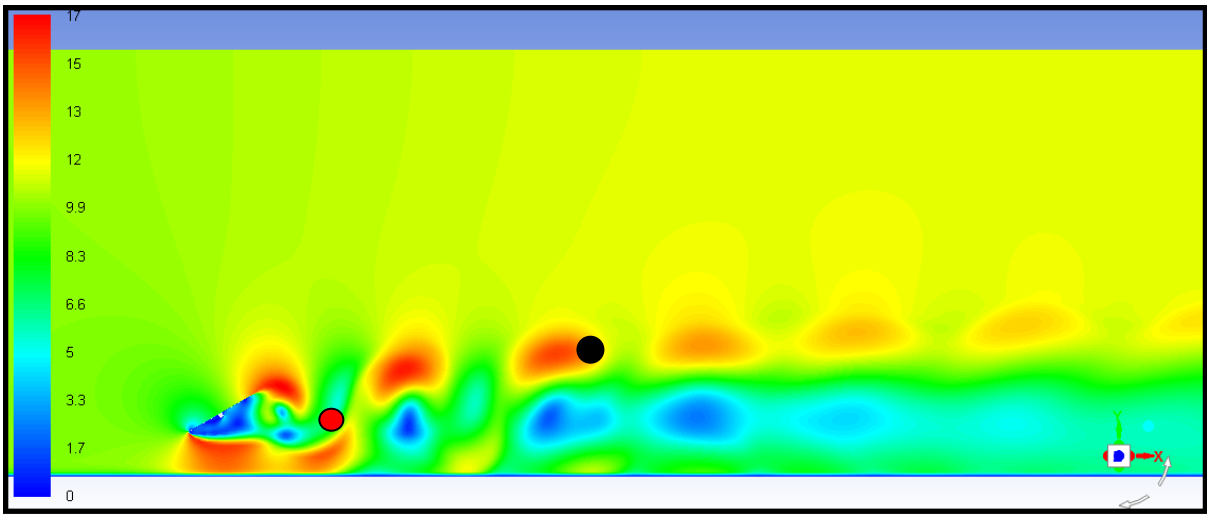

Figure 98: Velocity magnitude contour plot for the 2D 60 degree LH-2 case, RED = monitor point 1 (4.5,2.5), BLACK = monitor point 2 (10,6) (m/s).

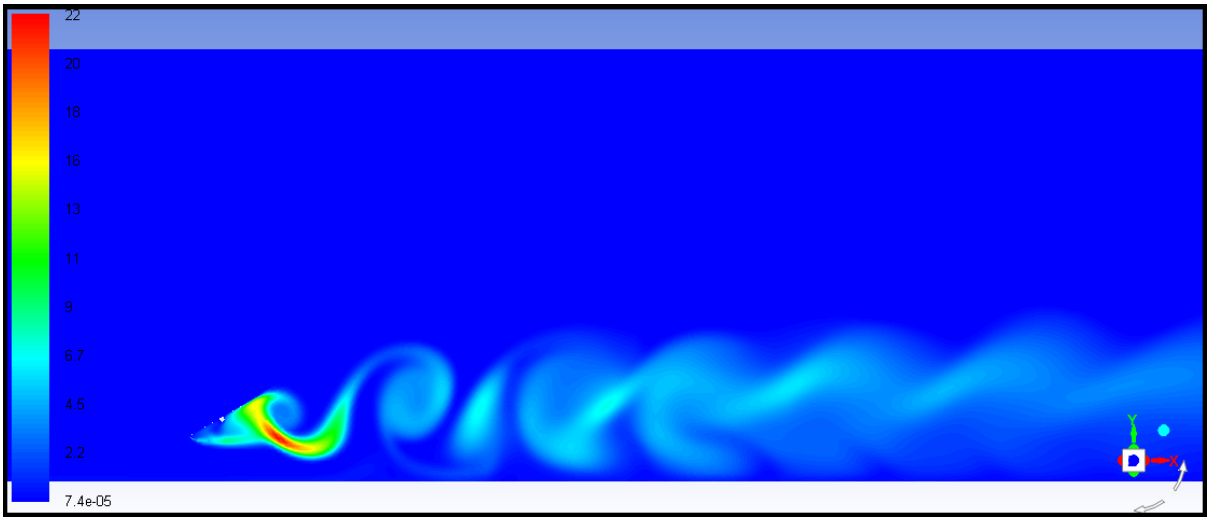

Figure 99: Turbulent kinetic energy contour plot of the 2D 60 degree LH-2 case.

As can be seen from the contour plots in Figures 114 and 115, there is strong pattern of vortex shedding developed in the wake behind the heliostat. It is stressed once again that this vortex shedding attained using URANS modelling is not possible with 3D URANS. Two velocity point monitors were used to track the vortex shedding in the heliostat wake as seen in Figure 114. The signal of the two velocity monitor points can be seen in Figure 116 and Figure 117 with the corresponding FFTs of the signals in Figures 118 and 119, respectively.

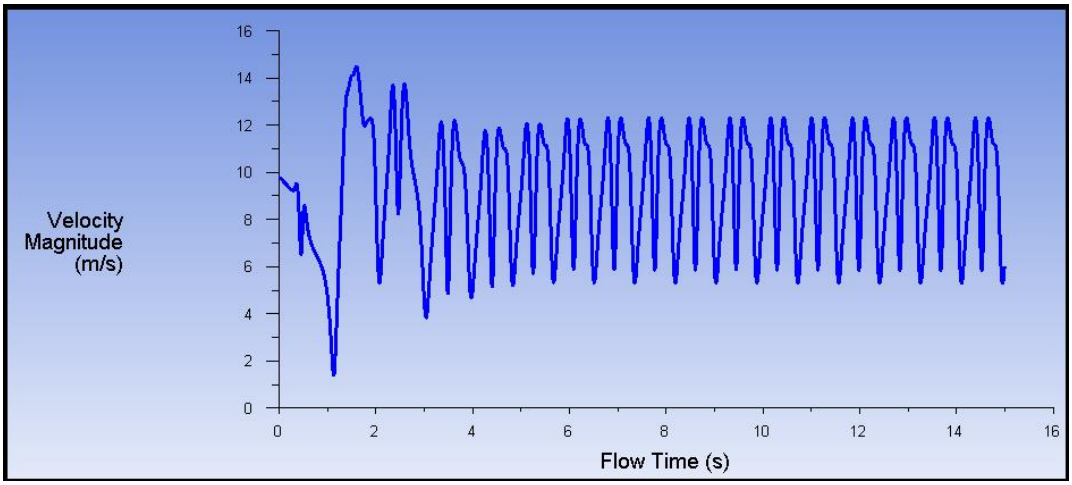

Figure 100: Velocity magnitude signal at monitor point 1.

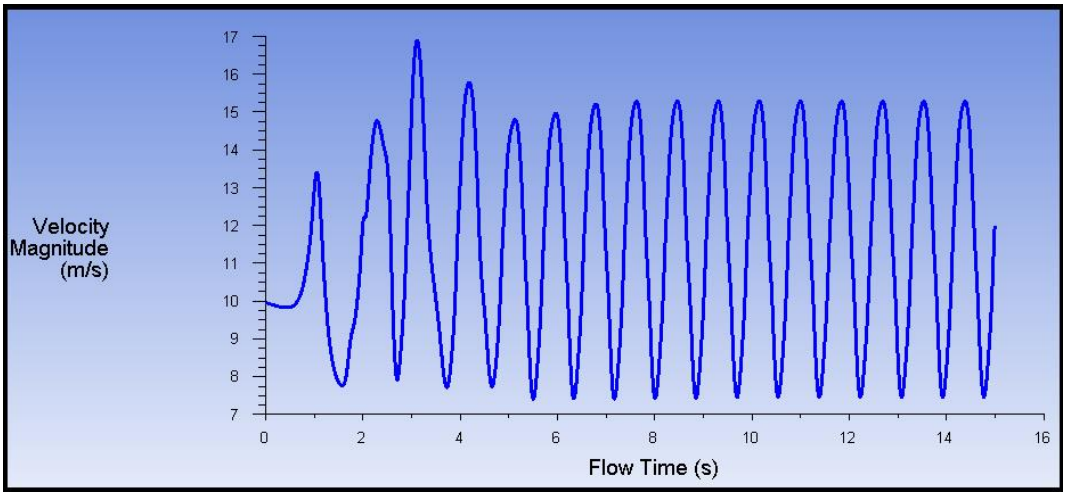

Figure 101: Velocity magnitude signal at monitor point 2.

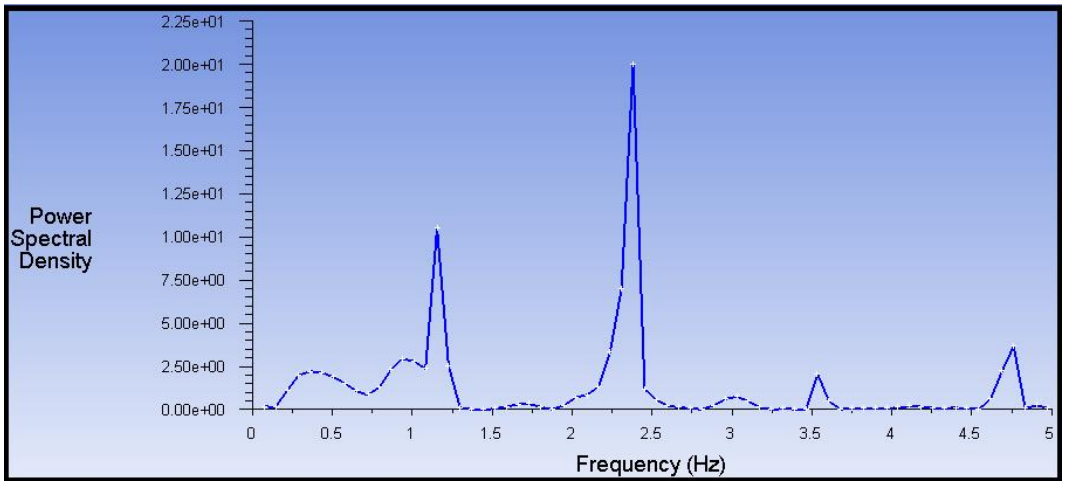

Figure 102: FFT of velocity monitor signal at point 1.

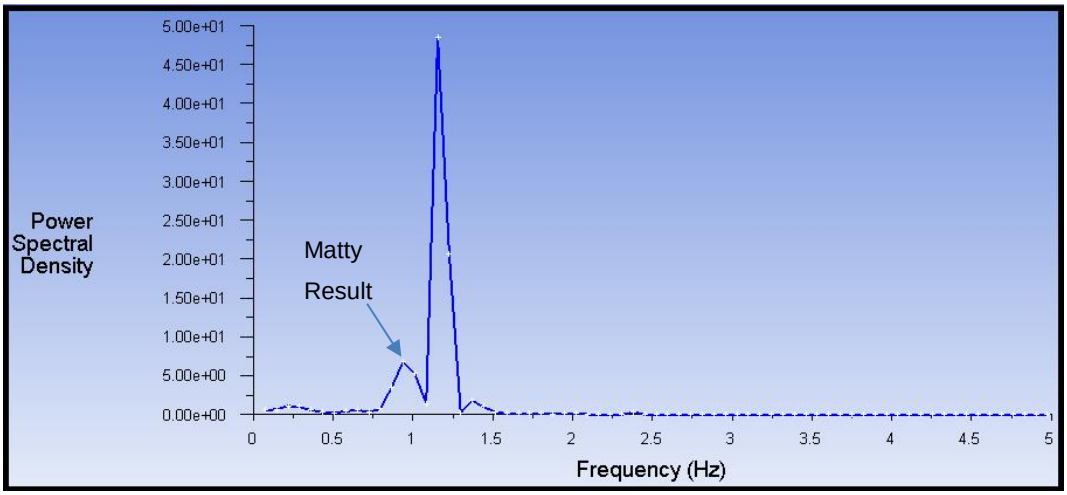

Figure 103: FFT of velocity monitor signal at point 2.

Looking at Figure 118 for the FFT of monitor point 1, two strong frequency spikes are present. The first has a frequency of 1.15Hz and the second spike is at 2.38Hz. The second spike is not representative of the

shedding frequency. Looking at the second monitor position in Figure 114 in the velocity magnitude contour plot, the second spike at 2.38Hz is due to the monitor point picking up the front and back side of a single shed vortex. The first spike of monitor 1 is the actual shedding frequency. Looking at Figure 119 of the FFT of monitor point 2 there are two frequency spikes present. The first spike at a frequency 0.938Hz matches the approximation of the vortex shedding from (Matty, 1979) exactly. The second spike at 1.15Hz matches monitor point 1 and represents the actual vortex shedding frequency obtained for the LH-2 heliostat at 60 degrees using 2D URANS modelling. It is important to note that looking at Figure 114 for the velocity contour plot with the monitor points shown, one can see that this point only tracks the passing of an entire single vortex at a time. Once again the 2D URANS modelling of the LH-2 appears to be successful, according to comparisons with (Matty, 1979), in modelling the vortex shedding. There is a frequency component (in monitor 2) that matches the (Matty, 1979) predictions with no error while the main shedding frequency has a 19% error when compared to (Matty, 1979).

The same CFD mesh is used for the FSI simulation as used above for the 2D CFD LH-2. The exact same Fluent boundary conditions, solver settings and calculation settings are used for the FSI. The only difference is the use of dynamic remeshing where smoothing and remeshing are implemented to allow for the deformation of the LH-2 structure in the fluid flow. The Mechanical material properties of structural steel are prescribed for the LH-2. These were given in Table 5 above. A swept mesh containing 3D quadrilateral elements with a maximum face size of 4mm is used for the LH-2 structure. The final structural mesh can be seen in Figure 120, the mesh contains approximately 2 700 elements. The cylindrical torque tube has been replaced in the mechanical model with a square torque tube as can be seen below. This is due to the need to prescribe a fixed surface which is set as the right wall of the square torque tube. The shape of the torque tube has a negligible effect on the CFD results as the flow is not affected by the leeward side of the LH-2. The boundary conditions for the Mechanical model consist of the previously mentioned fixed support on the right torque tube wall and the FSI interface prescribed for the entire heliostat edge surface.

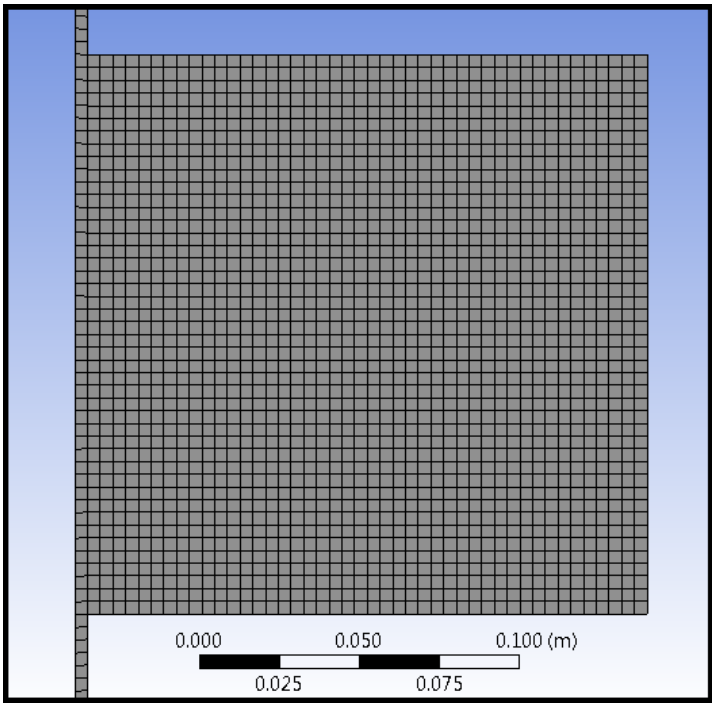

Figure 104: Mechanical mesh of LH-2, close up.

A full two-way FSI simulation is performed using Workbench and System Coupling. The System Coupling settings for this simulation involved running the simulation for a total of 10 seconds with a time step size of 0.001 seconds and a maximum number of coupling iterations set at 5.

The 2-way FSI CFD results are presented first. Looking at the velocity contour plot of the FSI seen in Figure 121, there is very little difference between the pure CFD and FSI CFD plots. The difference between the two that can be seen is due to the difference in simulation times, with the CFD plotted at a time of 15 seconds and the FSI plotted at a time of 10 seconds.

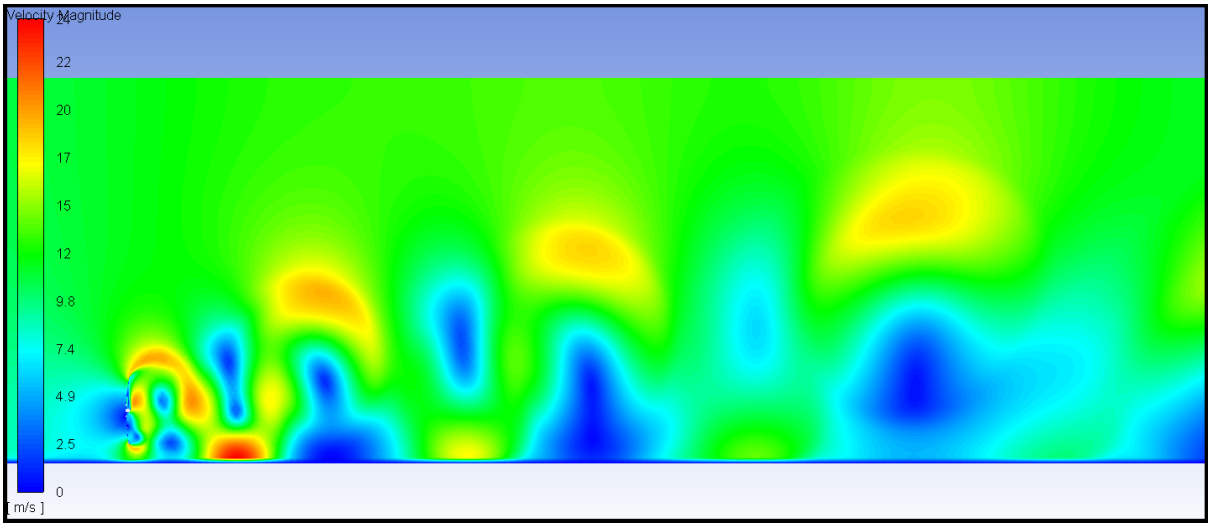

Figure 105: Velocity magnitude contour plot of the FSI CFD (m/s).

The static pressure and turbulent kinetic energy contour plots, despite the time differences, both look identical to the CFD plots. A close up of the velocity magnitude contour plot can be seen in Figure 122 in order to exhibit the deformation of the heliostat in Fluent due to the System Coupling with Mechanical. In this figure, the vertical line structure of the rigid heliostat in the straight CFD result (Figure 106) is now convex to the oncoming flow due to the force of the wind, with its concave side facing the wake vortices as it vibrates around this configuration.

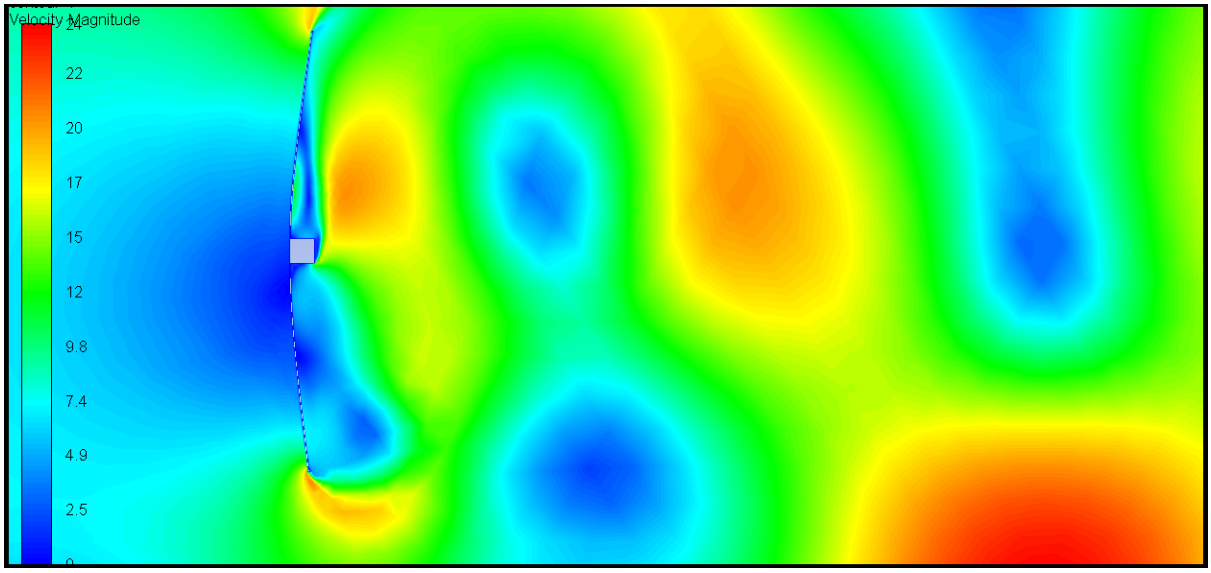

Figure 106: Close up of the velocity magnitude contour plot (m/s).

The FFTs of both monitor point A and B for the FSI CFD show almost the exact same frequency content as the CFD monitor points before. The FFTs for the two points can be seen below in Figures 123 and 124, respectively.

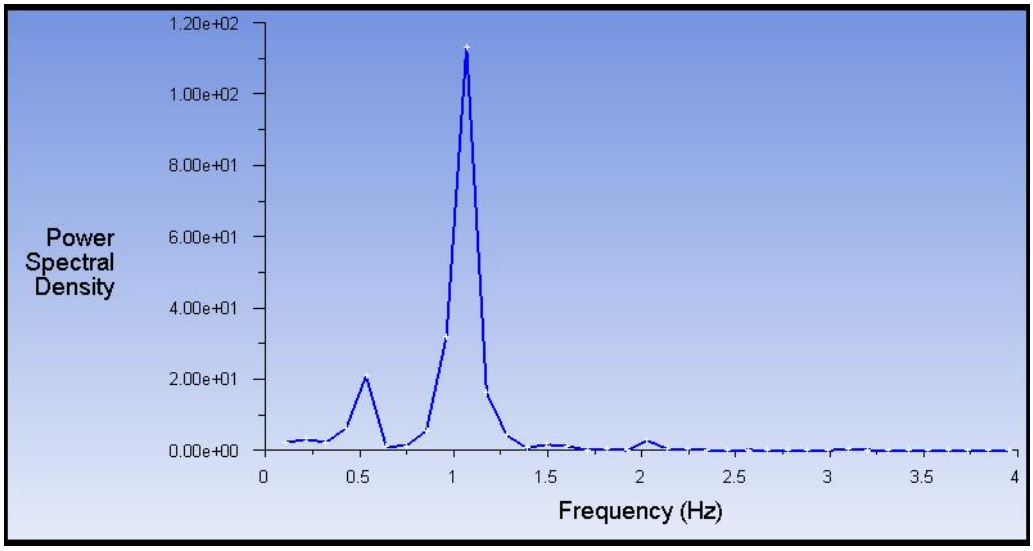

Figure 107: FFT of velocity monitor point A (4,3)m for FSI.

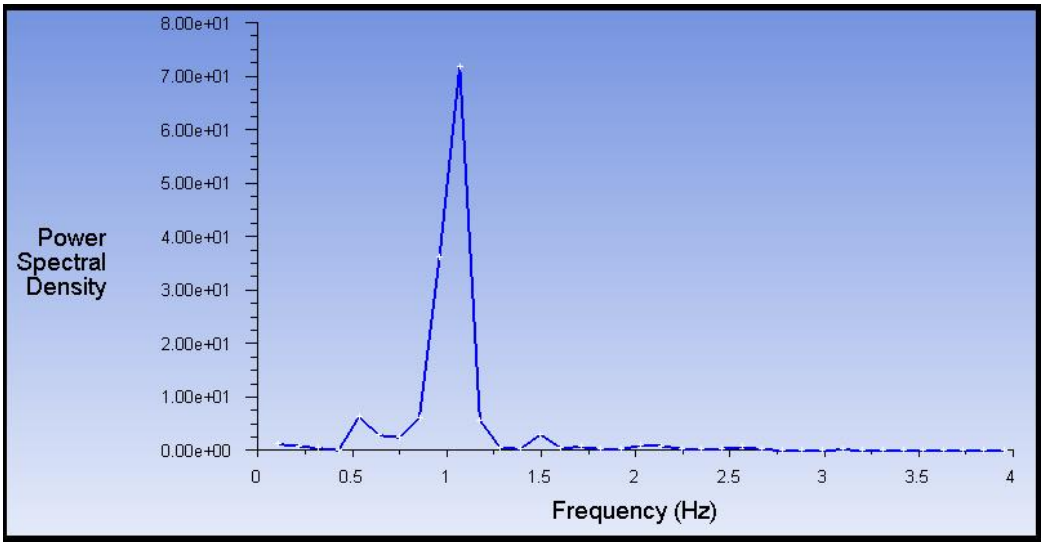

Figure 108: FFT of velocity monitor point B (5,4)m for FSI.

Looking at the FFT of the drag coefficient signal however, as seen in Figure 125, there is a very noticeable difference between the CFD and FSI FFTs. This difference is in the fact that the vortex shedding for the CFD simulation happens at a frequency of 0.5Hz as seen on the CFD Cd FFT. The FSI Cd FFT shows that while the dominant frequency of the signal still occurs at a frequency of 0.53Hz the frequency of 1.06Hz is nearly as dominant.

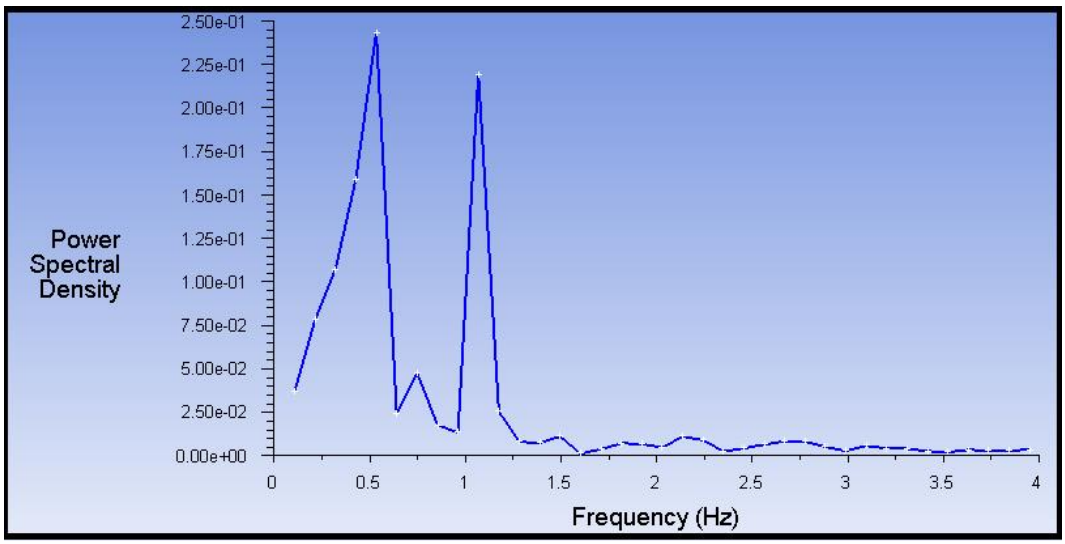

Figure 109: FFT of the FSI drag coefficient.

Looking at Figures 126 and 127 below for the drag coefficient signal for the CFD and FSI, respectively, one will also notice a substantial difference in the patterns of the signals. The drag signal for the CFD case is rugged and reflects the aggressive nature of the vortex shedding from the heliostat. When the heliostat is able to move in the flow, as is the case for the FSI simulation, the drag signal is now smoothed. The fluid flow is also affected by the response of the structure. The average drag coefficient for the CFD case is Cd=2.25 and the average drag coefficient for the FSI case is Cd=2.17. There is thus a slight decrease in the

drag coefficient for the FSI case of around 4%. This may be due to the ever so slight increase of the shape of the heliostat towards being streamlined as the top and bottom edges flex backwards.

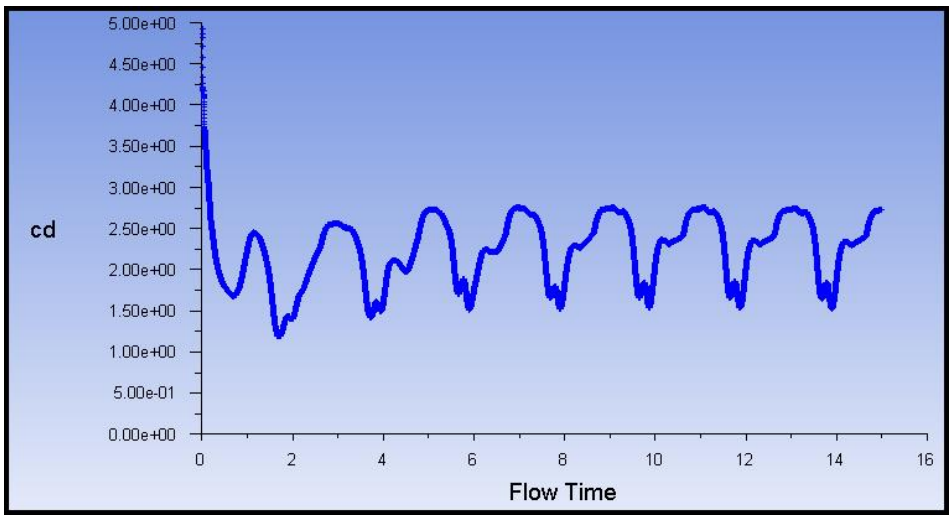

Figure 110: CFD simulation drag coefficient signal (seconds).

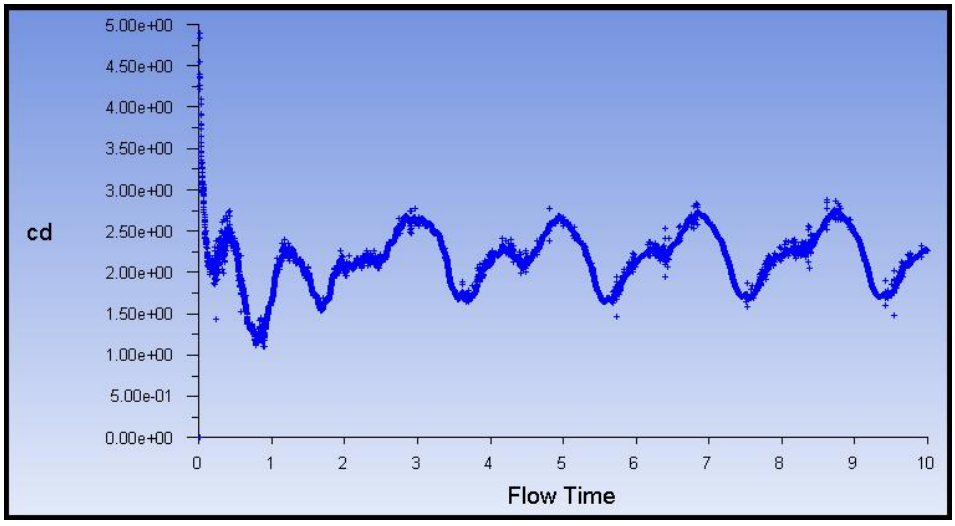

Figure 111: FSI simulation drag coefficient signal (seconds).

The transient structural results from the two-way FSI in Mechanical are seen below. The displacement of the top vertex of the mirror for the FSI simulation can be seen in Figure 128. The FFT of this displacement signal can be seen in Figure 129. The FFT shows that the dominant frequency present in the vertex displacement is a 0.53Hz signal, followed by a 1.07Hz signal and a 1.5Hz signal.

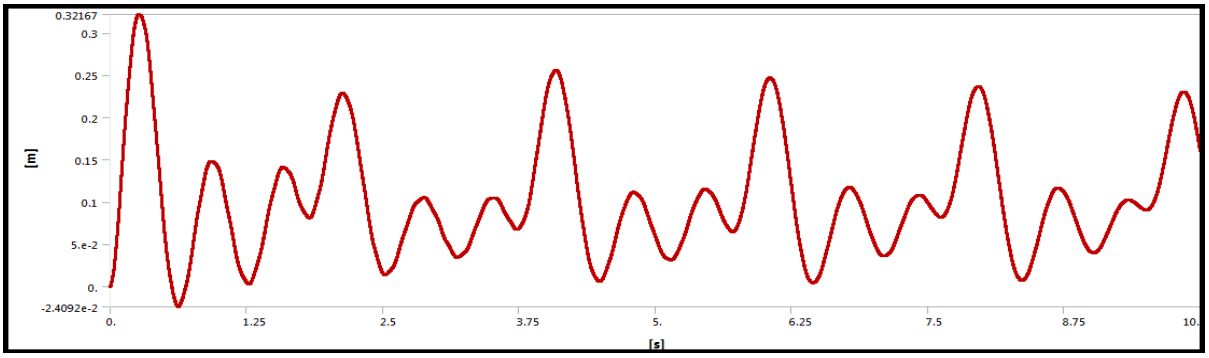

Figure 112: Displacement signal of the top mirror vertex in FSI.

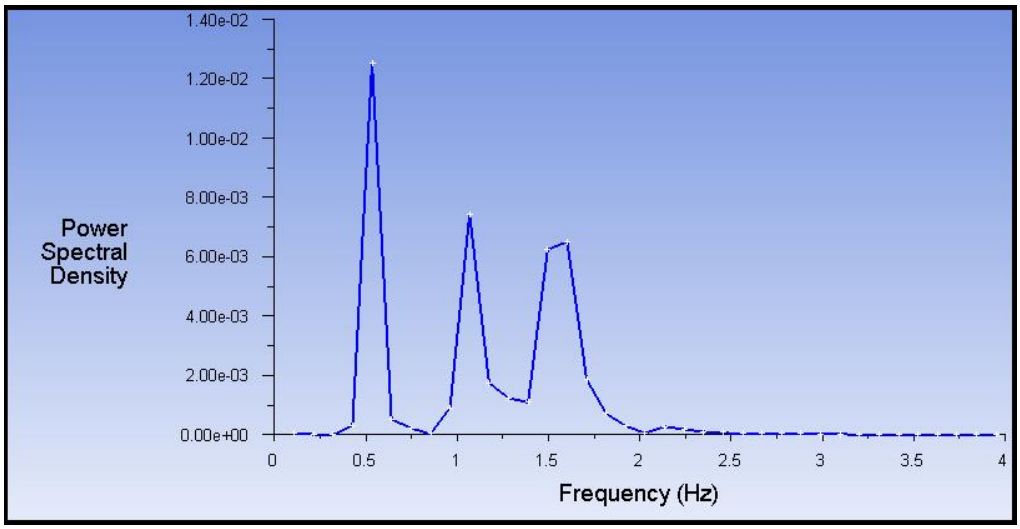

Figure 113: FFT of the vertex displacement signal.

A modal analysis was conducted on the 2D LH-2 heliostat in order to find the natural frequencies of the structure. Although the modes of the 2D structure differ drastically from the modes of the full 3D heliostat structure given in section 4.2, this still provides insight into the dynamic interaction between the fluid flow and the structural response. The first 10 modes of the 2D heliostat can be seen in Table 8. The first mode is the only mode of interest. This is the mode shape that occurs in the fluid flow and involves the top and bottom mirrors flexing symmetrically in a backward direction. The second mode shape has the exact same frequency but occurs when the bottom mirror flexes forward.

Mode	Frequency (Hz)
1	1.4806
2	1.4806
3	9.2785
4	9.2785
5	25.979
6	25.979
7	50.903
8	50.903
9	84.138
10	84.138

Table 8: First 10 modes of the 2D LH-2 heliostat structure.

Looking at the strictly 2D CFD FFT results performed on the LH-2 before the FSI simulation, the frequency content of 1.5Hz is visible and present in the velocity point and drag monitors. Looking then at the FSI structural results, particularly the FFT of the vertex displacement in Figure 129 above, this almost negligible frequency seems to excite the structure at this first mode. This demonstrates the negative effects that vortex shedding can have on a structure. Allowing this simulation to run further, the structural response of the heliostat may influence the flow to a point where the vortex shedding occurs at this modal frequency leading to catastrophic structural damage.

The first mode of the full-scale 3D LH-2 heliostat as provided in Table 6 in section 4.2 is 1.7807Hz. This is in the range of the first mode found here for the 2D heliostat. It is impossible to predict if the 3D heliostat would be affected in the same manner as the 2D heliostat to the vortex shedding simulated in the 2D CFD. The full 3D vortex shedding is considerably more complex and may have frequency content that excites one of the heliostats modes. The interaction between the 3D heliostat structure and the fluid needs to be simulated in a high fidelity manner in order to draw conclusions.

4.6 CONCLUSION

In this chapter the modal frequencies and shapes of the full-scale LH-2 heliostat were calculated. This provided insights into the frequencies of interest when dealing with the possible vortex shedding from the heliostats. A one-way FSI simulation was concluded which provides the mean forces on the heliostat structure. The equivalent stress and deformation can easily be calculated from this, providing helpful design insight for the heliostat. This is an easy and effective way of designing and possibly optimizing a preliminary heliostat. The CFD results from this simulation however confirmed, along with previous research done, that URANS CFD efforts are futile in resolving vortex shedding for these particular geometries in 3D. With this knowledge a 2D simulation of the work by (Matty, 1979) was performed. It was concluded that 2D CFD can resolve the major vortex shedding present for these flows.

The method was then extended to the geometry of the LH-2 heliostat in 2D. This provided reasonably promising results for the shedding frequencies that were in agreement with the (Matty, 1979) experimental results. Following this, a full two-way FSI simulation was conducted in order to get a better understanding of the interaction between the shed vortices in the fluid and the response of the structure to these vortices. Likewise, the response of the fluid to the movement of the structure is also important. The conclusions drawn from this were that for a small, seemingly insignificant frequency component present in the fluid, the structure can still be excited by this component near one of the modes of the structure, leading to potential structural damage. It can be said that a simple quick 2D CFD simulation can be used to resolve the major flow instability, namely vortex shedding for these geometries with URANS where 3D URANS fails. This is a helpful result in the design process as expensive wind tunnel experiments can be avoided during the design process and the structure's modes can be designed away from these frequencies.

The fact still persists that URANS cannot resolve the smaller flow structures present in a complex flow like this. These structures also have the ability to excite the heliostat in a negative manner. Due to this, SRS

modelling can be used to resolve 90% of the content of the flow and provide peace of mind in the design of a heliostat. This is the topic of the next chapter.

5 SCALE-RESOLVING SIMULATIONS

5.1 INTRODUCTION

In the previous work presented in the earlier chapters, the RANS modelling approach showed promise in predicting the mean loading on the heliostats. SRS methods are needed in order to resolve a significant portion of the turbulence spectrum as well as confirm the shedding frequency. SRS will also provide crucial peak loading information vital for the structural modelling of heliostats.

The advantage of SRS modelling is the ability to resolve fine turbulent scales and coherent structures. These smaller elements have the ability to excite the structure at frequencies other than the primary vortex shedding frequency. Another benefit of SRS is allowing an oscillating velocity profile to be specified at the inlet of the domain. This provides the generation of spatially coherent turbulence similar to that normally found in the ABL. These coherent structures in the approaching wind are the biggest contributors to peak wind loadings on the heliostats (Peterka, et al., 1986). The full-scale LH-2 heliostat is modelled in this chapter.

5.2 PRECURSOR RANS

The SRS model used in this research is the SBES model which combines LES and RANS capabilities with shielding functions and stress blending as discussed in the literature study. The benefit of SBES being a hybrid model is the fact that RANS is used to model the near-wall flows while LES resolves the larger turbulent eddies of importance to this research. The first step in conducting an accurate SRS simulation is performing a precursor RANS simulation. The RANS simulation uses the same mean velocity and turbulence inlet profiles and will allow judgements to be made regarding the suitability of the current mesh. The mesh is required to be fine enough to resolve the desired turbulent structures when the SBES model switches to LES.

According to (Menter, 2015) if the RANS simulation provides a meaningful solution then the main quantity of relevance when it comes to the suitability of the mesh in the LES region is the ratio between the integral length scale and the grid size. This is the third point as listed in the literature study given by (Gerasimov, 2016) when setting up an LES simulation. The equation for the integral length scale, the grid size and the ratio can be seen in Equation 70.

$$l_o = \frac{k^{0.5}}{C_\mu \omega} \quad ; \quad \Delta = \sqrt[3]{CellVolume} \quad ; \quad R = \frac{l_o}{\Delta} \tag{70}$$

According to (Gerasimov, 2016) a ratio of R=12.5 translates to approximately 90% of turbulent kinetic energy being resolved. When this ratio is plotted over the entire domain, areas where the ratio is lower than 12.5 indicate a mesh that is too coarse for that particular area in order to resolve up to 90% of the turbulence. In other words, a low ratio area (<12.5) in the mesh equates to a mesh region that could be refined before the SRS simulation is conducted. This ratio equates to having approximately 10-12 cells across a length scale to warrant 90% resolution. It should be noted that the equation used to obtain the cell size is a crude estimate and thus the ratio used here gives a rough but useful insight into the suitability of the mesh for SBES. Aiming for a 90% resolution of the turbulence is a fair goal. This is due to the bulk of the

turbulent structures of importance, that exhibit anisotropic behaviour and influence the flow and structure the most, are resolved well before this point.

In this section the SBES model is simulated on the precursor RANS mesh as well as the adapted refined fine mesh. Throughout this section the precursor RANS mesh is referred to as the coarse mesh and the adapted mesh is referred to as the fine mesh. Both meshes are used in the simulation of the 0^o and 60^o elevation angle cases. The first case is where the maximum drag would be experienced while the second case is where the maximum lift and torque tube moment is experienced. The precursor RANS mesh is used simply due to its availability as the predecessor to the fine mesh and its rapid solve time. The coarse mesh used for the precursor RANS simulation is the same mesh as seen in section 4.3 of this report. The mesh is a block-structured mesh having approximately 4.3 million cells. The fine mesh used is a regionally adapted version of the coarse mesh where the area around the heliostat extending into the wake is adapted with the final mesh containing approximately 27.8 million cells.

The precursor RANS simulation boundary conditions and numerical setup is identical to that used in section 4.3. The major difference being that the RANS model used is the SST k-ω. This thus becomes the underlying RANS model in the SBES model implemented in this section. The inlet has specified inlet velocity, turbulent kinetic energy and specific dissipation rate profiles prescribed via a UDF so as to model the ABL as noted in previous chapters.

A contour plot of the ratio between the integral length scale and the cell size is shown in Figure 130, for both the coarse and fine meshes. The contours are plotted up to a ratio R=12.5. This allows one to easily visualise the regions of the mesh that will not be able to resolve the turbulence to more than 90%. As seen in Figure 130A, the mesh in the coarse model has a region of concern in the shear layer, formed as a result of flow separation on both the top and bottom of the heliostat, as well as a large section in the wake where the mesh is evidently not fine enough. These sections diminish drastically as the mesh is refined to the fine mesh used as seen in Figure 130B. The fine mesh should be adequate in resolving most of the turbulence in the shear layer and wake. Highlighted in both plots however, is the heliostat structure, where the mesh resolution is not adequate. This is not of concern as the RANS portion of the SBES model will be used to model this. Another area where care needs to be considered is upstream of the heliostat on the ground plane. It should be confirmed that this area is not too heavily modelled by RANS and that the synthetic turbulent structures created by the vortex method reach the bottom section of the heliostat.

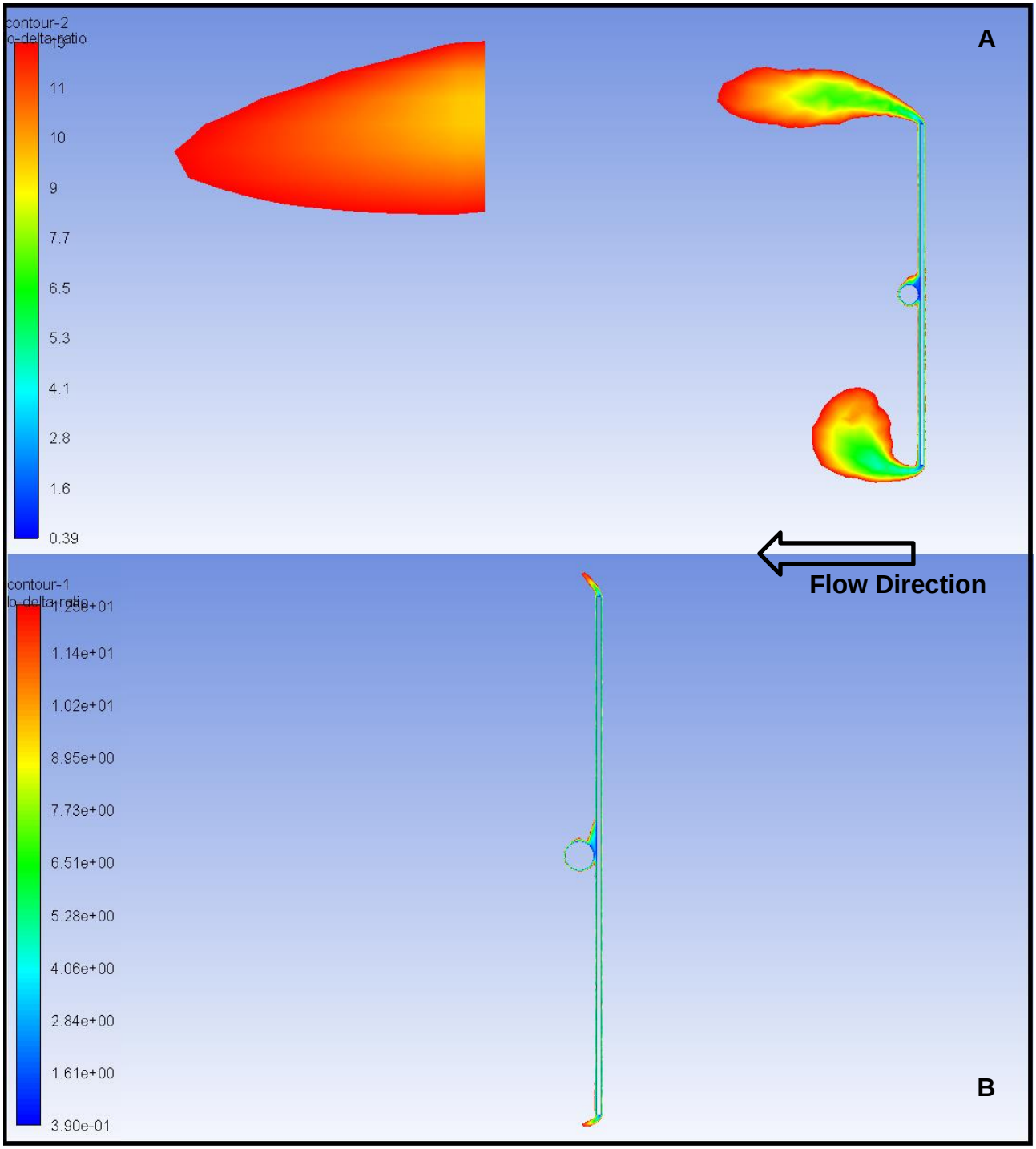

Figure 114: Contour plots showing the ratio between integral length scale to cell size up to a value of R = 12.5 A) coarse mesh B) fine mesh.

After the mesh resolution is studied, the time step size that is required in order to achieve an accurate solution using SBES can be investigated and gained from the precursor RANS. The time step should be selected so as to achieve a Courant number (CFL number) of one or below. The CFL number can be seen as the number of computational cells the flow will pass through in a single time step. The CFL number can be seen in Equation 71. The temporal resolution should match or exceed the spatial resolution. Good practice

to account for the differences between instantaneous and averaged velocities as well as for the errors introduced from RANS is to use a CFL number of 0.5 or less.

$$CourantNumber = \frac{U\Delta t}{\sqrt[3]{CellVolume}} = 0.5 \tag{71}$$

In Figure 131, a contour plot of the estimated time step size, limited to a value of 0.05s is presented for the fine mesh. Evident from the plot is that the lowest required time step size to ensure a CFL number of approximately 1 is 0.000368s. The time step used in the fine mesh SBES simulation is 0.0003s. The coarse mesh time step is set to 0.0008s, this adds an additional buffer to ensure that the CFL value does not exceed 1.

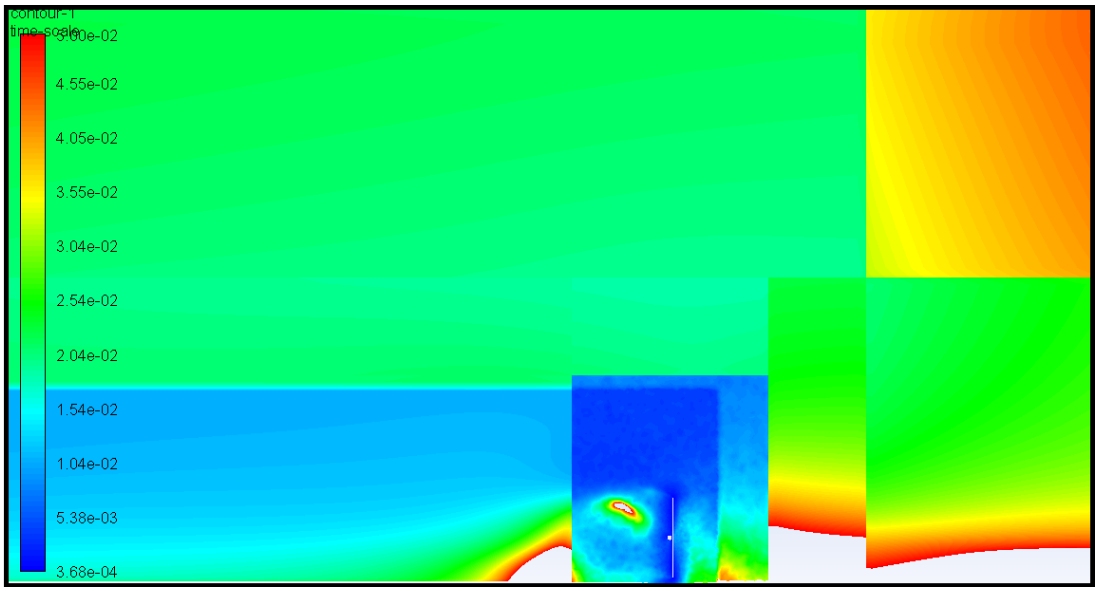

Figure 115: Contour plot of the estimated time step size for the fine mesh, limited to 0.05s.

The spatial and temporal estimates gained from the precursor RANS simulation provide a good starting point for the SBES simulation. Optimal settings are required for the SBES simulation in order to obtain useful and accurate results for the transient peak wind loadings on the heliostat. Once the precursor RANS simulations have been completed and the spatial and temporal estimates are satisfactory, the SBES simulation can be set up and implemented. The vortex method is implemented in order to generate the synthetic turbulence in the form of velocity perturbations that are added at the inlet of the domain. As stipulated by (Gerasimov, 2016), the number of vortices prescribed is set to 1825, providing approximately four vortices for every four cells on the inlet face. The SIMPLEC pressure-velocity coupling scheme is employed. The settings for the spatial discretisation are changed from the usual RANS settings implemented previously. Bounded Central Differencing (BCD) is used for the momentum discretisation with the Bounded Second-Order Implicit transient formulation used along with higher-order term relaxation. The sub-grid scale model used in the SBES simulation is the WALE model. The sub-grid scale stresses from the filtering operation are unknown and need to be modelled. In ANSYS Fluent the sub-grid scale models employ the Boussinesq hypothesis similarly to the RANS models.

The benefit of SRS modelling is the ability to resolve the turbulence spectrum to a limit defined by the grid size. The energy cascade present in turbulent flows, describes how the larger eddies have an anisotropic

nature. This makes it important for them to be resolved as they are normally the structures that play the most significant role in the fluid flow in terms of influencing other structures as they contain the most amount of kinetic energy. Following from these large scales is the inertial subrange, where the turbulent kinetic energy is transferred to smaller and smaller scales. The eddies in this range are statistically isotropic, meaning that they are inherently easier to model. After the inertial subrange is the dissipation range, where the fluid's viscosity dissipates the remaining energy of the turbulence. The grid size implemented in the simulation will define the amount of the inertial subrange that is resolved by LES and the amount that is modelled by the SGS model. The turbulent kinetic energy spectrum can be seen on the graph in Figure 132. According to Kolmogorov's law, the slope of the inertial subrange can be found to be -5/3, this can be confirmed with dimensional analysis.

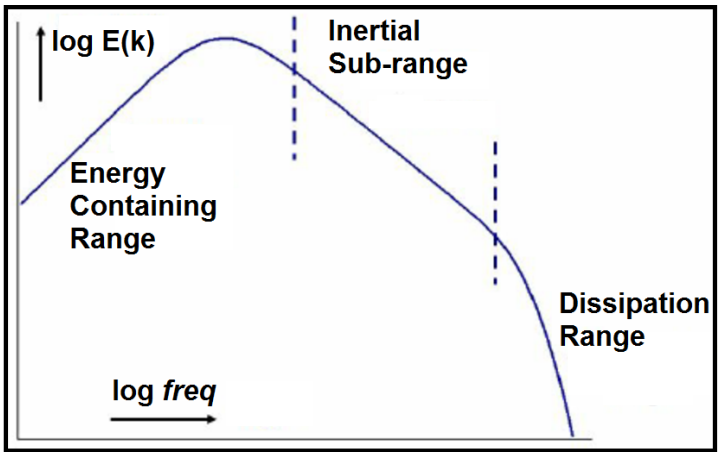

Figure 116: Turbulent kinetic energy spectrum.

To confirm that the vortex method is generating the required level of turbulence and that the turbulence is being resolved adequately with LES, the turbulence spectrum of the freestream flow is plotted below in Figure 133 for both the coarse and fine mesh. The freestream is quantified by the temporal streamwise velocity profile of a monitor point 5m upstream of the full-scale heliostat.

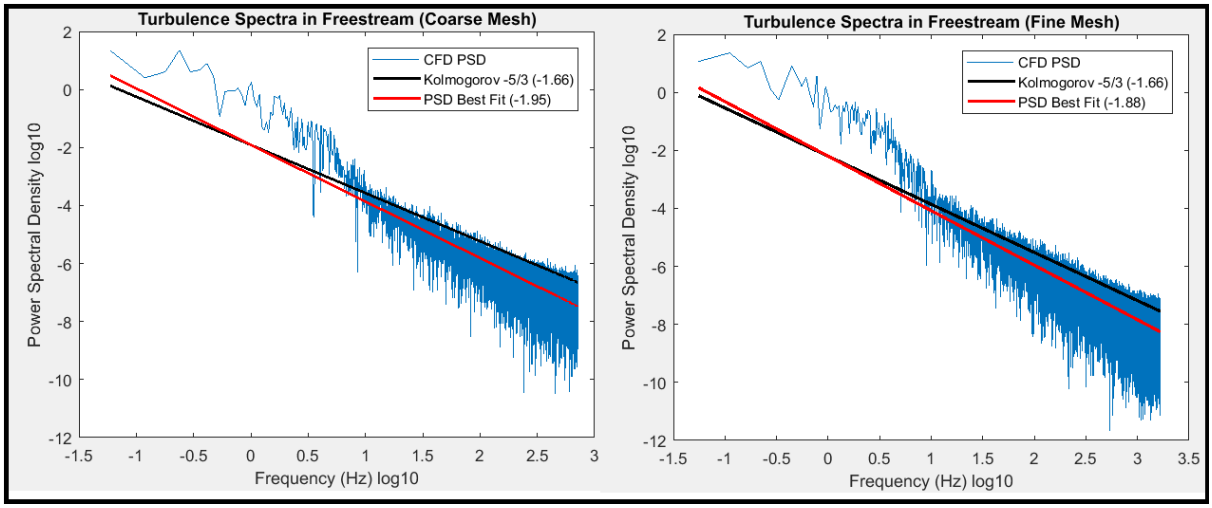

Figure 117: Freestream turbulence spectra for coarse and fine mesh.

The agreement of both the coarse and fine mesh slopes with the Kolmogorov slope is evident. Also evident is the increase in accuracy with the mesh refinement. As stated previously, only minor mesh refinement was conducted in the upstream region of the mesh with the majority of the refinement focused around the heliostat and wake region. Perhaps with further refinement of the upstream region a better approximation to the Kolmogorov law can be achieved.

For these SBES simulations run on the Lengau cluster of the Centre for High Performance Computing (CHPC) using 248 Intel Xeon 2.6 GHz processors, 1 second of real time flow took approximately 48 hours. In contrast to 1 hour computational time for one second of real time flow using URANS on an Intel i-7 2630QM 2 GHz processor.

5.3 SRS RESULTS

The SRS SBES results are shown below for both the coarse and fine meshes. It should be noted that, as seen in Figure 130, that the coarse mesh is highly inadequate when resolving the flow. For this reason, the coarse mesh results are displayed and used merely as a comparison aid between a good RANS mesh SBES result (coarse mesh) and a good SRS mesh SBES (fine mesh) result. It is ensured that the scale residuals converge to $1e^{-4}$ within 50 iterations per time-step. For the fine mesh 0 degree case, the iteration count occasionally neared the 50 mark. In order to decrease the simulation time of the 60 degree fine mesh case, the convergence limit for the continuity (the limiting residual) was decreased to $5e^{-4}$. In order to visualise the coherent turbulent structures of the flow, iso-surfaces of the Q-criterion are plotted, coloured by velocity magnitude. The Q-criterion is defined as:

$$Q = \frac{1}{2}\left(\Omega^2 - \mathrm{S}^2\right) \tag{72}$$

where:
$\Omega = Vorticity\ rate$
S= Strain rate

A comparison between the coarse and fine mesh for both the 0 and 60 degree cases is shown below.

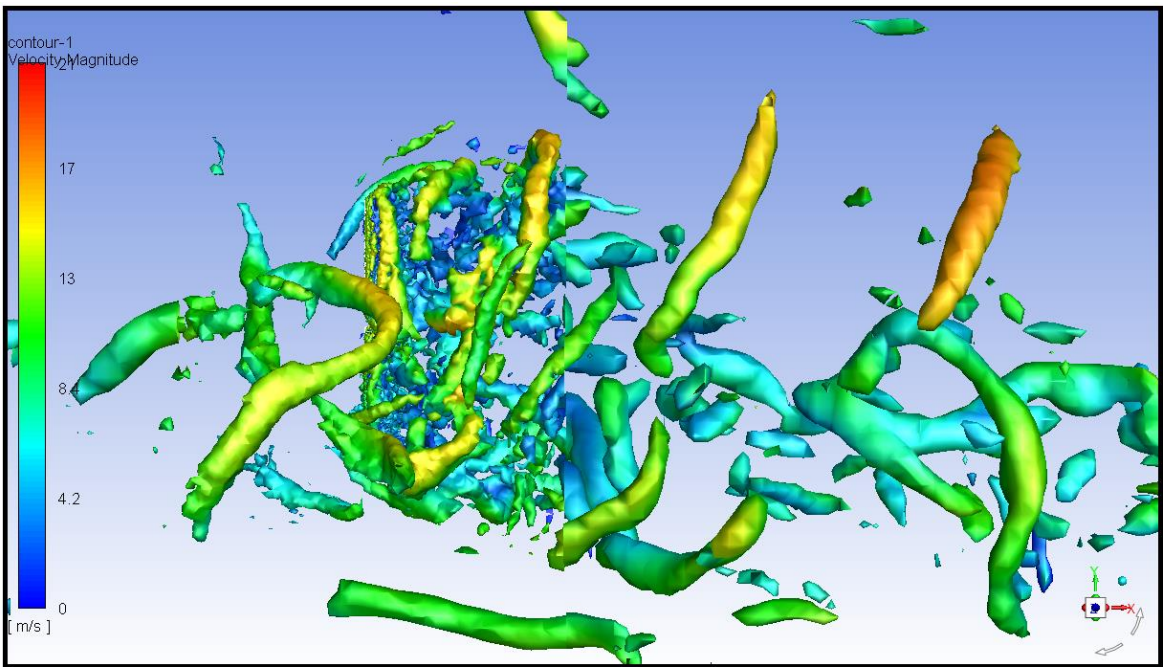

Figure 118: Iso-Surfaces of Q-criterion coloured by velocity magnitude of SBES coarse mesh 0 degree ($Q=100s^{-2}$).

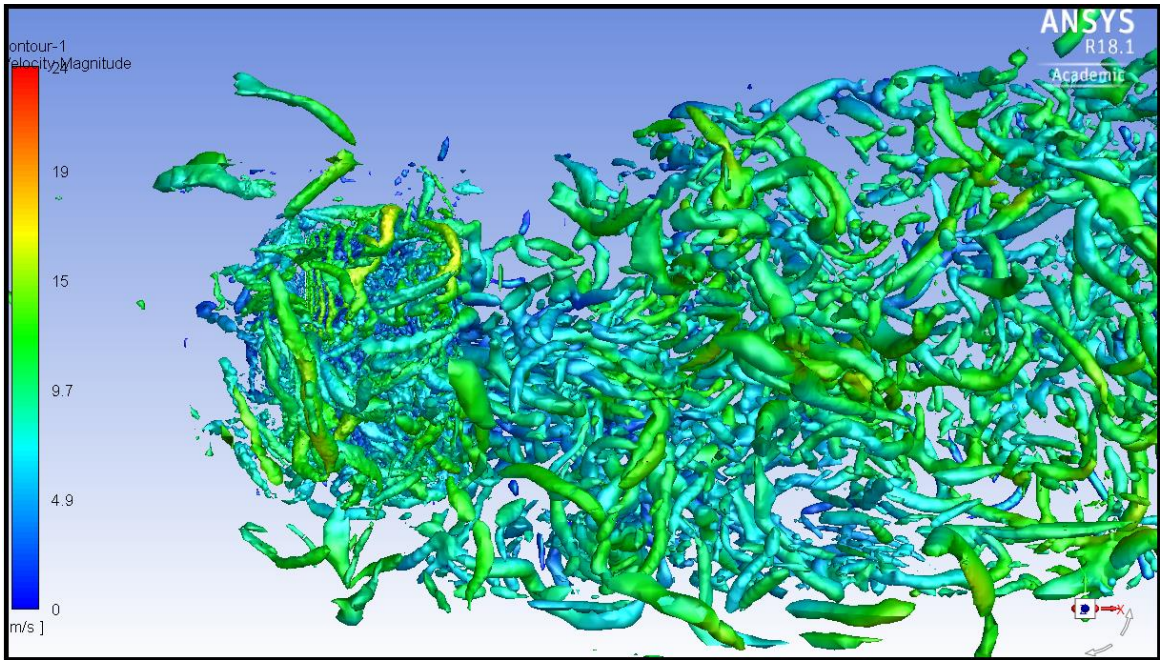

Figure 119: Iso-Surfaces of Q-criterion coloured by velocity magnitude of SBES fine mesh 0 degree ($Q=100s^{-2}$).

As can be seen from the comparison between the coarse and fine mesh shown in Figures 134 and 135, respectively, where the Q-criterion displays the coherent vortical structures of the flow, there exists a far greater amount of detail in the fine mesh. The smaller structures present in the fine mesh are important as they still have the ability to influence the heliostat. The fine mesh provides the SBES model the ability to resolve these small structures that are shed from the edges of the heliostat mirrors that will in turn influence the LH-2. An isometric view in Figure 136 of the 0 degree fine case provides information as to the turbulent nature of the wake behind the heliostat.

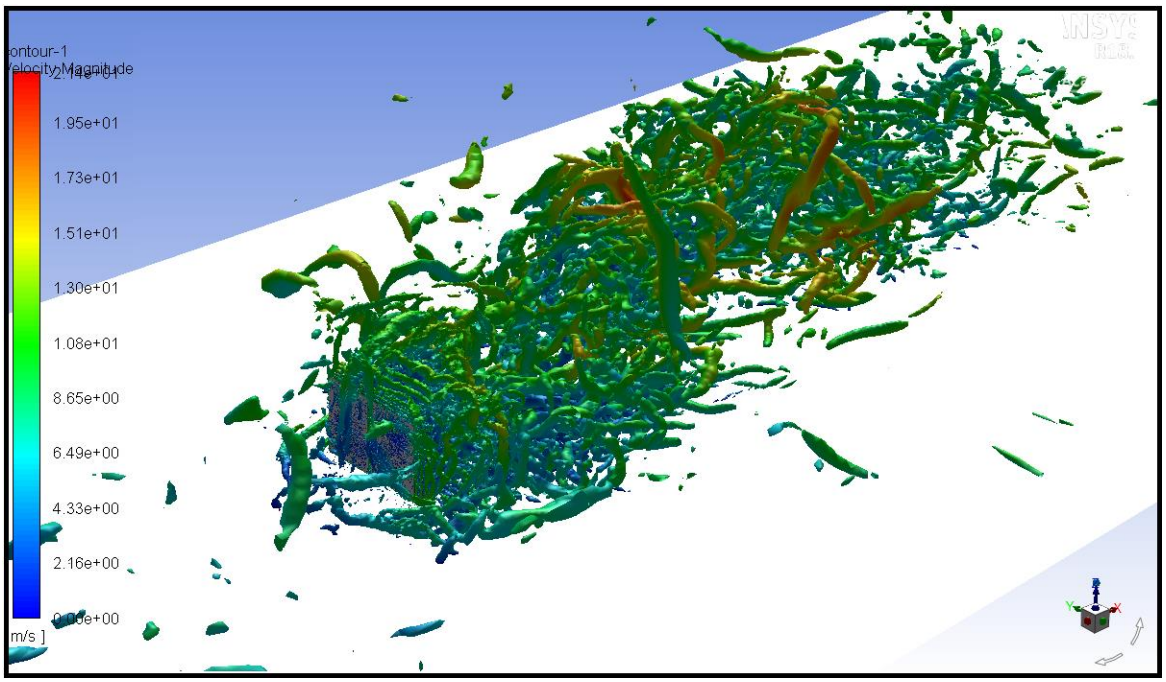

Figure 120: Isometric Iso-Surfaces of Q-criterion coloured by velocity magnitude of SBES fine mesh 0 degree (Q=100s^{-2}).

Figure 137 below shows a close-up isometric view of the 0 degree fine mesh Q-criterion iso-surfaces. The vortical structures being shed from the edges of the heliostat mirrors are clearly evident. They can be seen breaking away and interacting with the wake flow. The same vortical structures can be seem shedding from the edges of the heliostat in the 60 degree fine mesh case as shown in Figure 138. The smaller eddies are visualized using higher Q-criterion values.

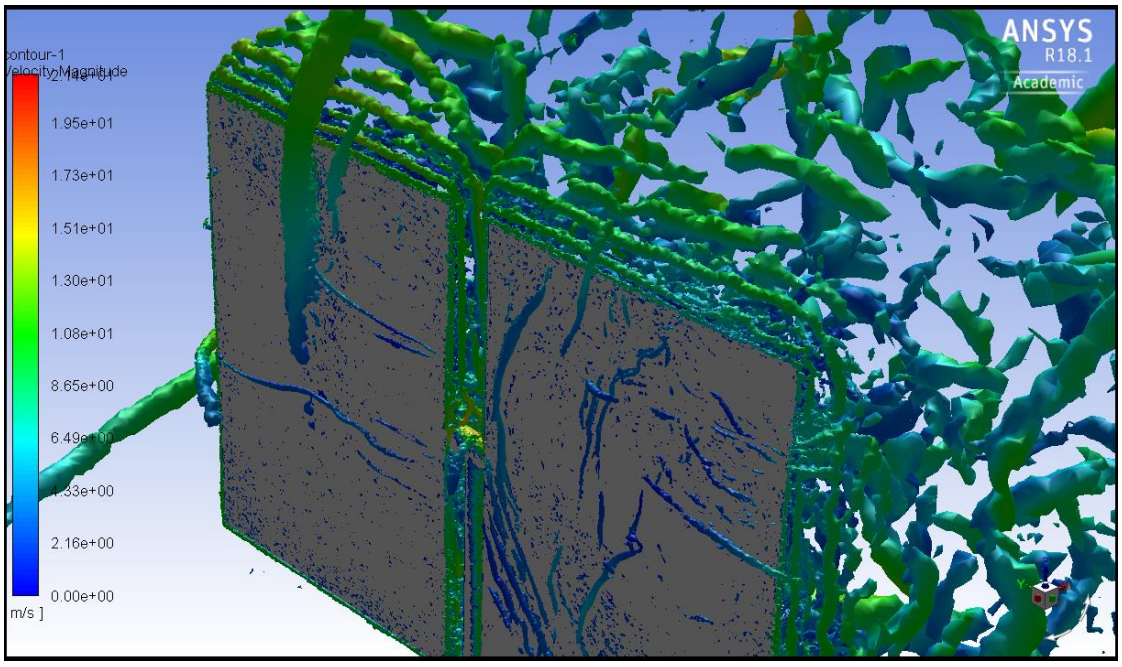

Figure 121: Isometric Iso-Surfaces of Q-criterion coloured by velocity magnitude of SBES fine mesh 0 degree (Q=1000s^{-2}).

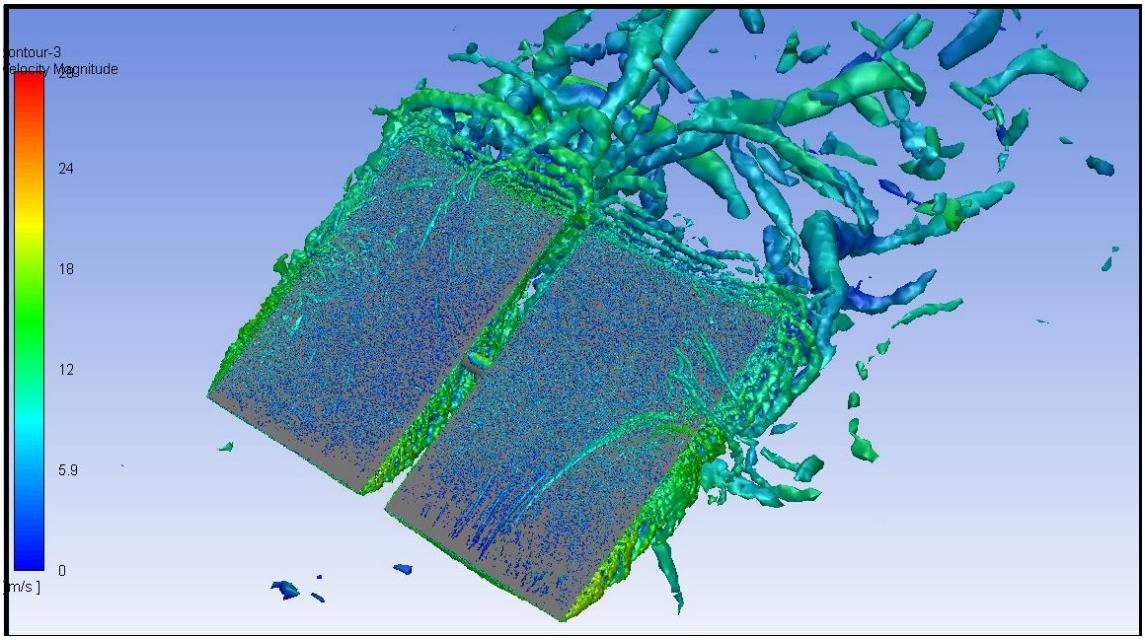

Figure 122: Isometric Iso-Surfaces of Q-criterion coloured by velocity magnitude of SBES fine mesh 60 degree ($Q=500s^{-2}$).

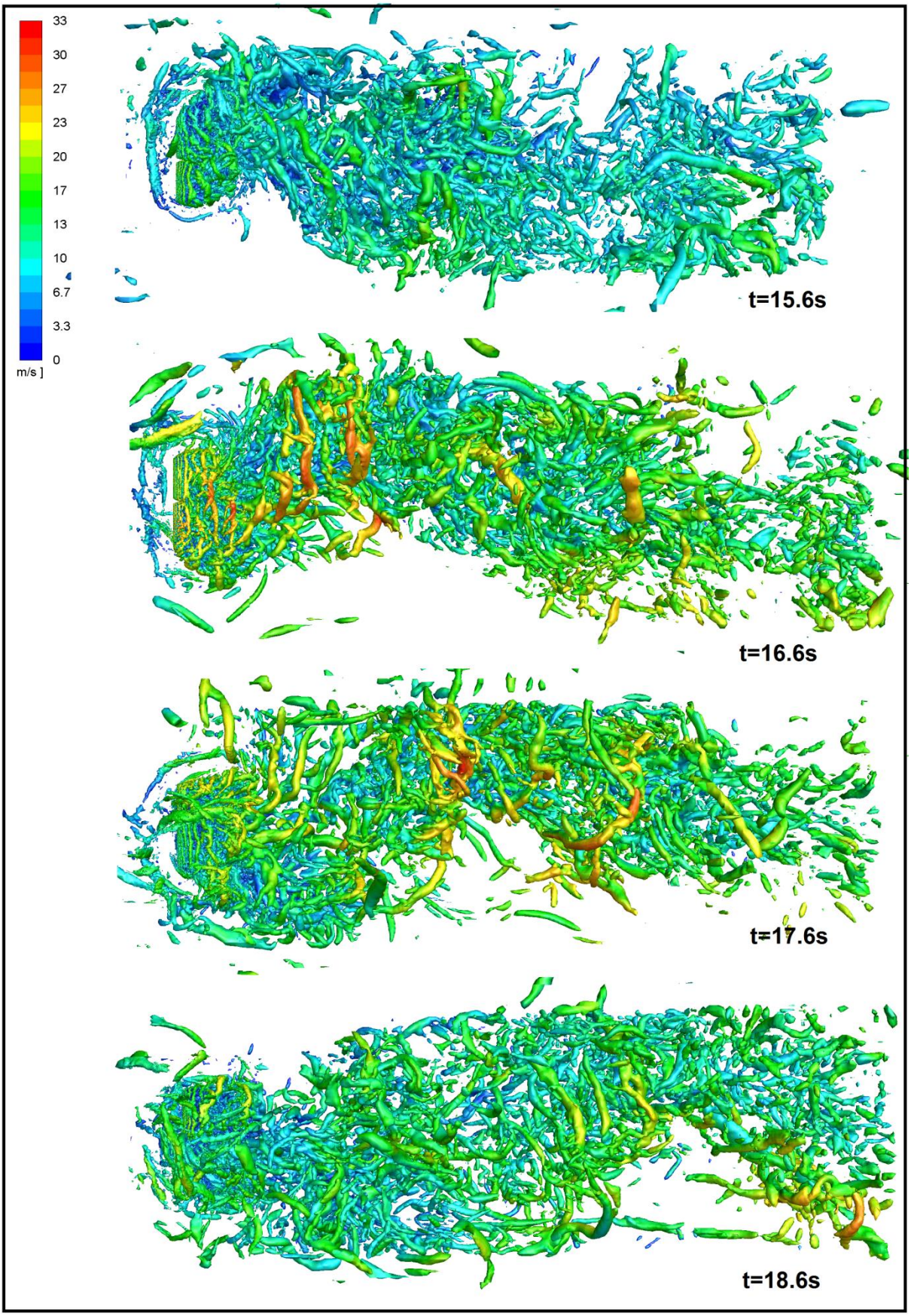

Figure 123: Iso-Surfaces of Q-criterion coloured by velocity magnitude of SBES fine mesh 0 degree over 4 seconds ($Q=100s^{-2}$).

In Figure 139 a Q-criterion plot of the flow in the wake of the heliostat is displayed at different times. This illustrates how the flow and fluid structures in the wake change. What can be easily seen is the change in the direction of the entire wake from 16.6 seconds to 18.6 seconds. This demonstrates the complex nature of the wake flow in the fact that there exist multiple avenues for the heliostat to be excited. These range from the smaller vortices shed from the mirror edges (Figure 137) to the much larger motion of the entire wake due to vortex shedding (Figure 139). From a global glance at this figure, one can discern a snake-like oscillatory behaviour of the flow in the wake, of which the period can be determined and compared to the FFT of a monitor point velocity in the wake.

The aim of performing SRS simulations of the LH-2 heliostat is to obtain transient loadings on the structure as well as peak loadings and to determine the main frequencies present in the vortex shedding in order to design away from potential structural damage and self-excitation. The advantage of using SRS models is the ability to have upstream turbulence present in the flow. As previously discussed, the vortex method is used to generate the synthetic turbulence at the inlet. This consequently means that there is already frequency content in the flow that may influence the heliostat regardless of the downstream behaviour and vortex shedding. This will be investigated later in the chapter.

The results of the fine mesh 0 and 60 degree cases are shown below. These include the velocity magnitude point monitor in the wake of the flow and drag coefficient for both cases. The position of the wake velocity magnitude monitor point is x = 14m and y = 1.9m (Seen as the red dot in Figure 106). The lift coefficient and the torque-tube moment coefficient are displayed for the 60 degree case.

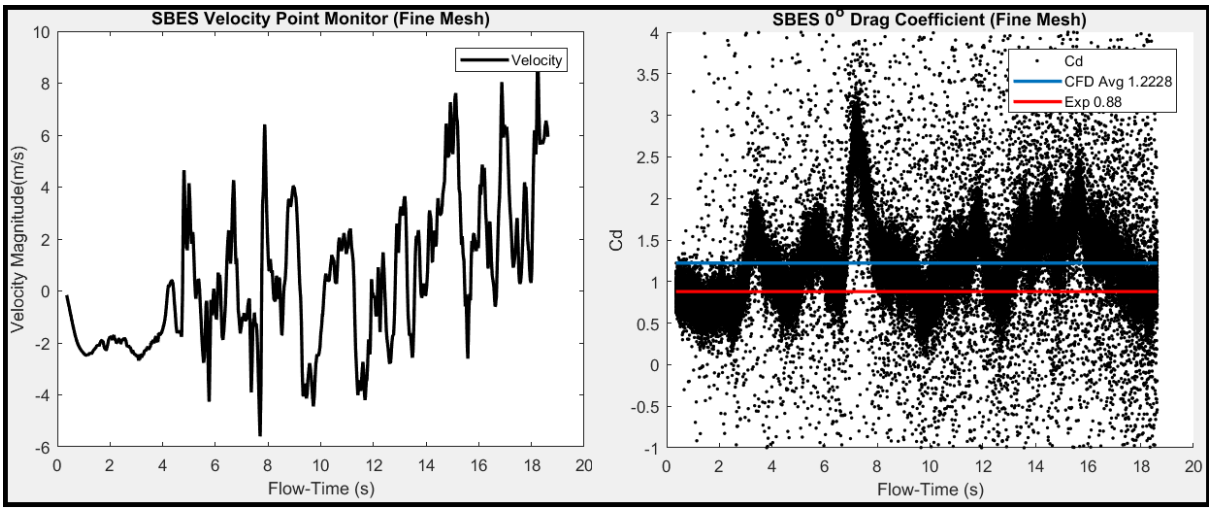

Figure 124: Velocity magnitude in wake and drag coefficient results for 0 degree fine mesh.

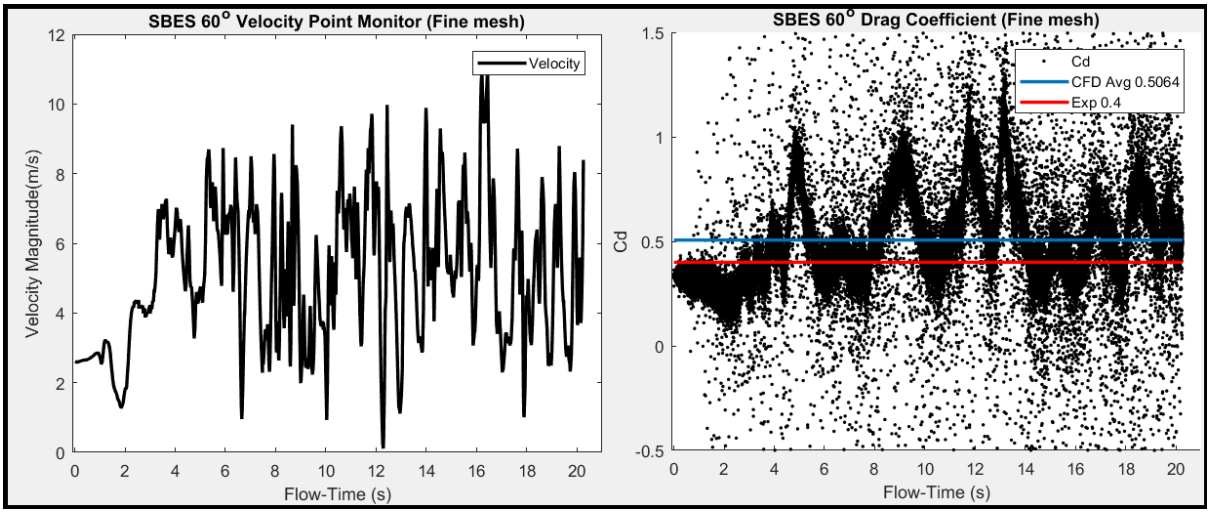

Figure 125: Velocity magnitude in wake and drag coefficient results for 60 degree fine mesh.

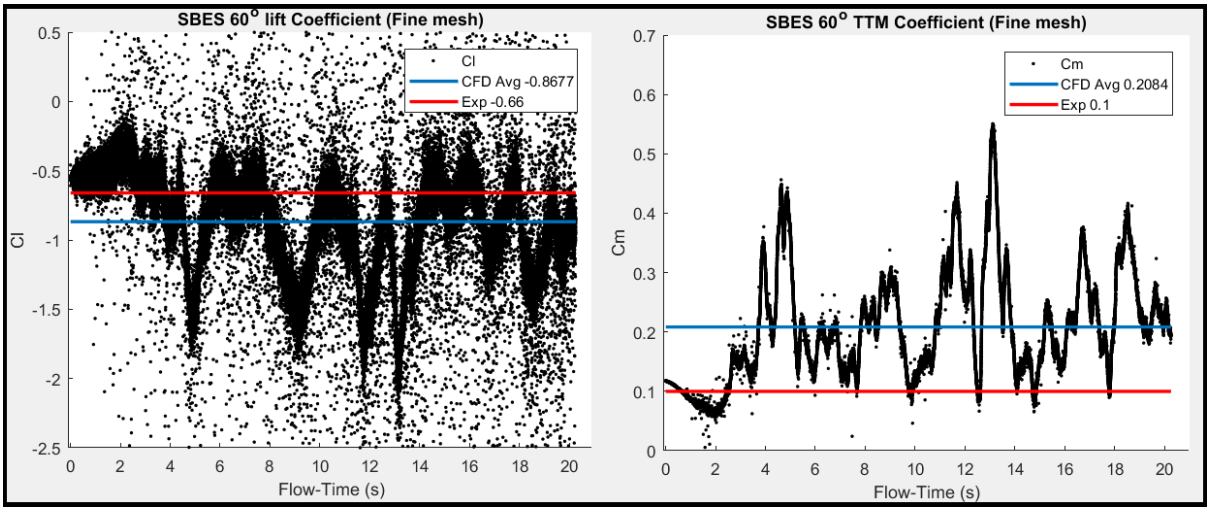

Figure 126: Lift coefficient and torque-tube moment coefficient results for 60 degree fine mesh.

The fine mesh drag coefficient results for the 0 degree case are from 0 seconds to 19 seconds. The first observation from Figures 140 and 141 is that the simulations probably need to be run longer for the average values to converge. Nevertheless, given the cost of the simulations, some trends in average values can be seen. The mean drag coefficient value for the period is 1.223. The deviation from the experimental mean value is 28%. Visible in the drag coefficient plots is the very sporadic nature of the points. These spurious outlying points are believed to be caused by the vortex method. They are most likely non-physical pressure fluctuations that should not exist. More research needs to be conducted on this phenomena but that goes beyond the scope of this research. The rather large deviation between the SBES and experimental flow results seen in the fine mesh is most likely due to the need for further run time as the flow field is only just developing. Another reason for this nonconformity is due to the uncertainty in the turbulence intensities prevalent in the experimental tests. Looking at the velocity monitor point plots, the abundant amount of frequency content present in the flow is evident. This content is only possible with SRS modelling.

The 60 degree drag coefficient deviation from the experiment is 21%, lift coefficient is 24% and the torque-tube moment coefficient is 51%. The reasons for these deviations will be discussed later in this chapter. The coarse mesh results can be seen in Appendix E.

Shown in Figure 143 is the fine mesh drag coefficient signal compared with the coarse mesh signal for the 0 degree case. The mean of both signals is shown along with the Root Mean Square (RMS) and Standard Deviation (SD) of the signals. The fine mesh is able to capture the peaks of the signal better than the coarse mesh. This is evident simply by looking at the signal but can be confirmed by the higher RMS value. The RMS value gives the square root of the mean data squared thus providing an indication of the mean taking into account and giving emphasis to the peak values. The SD value also shows that the fluctuation of the fine mesh data is far greater than the coarse mesh result, evidence of the peak forces and turbulence being better resolved and captured. There is a much greater amount of frequency content visible in the fine mesh signal. This is again indicative of the superior capabilities of the fine mesh to resolve a greater amount of turbulent content in the flow, compared to the coarse mesh. The increase in the drag coefficient can be attributed to the increase in the size of the peaks of the force.

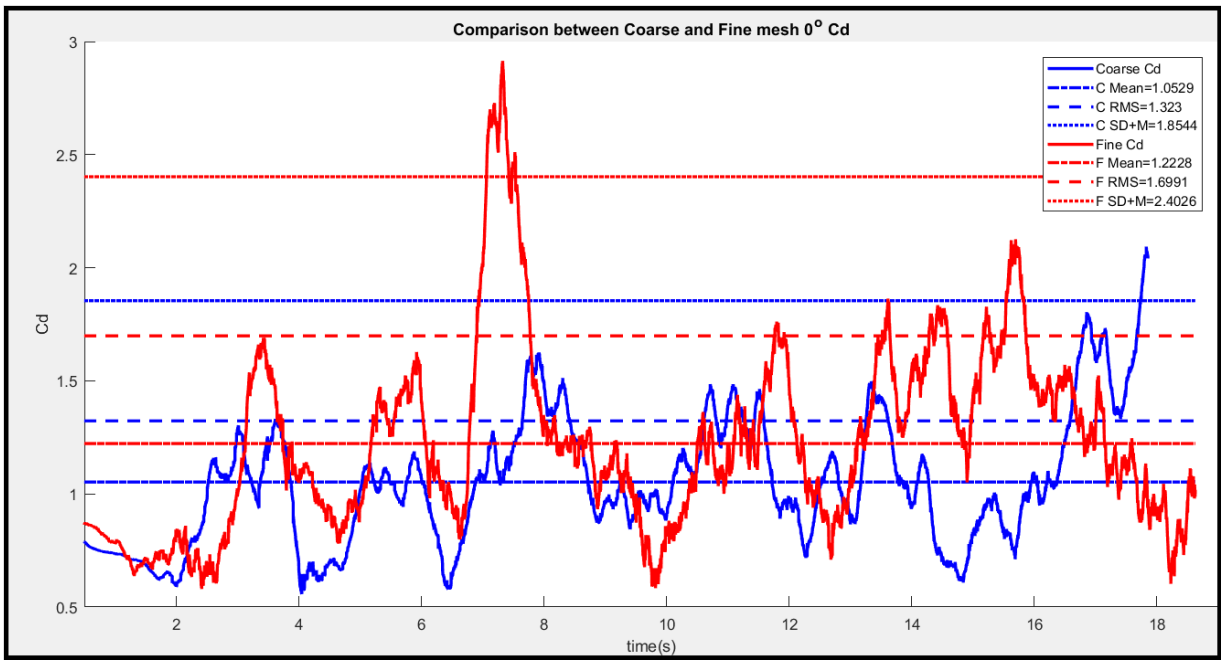

Figure 127: Comparison between Coarse and Fine mesh 0deg Cd.

The 60 degree case is compared in Figure 144 for the fine and coarse mesh. This case perhaps reveals the advantage of the fine mesh over the coarse mesh better than the 0 degree case. The mean value for the drag coefficient is comparable as seen by the proximity of the mean Cd lines. However both the RMS and SD values for the fine mesh are significantly higher than that of the coarse mesh. This once again demonstrates the capabilities of the fine mesh in resolving the peak loadings on the heliostat.

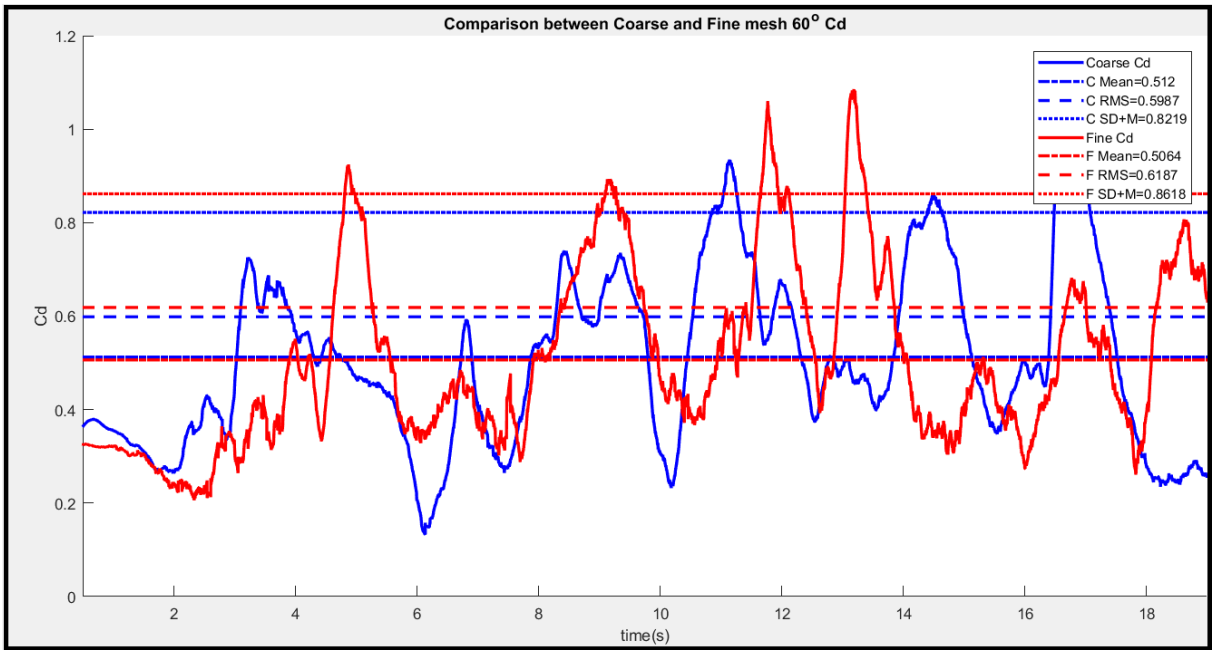

Figure 128: Comparison between Coarse and Fine mesh 60deg Cd.

In Figure 145 the torque-tube moment coefficient signals can be seen. The fine mesh result has a mean value of 0.2084. While this value deviates from the experimental value by some margin, it is very comparable to the results of (Peterka, 1989). In the results from (Peterka, 1989), the mean torque-tube moment coefficient is given as 0.27 while the peak value is given as 0.6. In the uncertainty of the results of (Huss, 2011) this provides some validity to the SBES results as the Peterka heliostat is comparable to the LH-2.

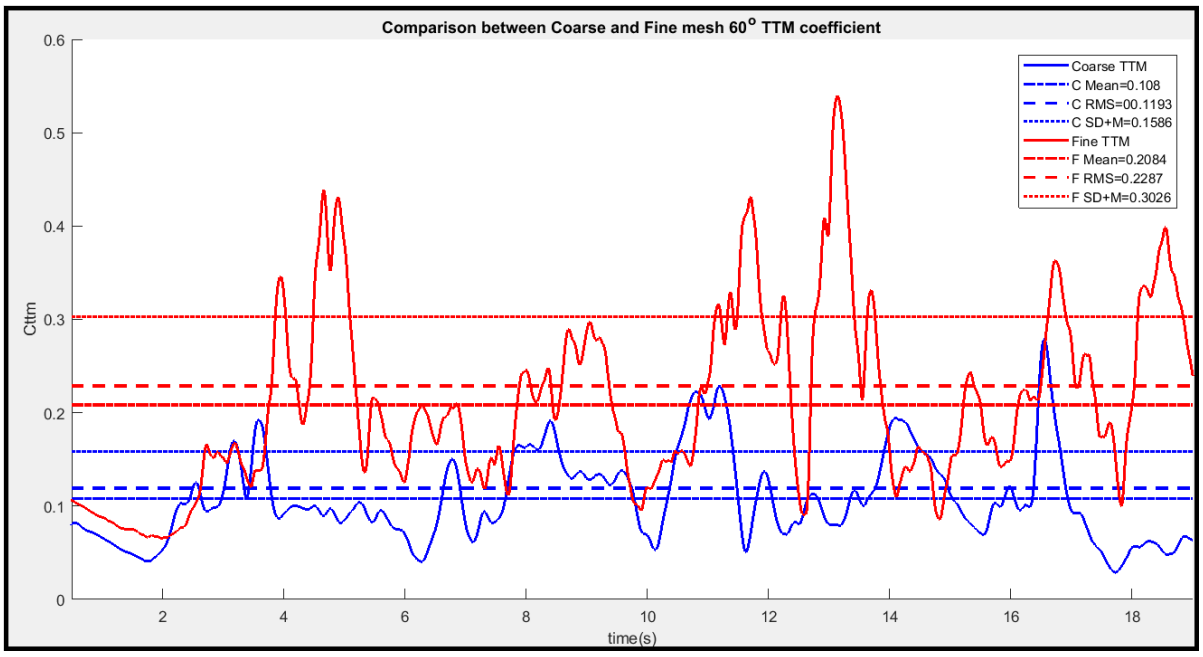

Figure 129: Comparison between Coarse and Fine mesh torque-tube moment coefficient.

The SBES CFD results have a sample rate of 3333.3Hz, (Huss, et al., 2011) fails to give a data sampling rate. (Peterka, et al., 1986) wind tunnel results are sampled at a rate of 18Hz. Shown in Figure 145 are the results for the drag coefficient of the 0 degree fine mesh case where filtering has been applied and the comparison between the original 3333Hz signal and the filtered 18Hz signal can be seen. The filtered results in this case provide a slightly higher drag than the original results and it can be said that no substantial difference is achieved with filtering.

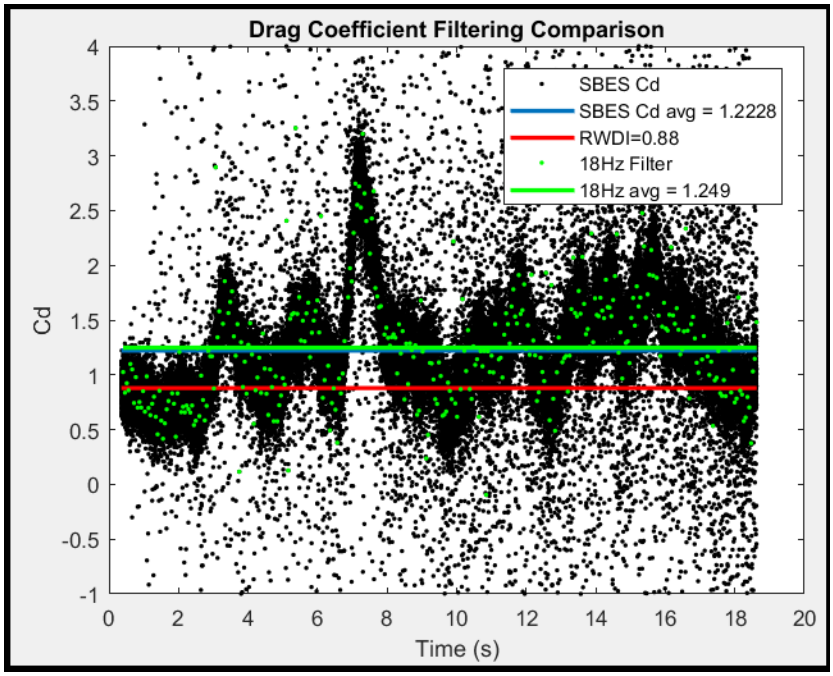

Figure 130: Drag coefficient filtering comparison, 0 degree fine mesh.

Modelling the ABL with SBES also leads to horizontal homogeneity problems. The x-direction turbulence intensity profile prescribed at the inlet as well as at 5m upwind from the heliostat can be seen in Figure 147 compared to the ABL profile of Peterka (1986). The intensity specified at the inlet HCL is 20%. By the time the profile makes contact with the heliostat the turbulence intensity on the bottom side of the mirror is a percentage greater. This is one possible reason for the disagreement between the experimental torque-tube moment coefficient value and the SBES value. According to (Peterka, 1989), a slight difference in the turbulence intensity can lead to a massive difference in the aerodynamic coefficient values. A difference of 18% in the turbulence intensity of the torque-tube moment coefficient can lead to a difference of 81% in that coefficient (Peterka, et al., 1989). It should be noted that the wind tunnel results obtained by RWDI are not entirely trusted in the fact that the experimental information is not fully available. No profile information is available and no data on the turbulence intensity levels downstream from the inlet of the wind tunnel are provided (Huss, et al., 2011). (Peterka, 1989) shows that a difference in turbulence intensity of 17% can lead to a 42% difference in the drag coefficient. This is an area of concern considering no profile data is given for (Huss, et al., 2011) and the accuracy of the results are inconclusive. Noteworthy is the fact that Huss et al. (2011) states that the turbulence intensity of 20% is achieved in the wind tunnel at the inlet of the tunnel at the scale HCL. As stated earlier, whether this intensity is achieved downstream at the heliostat and whether the full-scale result is comparable is unknown. The SBES inlet turbulence intensity profile matches fairly well with that of Peterka (1986) and can be seen to change as it is

transported downstream due to the synthetic turbulence generated via the vortex method. The shape of the profile that makes contact with the heliostat is still very respectable and the horizontal homogeneity is acceptable due to the fact that the HCL turbulence intensity value remains constant.

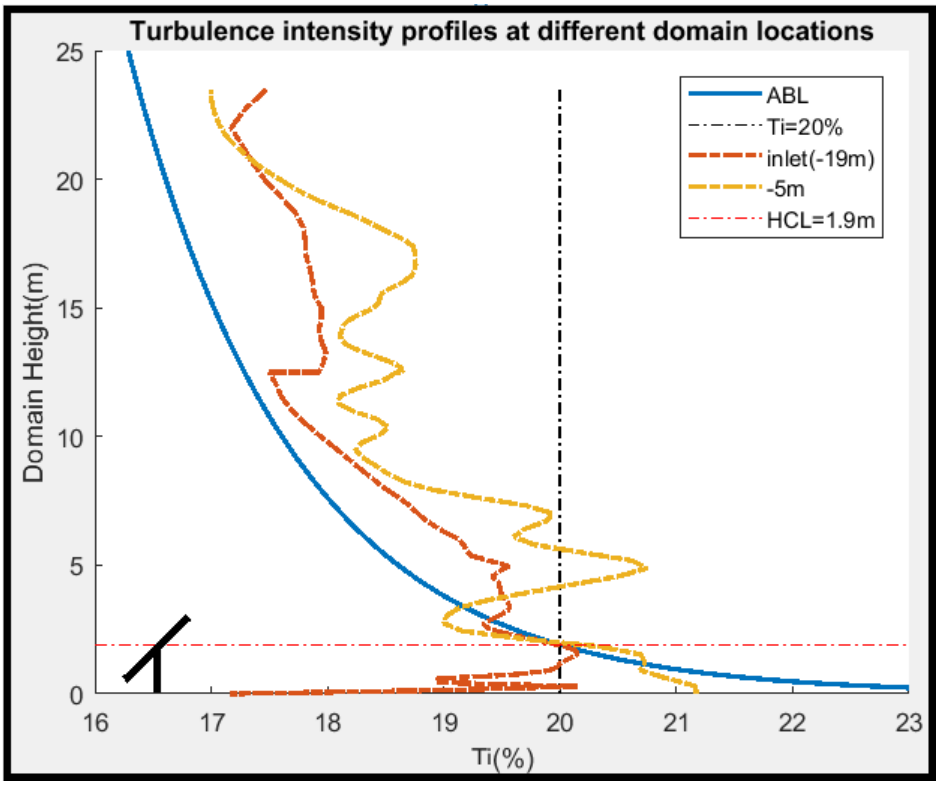

Figure 131: Turbulence Intensity profiles at different domain locations compared to RWDI.

In Figure 148, the 0 and 60 degree drag coefficients for both the coarse and fine mesh are compared to the 0, 30 and 60 degree results of Peterka (1986). The mean value of the experimental results is shown along with the maximum and minimum drag values. The SBES simulation points are shown with the corresponding standard deviations for the coarse and fine meshes. This is plotted as an additional means of validating the SBES results. The fine mesh mean SBES drag lies almost exactly on the experimental mean. The coarse SBES results are also fairly close to the experimental mean. Interestingly though and as shown previously, the fine mesh variation is considerably greater than that of the coarse mesh for the 0 degree case and is fairly comparable to the upper peak value of Peterka (1986). The data for the 60 degree case are almost identical between the fine mesh, coarse mesh and experimental values. This demonstrates that the SBES CFD simulation results are believable and can be trusted.

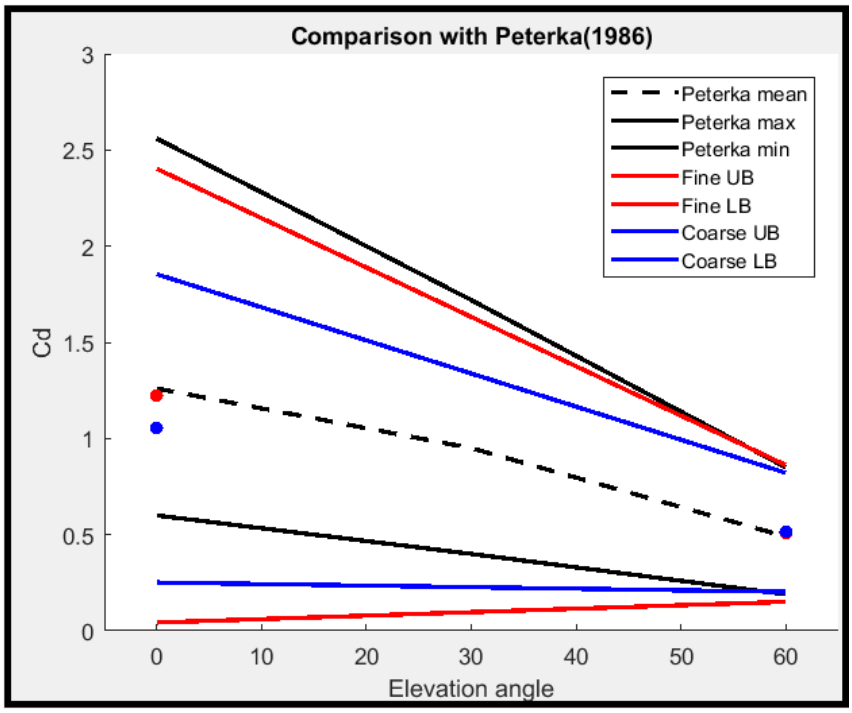

Figure 132: SBES drag coefficient results compared to (Peterka, 1986).

FFT's of the SBES flow cases are given below and compared with the 2D URANS cases presented in chapter 4. In Figure 149, the upwind freestream streamwise velocity FFT is shown at x = -5m and y = 1.9m. This FFT shows the frequency content present in the flow generated by the vortex method, similarly to Figure 133, but without log scales used on the axes. As can be seen there is low frequency content in the freestream flow that may influence the response of the heliostat regardless of vortex shedding. This low frequency content is representative of the larger energy containing turbulent structures in the flow. Comparing the FFT's for the upstream velocity and the wake velocity point monitors (Figure 151, 153), it can be seen that some of the very low frequency content still exists in the wake of the flow, as would be expected. The 0.444Hz spike seen in the upstream flow is shifted to 0.499Hz in the drag coefficient. This 0.499Hz is the vortex shedding frequency from the LH-2 heliostat at 0 degrees.

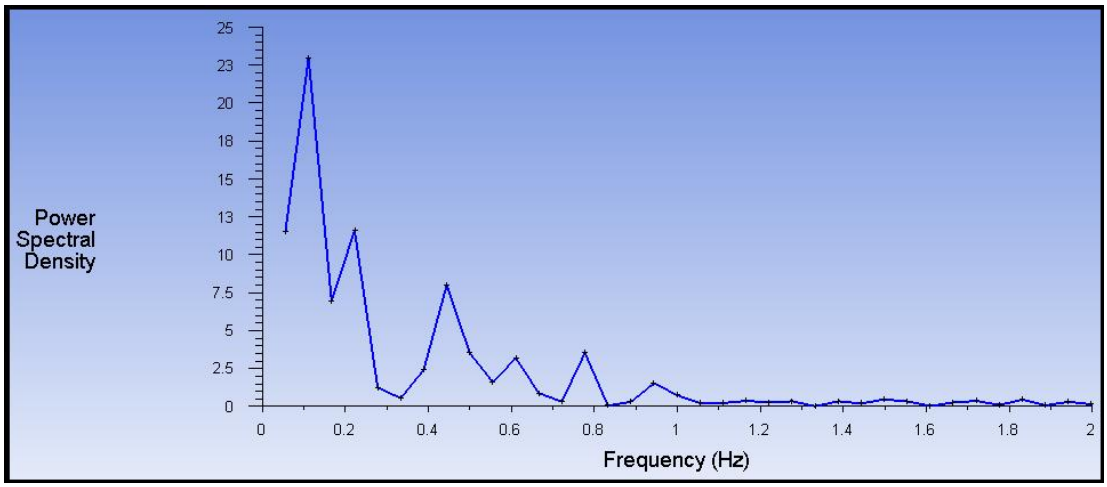

Figure 133: FFT of the upwind freestream velocity monitor point.

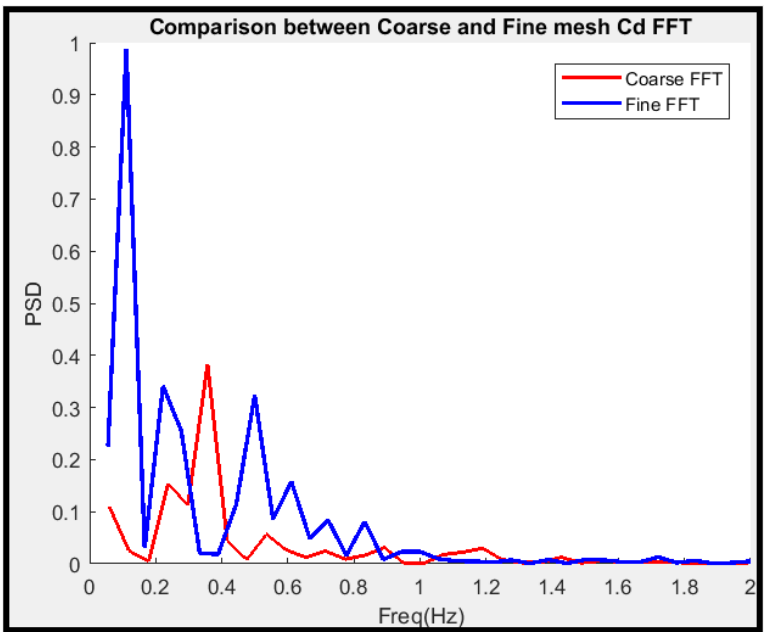

Figure 134: Comparison between Coarse and Fine mesh 0deg Cd FFT.

Looking at the FFT of the velocity magnitude monitor point in the wake of the heliostat (Figure 151), there exists a frequency of 1.1Hz, double the vortex shedding frequency, due to the monitor point catching the front and back of a single vortex, as seen earlier in chapter 4. The coarse mesh used in the wake region of the heliostat flow is unable to resolve the accurate vortex shedding behaviour and subsequent frequencies. This can be seen in Figure 151 as the vortex shedding frequency spike is incorrect for the coarse mesh and the secondary spike, representing the double vortex shedding frequency is hardly present in the FFT.

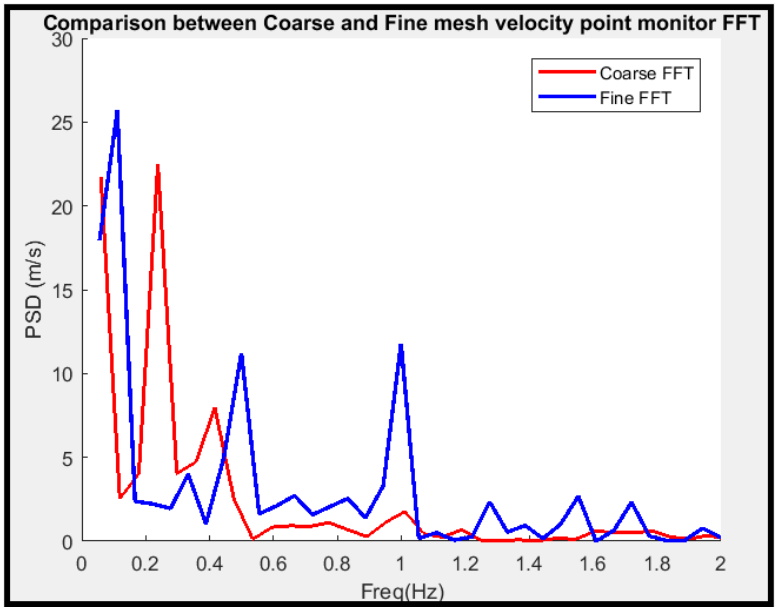

Figure 135: Comparison between Coarse and Fine mesh 0deg wake velocity magnitude point monitor FFT.

The vortex shedding frequency established using 2D URANS for the 0 degree case as presented in chapter 4 is 0.505Hz with the frequency from the SBES simulation found to be 0.499Hz. This is a difference of 1% and the difference between the SBES frequency and that approximated from (Matty, 1979) is 6.4%. The FFT results of the 60 degree case are presented below.

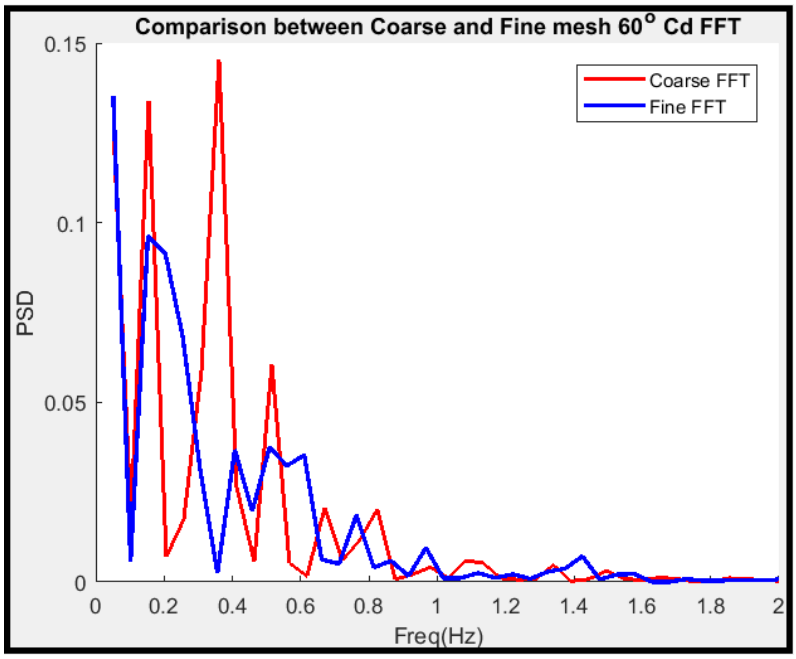

Figure 136: Comparison between Coarse and Fine mesh 60deg Cd FFT.

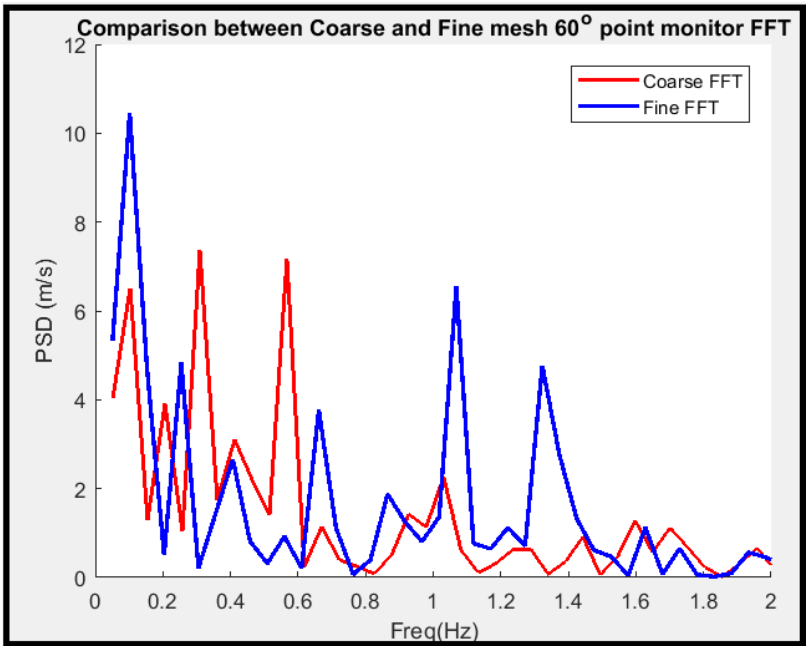

Figure 137: Comparison between Coarse and Fine mesh 60deg wake velocity magnitude point monitor FFT.

Looking at the freestream velocity FFT for the 60 degree case, it is clear that there are a considerable amount of low frequency turbulent components existing in the flow upwind of the heliostat. This makes it difficult to distinguish which frequency components found in the monitors of the heliostat are due to the vortex shedding and which are a result of the general flow field. Looking at the velocity point monitor, Figure 153, a signal spike at 1.11Hz can be seen. All the frequency content lower than this value can be seen as an altered form of the synthetically generated turbulence upstream of the heliostat. The amplitude of the spikes in the PSD are representative of the physical amplitude change in the velocity of the flow. It can be concluded that the main vortex shedding frequency from the 60 degree SBES case is 1.11Hz. This equates to a difference of only 3% when compared to the 2D URANS 60 degree results.

5.4 CONCLUSION

The results of the SBES simulations for both the 0 and 60 degree cases show a very strong association with the results obtained using 2D URANS. So far it could be said that the main vortex shedding frequency from the heliostat could easily be found using 2D URANS. The cost of running an SBES simulation is considerably more expensive than URANS. The SBES simulation is still necessary as 3D URANS fails to resolve the peak loads as well as all the other frequency content present in the flow. These fluctuating forces are required to properly evaluate the loading on the LH-2 structure. These fluctuating pressure loads are applied to the heliostat in a one-way FSI using external data in the following chapter.

6 ONE-WAY FLUID-STRUCTURE INTERACTION

6.1 INTRODUCTION

In the previous chapter scale resolving CFD simulations were conducted on the LH-2 heliostat at both 0 and 60 degrees using the SBES SRS model. This allowed transient peak loadings to be resolved for the heliostat. The fluctuating time-dependent pressures are then applied to the heliostat surfaces in this chapter. This is achieved by employing the External data component in ANSYS Workbench and linking it to the Transient Mechanical component in order to perform a one-way FSI simulation. The transient loading on the heliostat results in a time-varying structural response. This structural response is investigated further in this chapter in order to identify any interesting characteristics and possible areas of concern.

6.2 ONE-WAY FSI SETUP

As stated in the introduction, the SBES SRS results of the previous chapter are used to perform the one-way fluid structure interaction of this chapter. During the CFD simulation, the static pressure on the front and back mirror faces as well as the torque-tube and pylon surfaces were extracted. These extracted data were written to comma-delimited ASCII files. The data contained in each file consisted of each fluid mesh node, the nodes' position in Cartesian coordinates and the relevant static pressure value at each node. The CFD simulation had a time-step of 0.0003 seconds. The pressure files were extracted every 10 time-steps or every 0.003 seconds. In total for the 0 degree LH-2 configuration, 990 pressure files were extracted resulting in 2.97 seconds of flow time. For the 60 degree configuration, 796 files, resulting in 2.388 seconds, were extracted. These pressure files were imported into an External data component in the ANSYS Workbench environment. This process required around 6 hours to complete. The files were processed in batch inside this External data component before being linked to a Transient Structural component. The Workbench layout for both the 0 and 60 degree cases is shown below in Figure 154.

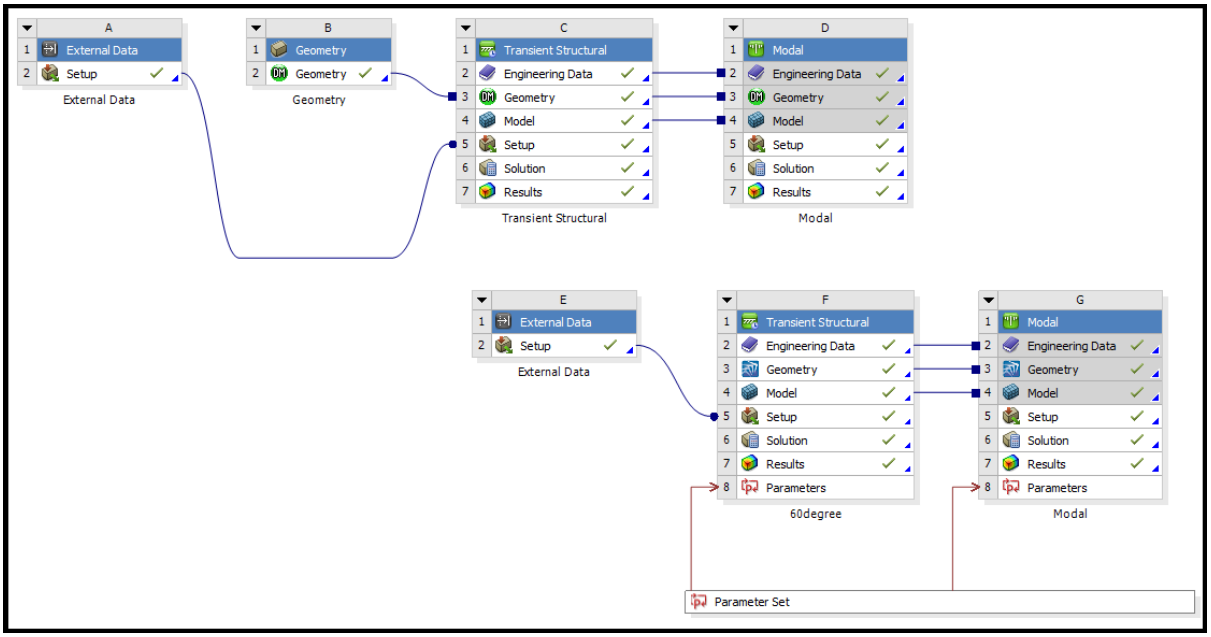

Figure 138: Workbench setup of one-way FSI workflow using External data.

The LH-2 heliostat geometry was changed slightly from the original seen in chapter 4. This was due to a simplified LH-2 geometry being implemented in the CFD simulation that lacked the backing support structure. In order to correctly map the imported pressure from the CFD onto the structural LH-2 model the mirror had to be recessed by 73mm. This means that the supporting struts as seen in Figure 155 on the left original model disappear. This was performed for the 60 degree model as well.

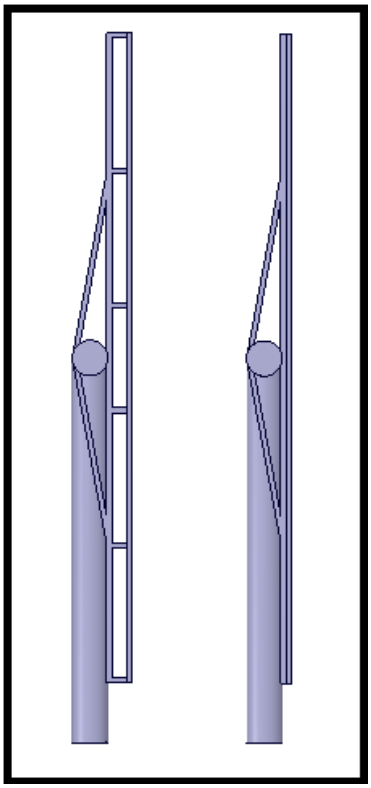

Figure 139: Original LH-2 structure (left) vs. modified recessed mirror LH-2 structure (right).

The new structural LH-2 model is meshed with 3D tetrahedral elements with a maximum size of 5cm and contains approximately 30 000 elements. The model is assigned the properties of Structural Steel seen in Table 9. The meshed LH-2 can be seen in Figure 156. The base of the pylon is assigned as a fixed support boundary condition as shown in Figure 156. The analysis settings used in the one-way FSI simulation for the 0 degree configuration are as follows, the step end time is set at 2.97s with auto time stepping set to off and the time step size prescribed as 0.003 seconds. The only change to the analysis settings for the 60 degree configuration is the step end time is set as 2.388 seconds. The CFD simulation time used to extract the pressure files is from 15 seconds, thus the flow field can be assumed to be developed, as this equates to 1.5 flow-through times for the computational domain.

Young's Modulus	$2x10^{11}$ Pa
Poisson's Ratio	0.3
Density	7 850 kg/m^3

Table 9: Structural steel material properties of LH-2 heliostat.

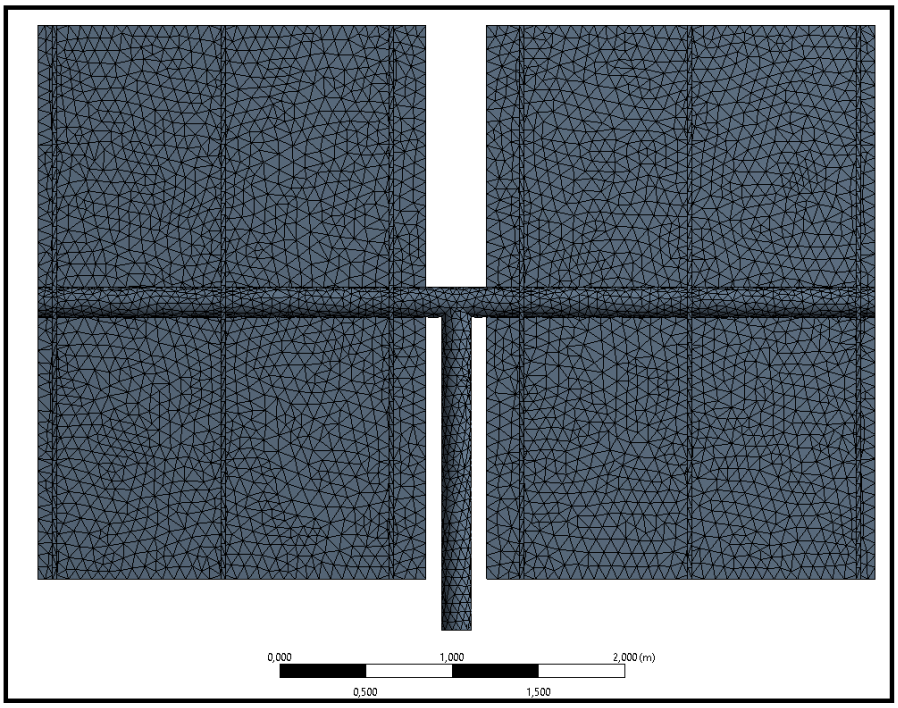

Figure 140: LH-2 tetrahedral mesh on back face for structural model.

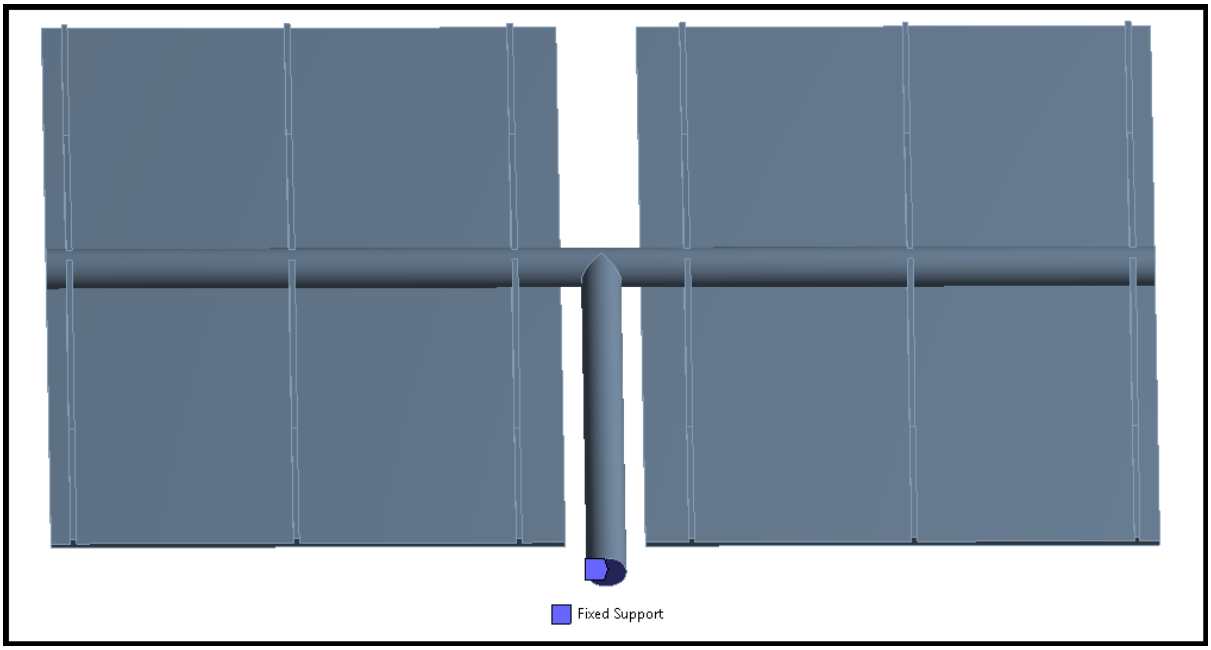

Figure 141: Fixed support boundary condition of the LH-2 1-way FSI.

As mentioned, the pressure is imported into the Transient Structural component via the External data component. Contours of static pressure on the front and rear faces of the LH-2 for the first imported pressure file can be seen in Figures 158 to 161. The non-uniform pressure distribution is evident on the faces of the heliostat as well as the asymmetric pressure distribution between the left and right sides of the heliostat. This is thanks to the SBES CFD model being able to resolve the turbulence of the flow in order to achieve a more realistic flow scenario compared to URANS.

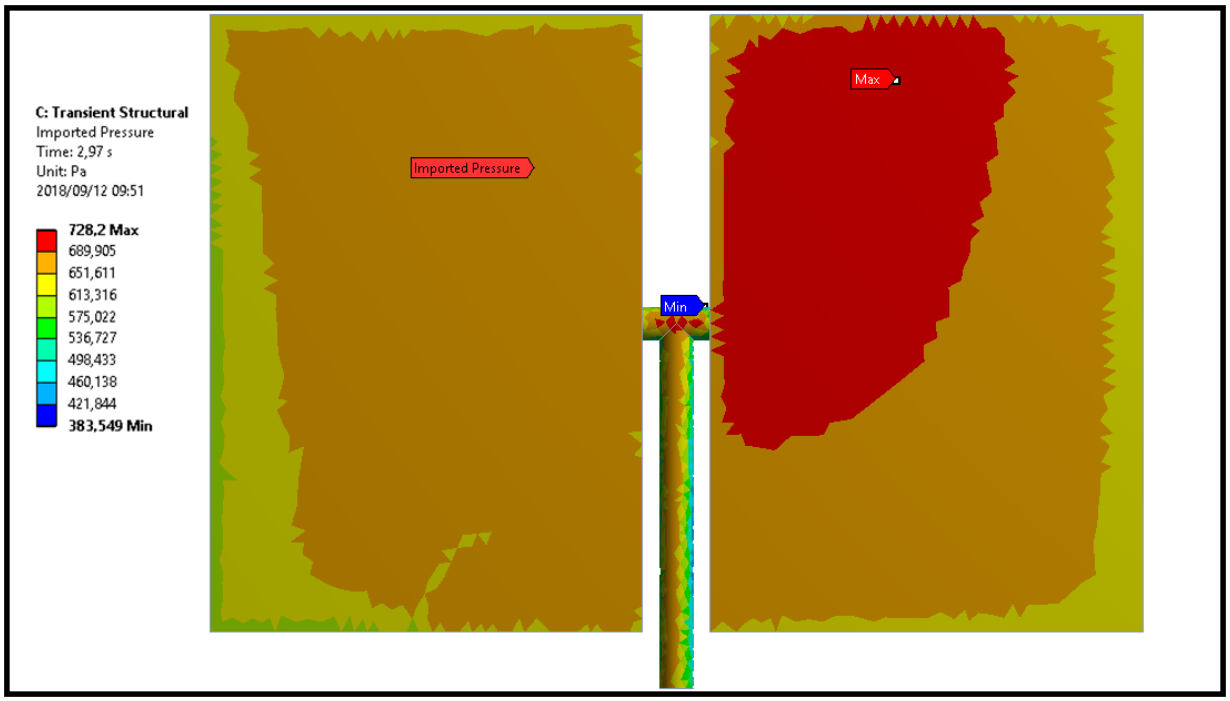

Figure 142: Imported pressure distribution on front face of 0 degree LH-2.

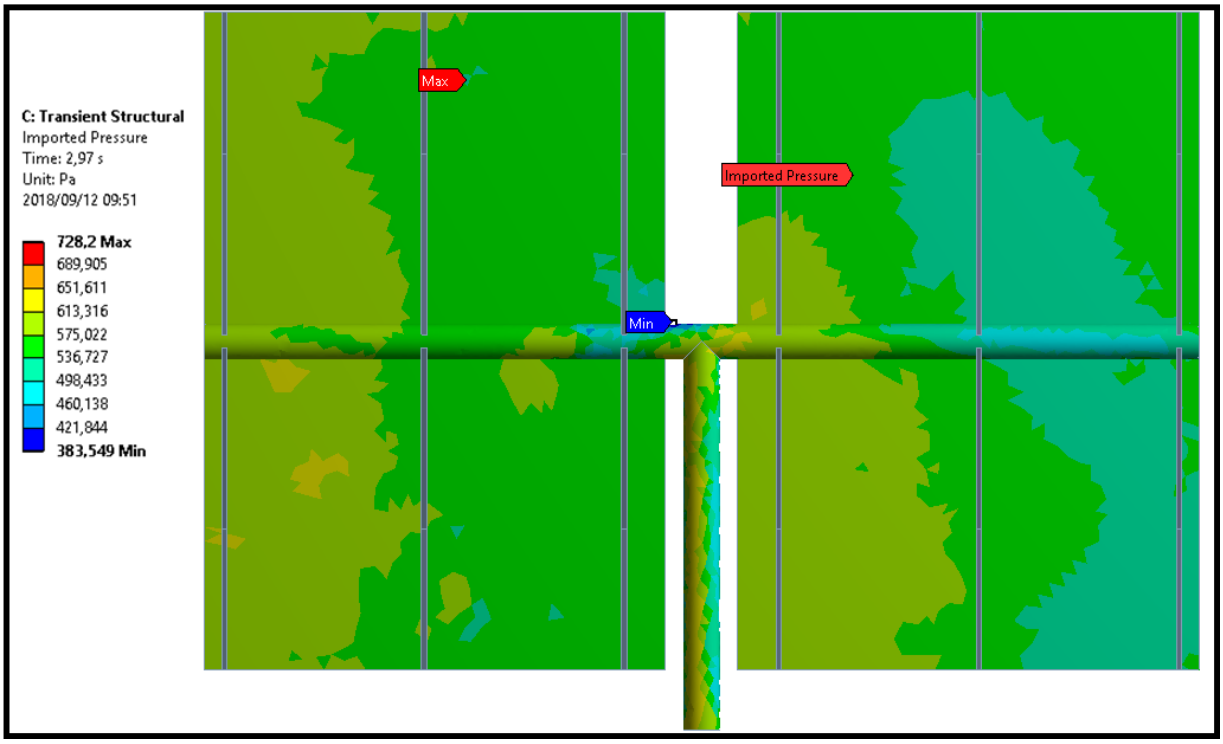

Figure 143: Imported pressure distribution on rear face of 0 degree LH-2.

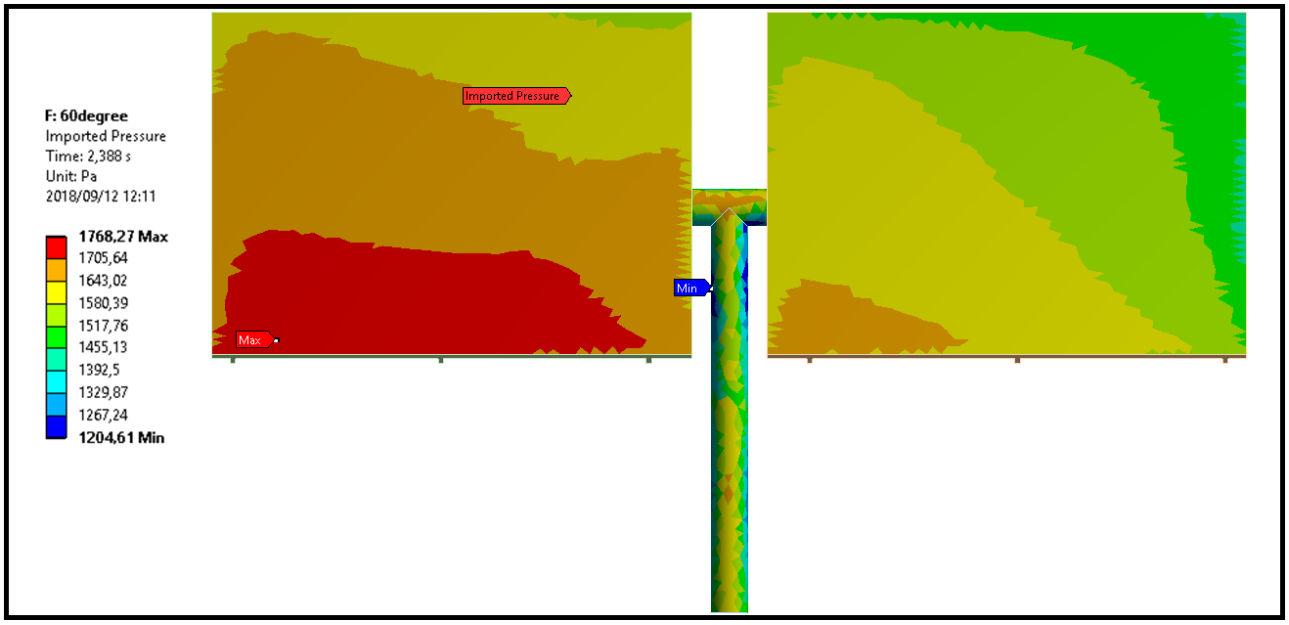

Figure 144: Imported pressure distribution on front face of 60 degree LH-2.

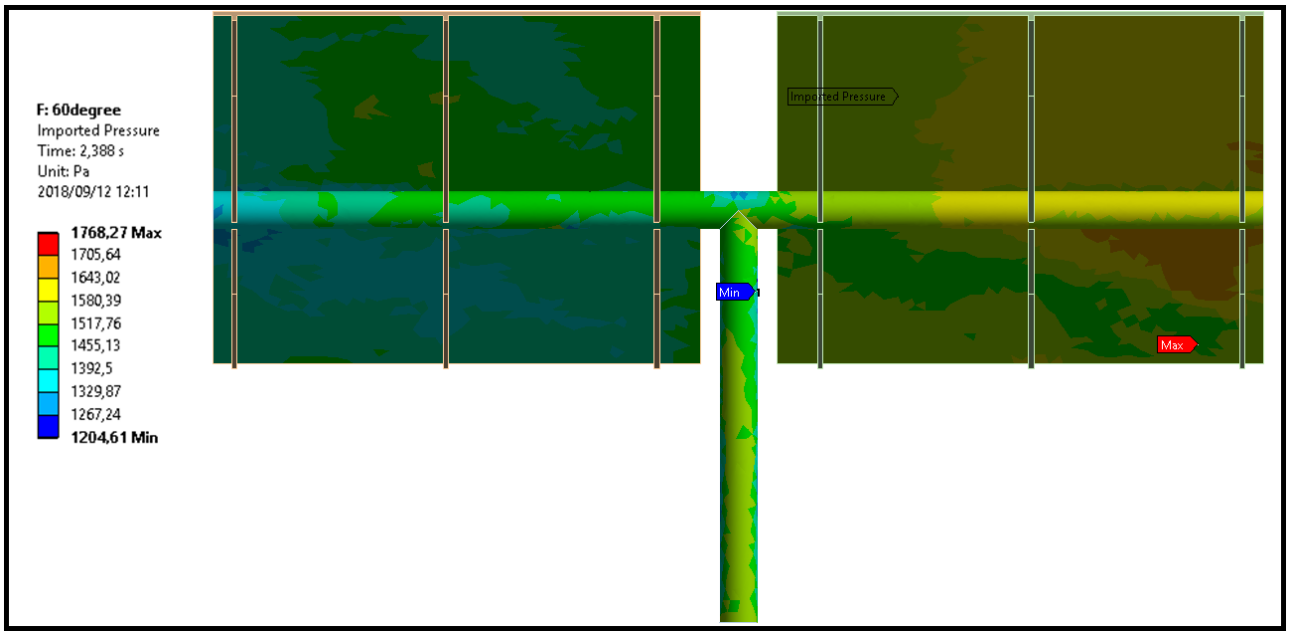

Figure 145: Imported pressure distribution on rear face of 60 degree LH-2.

In Figure 162, the imported pressure distribution for the 0 degree case at a time of 18.747s can be seen. The maximum pressure has a value of 21 770Pa with a minimum pressure of 20 848Pa. This pressure distribution equates to a total force of approximately 15 500kg per mirror or a total of 31 tons. Evidently this extreme force on the heliostat is unrealistic for any wind loading conditions, particularly at 10.5m/s. This unphysical pressure distribution is related to the vortex method and at this time is unexplainable. The spurious spikes present in the drag coefficient seen in chapter 5 are directly related to the pressure spikes of this nature. It would seem though that due to the very short duration of the spikes, their effect on the structure is negligible.

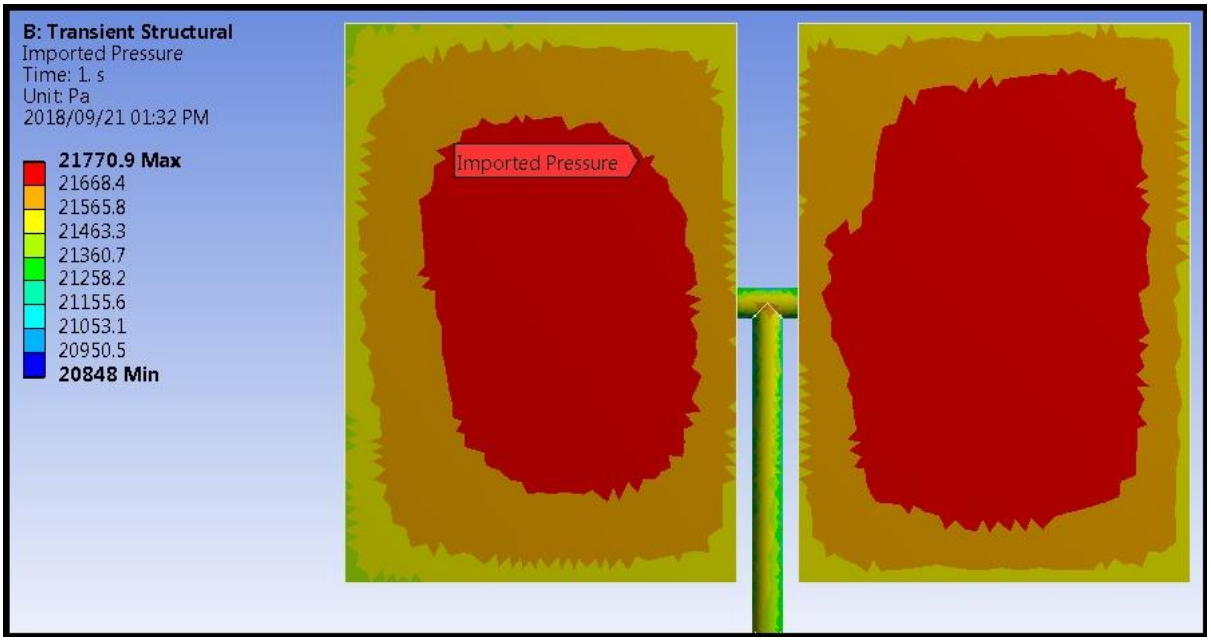

Figure 146: Imported SBES pressure distribution at t=18.747s for 0 degree LH-2.

An algorithm internal to ANSYS Workbench is used to map the nodes of the Fluent mesh to the nodes of the structural mesh. This is necessary as the Fluent mesh has approximately 344 062 nodes containing pressure information which needs to be transferred to the structural mesh containing approximately 60 000 nodes. As the variable being mapped is pressure, a profile preserving mapping is used. This mapping simply takes the profile of the variable on the original mesh (Fluent) and matches it to the other mesh (Transient Structural) as best as it can using a weighting. The weighting used is triangulation. Triangulation creates temporary elements from the closest source nodes to find the closest points that will contribute portions of their data values. If the target point is found within the element, weights are calculated based on the target's location inside the element. In Figure 163, the Fluent mesh nodes are shown on the surface of the LH-2 at time = 15s.

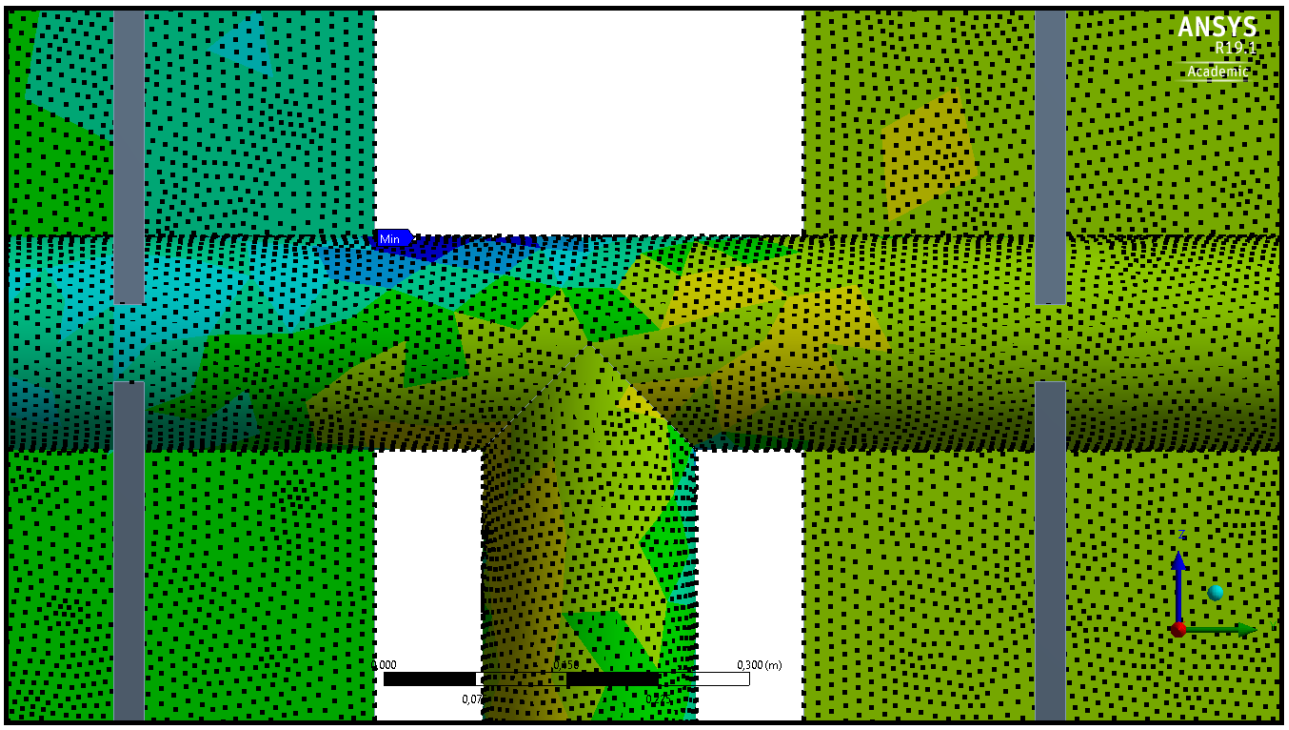

Figure 147: Fluent mesh nodes on the surface of the LH-2 (time = 15s).

In order to assess the accuracy of the mapping of the source mesh onto the target mesh, a mapping validation is performed. The validation used in this section is reverse mapping. In reverse mapping the results of the imported data are mapped back onto the source points. These new mapped values are compared to the source variables original values. The results for the mapping validation are shown in Figures 164 and 165 for both the 0 and 60 degree cases, respectively. A close-up of the 0 degree rear surface is shown in Figure 166.

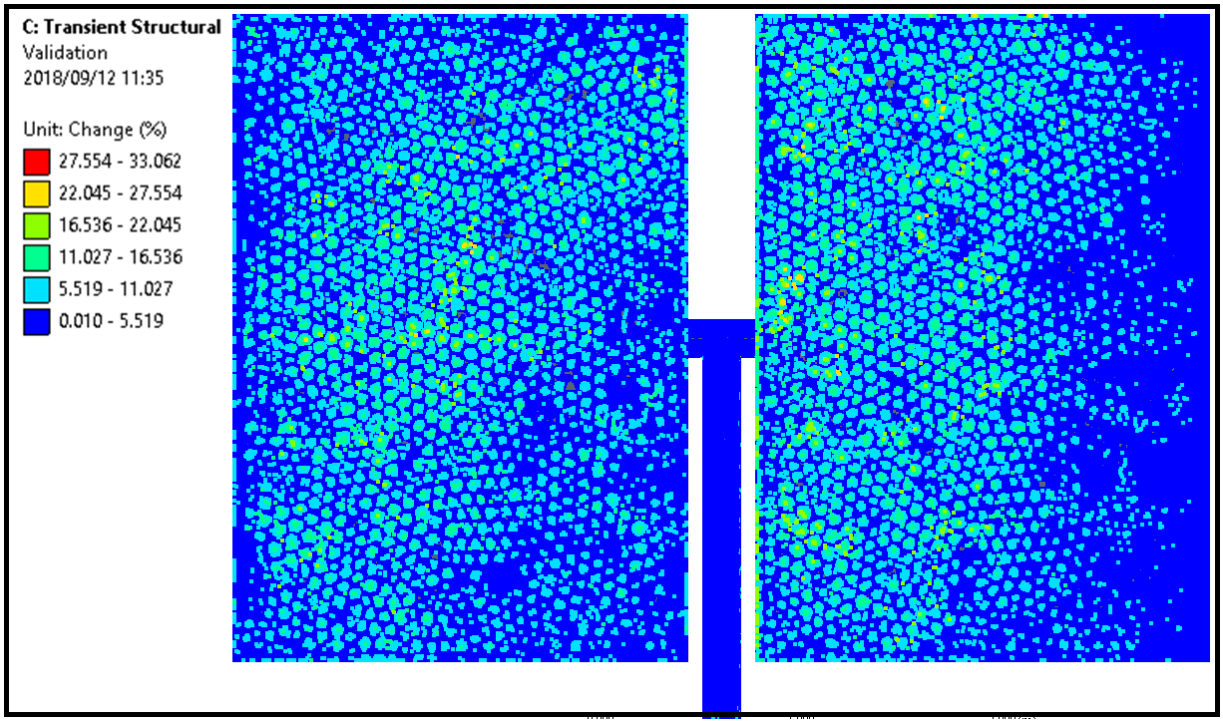

Figure 148: Mapping validation results for 0 degree LH-2 (time = 15s).

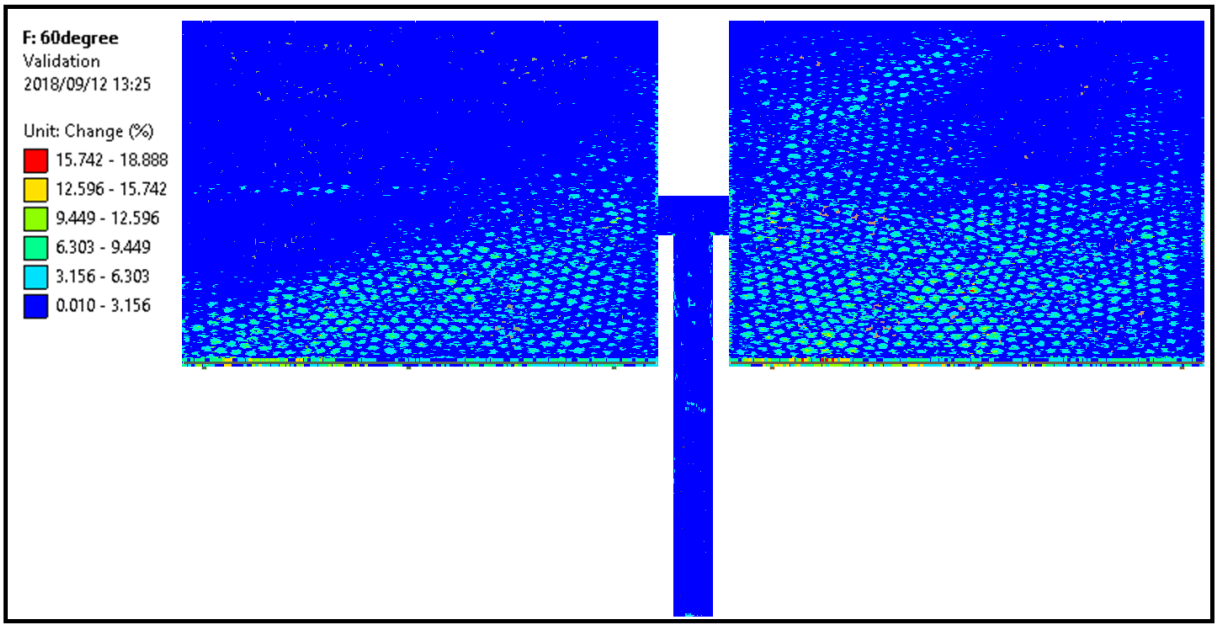

Figure 149: Mapping validation results for 60 degree LH-2 (time = 15s).

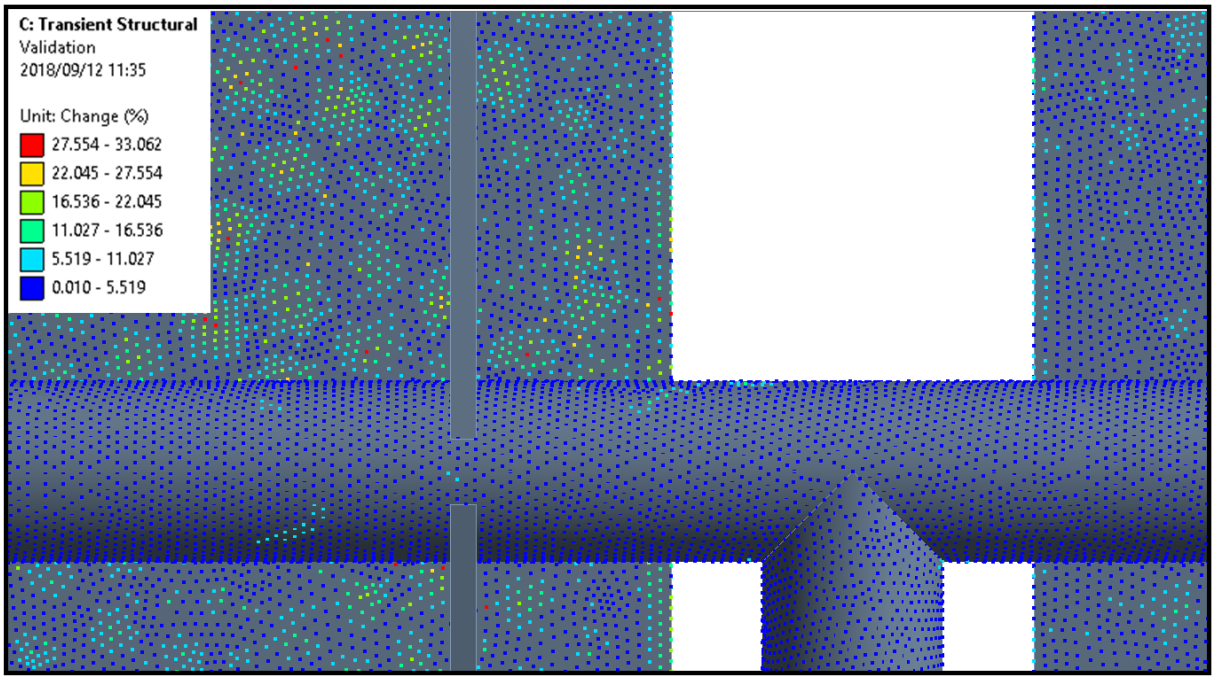

Figure 150: Close-up of rear face of mapping validation of 0 degree LH-2 (time = 15s).

The mapping validation for the 0 degree case shows a maximum relative error of 33%. This could be considered high but the average error as seen across the face is less than 5%. This error is for the last time step pressure file. The validation of the 60 degree case produces a maximum relative error of 19%. Again it should be noted that the average error is less than 3%. The clumping of the high validation errors seen in Figure 164 translates to the mesh cells present on that face of the LH-2. Overall the mapping of the pressure data from the Fluent mesh nodes onto the Structural mesh nodes is deemed successful. There is a 6 times reduction in the number of nodes from the source to the target mesh.

The modal frequencies of both the 0 and 60 degree LH-2 structures have been altered due to the mirrors being recessed. The modes are not drastically different but the table of the mode numbers and corresponding frequencies for both cases are given in Table 10. The modal frequencies and shapes are critical to this structural investigation as the deformation of the heliostat due to the flow field may excite a specific modal shape even if that mode is not at the vortex-shedding frequency.

Mode	Frequency (Hz)(0°)	Frequency (Hz)(60°)
1	1.9799	1.9272
2	2.2244	2.1123
3	2.699	2.636
4	5.485	6.0066
5	6.0105	6.4593
6	6.135	6.517
7	7.3064	7.5317
8	12.672	10.721
9	17.68	18.325
10	18.474	18.781

Table 10: Modes of 0 and 60 degree cases.

6.3 RESULTS

The Transient Structural one-way FSI results for the 0 degree LH-2 case are presented below. The response of the heliostat structure to the transient pressure loads derived from the SBES scale-resolving CFD simulation is investigated below. Particular importance is placed on the vibrational response of the structure in line with the vortex-shedding frequencies. Although the deformation of a heliostat is critical to the efficiency of an operating plant, it is not scrutinised in this section. The same can be said for the stress induced in the structure due to the pressure, provided the yield stress of the material is not surpassed, no further investigation is performed.

For both the 0 and 60 degree cases, four important structural results are looked at. These include the directional deformation of critical points on the structure, the total deformation of the structure, the equivalent stress of the structure and the reaction force of the fixed support. These are then analysed and an FFT of the resultant graphs is produced in each case in order to draw comparisons to the CFD results and conclusions from the heliostat responses. The results for the two cases are analysed simultaneously for comparative purposes. The graph of the response signal of the top right mirror vertex is shown below in Figure 167 for the 0 degree case with the FFT of the signal in Figure 168.

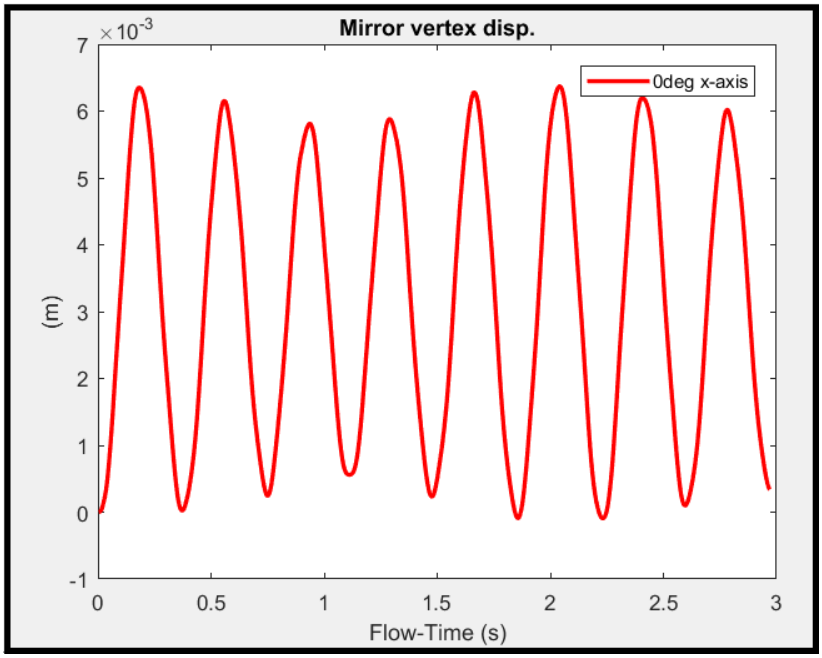

Figure 151: Top right vertex displacement (x-axis) for the 0 degree case.

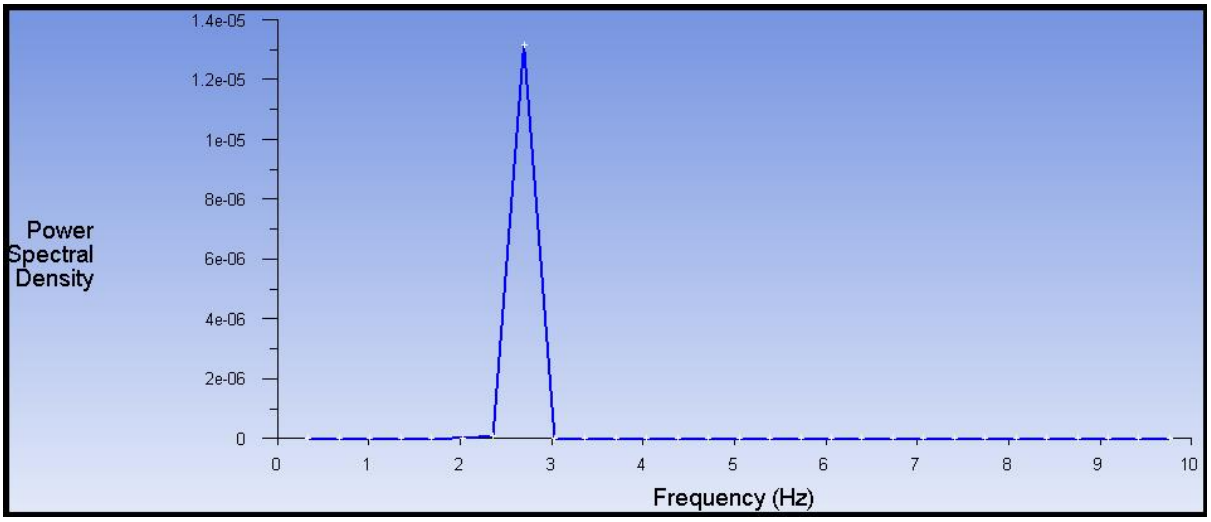

Figure 152: FFT of top right vertex displacement (x-axis) for the 0 degree case.

The response signal for the top right vertex of the 60 degree case in both the x-axis and z-axis is shown below with the corresponding FFTs.

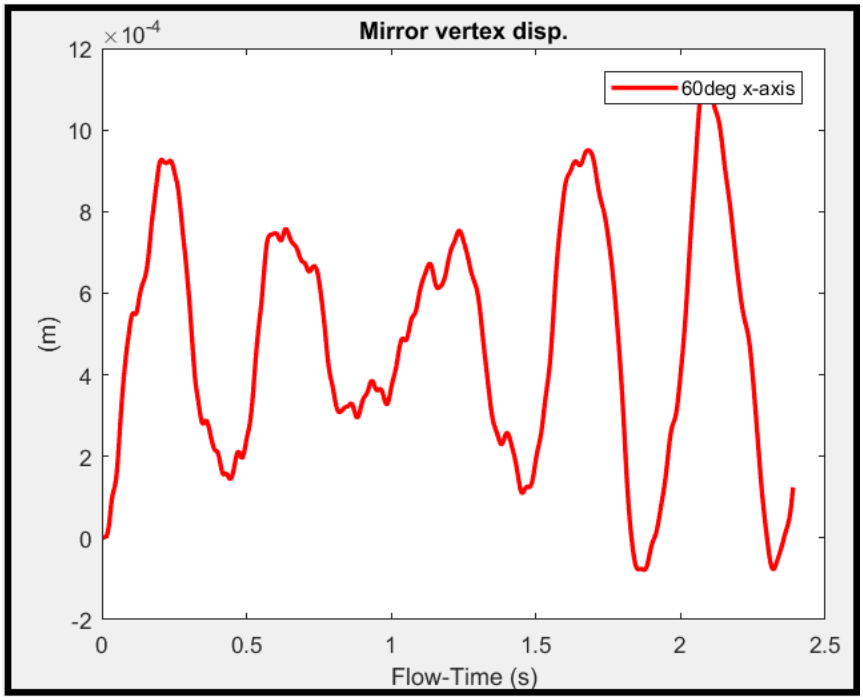

Figure 153: Top right vertex displacement (x-axis) for the 60 degree case.

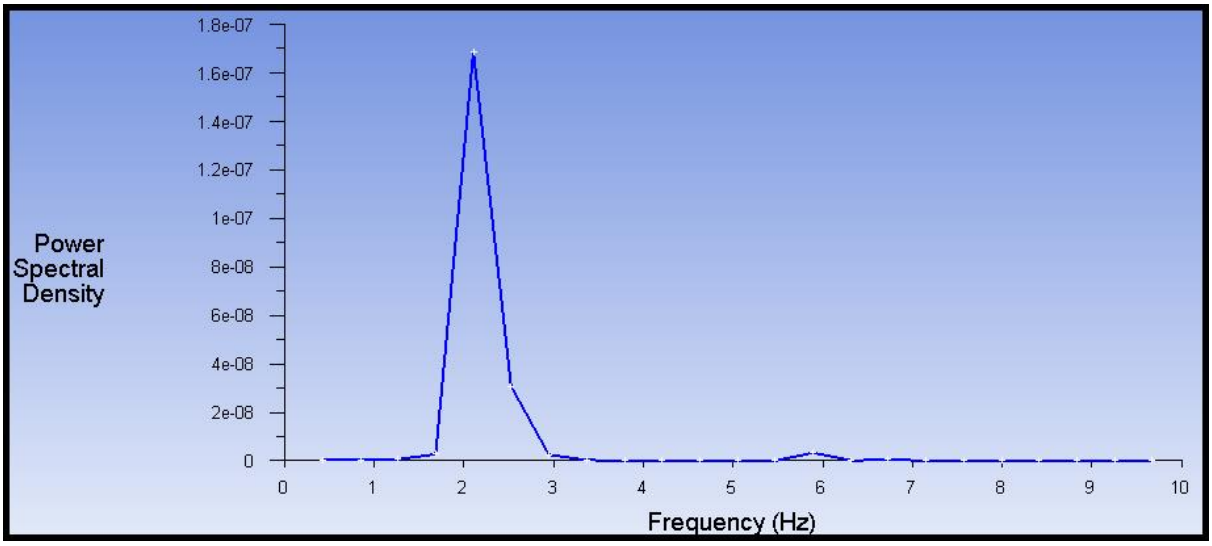

Figure 154: FFT of top right vertex displacement (x-axis) for the 60 degree case.

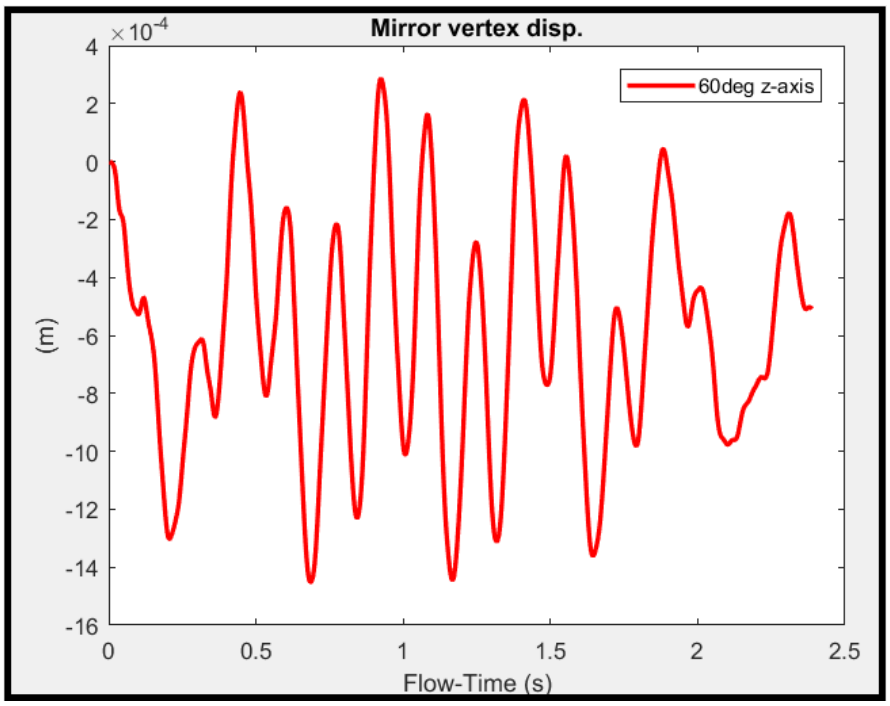

Figure 155: Top right vertex displacement (z-axis) for the 60 degree case.

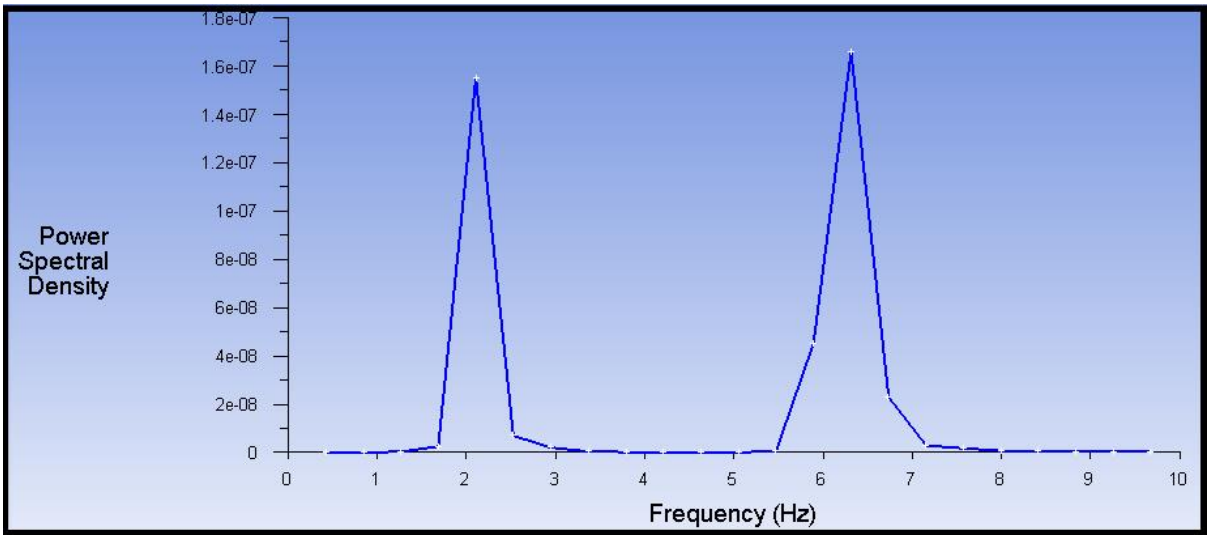

Figure 156: FFT of top right vertex displacement (z-axis) for the 60 degree case.

The results from the displacement of the top right mirror vertex show that for the 0 degree case the response signal has a very smooth sinusoidal behaviour. The maximum displacement seen by the vertex is 6.2mm. It appears as though there is a single driving frequency in the signal. This is confirmed via the FFT of the signal which shows a large single spike at 2.69 Hz. It is evident that this frequency is well outside the vortex-shedding frequency simulated in the previous chapter of 0.499 Hz. Looking at the table of mode shapes for the 0 degree case (Table 10), the 3rd mode has a frequency of 2.699 Hz. It appears that the heliostat, under the agitation of the SRS pressure field, is being excited at this modal frequency. This is due to the deformation of the structure being in line with this particular mode shape. This will be further investigated and demonstrated later in the chapter. The 60 degree case x-axis vertex displacement signal shown in Figure 172 is not as smooth as the 0 degree case. This reveals that there is underlying content present in the signal that needs to be examined. The FFT of this signal produces a frequency 2.1 Hz. As with the 0 degree case this frequency is far from the vortex shedding frequency obtained with the SRS CFD simulations of 1.11 Hz or 1.22 Hz. Further investigating how the vertex displaces in the z-axis direction, the signal in Figure 171 is seen. The FFT of this signal shows dominating frequency content at 2.1 Hz and 6.31 Hz. These frequencies once again are due to the LH-2 structure being deformed to the shapes of and thus being excited at the 3rd mode and a combination of the 4th, 5th and 6th modes (Table 10).

The total deformation of the entire heliostat structure is investigated below for both cases. The maximum deformation shape of the heliostat, along with contours of the deformation are shown. The transient signal of the deformation is given and an FFT is performed and evaluated. The total deformation of the heliostat for the 0 degree case is shown in Figure 173, followed by the deformation signal and FFT in Figures 174 and 175, respectively.

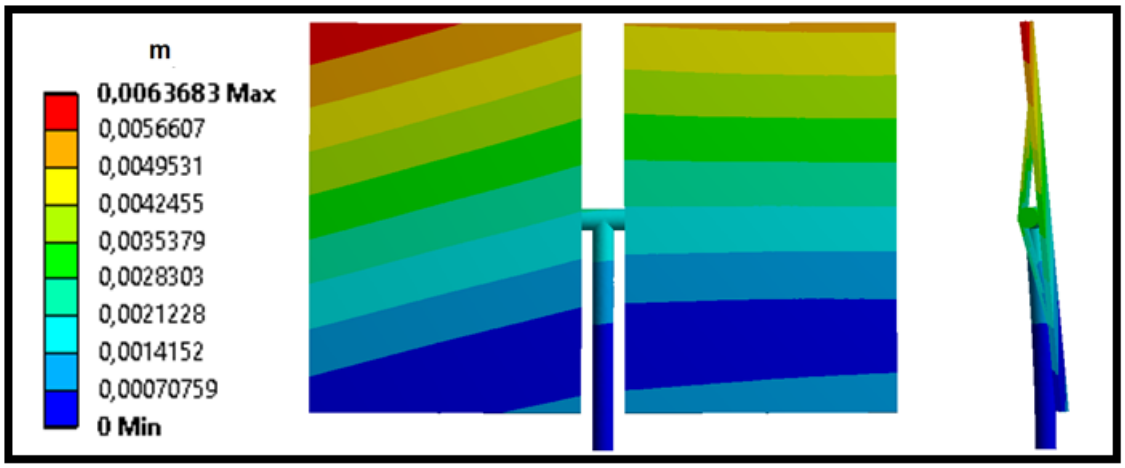

Figure 157: Maximum total deformation of LH-2 for 0 degree case (front) and (side).

The deformation of the heliostat for this 0 degree case is dominated by the entire heliostat deflecting backwards in the direction of the fluid flow. This would be the logical deflection of any structure being attacked with the force due to the fluid flow being normal to the mirror faces. Obviously the top mirror edge is deflected the furthest due to it being the furthest point from the fixed support.

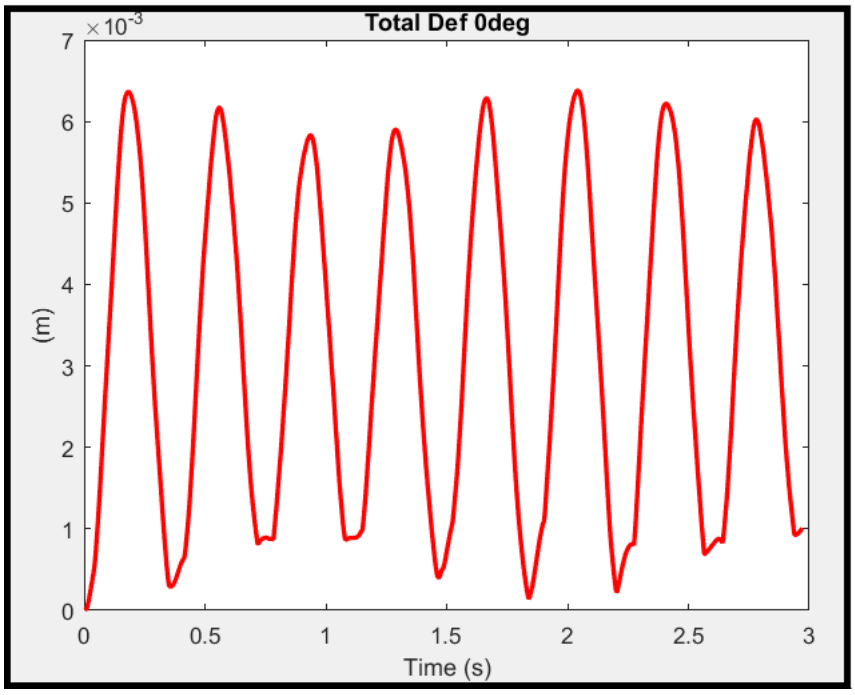

Figure 158: Total deformation signal for the 0 degree case.

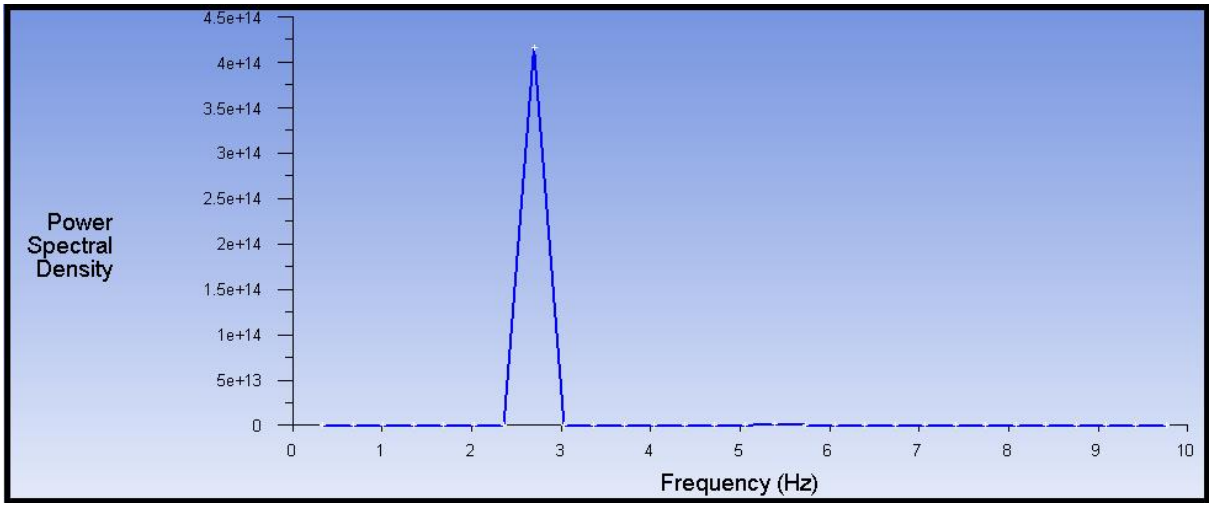

Figure 159: FFT of the total deformation signal for the 0 degree case.

The total deformation of the heliostat for the 60 degree case is shown in Figure 176, followed by the deformation signal and FFT in Figures 177 and 178, respectively.

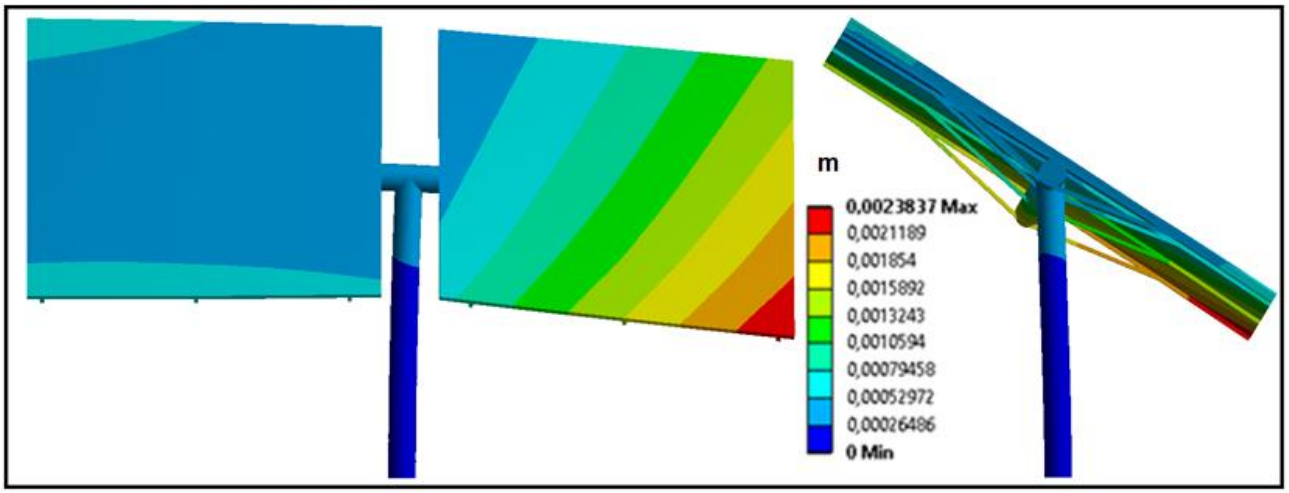

Figure 160: Maximum total deformation of LH-2 for 60 degree case (front) (side).

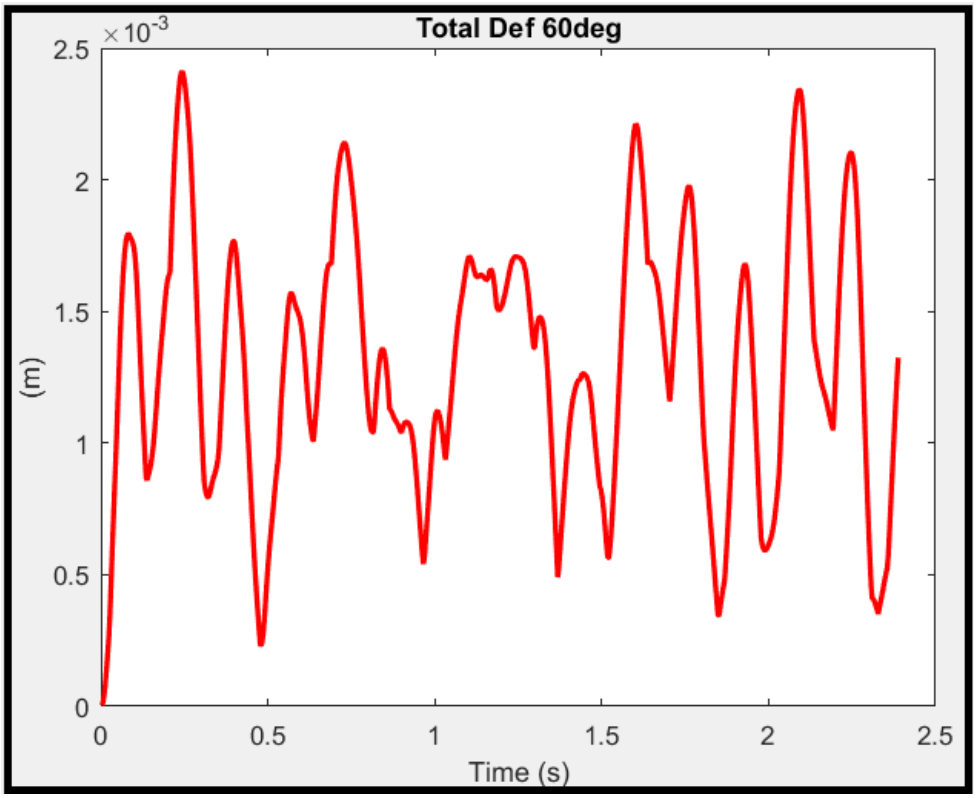

Figure 161: Total deformation signal for the 60 degree case.

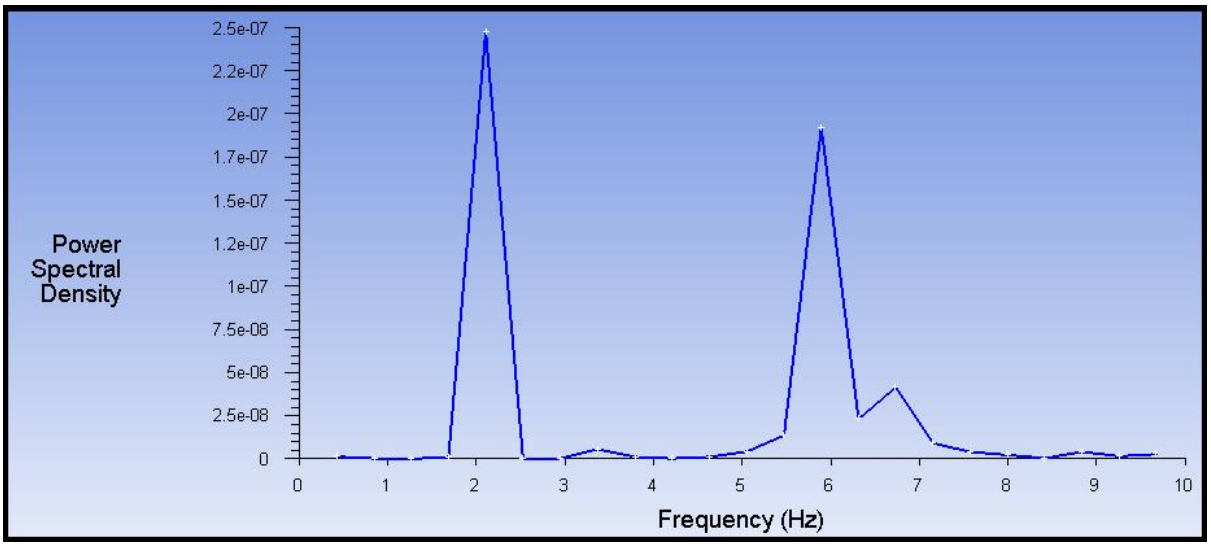

Figure 162: FFT of the total deformation signal for the 60 degree case.

The total deformation signal of the 0 degree case shows a similarity to the vertex displacement signal in the almost smooth sinusoidal nature of the signal. The FFT shows a dominating frequency component of 2.69 Hz, the exact same frequency found in the vertex displacement signal. Looking at the maximum deformation of the 60 degree structure in Figure 176, one can see that the main shape of the deformation has shifted from the 0 degree case of back and forth to the 60 degree case of side to side. This will be confirmed when looking at the mode shapes of these excited frequencies. The total deformation signal of

the 60 degree case once again contains a considerably greater amount of frequency content when compared to the 0 degree case. The FFT confirms that the strongest frequency present is the 2.1 Hz signal followed by a 5.89 Hz and a smaller 6.73 Hz signal. This means that the behaviour of the structure is dominated by the 3rd mode which could be assumed as a side to side mode (will be investigated further) and the other modes mentioned earlier. The Equivalent Von Mises stress in the LH-2 structure due to the wind loading is presented below for both cases. The stress contour plots are seen below in Figure 182 with the accompanying graph of the transient stress and FFT in Figures 180 and 181 for the 0 degree case.

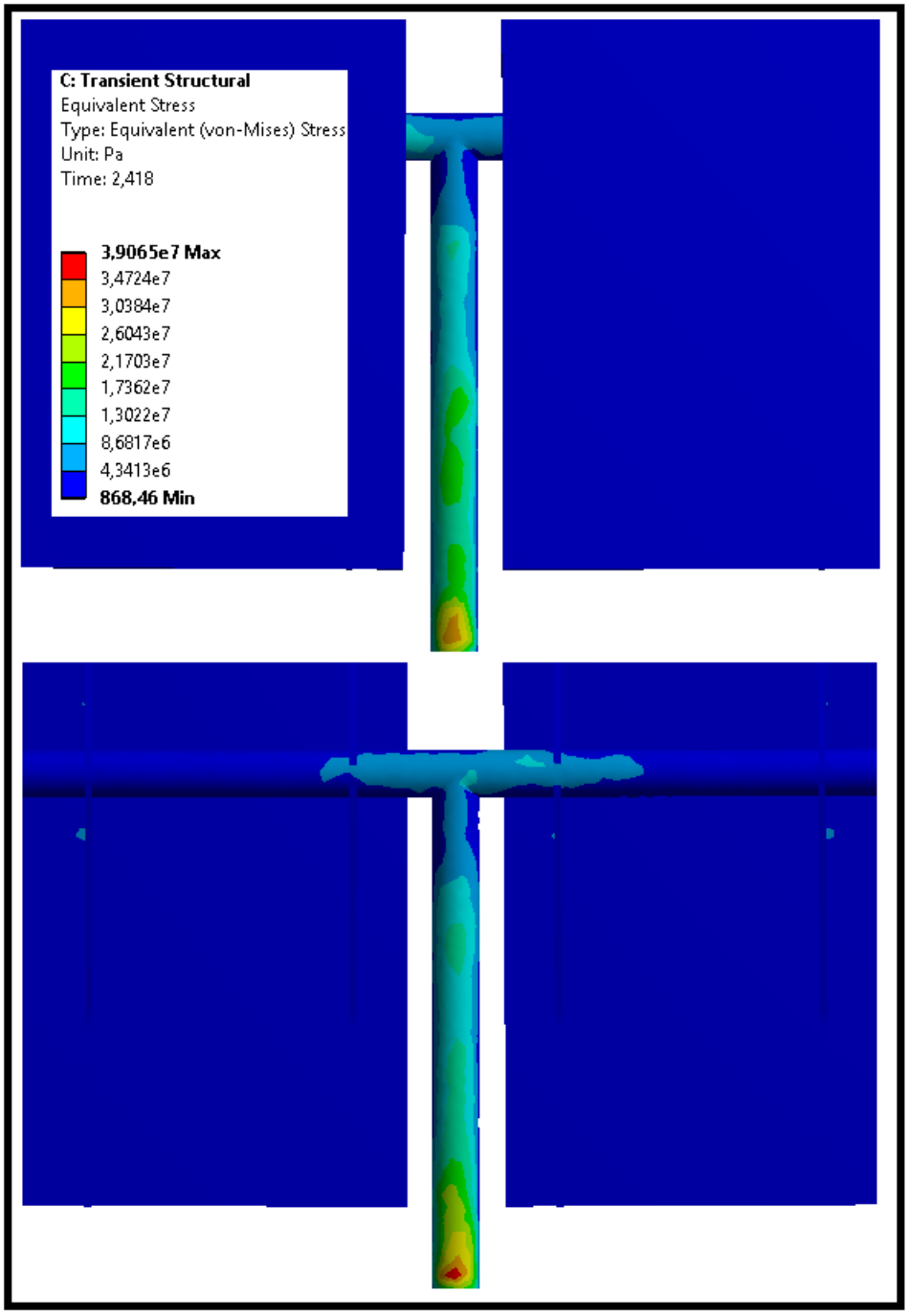

Figure 163: Maximum Von Mises stress contour for the 0 degree case (front and back faces).

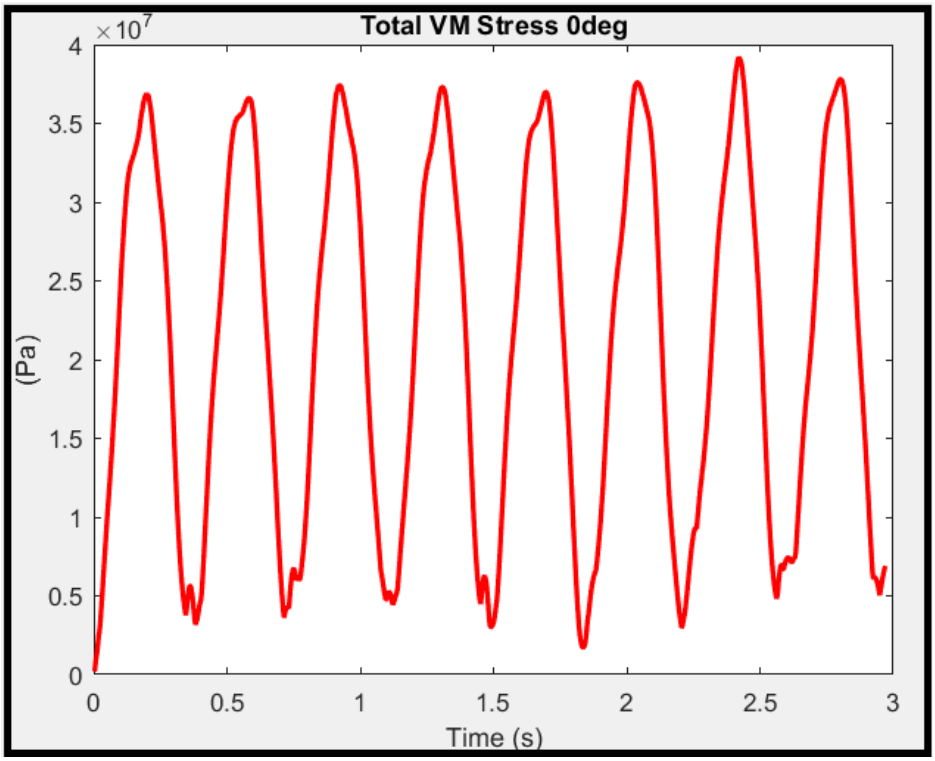

Figure 164: Maximum Von Mises stress signal for the 0 degree case.

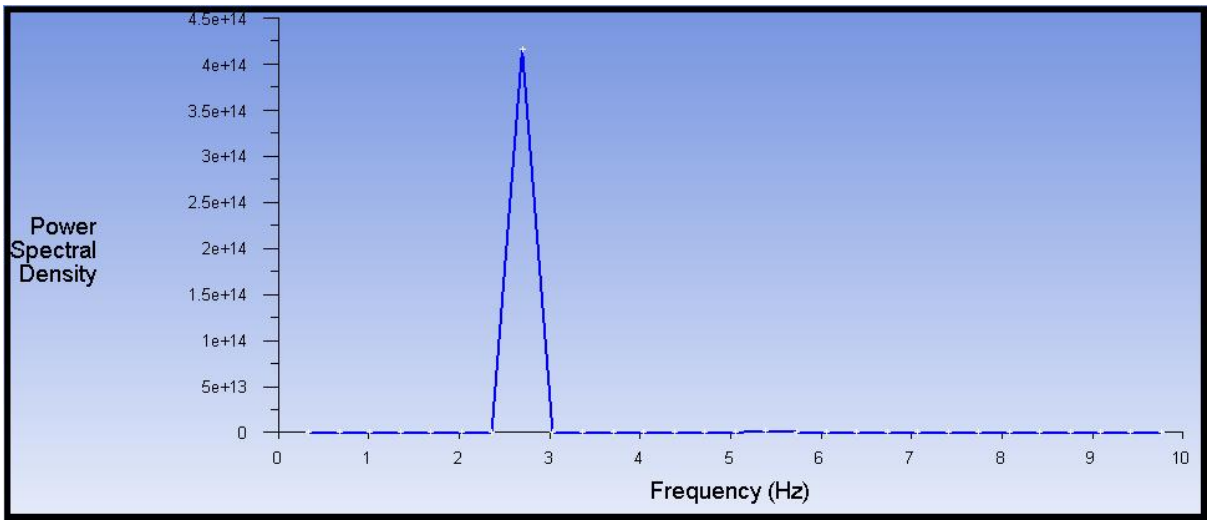

Figure 165: FFT of the Maximum Von Mises stress signal for the 0 degree case.

As shown in the contour plots of the stress for the LH-2, the highest induced stress in the structure over the loading period is 34 MPa. This is well below the yield strength of structural steel as expected as the wind velocity is only 10m/s. The aim of investigating the stress profile for the LH-2 is to see which areas of the structure experience the greatest stress and examine the resultant FFT of the stress signal. The peak stress is seen to be located near the base of the heliostat on the back face of the pylon. This compressive stress has an opposed tensile stress as seen on the front face of the pylon. This stress profile is expected due to the massive bending moment seen by the pylon as it opposes the oncoming wind pressure. Very little stress is induced in the mirrors and backing structure with a small stress seen in the torque-tube near the

intersection with the pylon. The critical member in this case would be the pylon. As expected, the FFT of the Von Mises stress signal shows the 2.69 Hz signal once again.

The stress contour plots are seen in Figures 182 and 183 with the accompanying graph of the transient stress and FFT in Figures 185 and 186 for the 60 degree case.

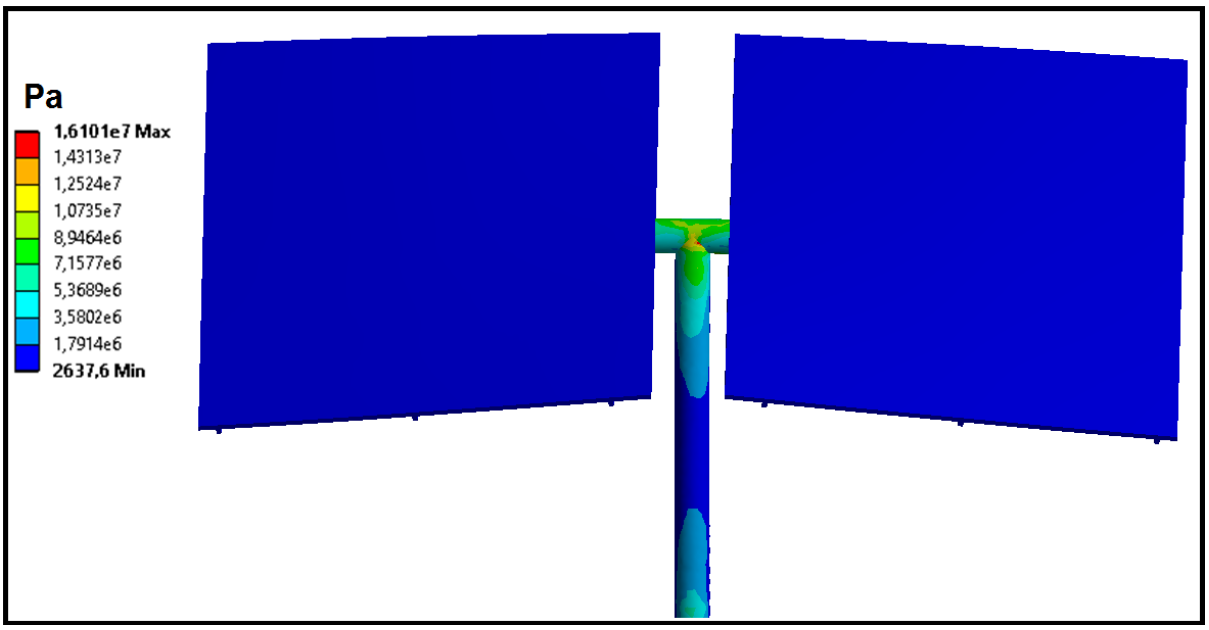

Figure 166: Maximum Von Mises stress contours for the 60 degree case (front face).

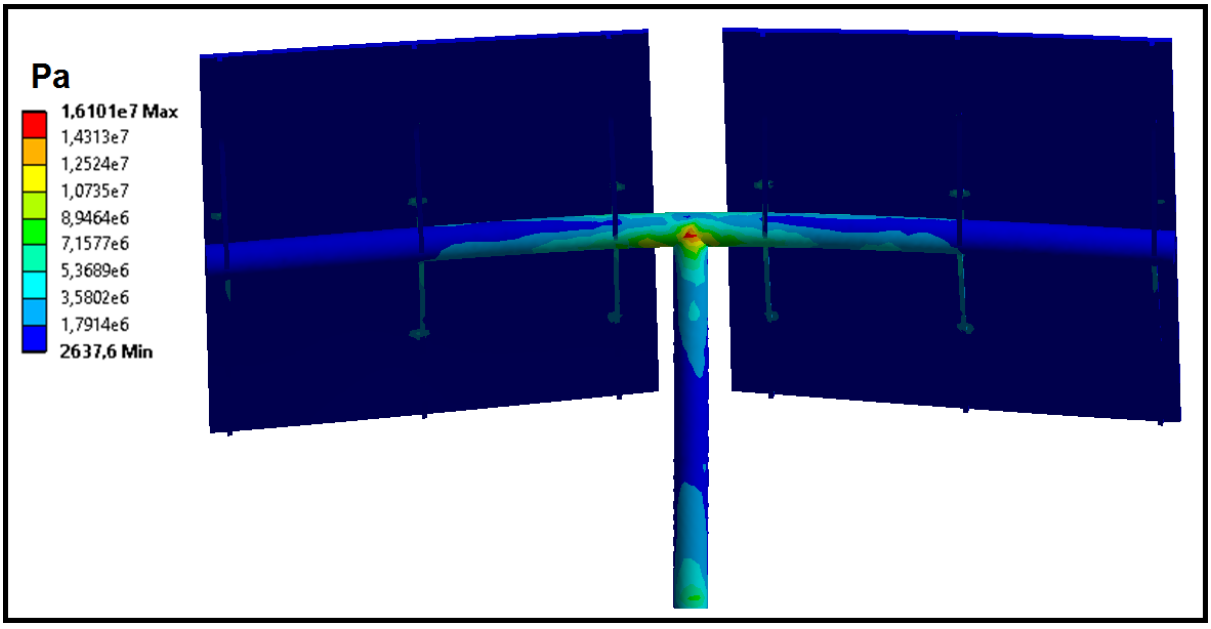

Figure 167: Maximum Von Mises stress contour for the 60 degree case (back face).

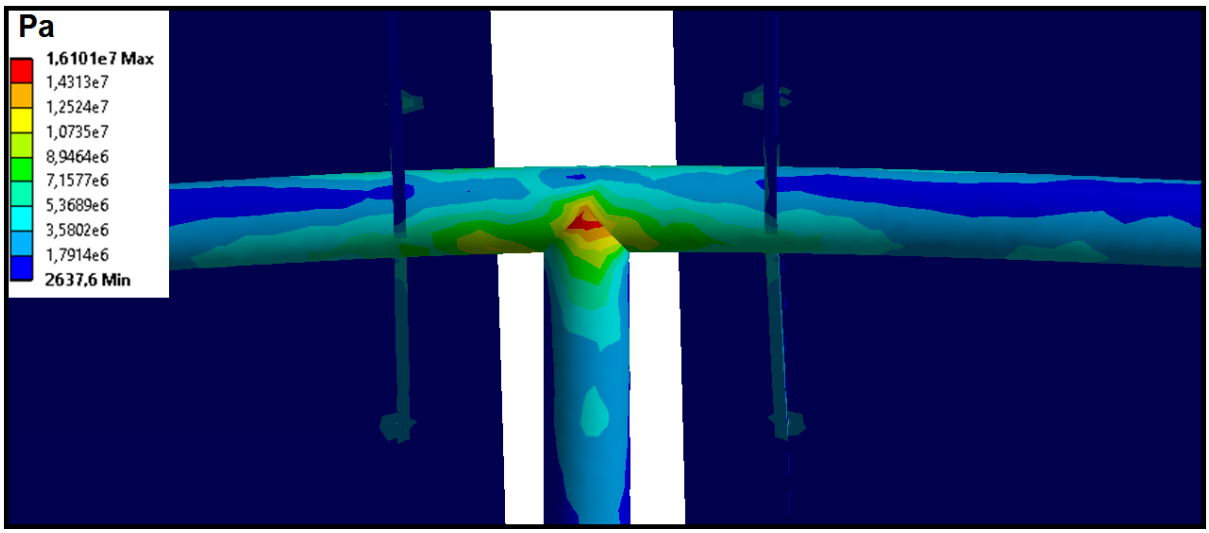

Figure 168: Close up of maximum Von Mises stress contours for the 60 degree case (back face).

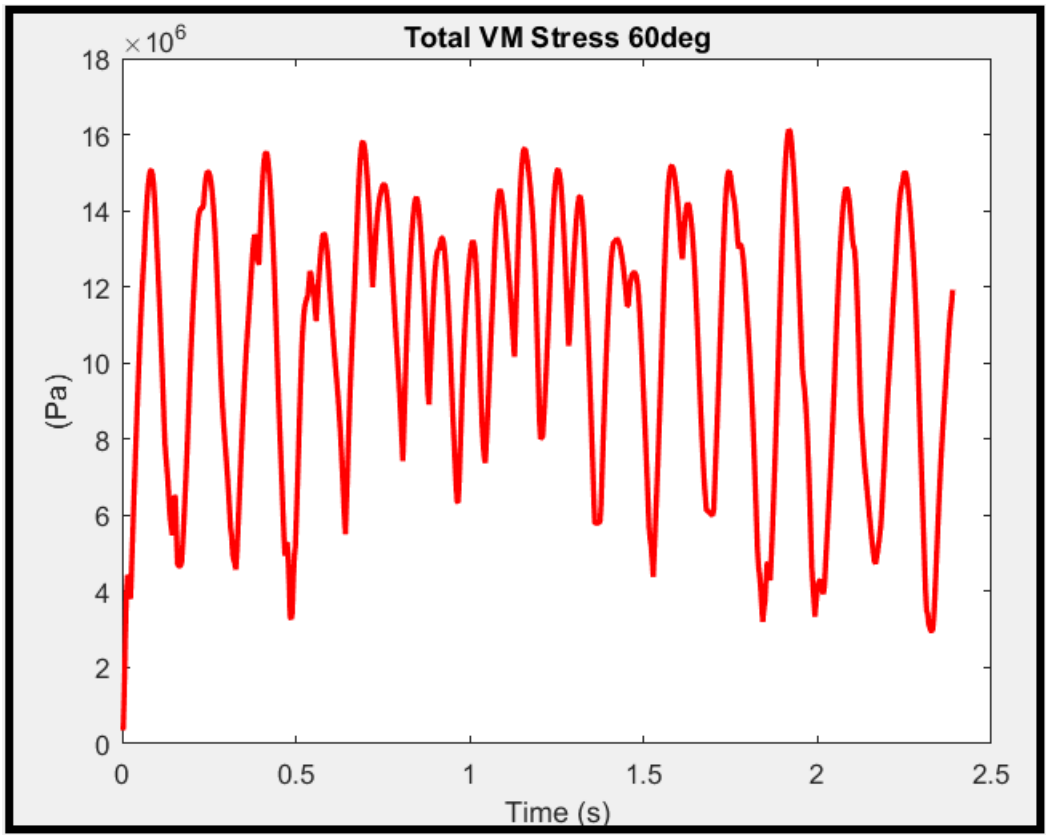

Figure 169: Maximum Von Mises stress signal for the 60 degree case.

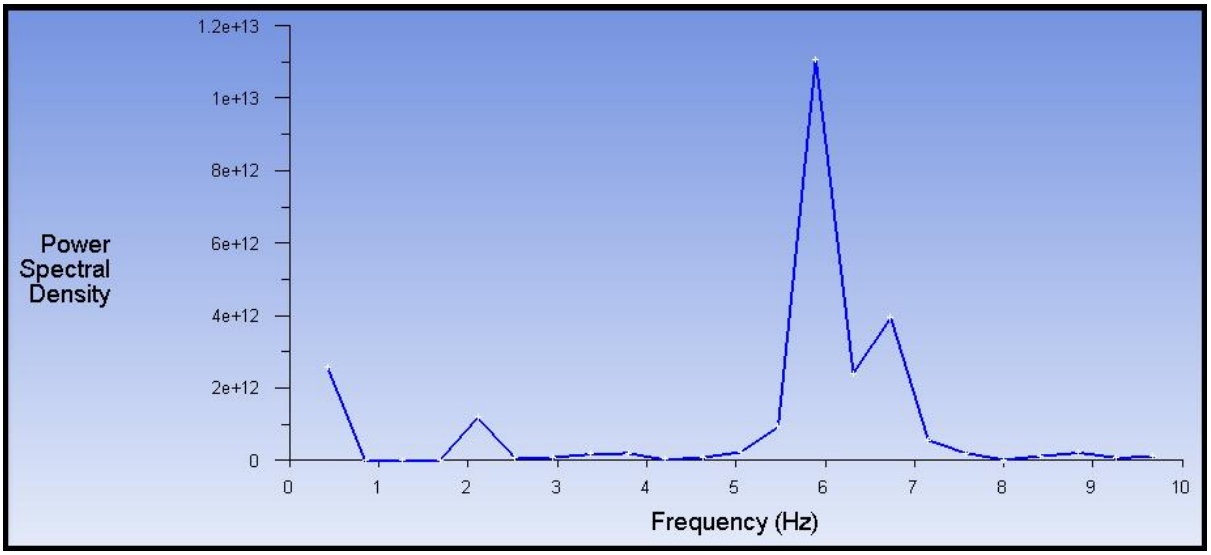

Figure 170: FFT of the maximum Von Mises stress signal for the 60 degree case.

Looking at the stress contours for the 60 degree case, the maximum induced stress in the LH-2 has decreased by about half to 16 MPa. This is expected as the frontal mirror area has decreased by approximately half. Interestingly the location of the maximum stress is no longer seen at the base of the pylon but is now located at the T-joint between the torque-tube and the pylon. This joint is now the critical member of the LH-2 structure at 60 degrees. This may be due to the different motion of the heliostat at this angle, compared to 0 degrees. Here there is side-to-side motion mixed with the mirrors flexing backward. This is compounded by the peak torque-tube moment experienced at 60 degrees. Looking at the stress signal in Figure 185, it is evident that there are multiple different frequencies present. The FFT shows a considerably smaller 2.1 Hz component compared to the previous 60 degree signals while the major frequency present is 5.89 Hz and 6.7 Hz. As stated earlier there are three modes in the 6 Hz range. The result of the 60 degree stress signal frequencies is due to the heliostat deflecting with these mode shapes simultaneously.

Even though the heliostat produces a defined vortex shedding frequency for its given configuration, the response of the structure appears to be more complex and involved than simply oscillating at this shedding frequency. The SRS CFD simulations produce a large amount of frequency content that can excite the heliostat. More importantly it seems as though the specific mode shapes for both the 0 and 60 degree cases happen to exist at the same deformation shapes one would expect of the heliostat in the fluid flow. This is no coincidence as the mode shapes illustrate how the structure would want to naturally deform. The vortex shedding of the 0 degree case calculated from the SBES simulations is 0.499 Hz. The structural response of the LH-2 furnished with the pressure field derived from the SBES simulation is dominated by a 2.69 Hz frequency. This is exactly the third mode of the LH-2 at 0 degrees. The mode shape can be seen below in Figure 187. The deformation of this mode is simply the entire heliostat rocking back and forth with the mirrors flexing ever so slightly outwards on the far edges.

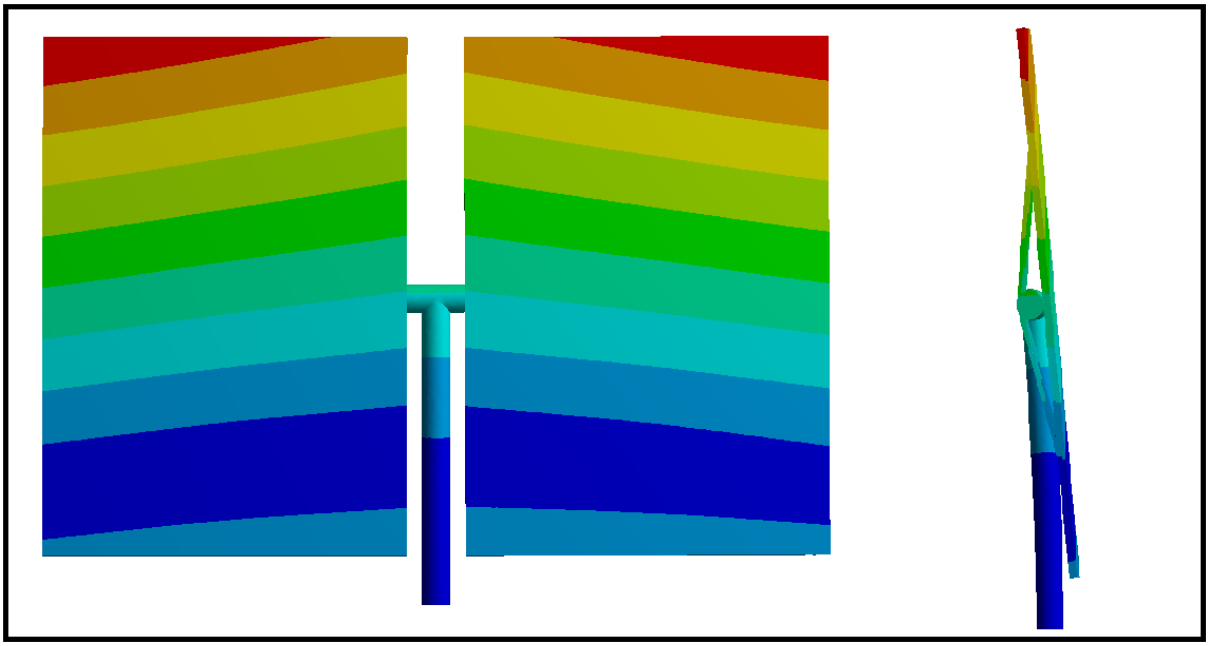

Figure 171: 3rd Mode of the LH-2 at 0 degrees, 2.669Hz.

The SBES vortex shedding for the 60 degree case is calculated at either 1.11 Hz or 1.22Hz. The frequency that is present in every signal output from the structural results is 2.1 Hz with a combination of 5.89 Hz, 6.3 Hz and 6.7 Hz. The 2.1 Hz frequency is an exact match to the 2nd mode. The 2nd, 4th, 5th and 6th mode shapes are shown in Figure 188 and Figure 189.

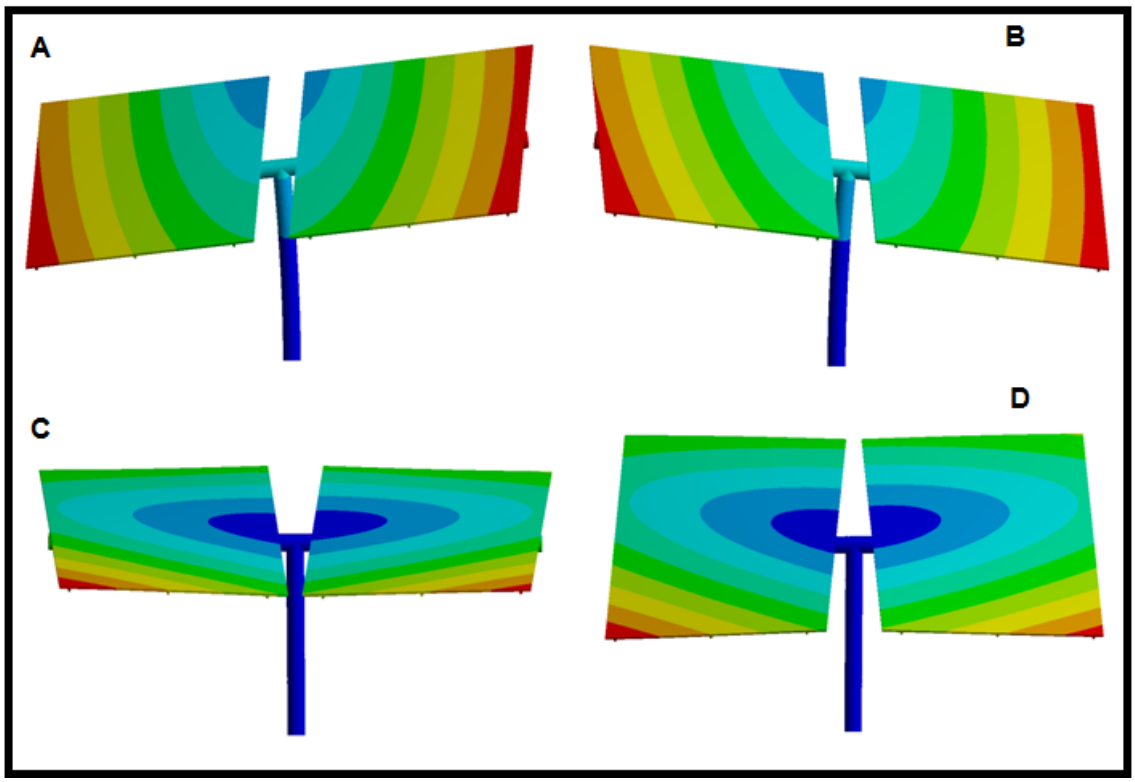

Figure 172: Mode shapes of the 60 degree LH-2. A+B, mode 2 @ 2.11Hz.C+D, mode 4 @ 6Hz.

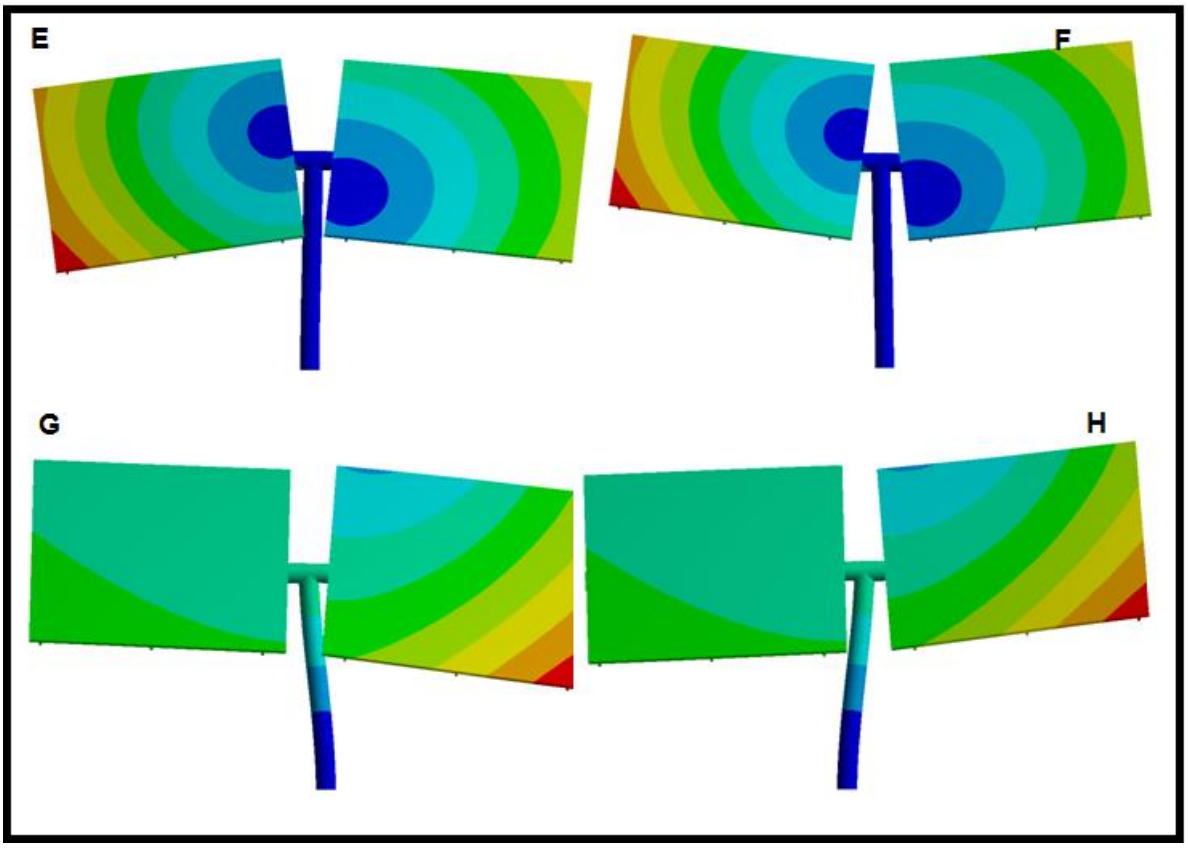

Figure 173: Mode shapes of the 60 degree LH-2. E+F, mode 5 @ 6.45Hz.G+H, mode 6 @ 6.51Hz.

From the results it can be concluded that the dominating movement of the LH-2 at 60 degrees is that of mode 2 at a frequency of 2.1 Hz. The remainder of the deformation is a simultaneous combination of modes 4, 5 and 6.

6.4 CONCLUSION

It can be concluded then that the response of the heliostat is not necessarily defined by the vortex shedding. The response is primarily dictated by the mode shapes and modal frequencies of the heliostat structure in this case. The vortex shedding along with the transient pressure results from the SBES simulation provides the transient loading necessary to initiate the oscillatory behaviour of the heliostat. It would not be sufficient to merely compare the main vortex shedding frequency computed from an SRS simulation to the modal frequencies. As seen in this chapter, the heliostat structure is excited at the modal frequencies even though the vortex shedding frequencies are well below the modal frequencies. It can also be concluded from this section that the heliostat, at least subject to this flow, is not under threat from self-excitation. Without the use of FSI this information would not be possible. Both the SBES and the FSI simulations should be extended as it cannot be concluded whether the excitation of the heliostat will lead to resonance and early fatigue. The FSI does demonstrate the importance of SRS simulations in the analysis of structural components as the results in this chapter would not exist if URANS CFD were implemented.

7 CONCLUSIONS AND RECOMMENDATIONS

7.1 CONCLUSIONS

The aim of this study was the investigation of FSI for a heliostat structure. This included the accurate modelling of the fully-developed atmospheric boundary layer, RANS CFD modelling, SRS CFD, 1-way and 2-way FSI. Some of the important results, conclusions and discoveries realised in each chapter of this study include.

1. The ABL is complex to model and the correct procedures need to be followed to ensure horizontal homogeneity of the flow. This is important as the profiles that are prescribed at the inlet are required to remain intact until they reach the model. In order to obtain horizontal homogeneity, certain boundary conditions are prescribed along with an aerodynamic roughness length. In doing so however, the turbulence intensity profile cannot be matched to the velocity profile. After optimizing both profiles to the data of (Peterka, et al., 1986), it was found that the optimized turbulence intensity profile with a corresponding velocity profile produces a lower aerodynamic coefficient error when compared to an optimized velocity profile and corresponding turbulence intensity profile.
2. (Boddupalli, et al., 2017) and (Breuer, et al., 2003) performed 3D URANS simulations on heliostats or heliostat like geometry and confirmed that transient vortex shedding behaviour could not be modelled without SRS CFD. This was confirmed in chapter 4 with the attempt to model 2-way URANS FSI. It was subsequently confirmed that 3D URANS FSI for the heliostat geometry is futile. 2D URANS CFD simulations however produced resultant vortex-shedding frequencies for both the 0 degree and 60 degree heliostat orientations that were in agreement with experimental work, this was later confirmed by the SBES SRS CFD simulations. The 2D URANS vortex-shedding frequencies matched those of (Matty, 1979) fairly accurately. It can be concluded that the (Matty, 1979) experimental results could be used as a rough starting estimate for the vortex shedding of a heliostat.
3. Scale Resolving Simulations are at the cutting edge of CFD technology. They are required in order to predict the peak loadings on the heliostat and resolve the turbulence in the attacking wind. These methods are extremely expensive and still require large amounts of computing power. It was concluded from the SBES SRS simulations that the free-stream turbulent kinetic energy in the ABL is enough to excite the heliostat structure. The synthetic turbulence generated by the vortex method appears to produce unrealistic pressure distributions in the attacking flow which creates unphysical drag spikes, but these are of very short duration.
4. Performing 1-way FSI with the transient SRS CFD pressure field on the LH-2 heliostat produced interesting results. It can be concluded that it does not suffice to simply match the vortex shedding obtained using SRS CFD to the modes of a structure. The behaviour of the heliostat for the 0 degree configuration is relatively simple, with a back and forth movement. The movement at the 60 degree orientation is highly complex and could not possibly be predicted without the use of FSI. The main conclusion of this chapter is that the LH-2 heliostat's response to the transient loading is not to react at the vortex shedding frequencies but rather to deform at one or more modal frequencies.

The result of this oscillatory behaviour will eventually be increased fatigue and possible damage to the structure if the oscillation amplitudes are large enough. This behaviour needs to be investigated with SRS 1-way FSI. In summary, it can be said that the structure is safe from self-excitation due to the vortex shedding.

7.2 FUTURE RECOMMENDATIONS

Any one of the chapters contained in this study could be extended with further work and research. Much research is still needed in the area of aerodynamic and structural optimization of heliostats in order to increase the viability of the technology. Some important areas for further work regarding this study are presented below.

- 2D 2-way FSI simulations need to be performed for the 60 degree orientation in order to find a possible relationship between the 2D 2-way and 3D 1-way FSI.
- More heliostat orientations need to be implemented and simulated for both the azimuth and elevation angles of the heliostat. This is necessary to conclude the accuracy of both the 2D URANS and 3D SRS vortex shedding predictions.
- The SBES simulations needs to be run for a longer period to ensure the flow is further developed so that the averaged aerodynamic forces are accurate and the statistics of the flow are precise.
- The 1-way FSI utilising the SRS pressure results should be simulated for a longer period to investigate whether the behaviour established for the approximately 3 second period is correct. Structural fatigue should also be further investigated with the oscillatory behaviour of the heliostat.
- 2-way FSI utilising SRS CFD is now possible with system coupling on the CHPC. This needs to be researched and compared to the 1-way FSI of chapter 6. This would however be a costly exercise and the coupling with or without remeshing would need to be established.
- Solar traces of the deformed heliostat geometry could be conducted to investigate the amount of radiation that is lost due to the deflections and oscillations owing to turbulence and vortex shedding.
- The vortex method needs to be further investigated in order to achieve a better understanding of the pressure fluctuations that are generated with this method.

8 BIBLIOGRAPHY

ADINA, 2012. *Theory and Modeling Guide Volume III: ADINA CFD & FSI,* s.l.: ADINA R&D Inc.

Amsbeck, L., Buck, R., Pfahl, A. & Uhlig, R., 2008. Optical performance and weight estimation of a heliostat with ganged facets. *Journal of Solar Energy Engineering.*

ANSYS, 2010. *Introduction to ANSYS Fluent Turbulence Modeling,* Canonsburg PA: ANSYS Inc.

ANSYS, 2016. *Fluent Theory Guide,* Canonsburg, PA: ANSYS Inc.

ANSYS, 2016. *Fluent User's Guide,* Canonsburg PA: ANSYS Inc.

ANSYS, 2016. *Overview of FSI in Workbench,* s.l.: s.n.

ANSYS, 2016. *System Coupling User's Guide,* Canonsburg PA: ANSYS Inc.

Banks, D., 2011. Measuring peak wind loads on solar power assemblies. *ICWE13.*

Barlev, D., Vidu, R. & Stroeve, P., 2011. Innovation in concentrated solar power. *Solar Energy Materials & Solar Cells.*

Blocken, B., Stathopoulos, T. & Carmeliet, J., 2007. CFD simulation of the atmospheric boundary layer: wall function problems. *Atmospheric Environment,* pp. 238-252.

Boddupalli, N., Goenka, V. & Chandra, L., 2017. *Fluid flow analyis behind heliostat using LES and RANS: A step towards optimized filed design in desert regions.* s.l., American Intstitute of Physics.

Breuer, M., Jovicic, N. & Mazaev, K., 2003. Comparison od DES, RANS and LES for the separated flow around a flat plate at high incidence. *International Journal for Numerical Methods in Fluids,* pp. 357-388.

Breuer, M., Munsch, M. & De Nayer, G., 2010. *Fluid-Structure Interaction of a Flexible Structure in a Turbulent Flow using LES,* s.l.: Michael Breuer.

Brightsource, 2014. *Brightsource Ivanpah.* [Online] Available at: http://www.brightsourceenergy.com/ivanpahsolar [Accessed 3 February 2017].

Bungartz, H. & Schafer, M., 2006. *Fluid-Structure Interaction: Modelling, Simulation, Optimisation.* Berlin: Springer.

Cebeci, T. & Bradshaw, P., 1977. *Momentum transfer in boundary layers,* New York: McGraw-Hill Book Co.

Collado, F. & Guallar, J., 2013. A review of optimized design layouts for solar power tower plants with campo code. *Renewable and Sustainable Energy Reviews,* pp. 142-154.

Forsberg, C., Peterson, P. & Zhao, H., 2007. High-Temperature Liquid-Flouride-Salt Closed-Brayton-Cycle Solar Power Towers. *Journal of Solar Energy Engineering,* pp. 129-141.

Fourakis, E. & Severson, A., 1977. Low-Profile heliostat design for solar central reciever systems. *Solar Energy,* pp. 349-356.

Gerasimov, G., 2016. *Quick Guide to Setting Up LES-type Simulations V.1.4,* Sweden: ANSYS Inc.

Ghanadi, F. et al., 2017. *Numerical investigation of wind loads on an operating heliostat.* s.l., American Institute of Physics.

Griffith, T., Moya, A., Clifford, H. & Hunter, P., 2015. Structural Dynamics Testing and Analysis for Design Evaluation and Monitoring of Heliostats. *Solar Energy Engineering.*

Huss, S. et al., 2011. *Evaluating the effects of wind loads on heliostat design.* Grenada, Spain, s.n.

Landman, W., 2016. *HelioPod Heliostat System for MGT CSP.* Stellenbosch, STERG.

Larmuth, J., Malan, K. & Gauche, P., 2014. *Design and cost review of 2m heliostat prototypes.* Port Elizabeth, s.n.

Lienhard, J., 1966. *Synopsis of lift, drag and vortex frequency data for rigid circular cylinders,* s.l.: Washington State University, College of Engineering, Research Division bulletin.

Liu, X. et al., 2007. *A study of non-metallic structures of heliostats.* s.l., s.n.

Lutchman, S., Groenwold, A., Gauche, P. & Bode, S., 2014. On using a gradient-based method for heliostat field layout optimization. *Energy Procedia,* pp. 1429-1438.

Marais, M., 2016. *Computational fluid dynamics investigation of wind loads on heliostat structures,* s.l.: s.n.

Mathey, F., Cokljat, D., Bertoglio, J. & Sergent, E., 2006. Assesment of the vortex method for Large Eddy Simulation inlet conditions. *Progress in Computational Fluid Dynamics,* pp. 58-67.

Matty, R., 1979. *Vortex shedding from square plates near a ground plane: An experimental study,* Texas Tech University: Masters in Mechanical Engineering.

Mavis, C., 1989. *A Description and Assessment of Heliostat Technology,* s.l.: Sandia National Laboratories.

Menter, F., 2011. *Turbulence Modeling for Engineering Flows,* Canonsburg: ANSYS Inc.

Menter, F., 2015. *Best Practice: Scale-Resolving Simulations in ANSYS CFD V.2,* Germany: ANSYS Inc.

Noone, C., Torrilhon, M. & Mitsos, A., 2012. Heliostat field optimization: A new computationally efficient model and biomimetic layout. *Solar Energy,* pp. 792-803.

Peterka, J., Bienkiewicz, B., Tan, Z. & Cermak, J., 1989. Mean and Peak Wind Loads on Heliostats. *Jouranl of solar energy engineering,* pp. 15-164.

Peterka, J. & Derickson, R., 1992. *Wind load design methods for ground based heliostats and parabolic dish collectors,* Springfiled, Alabama, USA: Sandia National Laboratories.

Peterka, J., Hosoya, N., Bienkiewicz, B. & Cermak, J., 1986. *Wind load reduction for heliostats,* s.l.: Solar Energy Research Institute SERI.

Pfahl, A. et al., 2017. Progress in heliostat development. *Solar Energy,* pp. 3-37.

Pfahl, A., Randt, M., Carsten, H. & Unterschutz, S., 2013. Autonomous light weight heliostat with rim drives. *Solar Energy,* pp. 230-240.

Pope, S., 2000. *Turbulent Flows.* Cambridge: Cambridge University Press.

Richards, P. & Hoxey, R., 1993. Appropriate boundary conditions for computational wind engineering methods using the k-e turbulence model. *Jouranal of Wind Engineering and Industrial Aerodynamics,* pp. 145-153.

Richards, P. & Norris, S., 2011. Appropriate boundary conditions for computational wind engineering models revisited. *Journal of Wind Engineering and Industrial Aerodynamics,* pp. 257-266.

Sun, H., Gong, B. & Yao, Q., 2014. A review of wind loads on heliostats and trough collectors. *Renewable and Sustainable Energy Reviews,* pp. 206-221.

Techet, A., 2005. *Design Principles for Ocean Vehicles (13.42).* [Online] Available at: https://ocw.mit.edu/courses/mechanical-engineering/2-22-design-principles-for-ocean-vehicles-13-42-spring-2005/readings/lec20_viv1.pdf
[Accessed 15 June 2017].

Teufel, E. et al., 2008. *Dimensioning of heliostat components under wind and gravity load: The map approach.* Las Vegas, s.n.

White, F., 2011. *Fluid Mechanics.* New York: McGraw Hill.

Wu, Z. et al., 2010. An experimental and numerical study of the gap effect on wind load on heliostats. *Renewable Energy,* pp. 797-806.

Appendix A

User Defined Function for ABL coded in C

```
#include "udf.h"
#define k 0.433 /* Von Karman constant */
#define z0 0.0107615 /* Aerodynamic roughness length 0.000199 */
#define Cmu 0.09 /* Turbulence model constant */
#define Uref 10.5 /* Refernece velocity at height Zref [m/s]15 */
#define Zref 1.4286 /* Reference height [m]1.377 */
#define uABL Uref*k/log(Zref/z0) /* Atmospheric BL friction velocity */

DEFINE_PROFILE(x_velocity,thread,nv)
{
real pos[ND_ND], z;
face_t f;
begin_f_loop(f, thread)
{
F_CENTROID(pos,f,thread);
z = pos[2];
F_PROFILE(f, thread, nv) = Uref*log(z/(z0))/(log(Zref/(z0)));
}
end_f_loop(f,thread)
}

/* Turbulent kinetic energy profile */
DEFINE_PROFILE(k_profile,thread,nv)
{
real pos[ND_ND];
face_t f;
begin_f_loop(f, thread)
{
F_CENTROID(pos,f,thread);
F_PROFILE(f, thread, nv) = (pow(uABL,2)/sqrt(Cmu));
}
end_f_loop(f,thread)
}

/* Turbulent dissipation rate profile */
DEFINE_PROFILE(epsilon_profile,thread,nv)
{
real pos[ND_ND], z;
face_t f;
begin_f_loop(f, thread)
{
F_CENTROID(pos,f,thread);
z = pos[2];
F_PROFILE(f, thread, nv) = pow(uABL,3)/(k*z);
}
end_f_loop(f,thread)
}

/* Specific dissipation rate profile */
DEFINE_PROFILE(omega_profile,thread,nv)
{
real pos[ND_ND], z, e, kay;
face_t f;
begin_f_loop(f, thread)
{
```

```
F_CENTROID(pos,f,thread);
z = pos[2];
kay = pow(uABL,2)/sqrt(Cmu);
e = pow(uABL,3)/(k*z);
F_PROFILE(f, thread, nv) = e/(Cmu*kay);
}
end_f_loop(f,thread)
}

/* Equivalent sandgrain roughness for bottom wall */
DEFINE_PROFILE(roughness_profile,thread,nv)
{
real pos[ND_ND];
face_t f;
begin_f_loop(f, thread)
{
F_CENTROID(pos,f,thread);
F_PROFILE(f, thread, nv) = 9.793*z0/0.5;
}
end_f_loop(f,thread)
}
```

Appendix B

MATLAB code for ABL profile optimisation

```
clear all
clc
format long
yref = 1.13538; % Reference height
Uref = 10; % Reference velocity
k = 0.433; % Von Karman constant for standard k-e model
Cu = 0.09; % Standard k-e constant
zref_coeff = 0.16764; % Reference height for aerodynamic coeff calcs
load pat_turb.dat
load pat_vel.dat
pvel=pat_vel(:,1).*Uref;
pzvel=pat_vel(:,2).*yref;
pturb=pat_turb(:,1)./100;
pzturb=pat_turb(:,2);%.*yref;
options = optimoptions('fminunc');
options.TolX = 0.00001;
options.MaxIter = 1000;

Ervel=@(c) sum((pvel-(Uref*(log(pzvel/c(1)))/(log(yref/c(1))))).^2);
[zov,F1] = fminunc(Ervel,[0.00001],options)
Erturb=@(d) sum((pturb-
((sqrt((2/3).*((Uref*k)/(log((yref+d(1))/(d(1)))))).^2/(sqrt(Cu)))).(Uref*(log(p
zvel/d(1)))/(log(yref/d(1))))))).^2)
[zot,F2] = fminunc(Erturb,[0.00001],options)
%% Velocity optimization %%
uABL = (Uref*k)/(log((yref+zov)/zov));
K=(uABL^2)/(sqrt(Cu)); % Turbulent kinetic energy
xx=linspace(0.01,1.2,1000);
yy=linspace(0.01,1.2,1000);
optpat=Uref*(log(yy/zov)/log(yref/zov));
figure(1)
subplot(1,2,1)
hold on
plot(pvel/Uref,pzvel/yref)%paterka
plot((optpat/10),yy)
xlabel('U(Z)'); ylabel('Z [m]');
title(['Z0 = ',num2str(zov)])
Ti=sqrt(2/3*K)./(optpat);
subplot(1,2,2)
hold on
plot(pturb.*100,pzturb)%paterka
plot((Ti.*100),yy)
xlabel('Ti [%]'); ylabel('Z [m]');
hold off
%% Turbulence Optimization %%
uABLt = (Uref*k)/(log((yref+zot)/zot));
Kt=(uABLt^2)/(sqrt(Cu)); % Turbulent kinetic energy
xx=linspace(0.01,1.2,1000);
yy=linspace(0.01,1.2,1000);
optpatt=Uref*(log(yy/zot)/log(yref/zot));
figure(2)
subplot(1,2,1)
hold on
plot(pvel/Uref,pzvel/yref)%paterka
plot((optpatt/10),yy)
xlabel('U(Z)'); ylabel('Z [m]');
```

```
title(['Z0 = ',num2str(zot)])
Tit=sqrt(2/3*Kt)./(optpatt);
subplot(1,2,2)
hold on
plot(pturb.*100,pzturb)%paterka
plot((Tit.*100),yy)
xlabel('Ti [%]'); ylabel('Z [m]');
hold off
```

Appendix C

PBS job scheduler script and journal script for running the SBES simulations at the CHPC

PBS Script

```
#!/bin/bash
#PBS -l select=10:ncpus=24:mpiprocs=24
#PBS -l aa_r_cfd=1
#PBS -l aa_r_hpc=224
#PBS -q normal
#PBS -P MECH0873
#PBS -l walltime=48:00:00
#PBS -o /home/jwolmarans/scratch/FluentTesting/fluent.out
#PBS -e /home/jwolmarans/scratch/FluentTesting/fluent.err
##### Running commands
export LM_LICENSE_FILE=1055@chpclic1
export ANSYSLMD_LICENSE_FILE=1055@chpclic1
export PATH=/apps/chpc/compmech/CFD/ansys_inc/v181/fluent/bin:$PATH
export FLUENT_ARCH=lnamd64
export PBS_JOBDIR=/home/jwolmarans/scratch/FluentTesting
cd $PBS_JOBDIR
nproc=`cat $PBS_NODEFILE | wc -l`
exe=fluent
$exe 3ddp -t$nproc -pinfiniband -ssh -cnf=$PBS_NODEFILE -g <
/home/jwolmarans/scratch/FluentTesting/LH2/LH2_0.jou > run.out
```

Journal Script

```
(in-package threads-package
  (in-package boundary-thread
    (in-package vm-number-of-vortices
      (define-method (max) 100000))))
/file/read-case-data /home/jwolmarans/scratch/FluentTesting/LH2/LH2_SBESPres_62080.cas.gz
/solve/dti 3300 70
/file/write-case-data /home/jwolmarans/scratch/FluentTesting/LH2/LH2_SBESPres_%t.cas.gz
exit y
```

Appendix D

Side view of SBES Iso-Surfaces of Q-criterion coloured by velocity magnitude of SBES fine mesh 0 degree over 3 seconds Q=100s^{-2}.

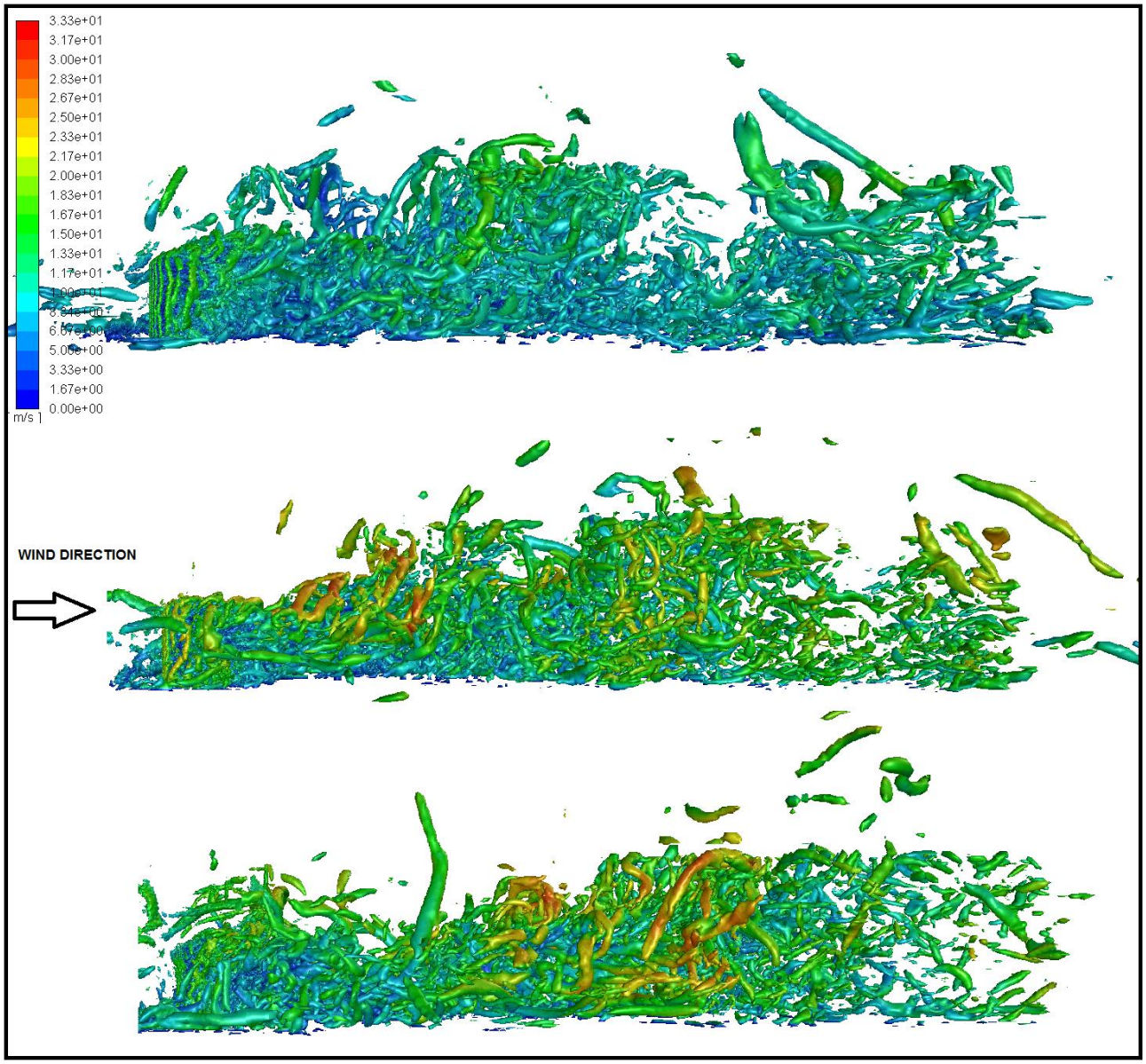

Appendix E

Coarse mesh SBES results.